Mapping of multitemporal rice (*Oryza sativa L.*) growth stages using remote sensing with multi-sensor and machine learning

A thesis dissertation presented in partial fulfilment of the

requirements for the degree of

Doctor of Philosophy

in

Earth Science

at Massey University, Manawatū, New Zealand.

Fadhlullah Ramadhani

2022

[intentionally blank]

Abstract

Rice (*Oryza Sativa*) plays a pivotal role in food security for Asian countries, especially in Indonesia. Due to the increasing pressure of environmental changes, such as land use and climate, rice cultivation areas need to be monitored regularly and spatially to ensure sustainable rice production. Moreover, timely information of rice growth stages (RGS) can lead to more efficient of inputs distribution from water, seed, fertilizer, and pesticide. One of the efficient solutions for regularly mapping the rice crop is using Earth observation satellites. Moreover, the increasing availability of open access satellite images such as Landsat-8, Sentinel-1, and Sentinel-2 provides ample opportunities to map continuous and high-resolution rice growth stages with greater accuracy. The majority of the literature has focused on mapping rice area, cropping patterns and relied mainly on the phenology of vegetation. However, the mapping process of RGS was difficult to assess the accuracy, time-consuming, and depended on only one sensor.

In this work, we discuss the use of machine learning algorithms (MLA) for mapping paddy RGS with multiple remote sensing data in near-real-time. The study area was Java Island, which is the primary rice producer in Indonesia. This study has investigated: (1) the mapping of RGS using Landsat-8 imagery and different MLAs, and their rigorous performance was evaluated by conducting a multitemporal analysis; (2) the temporal consistency of predicting RGS using Sentinel-2, MOD13Q1, and Sentinel-1 data; (3) evaluating the correlation of local statistics data and paddy RGS using Sentinel-2, PROBA-V, and Sentinel-1 with MLAs.

The ground truth datasets were collected from multi-year web camera data (2014-2016) and three months of the field campaign in different regions of Java (2018). The study considered the RGS in the analysis to be vegetative, reproductive, ripening, bare land, and flooding, and MLAs such as support vector machines (SVMs), random forest (RF), and artificial neural network (ANN) were used. The temporal consistency matrix was used to compare the classification maps within three sensor datasets (Landsat-8 OLI, Sentinel-2, and Sentinel-2, MOD13Q1, Sentinel-1) and in four periods (5, 10, 15, 16 days). Moreover, the result of the RGS map was also compared with monthly data from local statistics within each sub-district using cross-correlation analysis.

The result from the analysis shows that SVM with a radial base function outperformed the RF and ANN and proved to be a robust method for small-size datasets (< 1,000 points). Compared to Sentinel-2, Landsat-8 OLI gives less accuracy due to the lack of a red-edge band and larger pixel size (30 x 30 m). Integration of Sentinel-2, MOD13Q1, and Sentinel-1 improved the classification performance and increased the temporal availability of cloud-free maps. The integration of PROBA-V and Sentinel-1 improved the classification accuracy from the Landsat-8 result, consistent with the monthly rice planting area statistics at the sub-district level. The western area of Java has the highest accuracy and consistency since the cropping pattern only relied on rice cultivation.

In contrast, less accuracy was noticed in the eastern area because of upland rice cultivation due to limited irrigation facilities and mixed cropping. In addition, the cultivation of shallots to the north of Nganjuk Regency interferes with the model predictions because the cultivation of shallots resembles the vegetative phase due to the water banks. One future research idea is the auto-detection of the cropping index in the complex landscape to be able to use it for mapping RGS on a global scale.

Detection of the rice area and RGS using Google Earth Engine (GEE) can be an action plan to disseminate the information quickly on a planetary scale. Our results show that the multitemporal Sentinel-1 combined with RF can detect rice areas with high accuracy (>91%). Similarly, accurate RGS maps can be detected by integrating multiple remote sensing (Sentinel-2, Landsat-8 OLI, and MOD13Q1) data with acceptable accuracy (76.4%), with high temporal frequency and lower cloud interference (every 16 days).

Overall, this study shows that remote sensing combined with the machine learning methodology can deliver information on RGS in a timely fashion, which is easy to scale up and consistent both in time and space and matches the local statistics. This thesis is also in line with the existing rice monitoring projects such as Crop Monitor, Crop Watch, AMIS, and Sen4Agri to support disseminating information over a large area. To sum up, the proposed workflow and detailed map provide a more accurate method and information in near real-time for stakeholders, such as governmental agencies against the existing mapping method. This method can be introduced to provide accurate information to rice farmers promptly with sufficient inputs such as irrigation, seeds, and fertilisers for ensuring national food security from the shifting planting time due to climate change.

Acknowledgements

"In the name of Allah, the Most Gracious, the Most Merciful."

First and above all, I praise Allah SWT, the almighty God, for providing me with this opportunity and granting me the finish the last step of my doctoral study. This final thesis comes from the assistance and guidance of some people. I would like to give all of them my sincere thanks as follows:

Firstly, I would like to thank my supervisors (Dr Reddy Pullanagari, Dr Gabor Kereszturi, and Prof. Jonathan Procter) for their constant help, support, and encouragement for finishing this degree even my performances are not always at the top. I also thank Mike Thouy for letting me enrol at Massey University.

I gratefully acknowledge the help and expertise of many other people from the Indonesian Agency for Agricultural Research and Development as follows Dr Gatot Irianto, Dr Haris Syabuddin, Dr Haryono, Dr Husnain, Dr Harmanto, Dr Yayan Apriyana, Dr Rizatus Shofiyati, late Dr Eleonora Runtunuwu, and all my colleagues from Indonesian Agroclimate and Hydrology Research Institute and Prof M. Rokhis Khomarudin and Dr Dede Dirgahayu from LAPAN.

I would like to thank my colleagues (Frederico, Sue Chok, Tom, Megan, Fernando, Istvan Hajdu, Suha, Bawa, Fernando, Setfi) for their encouragement and support during the fun and hard time in AHB 1.10.

I am thankful for the scholarship and the financial support from the Indonesian Agency for Agricultural Research and Development scholarship with the SMART-D programme and all the teams, especially Ibu Arini, Ibu Zizi, dan Pak Mulyadi.

I would like to thank my wife Farida Hanum, and my son Fardhan Hasan Ramadhani, my sisters Fathnuriati Hidayah and Fatma Fajar Yani, and my mother-in-law Rusna Ibrahim, and friends in Indonesia (Ronal, Erni Susanti, Elsa Suharmaini, and Misnawati) and Palmerston North (Nandi, Yuni, Yulfia, Arini, Kodrat, Rijal, Ratna, Idry, Arini, and Gina) for the moral support.

Lastly, to my late mother (Maryati) and my late father (Alfatah), thank you for your patience, advice, and showering me with love throughout my life. May we all gather in Jannah.

"Praise be to Allah, the Lord of the Universe"

Table of contents

List of figures

List of tables

List of appendices

Abbreviations

ALOS	:	Advanced Land Observing Satellite
AMIS	:	Agricultural Market Information System
ANN	:	Artificial neural networks
ANOVA	:	Analysis of variance
ASTER	:	Advanced Spaceborne Thermal Emission and Reflection Radiometer
AVHRR	:	Advanced Very High-Resolution Radiometer
BPS	:	*Badan Pusat Statistik*/ Indonesian Statistics Agency
CAS	:	Chinese Academy of Sciences
CART	:	Classification and Regression Tree
CCD	:	Charge-coupled device
CCTV	:	Closed-circuit television
CFMASK	:	Code based on the Function of Mask (Fmask) algorithm
CGL	:	Copernicus Global Landcover
CHC	:	Climate Hazards Center
CHIRPS	:	Climate Hazards Center InfraRed Precipitation with Station data
COSMO	:	Constellation of Small Satellites for Mediterranean basin Observation
CRAN	:	Comprehensive R Archive Network
DEM	:	Digital Elevation Model
DOI	:	Digital Object Identifier
ECMWF	:	European Centre for Medium-Range Weather Forecasts
EnMAP	:	Environmental Mapping and Analysis Program
ENSO	:	El Niño-Southern Oscillation
EO	:	Earth observation
EU	:	European Union
ERS	:	European Remote Sensing
ESA	:	European Space Agency
ETM	:	Enhanced Thematic Mapper
ESTARFM	:	Enhanced Spatial and Temporal Adaptive Reflectance Fusion Model
EVI	:	Enhanced vegetation index
EVI2	:	Enhanced vegetation index with two bands
EW	:	Extra-Wide Swath Mode
FAO	:	Food and Agriculture Organization
FAOSTAT	:	Food and Agriculture Organization Corporate Statistical Database
FMASK	:	Function of mask

FSDAF	:	Flexible Spatiotemporal DAta Fusion
GEE	:	Google Earth Engine
GEOGLAM	:	GEO Global Agricultural Monitoring
GIEWS	:	Global Information and Early Warning System
GIS	:	Geographic Information System
GMES	:	Global Monitoring for Environment and Security
GLCM	:	Gray Level Co-occurrence Matrix
GPR	:	Gaussian process regression
GPS	:	Global Positioning System
HJ	:	*Huanjing*
HV	:	Horizontal-vertical backscatter
IAARD	:	Indonesian Agency for Agricultural Research and Development
IAHRI	:	Indonesian Agroclimate and Hydrology Research Institute
IRRI	:	International Rice Research Institute
IW	:	Interferometric Wide Swath
LAI	:	Leaf area index
LANDSAT	:	Land Satellite
LAPAN	:	*Lembaga Penerbangan dan Antariksa Nasional*/Indonesian National Institute of Aeronautics and Space
LOOCV	:	Leave-one-out cross-validation
LSWI	:	Land Surface Water Index
MAD	:	Mean of absolute differences
MARS	:	Monitoring Agricultural ResourceS
METEOSAT	:	Meteorological Satellite
ML	:	Machine learning
MLA	:	Machine learning algorithm
MOD13Q1	:	MODIS/Terra Vegetation Indices 16-Day L3 Global 250m SIN Grid
MODIS	:	Moderate Resolution Imaging Spectroradiometer
MSS	:	Multispectral Scanner System
NASA	:	US National Aeronautics and Space Administration
NDVI	:	Normalized Difference Vegetation Index
NIR	:	Near InfraRed
NOAA	:	US National Oceanic and Atmospheric Administration
NPP	:	National Polar-orbiting Partnership
OA	:	Overall accuracy
OECD	:	Organisation for Economic Co-operation and Development
OLI	:	Operational Land Imager
PA	:	Producer's Accuracy
PALSAR	:	Phased Array type L-band Synthetic Aperture Radar
PRISMA	:	*PRecursore IperSpettrale della Missione Applicativa*

PROBA-V	:	Project for On-Board Autonomy-Vegetation
PUSDATIN	:	Center of Agriculture Information, Indonesian Ministry of Agriculture
RADAR	:	Radio Detection and Ranging
RADARSAT	:	RADAR Satellite
RADI	:	Institute of Remote Sensing and Digital Earth
RF	:	Random Forest
RGB	:	Red, Green, Blue
RIICE	:	Remote Sensing-based Information and Insurance for Crop in Emerging Economies
RGS	:	Rice growth stage
RMSE	:	Root Mean Square Error
RS	:	Remote sensing
SAR	:	Synthetic Aperture Radar
SAVI	:	Soil Adjusted Vegetation Index
SLC	:	Scan line corrector
SMART-D	:	Sustainable Management of Agricultural Research and Technology Dissemination
SPOT	:	*Satellite Pour l'Observation de la Terre*
SRTM	:	NASA's Shuttle Radar Topography Mission
STARFM	:	Spatial and Temporal Adaptive Reflectance Fusion Model
SVM	:	Support vector machine
SWIR	:	Short-wave infrared
TIRS	:	Thermal infrared sensor
TM	:	Thematic Mapper
TS	:	Theil-Sen
UA	:	User's Accuracy
UAV	:	Unmanned aerial vehicle
US	:	United State of America
USGS	:	United States Geological Survey
UTM	:	Universal Transverse Mercator
VH	:	Vertical-horizontal backscatter
VI	:	Vegetation index(es)
VIIRS	:	Visible Infrared Imaging Radiometer Suite
VV	:	Vertical-vertical backscatter
WGS	:	World Geodetic System

Chapter 1 Introduction

1.1 Background

Rice is an important crop in Indonesia as it is a staple food, along with maize and sago. Indonesia produced ~54.6 million tonnes of dry unhusked rice (equal to ~36.4 million tonnes of rice milled) in 2019 to maintain food security (FAOSTAT, 2021). However, this production rate will not be sufficient to secure food for more than 284 million people who are projected to exist in 2025 (FAOSTAT, 2016) with a rice consumption rate of 163 kg per capita (OECD, 2015) and limited productive wetland. Productive and profitable rice production has some critical issues to manage, such as the availability of water, healthy seeds, machinery, fertiliser, soil, climate, and human resources.

Moreover, rice cultivation in Indonesia faces serious challenges, such as a high rate of land-use change due to urbanisation of the productive paddy area, as 109,000 hectares of rice growing area has been converted in the last two decades (Simatupang & Peter Timmer, 2008). Moreover, drought and flooding will be more frequent in the future due to global warming (Surmaini et al., 2015). The consequent reduction in rice production was estimated to be short of the average by a million tonnes during drought years due to El-Niño in Indonesia between 1997 and 1998 (D'Arrigo & Wilson, 2008). This can also drive market prices higher than usual. The main rice producers are mainly Asian countries except for those on the American continent, such as the United States of America and Brazil (Figure 1.1). Moreover, Indonesia is also dependent on other countries, such as Vietnam and Thailand for extra rice storage buffer. Thus, monitoring the paddy area is crucial for agricultural stakeholders to prepare and mitigate if any disaster occurs, which could disrupt a regular production cycle.

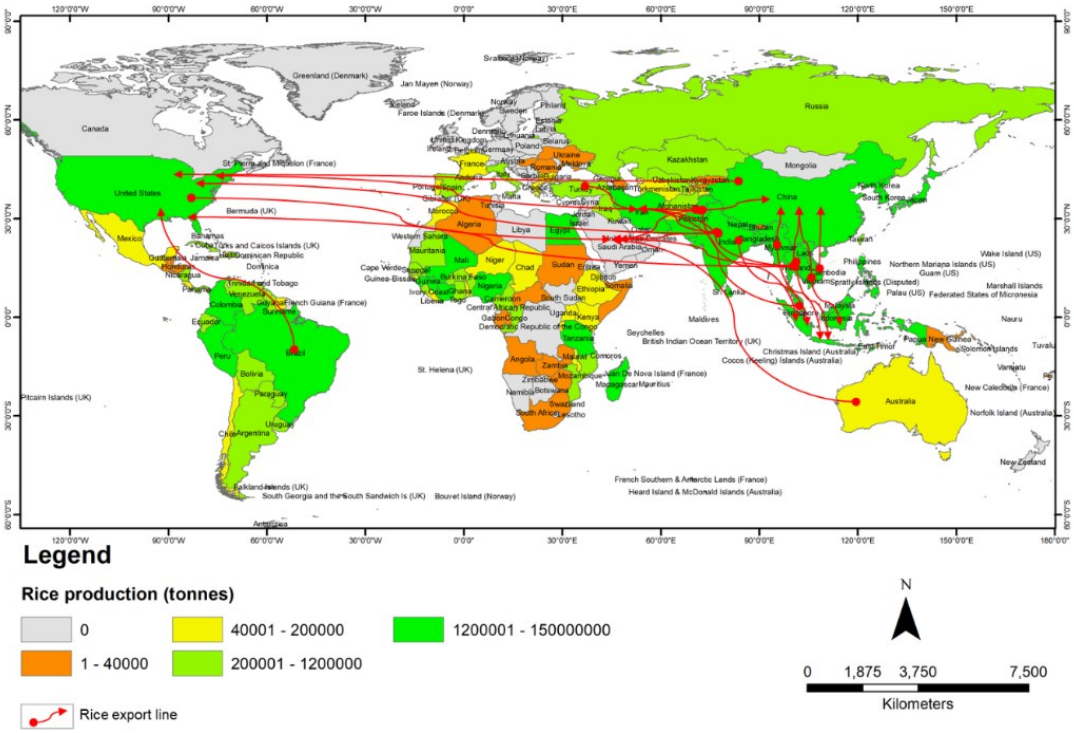

Figure 1.1 Worldwide rice production map and top four rice importing countries from top five rice exporters in 2019. Compiled from http://www.fao.org/faostat, http://www.worldstopexports.com/, and https://www.bps.go.id/

1.2 Mapping rice growth stages using a remote sensing approach

In Indonesia, the common practices for monitoring paddy areas are carried out by tabular hierarchical reporting from government extension workers to the upper level, such as the district level, regency level, province-level up to the Ministry of Agriculture (MoA) within more than one month (BPS, 2018). This data is spatially biased since the extension workers measure and extrapolate the area based on visual estimation. Thus, an objective and spatially unbiased approach is required to accompany the management practices in rice cultivation areas.

Remote sensing technology offers an opportunity to monitor rice crops on a large scale and provides continuous spatial information, more so than the conventional estimation can. Moreover, the monitoring of a rice area could be separated based on the rice's growth stage, which can be divided into three key growing stages: (1) vegetative stage begins with germination and ends with panicle initiation. The length of vegetative growth varies with variety, typically from 45 to 65 days, (2) reproductive stage includes panicle to flowering,

which lasts approximately 35 days, and (3) ripening stage begins with flowering and ends with the mature grain (approximately 25 to 30 days) (Vergara, 1991). Each growth stage has contrasting optical properties, which enable the detection of the rice growth stages (RGS) accurately using remote sensing. For example, the vegetative stage can be discriminated from other stages based on low reflectance in the visible region (wavelength: 370 to 700 nm) due to inundated paddocks with water. The greenest stage is the reproductive stage because of the highest reflectance values in the near-infrared (NIR) region (wavelength: 701 to 900 nm), followed by a decrease in the NIR band(s) values at the ripening stage due to the yellowing of the leaves (K.-W. Chang et al., 2005). A specific signal of bare land could be spotted with low reflectance in the NIR region and the highest reflectance in the short-wave infrared (SWIR) region (1 to 1,3 μm) since there is no paddy cultivated (Li et al., 2014).

Several techniques for mapping the rice area have been developed over several decades by using various satellite sensors and computational algorithms. According to Dong and Xiao (2016), the source of the data can be divided into three categories: (1) optical satellite data such as Landsat Multispectral Scanner System (MSS), Landsat Thematic Mapper (TM), Landsat 5-8, SPOT XS, ERS-1, Moderate Resolution Imaging Spectroradiometer (MODIS), FormoSat, and Sentinel-2; (2) Synthetic aperture radar (SAR) is a type of active sensor that produces its own energy in the microwave and radio portions of the electromagnetic spectrum and then records the reflected energy from the Earth's surface. The SAR signals can penetrate through clouds to detect the surface cover. The SAR sensors are divided into different categories depending on their wavelength, also referred to as bands. For example, C-band (7.5 to 3.8 cm) sensors are RADARSAT and Sentinel-1, with moderate penetration capacity to interact with surface features. The Advanced Land Observing Satellite (ALOS)/ Phased Array type L-band Synthetic Aperture Radar (PALSAR) L band sensor (30 to 15 cm) has greater penetration capacity and is widely used for forest and geophysical monitoring. TanDEM-X is an X-band sensor that has low penetration capacity. (3) A hybrid composition between two or more optical and/or SAR data. Among these data sources, the investigators prefer the optical sensor due to ease of access and detailed information, even if there are some drawbacks from the thick haze and long-lasting cloud cover in tropical countries (Shao et al., 2001).

The European Space Agency (ESA), with the Copernicus project, complements efforts at the USGS to monitor the Earth in near-real-time from satellites (Malenovský et al., 2012). The Copernicus project with the Sentinel mission has launched four satellites with different purposes and specifications. Sentinel-1 has a two satellites constellation with a revisit time of six days (Torres et al., 2012). The primary purpose of Sentinel-1 is to provide data under all-weather conditions using C-band Synthetic Aperture Radar (C-SAR) because of its ability to capture the Earth's surface during both day and night and penetrate cloud and haze. The resolution of Sentinel-1 varies from 3.5 m to 100 m, depending on the acquisition mode.

Regular rice growth monitoring requires high-frequency temporal data (e.g., three days) to better recognise its rapidly changing phenological stages in tropical climates where cloud and shadow reoccurrence is common. The previous studies relied only on MODIS data with coarse resolution (Sakamoto et al., 2005). Studying the integration of multiple satellite images with better resolution such as Landsat-8, Sentinel-1, and Sentinel-2 for the temporal analysis of rice growth is still limited, especially in developing countries due to researchers being more focused on determining rice area.

Rice or paddy cultivation area monitoring with remote sensing has been developed on a regional scale, such as Crop Monitor from Group on Earth Observations Global Agricultural Monitoring Initiative (GEOGLAM) using the normalised difference vegetation index (NDVI) values. It can be accessed through cropmonitor.org (Whitcraft et al., 2015). It shows an early warning of the crop's condition, such as favourable or failure and the leading cause of the condition based on season predictions such as flooding or drought. However, the information cannot be accessed at the sub-district level due to coarse resolution (250 x 250 m). Another project is Remote Sensing-based Information and Insurance for Crops in Emerging economies (RIICE), a project of IRRI using Sentinel-1 data. However, this project cannot provide information in Indonesia (Nelson et al., 2014). Thus, the Indonesian government, through the National Institute of Aeronautics and Space (LAPAN) and the Indonesian Agency for Agricultural Research and Development (IAARD), has launched a programme using MODIS and the enhanced vegetation index (EVI) threshold method from 2013. They monitor RGS in different rice ecosystems in Indonesia with a 250 m spatial resolution (Domiri, 2017). To increase the spatial clarity of the observations, they have started using Landsat-8 OLI in 2015 (Parsa & Dirgahayu,

2013). The spatial rice growth phases information in GEOGLAM and LAPAN is calculated based on different models and outputs. The MODIS-based map gives six classes (flooding, vegetative 1, vegetative 2, generative 1, generative 2, and bare land). On the other hand, the RGS map based on Landsat-8 gives users eight classes, including bare land, cultivated, vegetative 1, vegetative 2, maximum vegetative, generative 1, generative 2, and harvested. Moreover, they have weaknesses such as: (1) the consistency of both models has not been investigated yet, (2) the accuracy of both models is difficult to check due to coarse resolution and restricted access, and (3) improving the model is not an easy task since both models rely on EVI time series data. Thus, the need to build a robust method using multi-source remote sensing data is growing unprecedentedly.

The development of rice monitoring based on remote sensing has been a complex process from obtaining field data, labelling the dataset, the analysis process and dissemination to users or stakeholders through the internet. One of the alternatives to shorten the process is to use Google Earth Engine (GEE) which can increase the processing speed, modelling, display, and information sharing to the public. GEE stores planetary-scale and long-time series remote sensing data from multiple satellites that can be used instantly through cloud computing (Gorelick et al., 2017). The GEE interface is accessible to everyone and programmable using Java and Python, with a strong community and shared code through StackOverflow and Github.

Many researchers have used the GEE as their data source or hub and created geospatial applications. Examples of the use of the GEE environment include mapping cropland (Aneece & Thenkabail, 2018; Teluguntla et al., 2018), wetland (Amani, Brisco, et al., 2019; Amani, Mahdavi, et al., 2019; Hao et al., 2019; Mahdianpari et al., 2020; Mahdianpari et al., 2018), land-use change (Hao et al., 2019; Li et al., 2019; Pulighe & Lupia, 2016; Sidhu et al., 2018; Venkatappa et al., 2019; Zurqani et al., 2018), and many more. However, the implementation of rice monitoring is still limited, and it has only exploited the data access from GEE (Ramadhani et al., 2020a, 2020b; Rudiyanto et al., 2019) for mapping rice growth stages, the rice area, and cropping pattern.

1.3 Research objectives

The overall purpose of this research is to use combined satellite imagery sources to map the rice growth stages based on four specific objectives, on the different scenarios as follows:

a) To investigate the accuracy of prediction models using different machine learning classifiers for mapping rice growth stages with Landsat-8 and their temporal performance over different years.
b) To predict rice growth stages using multi-source remote sensing data Sentinel-2, MOD13Q1, and Sentinel-1 in the dry season.
c) To investigate the correlation between rice growth stages with 100m spatial resolution from PROBA-V and Sentinel-1 and rice planting and harvested areas from local statistics at the sub-district level.
d) To investigate the capability of Google Earth Engine for mapping the lowland rice area and rice growth stages and assessing its accuracy.

The contribution of these works will be significant for building sustainable and near-real-time monitoring of rice production in Indonesia to replace the existing monitoring. Moreover, some methods from this thesis are applicable to monitor other crops, such as maize, sugarcane and wheat; this application comes with no extra costs.

1.4 Thesis outline and structure

This thesis consists of seven chapters. The second chapter after the introduction is a literature review to critically review the existing work, identify the knowledge gaps, and inform the development of research methods to produce rice growth stages maps. The third until the sixth chapters are in journal form, which serves to fulfil the objectives of this thesis. The third, fourth, fifth chapters have already been published, and the sixth chapter is submitted to respected international journals. Each publication contains its introduction, methods, results, discussion, and conclusion. Since the aim of each publication is nearly similar, there is some overlapping of the introduction and conclusion. However, the methods, results, and discussion are distinctly different. Each manuscript publication was written by this thesis author and guided by supervisors. Moreover, all the submissions and emendations from the reviewers have been completed by this thesis author along with

helpful comments from the supervisors. The last chapter is the general discussion to summarise and conclude the thesis results. The workflow of this thesis can be seen in Figure 1.2.

The structure of this thesis is as follows:

Chapter 1 : Provides the background and the objectives outlining the research in the thesis.

Chapter 2 : Gives a general overview of previous knowledge and explains the knowledge gap about existing rice monitoring.

Chapter 3 : Investigates the use of the existing in-situ monitoring using webcam stations to build a high accuracy model of Landsat-8 and its consistency over three years.

Chapter 4 : Building a fusion model from Sentinel-2, MOD13Q1, and Sentinel-1 to map rice growth stages using field campaign data with 10m spatial resolution and its consistency over a 16-day period in the dry season.

Chapter 5 : Assessing the correlation between rice growth stages from PROBA-V and Sentinel-1 and the rice planting area and harvested area from local statistics.

Chapter 6 : Investigating Google Earth Engine for mapping the rice area and rice growth stages in the lowland areas.

Chapter 7 : Summarise the findings from Chapters 3 to 6. It also provides advantages, limitations, future research, and finally, concludes the thesis from the introduction to the general discussion

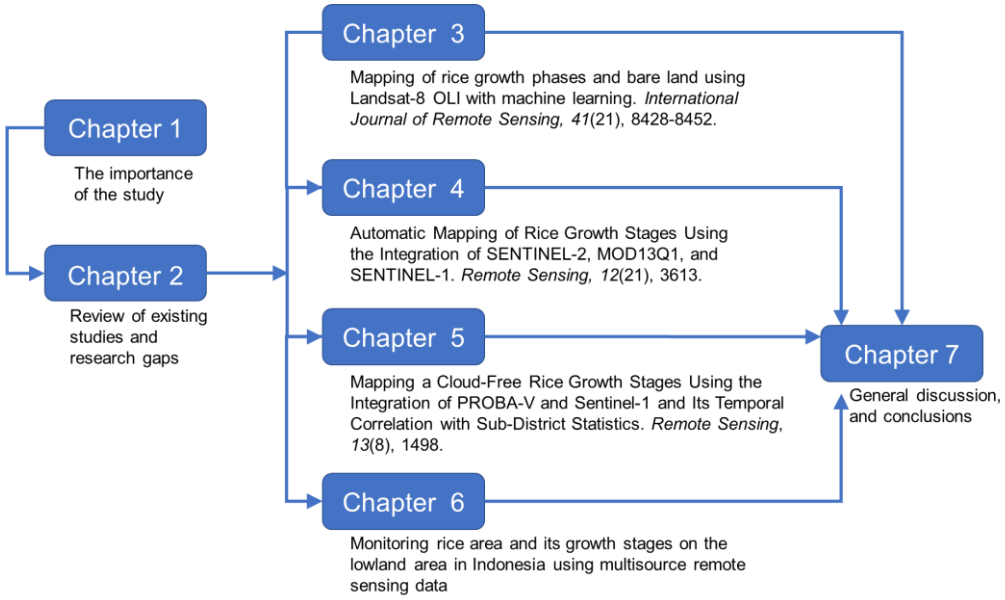

Figure 1.2 The thesis outline.

Chapter 2 Mapping rice area and rice growth stages

2.1 Introduction

Rice is one of the essential cereal commodities, especially in Asian countries, with a total production of 677 million tonnes in 2019 and tends to grow over time. For example, rice production has steadily increased in Indonesia from 8 million tonnes in 1961 to 39 million tonnes in 2018 by introducing high yielding varieties as a result of the "Green Revolution" (Djurfeldt & Jirström, 2005) (Figure 2.1). Despite the increased demand for food, productivity has been increased and stabilised since 1997, but the area has slightly increased to maintain the higher production (Panuju et al., 2013). Moreover, the trendlines show that the population of Indonesia has been increasing by ~316,000 annually and is projected to be ~330 million by 2050. Innovations are needed to increase the harvested area and productivity, such as opening new rice fields (Putra et al., 2008), introducing new super rice varieties (Yu et al., 2020), and mechanisation (Mano et al., 2020). The remote sensing-based rice monitoring projects could provide insights about the rice's condition which are regularly updated to have better spatial information with a minimal cost.

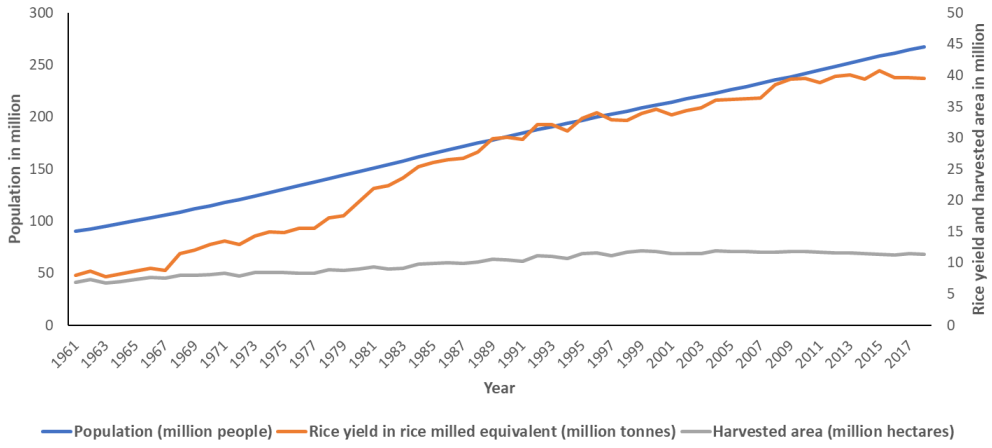

Figure 2.1 The population statistics, rice production in milled rice equivalent, and harvested area in Indonesia from 1961 to 2018. Compiled from FAOSTAT (2020a)

The detailed information about rice cultivation and its growth stages is vital for understanding rice physiology. Rice is an annual grass with round, long grains with collars joined with sheaths of leaves; delicate, sickle-shaped, hairy heads; short, acute, or double split panics; and terminal panicles. The life cycle of rice varies from 105 to 145 days,

depending on the variety and the climate. RGS can be split into three stages: 1) vegetative, 2) reproductive, and 3) ripening. The process of vegetative growth is characterised by active tillering, a gradual increase in plant height and the frequent appearance of leaves. It starts from seed germination, seedling emergence, small tillering which develops into maximum tillering. The second phase is reproductive, characterised by the elongation of the culm, the decrease in tillers, booting, flag leaf emergence, heading, and flowering. In most cultivars, the reproductive phase usually lasts approximately 30 days. The final stage is grain filling, and the ripening and ripening process is distinguished by ovarian fertilisation. Over that period, the grain increases in size and weight as the starch and sugars are transferred from the crests and leaf sheaths; the grain colour changes from green to gold or straw when ripened, and rice plant leaves start senescing. Figure 2.2 illustrates the process of RGS during the growth cycle.

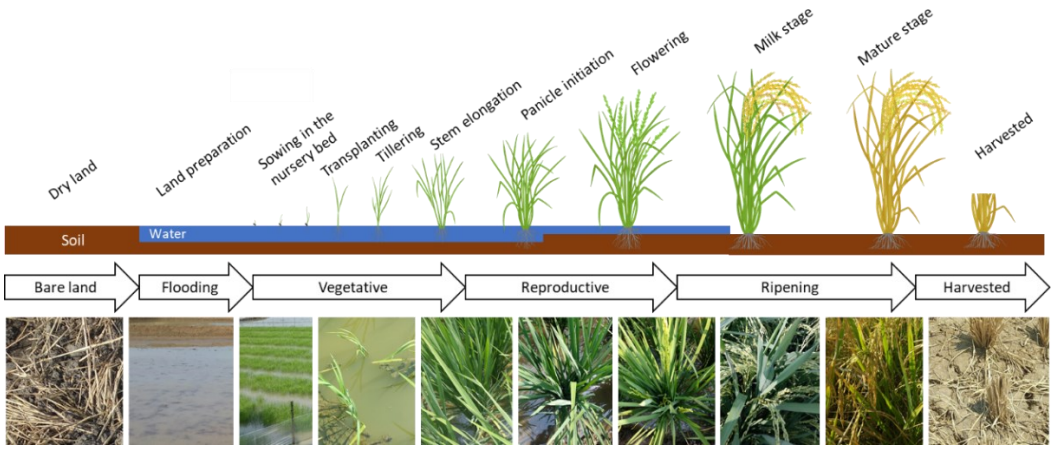

Figure 2.2 The rice growth stages with photos from the field survey. Modified from Kawamura et al. (2018)

Remote sensing collects information about an object without physical contact (Jensen, 2015). The information can be of several types, including differences in force distribution, acoustic wave distribution, or electromagnetic energy delivery to a sensor. Remote sensing can be divided into several major parts: capturing object information using a sensing system and interpreting the digital images into information products for the user. The workflow of the remote sensing system can be seen in Figure 2.3.

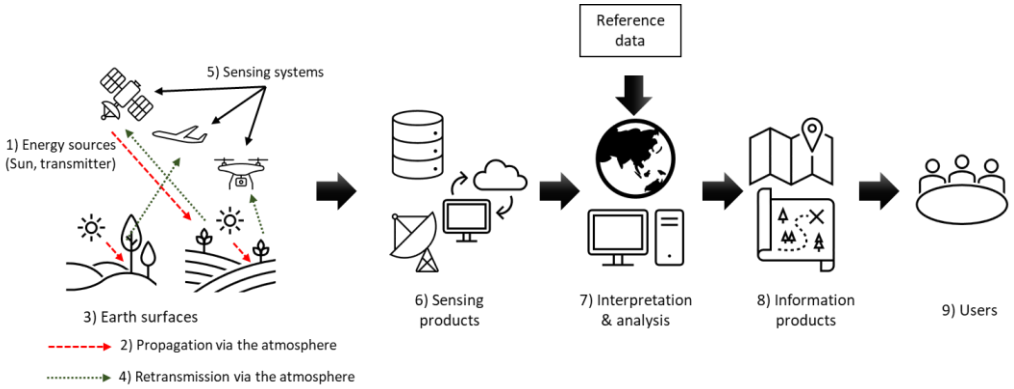

Figure 2.3 The typical process of remote sensing processing. Adopted from Lillesand et al. (2015)

Remote sensing is capable of producing timely and reliable information related to rice ecosystems. Consequently, a wide range of applications have been developed at various levels and scales such as tracking and mapping rice area's development, mapping RGS, cropping patterns, rice health, disease infestation and pests, forecasting rice yields, and estimation of methane fluxes, as shown in Table 2.1

Table 2.1 The examples of remote sensing research on different applications and scales.

No	Application	Scale	References
1	Mapping rice area	> million ha	(Bazzi et al., 2019; Gumma et al., 2011; Jin et al., 2016; Qiu et al., 2015; Salmon et al., 2015; Xiao et al., 2006)
2	Mapping rice growth stages	> million ha	(Ramadhani et al., 2020a, 2020b, 2021; Rudiyanto et al., 2019)
3	Mapping cropping pattern	> million ha	(Bharathkumar & Mohammed-Aslam, 2015; Chandna & Mondal, 2020; Ding et al., 2020; Z. Liu et al., 2019; Lunetta et al., 2010; Minh et al., 2019; Rudiyanto et al., 2019; Sianturi et al., 2018; Tingting & Chuang, 2010)
4	Mapping drought and floods in a particular rice area	< million ha	(Kwak et al., 2015; Parida et al., 2008; Son & Thanh, 2020; Wassmann et al., 2019)
5	Forecasting yields	< thousand ha	(Alam et al., 2019; Pagani et al., 2019; Peng, 2009; Peng et al., 2014; Son et al., 2014; Y. Zhang et al., 2017)
6	Mapping disease and pests affected rice area	< thousand ha	(Huang et al., 2012; Prasannakumar et al., 2014; Qin & Zhang, 2005; Zhihao et al., 2003)
7	Estimating greenhouse gasses	> million ha	(Torbick, Salas, et al., 2017; Zhang et al., 2011)

Tracking rice growth is essential nowadays. The development of rice areas is slowing down due to unprecedented land-use changes. For example, many rice areas in Indonesia are being converted into palm oil areas because they are more profitable than cultivating rice (Daulay et al., 2016). Moreover, the rice areas are scattered in many islands, especially on low-lying land and the flat areas near the seacoast.

The review of rice mapping has been discussed thoroughly in several publications: (i) (Niel & McVicar, 2004) conferred the potential of employing remote sensing in Australia to identify rice canopies using vegetation indices as a method of classifying the rice area and estimating the rice yield. They concluded that higher resolution images are essential to cover small paddocks. (ii) Kuenzer and Knauer (2013) discussed different techniques for mapping rice areas using radar backscattering to multitemporal vegetation indices derived from multiple resolutions images. Their conclusion is that the application of rice area mapping should be inexpensive, simple and easy to implement. Mosleh et al. (2015) focused on developing optical and radar-based techniques for mapping rice areas and estimating yields. For yield prediction, they considered auxiliary data such as meteorological information and crop models for accessing climate change effects in the future. Many authors are concerned about the uncertainty with wide-area implementation since the threshold value can differ depending on the cropping pattern. The latest review paper (Bégué et al., 2018) focused on the evolution of rice mapping methods from simple classification, phenological parameters, and machine learning with cloud computing. They concluded that cloud computing would become the forerunner of geospatial technology for quick analysis due to its ease of implementation.

Although a lot of literature focused on rice area mapping, limited studies have been conducted for mapping RGS. Mapping RGS is essential for stakeholders to approximate the distribution of fertiliser, machinery, and pesticides based on their vegetation status. Moreover, the ripening stage area can be used to calculate the rice yield from the local to national level.

This chapter aims to review the different techniques used for mapping the rice area and RGS. Moreover, this chapter discusses the performance of different sensors, mapping on local to global scales, mapping techniques, the existing rice monitoring projects, and the research gaps and future scope.

2.2 Sensors for mapping rice area and rice growth stages

The remote sensing methods for mapping can be divided into two major categories based on energy sources (Lillesand et al., 2015). The passive sensor relies on solar power, and the active sensor depends on its source of electromagnetic energy and captures the reflected energy in real-time. Both passive and active sensors have their strengths and weaknesses. Nevertheless, sensor integration can combine the advantages of multiple sensors, which leads to improvements in the predictions' accuracy. Hence, three types of sensors are described in the following subsections.

2.2.1 Passive sensor

The passive sensor uses the Sun's energy to measure the reflected energy from the Earth's surface (Lillesand et al., 2015). Multispectral sensors collect reflected information in discrete bands (typically 1-20) of the electromagnetic spectrum. On the other hand, it can be called a hyperspectral sensor as it captures hundreds of contiguous and narrow spectral bands (typically 100 to 1000). Based on the distance of the sensor to capture the object, the passive sensors can be categorized into three classes as follows:

(a) Proximal

Field level remote sensing has the advantage of operational flexibility and capturing spectral signatures in a small area with minimal interference from the atmosphere. A study by J. Sun et al. (2017) predicted the value of rice leaf nitrogen using a handheld spectroradiometer (ASD FieldSpec) with a high degree of accuracy. Moreover, Wang et al. (2014) have used time-series NDVI to investigate rice phenology correlation with the vegetation index using a handheld radiometer. RGS such as tillering, jointing and maturity can be detected accurately with NDVI and the red-edge chlorophyll index (Zheng et al. (2016). Both studies have shown bell-shaped NDVI curves with different cultivars through the rice's life cycle. The curve starts from a low NDVI value, where the water background is dominant over the biomass. It gradually increases until the maximum tillering stage, where it is stable for a few days until the late tillering wilting, and the panicle filling is starting. After that, the NDVI values decrease when the rice canopy turns into senescence due to the denaturation of chlorophyll, and finally, the rice grain becomes yellow and ready to be harvested (Figure 2.4). However, for operational or commercial work proximal sensing can potentially be cost-prohibitive for large spatial extents (regional or national).

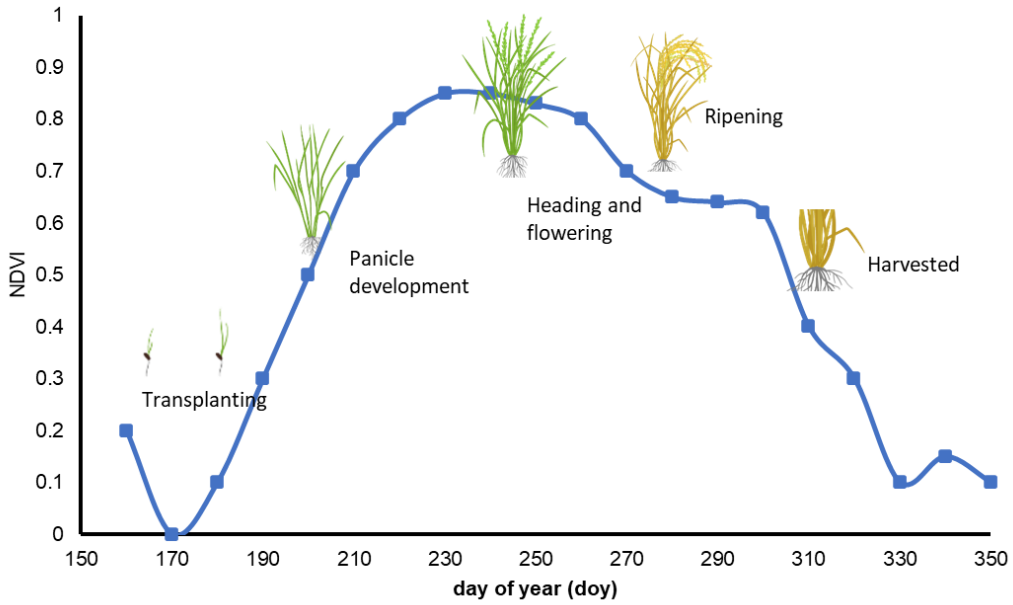

Figure 2.4 The examples of NDVI profile over rice growth in time series in 2011, China (Wang et al., 2014).

(b) Airborne

The airborne sensors can capture surface dynamics with high resolution, over a more extensive area than the field spectrometer, which covers tens to thousands of hectares in one mission to support precision farming for efficient fertiliser recommendation dosage (Pullanagari et al., 2016).

A small unmanned aerial vehicle (UAV) or drone can be divided into two types: those with a fixed motor such as senseFly eBee SQ and multirotor DJI P4 multispectral (Panday et al., 2020). The other type is the fixed-wing type which can cover a greater area than the multi-rotor type but can easily drift in windy situations. A drone can be equipped with a single RGB camera, a multispectral and/or hyperspectral camera. Moreover, the limited area that can be covered on a single mission is still challenging for operational bases, as it depends on the weight and flight time.

Several studies have used RGB cameras for mapping rice areas. Lyu et al. (2021) have successfully calculated the number of panicles using DJI Mavic Pro 2 Zoom using a CMOS sensor with 3840×2160 resolution in video mode. However, they concluded that significant uncertainties could occur due to extreme weather, and the final image needs to have less exposure. Another experiment has been done by Q. Yang et al. (2020) to capture rice

phenology in the BBCH-scale with eight main development parts. They used two sensors, such as RGB digital camera and multispectral sensor with five bands (red, green, blue, red edge, and NIR) for correlating BBCH-scale with a particular vegetation index called scaled wide dynamic range vegetation index (SWDRVI). They demonstrated that SWDRVI could predict rice growth stages in near-real-time, with deep learning and shape-fitting models with high accuracy (83.9%).

Wang et al. (2021) studied different RGS using hyperspectral sensors in 13 cultivars. They found that the similarities are high between cultivars, and the lodging feature in the reproductive stage is an important parameter to increase accuracy by over 5%. Despite high accuracy with airborne sensors, mapping large areas at the regional or national scale is challenging and expensive. Moreover, the information is not available at regular temporal intervals.

(c) Spaceborne

Spaceborne sensors are widely used for mapping Earth surface properties on a local to a global scale. One of the sensors is MODIS which is extensively used for mapping rice areas and RGS due to its high temporal frequency and continuous operation. Although MODIS collects images every day, composite products such as vegetation indices are produced to reduce cloud error (Table 2.2).

Table 2.2 The list of end products from MODIS, which is commonly used in rice-related mapping

#	Product name	Description	Strength	Weakness	References
1	MOD09Q1 (8-day composite/ 250 m)	Two surface reflectance (red and NIR band)	The highest resolution, usually used for fusion	Only two bands	(Zhang & Lin, 2019)
2	MOD09A1 (8-day composite/ 500 m)	Seven surface reflectance (red, NIR1, blue, green, NIR2, SWIR1, and SWIR2)	Commonly used to get multitemporal vegetation indices	Need to be smoothed	(Peng et al., 2011; Qiu et al., 2015; Sakamoto et al., 2006; Sakamoto et al., 2005; Xiao et al., 2006; G. Zhang et al., 2017)
3	MOD13Q1 (16-day composite/ 250 m)	NDVI and EVI based on MOD09Q1 and MOD09A1	Very useful for multitemporal analysis	Longer composite time	(Clauss et al., 2016; Fatikhunnada et al., 2020; Guan et al., 2016)

A vast number of studies exploited MOD09A1 as their primary data set for mapping rice areas because the composite time is shorter than MOD13Q1; this is essential to capture rice dynamics over a wide area such as China (Clauss et al., 2016), Vietnam (Guan et al., 2016), and Indonesia (Sianturi et al., 2018). MODIS data have frequently been used for mapping rice areas and rice intensity based on time-series pixel information and phenology-based algorithms.

Another coarse resolution sensor is Project for On-Board Autonomy (PROBA-V), which provides 100 m to 1 km spatial resolution daily and has a 10-days revisited time. PROBA-V is equipped with a multispectral sensor containing blue, red, NIR, and SWIR bands (Appendix 2). Due to its high resolution, the multitemporal PROBA-V dataset can monitor crop development with better results than the MODIS product, especially in fragmented fields (Zhang et al., 2016). However, MODIS and PROBA-V have limited potential to describe sub-pixel dynamics in small and fragmented rice areas.

Since the launch of the Landsat mission, the investigations of rice monitoring has increased due to increased resolution (30 m) and free datasets. The first investigation of rice mapping using Landsat-5 was a study in Australia using Landsat-5 images with 68 m x 83 m in the 1983/1984 season. They found that the accuracy differed slightly over time, but the differences in accuracy were less than those found in the manual survey. Another study (Tennakoon et al., 1992) successfully used the Landsat 7 TM for classifying rice from other vegetation classes (barren land, citrus, and perennial grass). A similar study has also been done in Japan with a comparable result, in which the classification result is less than the local statistics (Okamoto & Fukuhara, 1996). Oguro et al. (2003) developed multitemporal vegetation indices derived from Landsat-5 and Landsat-7 for mapping rice areas using a mixture model. P. Sun et al. (2017) developed a probability method to map rice areas using multitemporal Landsat-8 images with great accuracy (81 to 92%). A similar study (Su, 2017) in which great accuracy was achieved using an object-based image analysis approach to reduce the salt-and-pepper effect from pixel-based analysis, but they used a higher spatial resolution (15 m) using the pan-sharpening method. They used multitemporal NDVI and LSWI to discriminate rice areas in China and got higher accuracy (~96 to 97%) than other studies.

Recently, ESA has launched a high-resolution sensor (10 m), Sentinel-2, which provides an unprecedented opportunity to map rice dynamics on fragmented landscapes. The

uniqueness of Sentinel-2 with the other optical datasets is that it comprises three red-edge bands that are sensitive to vegetation dynamics (Griffiths et al., 2019). Moreover, Sentinel-2 has a satellite constellation that consists of two satellites: Sentinel-2A, launched in 2015 and Sentinel-2B in 2017. This configuration has reduced the revisit time to five days, which is ideal for monitoring rice vegetation dynamics. Consequently, diverse vegetation and soil indices such as NDVI, LSWI, the modified soil adjusted vegetation index and the modified normalized difference water index were developed for mapping rice (W. Zhang et al., 2020). While several studies have used optical data to monitor rice area and RGS, the usage has been limited by cloud cover, particularly in tropical countries.

2.2.2 Active sensor

Active sensors have been preferred for use over tropical countries due to the frequent cloud cover there; they have their own energy sources and use electromagnetic waves to penetrate through the clouds. However, the captured data is hard to interpret since the sensor only receives the scattered energy, which depends on the sensor's technical configuration and the spatial and dielectric properties of the objects on Earth. Moreover, the dielectric properties of the different soils are greatly affected by their moisture content (Ulaby et al., 1974).

One of the examples of an active sensor is Synthetic aperture radar (SAR). SAR works as the satellite emits an electromagnetic pulse aimed at the Earth’s surface and the sensor captures the echo while passing by (Flores-Anderson et al., 2019). Depending on their wavelength, SAR is divided into different band groups (e.g. Table 2.3).

Table 2.3 The list of different SAR sensors for crop monitoring. Modified from (Flores-Anderson et al., 2019)

Sensor (Resolution, Revisited, and Access)	Commodity	References
X (wavelength: 3.8 – 2.4 cm)		
TerraSAR-X: 0.2 m on spotlight mode, 11 days, commercial	rice, sugarcane, wheat	(Baghdadi et al., 2010; Koppe et al., 2013; Sonobe et al., 2015)
COSMO-SkyMed: ≤1m on spotlight mode, 16 days, commercial	rice, wheat	(Corcione et al., 2016; Kim et al., 2013)
C (wavelength: 7.5 – 3.8 cm)		
ERS-2: 26 m on range mode, 35 days, Limited	rice	(Soo Chin et al., 1998)
Radarsat-2: 1.5 m on spotlight mode, 24 days, commercial	rice, canola, wheat, corn, soybean, sorghum	(Canisius et al., 2018; He et al., 2018; Hoang et al., 2016; Jiao et al., 2011; Li et al., 2012; Liao et al., 2018; Selvaraj et al., 2021; Shuai et al., 2019; Wu et al., 2011; Xie, Lai, et al., 2021; Xie, Wang, et al., 2021; Xu et al., 2014; Yang et al., 2015; Yang et al., 2012; Yonezawa et al., 2012; Zhang et al., 2014; Y. Zhang et al., 2017; Zhao et al., 2017)

Sentinel-1: 5 m on strip map mode, five days, free	rice, maize, wheat, sunflower, canola, potato, grass	(Bazzi et al., 2019; Clauss et al., 2018; Gandharum et al., 2021; Han et al., 2018; Khabbazan et al., 2019; Kontgis et al., 2017; Lasko et al., 2018; Mandal et al., 2020; Mansaray et al., 2020; L. R. Mansaray et al., 2017; Minh et al., 2019; Modanesi et al., 2020; Nasirzadehdizaji et al., 2021; Nasrallah et al., 2019; Nguyen et al., 2016; Phung et al., 2020; Shu et al., 2020; Son et al., 2017; Song & Wang, 2019; Whelen & Siqueira, 2018)
L (wavelength: 15 – 30 cm)		
ALOS/PALSAR-2: 1 m on spotlight mode, 14 days, commercial	oil palm, maize	(Cheng et al., 2018; Gururaj et al., 2021)

One of the earliest studies (Wang et al., 2009) used ALOS PALSAR for mapping RGS and found that HH backscatter captures better RGS information than the HV type does. Moreover, based on their comparison with the radiative transfer model, the single date SAR image is more challenging to map rice characteristics than multitemporal images. Zhang et al. (2009) used multitemporal images and achieved 80.1% accuracy.

High-resolution commercial SAR sensors, such as TerraSAR-X (Koppe et al., 2012), COSMO-SkyMed (Mascolo et al., 2019), ERS-2 (Soo Chin et al., 1998), Radarsat-2 (Wu et al., 2011), contains rich information through multipolar data which can be effectively used for mapping a rice area with an accuracy between 85 to 95%. Despite this high accuracy, the effectiveness of deploying commercial SAR in developing countries is limited due to the financial burden. Moreover, it is more challenging to implement it for tracking the RGS every revisit time.

With the growing interest in SAR to monitor the Earth's surface, ESA launched the Sentinel-1 mission with two satellites in 2014 and 2016, with the same orbit path. Sentinel-1 constellation delivers ~6 days revisit time at the equator.

The Sentinel-1 with interferometric wide (IW) mode and double polarisation has been the main drive for mapping rice areas and RGS. L. R. Mansaray et al. (2017) showed that the rice area in China could be identified from areas with other land use from five consecutive images in 2015 with great accuracy (88.3%). The backscatter coefficient profile can easily differentiate between water, buildings and vegetation. A built-up area commonly has a high backscatter value (>-12 dB), and the water is otherwise (<24 dB). The rice areas have fluctuating backscatter profiles, depending on the amount of standing water and canopy growth (Singha et al., 2019). In contrast, trees usually show more stable backscatter values over time (Figure 2.5).

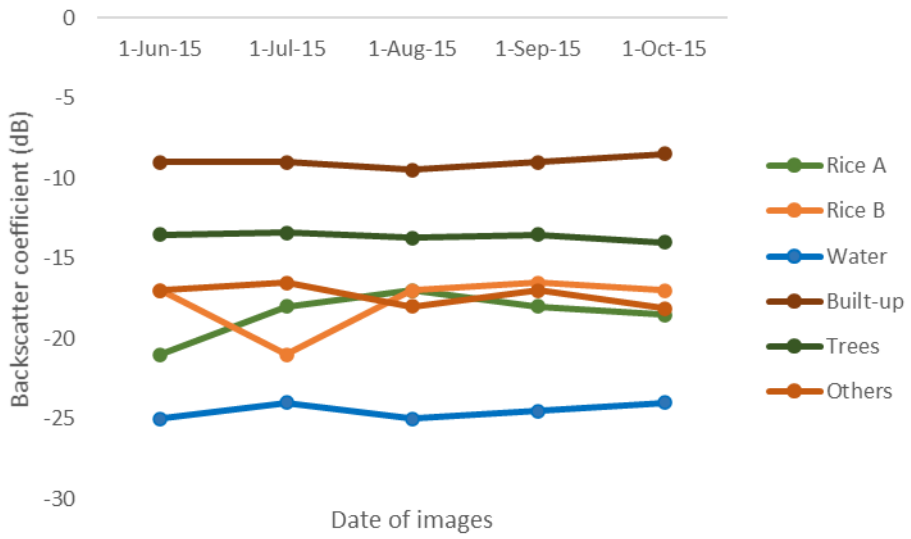

Figure 2.5 The example of the VH backscatter coefficients for different land use. Modified from L. R. Mansaray et al. (2017).

Although the commercial sensors (e.g. TerraSAR-X) has the potential to determine the RGS accurately, their usage is constrained by the high cost. Unlike commercial sensors, the publicly available Sentinel-1 has the least potential due to coarse resolution and limited polarisation modes.

2.2.3 Multi-source sensor

Over decades, there has been a growing interest in integrating multiple sensors to generate continuous maps. The primary purpose of multi-resolution is to enhance spatial resolution by blending low and high-resolution images, such as pan-sharpening, which can be generated from bands 1 to 7 with 30 meters with band 8 with 15 meters spatial resolution for Landsat 7 and 8, respectively (Gilbertson et al., 2017; King & Jianwen, 2001; Rahaman et al., 2017). The final/composite images can be used for crop classifications with greater accuracy. Furthermore, Feng et al. (2006) introduced a mature Landsat-MODIS fusion algorithm known as the spatial and temporal adaptive reflectance fusion model (STARFM), which blends data based on a deterministic weighting function generated by spectral similarity, the temporal difference and spatial distance. Another example is Ehlersa et al. (2010), who successfully fused an IKONOS image and a TerraSAR-X using Ehler fusion for pan sharpening and maintained the spectral characteristics of IKONOS. Fusing the

Sentinel-2 and Sentinel-1 datasets can improve the accuracy of land use classification (Steinhausen et al., 2018).

Furthermore, multitemporal information from multi-sensor data provides unique information from multiple features based on several images over time. Many researchers have used multitemporal information for detecting land cover changes. Abdi and Ardiansyah (2017) used time series vegetation indices to monitor rice areas because the specific trend of land use differs in temporal profiles. Table 2.4 shows examples of different combinations of multi-source remote sensing data used for the rice monitoring areas.

Table 2.4 The examples of application on the multi-source sensor on rice monitoring

#	Mapping application	1st dataset / its resolution	2nd dataset / its resolution	3rd dataset / its resolution	4th dataset / its resolution	Accuracy measurement	Area	Dataset's Year	References
1	Rice area	MODIS – MOD09A1 (500 m)	Landsat- 7 ETM+ (30 m)	PALSAR (100 m)	-	OA: 89%	China	2007	(Torbick et al., 2011)
2	Rice area and its intensity	MODIS - MOD09A1 (500 m)	Landsat-8 OLI (30 m)	-	-	OA: 92.95%	China	2015	(Ding et al., 2020)
3	Rice planting area	MODIS - MOD09A1 (500 m)	Landsat-8 OLI (30 m)	Landsat- 7 ETM+ (30 m)	-	OA: 98.19%	China	2000 – 2018	(Yin et al., 2019)
4	Rice area	MODIS – MOD09A1 (250 m)	Landsat-8 OLI (30 m)	-	-	OA: 95%	China	2013	(Zhou et al., 2016)
5	Planting, heading,	MODIS – MOD13Q1	Landsat-8 OLI (30 m)	-	-	OA: 89.7%	China	2018	(Li et al., 2021)

	harvesting date	(250 m)							
6	Rice area	MODIS – MOD13Q1 (250 m)	Landsat-8 OLI (30 m)	-	-	OA: 89.7%	China	2006 – 2007	(Son et al., 2016)
7	Rice area	MODIS – MOD13Q1 (250 m)	Landsat-8 OLI (30 m)	-	-	OA: 92.38%	China	2013	(Zhang & Lin, 2019)
8	Rice area and yield	MODIS – MOD09GQ (250 m)	Landsat-8 OLI (30 m)	Landsat-7 ETM+ (30 m)	ALOS-2/PALSAR-2 (25 m)	R^2 : 0.4, RMSE: 0.87 ton/ha	Vietnam	2015	(Guan et al., 2018)
9	Rice area	MODIS – MOD13Q1 (250 m)	Sentinel-2 (10 m)	Sentinel-1 (10 m)	-	OA: 85%	China	2018	(Cai et al., 2019)
10	Rice area	MODIS – MOD13Q1 (250 m)	HJ-1A (30 m)	HJ-1B (30 m)	-	OA: 82%	India	2014 – 2015	(Singha et al., 2016)

11	Rice area	Landsat-8 OLI (30 m)	Landsat-7 (30 m)	Sentinel-1 (10 m)	-	OA: 82.5%	China	2015	(Onojeghuo et al., 2018)
12	Rice area	Landsat-8 OLI (30 m)	Sentinel-1 (10 m)	-	-	OA: 92.47%	Indonesia	2019	(Arjasakusuma et al., 2020)
13	Rice – fallow pattern	Landsat-8 OLI (30 m)	Sentinel-1 (20 m)	-	-	OA: 83%	India	2015-16, 2016-17, and 2017-18	(Chandna & Mondal, 2020)
14	Rice area	Landsat-1, 2, 3, 4, 5& 7 (30 m)	ALOS PALSAR (6.25 m)	RADARSAT-1 (30 m)	-	OA: 88.00 – 94.33%	The U.S.A and South Korea	2003 – 2009	(Park et al., 2018)
15	Cropping system	Sentinel-2 (10 m)	Sentinel-1 (10 m)	-	-	OA: 88%	France	2016-2017	(Courault et al., 2020)

Note: OA = overall accuracy, RMSE = root mean square error

2.3 The methods and tools for mapping rice growth stages

Mapping a rice area and its characteristics is challenging, especially with double and triple cropping. Therefore, some techniques are required to extract the critical biophysical features from spectral reflections or radar backscatter data.

2.3.1 Vegetation indices

The vegetation indices (VI) are mathematical combinations of two or more bands to measure a biophysical characteristic. The first and commonly used vegetation index was NDVI with the Advanced Very High-Resolution Radiometer (AVHRR) sensor in 1981. NDVI is usually obtained from a combination of reflectance bands of the visible-red band (580 to 680 nm) and near-infrared (NIR) band (725 to 1,000 nm), which are sensitive indicators for the vegetation canopy (Lillesand et al., 2015). The range of NDVI is 0 to 1. A high NDVI value indicates healthy/dense vegetation, while low values correspond to stressed/sparse vegetation. NDVI is a widely used VI, used for approximating various vegetation properties, such as leaf area index (Zhou et al., 2017), vegetation health (Jana et al., 2016; Tran et al., 2017), cropping pattern (Lunetta et al., 2010; Nguyen et al., 2012), crop classification (H. Zhang et al., 2017), rice area (Xiao et al., 2005), and rice phenology (Boschetti et al., 2009).

Several VIs have been proposed to quantify the vegetation properties. The enhanced vegetation index (EVI) had been used in parallel with NDVI on the product from MODIS because EVI also includes the blue band range (450 to 510 nm), which reduces atmospheric scattering and adds a gain factor for minimizing soil background effects (Lillesand et al., 2015). EVI has been used to map the changes in vegetation dynamics in several studies (Peng et al., 2011; Setiawan & Yoshino, 2014).

To increase the accuracy for mapping rice areas, Xiao et al. (2005) used the land surface water index (LSWI) to detect rice in the presence of water (transplanting stage) by replacing the red band with a shortwave infrared band (900 to 1,700 nm). Moreover, researchers can compare with EVI or NDVI to determine, using a simple threshold method, between a rice area and a forest area since the rice area will always have a fallow period (LSWI + 0.05 > EVI) (Jin et al., 2016). The formulas for the four indices can be found in Table 2.5.

Table 2.5 The four vegetation/ water indices commonly used in rice-related studies

	Name	Abbreviation	Formula	The examples of application in remote sensing and rice conditions
1	Normalized difference vegetation index	NDVI	$\frac{\rho_{NIR} - \rho_{Red}}{\rho_{NIR} + \rho_{Red}}$	(Faisal et al., 2020; Guan et al., 2016; Nguyen et al., 2012; Zhang & Lin, 2019)
2	Enhanced vegetation index	EVI	$2.5 \times \frac{\rho_{NIR} - \rho_{Red}}{\rho_{NIR} + 6 \times \rho_{Red} - 7.5 \times \rho_{Blue} + 1}$	(J. Liu et al., 2019; Son et al., 2020; Tsujimoto et al., 2019; Zhu et al., 2019)
3	Two band – enhanced vegetation index	EVI2	$2.5 \times \frac{\rho_{NIR} - \rho_{Red}}{\rho_{NIR} + 2.4 \times \rho_{Red} + 1}$	(Kalpoma et al., 2019; J. Liu et al., 2019; Son et al., 2016; Wang et al., 2015)
4	Land surface water index	LSWI	$\frac{\rho_{NIR} - \rho_{SWIR1}}{\rho_{NIR} + \rho_{SWIR1}}$	(Jin et al., 2016; Kwak et al., 2015; J. Liu et al., 2019; Zhang et al., 2015)

Note: ρ = surface reflectance band, NIR = near infra-red, and SWIR1 = shortwave infra-red.

2.3.2 Multitemporal vegetation indices

The vegetation index value changes over time as the rice grows and is harvested. The NDVI and EVI are commonly low at the beginning of rice cultivation. They start to increase in parallel with the canopy built-up and reach a peak in the early reproductive stage where the canopy has reached maximum potency, and then they start decreasing until the grain is ready to harvest. This unique profile is used to determine the rice area and rice phenology. For example, Fatikhunnada et al. (2020) reported a technique based on MOD13Q1 that could map cropping patterns on Java Island. The multitemporal profiles can also determine wheat and rice crops in one year, as shown in Figure 2.6.

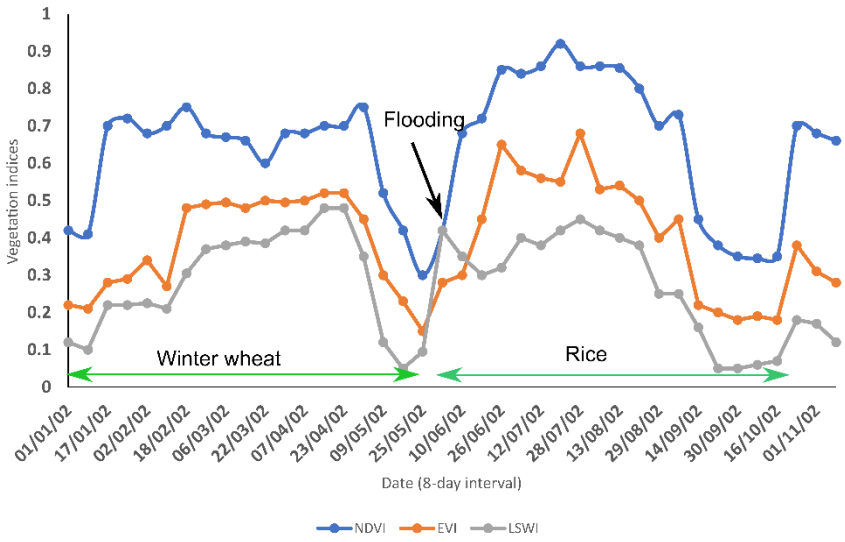

Figure 2.6 The examples of multitemporal values from NDVI, EVI, and LSWI in Jiangsu, China (Xiao et al., 2005)

The threshold method can be classified with the NDVI value for the RGS with bare land (<0.2), vegetative (0.21 to 0.4), reproductive (0.41 to 0.7), and ripening stages (0.4 to 0.5)(Dirgahayu & Made Parsa, 2019). However, this technique only works in a particular area and single date image classification. It cannot be transferred to other regions since the NDVI value threshold needs to be adjusted to capture the differences between rice varieties

and their cropping patterns. Moreover, the values of the ripening stage and the vegetative stage overlap and need additional input data to separate the ripening and reproductive phases which can make near-real-time applications for monitoring rice projects challenging.

2.3.3 Multitemporal backscatter value

The temporal information of backscattering values from SAR images (RADARSAT and ALOS PALSAR) can be used for mapping rice RGS. Low backscattering values can be seen during the flooding or transplanting stage due to specular reflection from the water's surface (Corcione et al., 2016). As the rice canopy becomes taller and more prominent, the backscatter signal is stronger because of the double bounce interaction caused by the vertical shape of the stems. The rice canopy consists of panicles, stems, and leaves during the reproductive phase, which randomly scatter results with low backscatter values. The final stage is the ripening phase, where the stems become drier and have a higher backscatter signal.

Rudiyanto et al. (2019) used multitemporal SAR images from Sentinel-1 for mapping rice areas in Indonesia and Malaysia. This technique uses the nadir of polarised backscatter to determine the rice cropping since a low backscattering shows the area is flooded and ready to be cultivated (Ramadhani et al., 2020a). The flooded area has a lower value than average since the reflectance off the water's surface will scatter in all directions. Figure 2.7 shows the peak and nadir of the rice cropping pattern through EVI and VH backscatter.

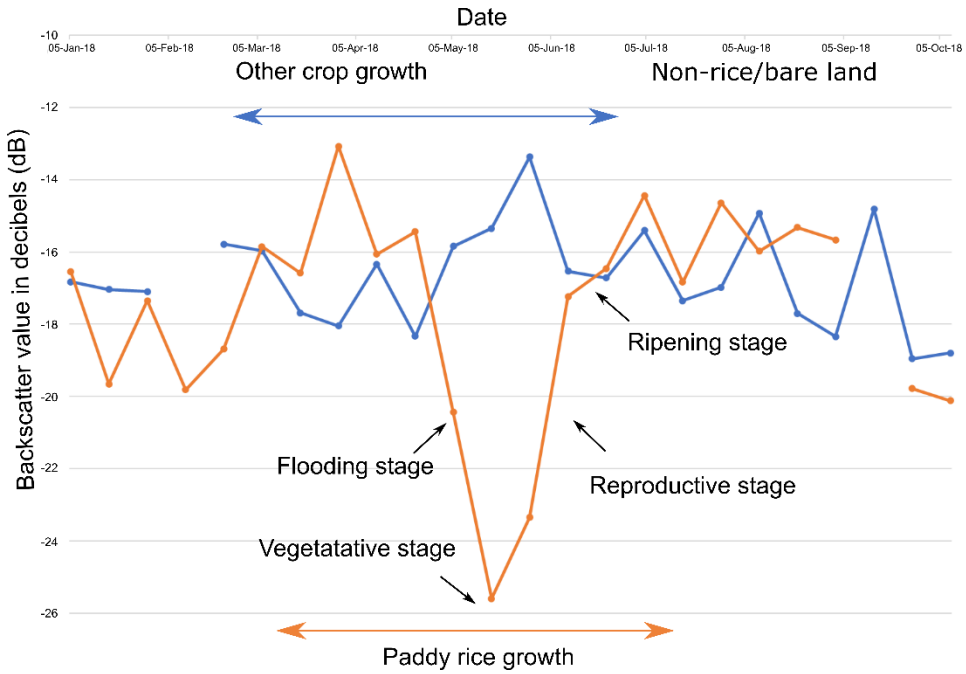

Figure 2.7 The example of multitemporal Sentinel-1 profile in Indonesia with rice cropping (orange line) and non-rice cropping (blue line) (Ramadhani et al., 2020a)

However, the previous techniques mentioned have some disadvantages for near-real-time rice monitoring, such as cloud occurrences, extensive local knowledge, and multitemporal radar data, which may provide different angles requiring remodelling the grouping. Moreover, none of these studies produced an open-source code to be checked or developed further by other researchers (Rocchini et al., 2017).

2.3.4 Multitemporal rice growth stages (RGS)

Multitemporal RGS is a new procedure to determine RGS based on the dataset's availability for a certain period. This method was inspired by land-use change analysis to calculate the difference between two land-use analyses in different periods. There are two ways to determine the RGS. The first uses multitemporal vegetation indices or backscatter profiles as the precursor of rice growth, as mentioned previously (Section 2.3.2 and 2.3.3). The second is to use a machine learning model to predict or classify based on random points

dataset from field survey. The first method has the advantage of having better accuracy than the latter but not in near real-time with minimum periods of one month (Rudiyanto et al., 2019). The second one is more promising to provide information quickly because the model can reuse in determining RGS with acceptable accuracy, as shown in a previous study for mapping rice area (W. Zhang et al., 2020).

The relationship of multi-source remote sensing with multitemporal rice growth stages is rarely investigated in previous studies. The proposed research focused only on classification based on single-source datasets such as MODIS (Panuju et al., 2021) and Landsat (Wang et al., 2015) for detecting rice growth stages for evaluating only, not for continuous monitoring application. In the application for monitoring rice growth stages, the need of real-time classification is needed to enable fast dissemination of information. The optical sensors have advantages for capturing rice fields using multi-spectral bands sensors. On the other hand, SAR satellites can capture objects day or night without cloud interference (Phung et al., 2020). However, the accuracy of SAR is limited due to speckles noise and is only sensible if there is a water background around the objects. Thus, the use of multi-source remote sensing is needed to integrate those sensors to more accurate information of rice growth stages in the application.

2.3.5 Machine Learning

Machine learning (ML) has become a valuable tool to extract versatile information from complex data through regression or classification tasks in agriculture (Liakos et al., 2018). ML can be described as an area of computer science that studies algorithms and techniques for automating solutions to challenging problems with traditional programming methods (Rebala et al., 2019). An ML algorithm aims to learn a model or a set of rules from a labelled data set so that the data indicate labels in the other data set which can be predicted correctly. This method is known as supervised machine learning, which mainly falls into

two categories: 1) regression or the capacity to predict continuous values and 2) classification which is the categorising of categorical values.

The classification process starts with training the model using training data to identify the type or class of the inputted feature. A binary classifier labels the data as belonging to one of the two output groups. A multi-class classifier defines the input vector as one of more than two categories. The standard classifiers on remote sensing can be explained as follows:

(a) Support Vector Machines (SVM)

The SVM algorithm aims to find a hyperplane separating the data set into a discrete predefined number of classes that are the most consistent with the training examples. The term optimal hyperplane separation refers to the decision boundary that minimises the misclassifications during the training step (Figure 2.8). Learning in SVM refers to the iterative process of finding a classifier with optimal decision boundaries to isolate the training and then separate the simulation data in the same configurations (Raghavendra & Deka, 2014). SVMs are gaining interest in remote sensing due to their ability to manage limited training datasets effectively, often resulting in higher classification accuracy than traditional methods (Mantero et al., 2005).

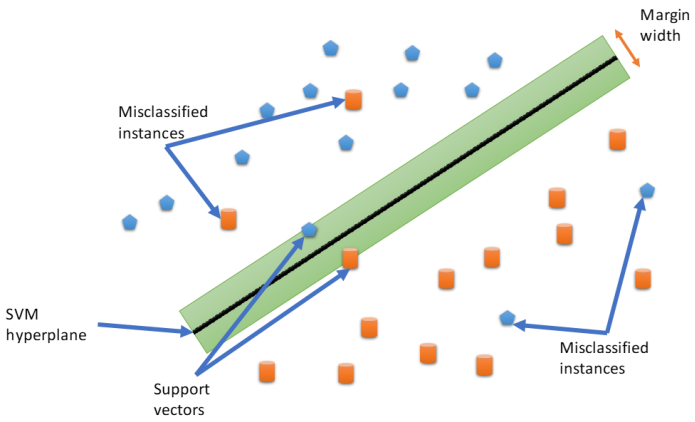

Figure 2.8 The illustration of the SVM linear algorithm. Adopted from Raghavendra and Deka (2014).

SVMs can accommodate data points that cannot be linearly segregated, using functions with unique properties called kernels by translating data points into higher dimensional regions. However, SVM has some drawbacks, such as a high sensitivity to mislabelled points and noisy data (Huang et al., 2008), slower computation and higher memory consumption than neural networks, and challenges in choosing the parameters (Holloway & Mengersen, 2018).

(b) Artificial Neural Networks (ANN)

Artificial neuron networks (ANN) are analogous to brain structures. ANN consists of the input layer, hidden layer, and output layer. The variables flow forward and backward from the input layer to the output layer through the hidden layer (Figure 2.9). ANN has considerable advantages over traditional methods, such as ordinary least squares regressions due to their ability to learn nonlinear and complex problems and incorporate different data types into the model. However, the performance of ANN depends on their architecture, the method of presenting the data, and carrying out the training.

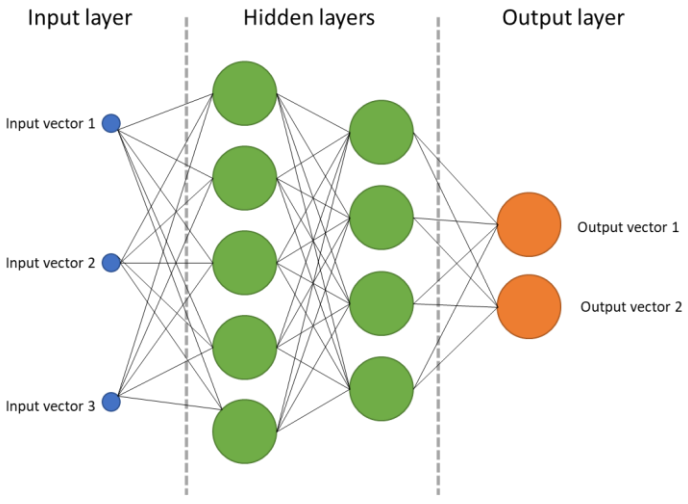

Figure 2.9 The illustration of the neural network algorithm. Modified from Gardner and Dorling (1998)

(c) Classification And Regression Tree (CART)

The CART algorithm is the most straightforward classification, which seeks the homogeneity for each class based on the recursive splitting of the training data set (Figure 2.10). The splitting rules can be divided into a few methods, such as reducing the misclassification cost and prior distributions. Thus, the Gini index can be used to measure tree impurity values. The last rule is the stopping split rule, which depends on the maximum value for tree impurity (Breiman et al., 1984).

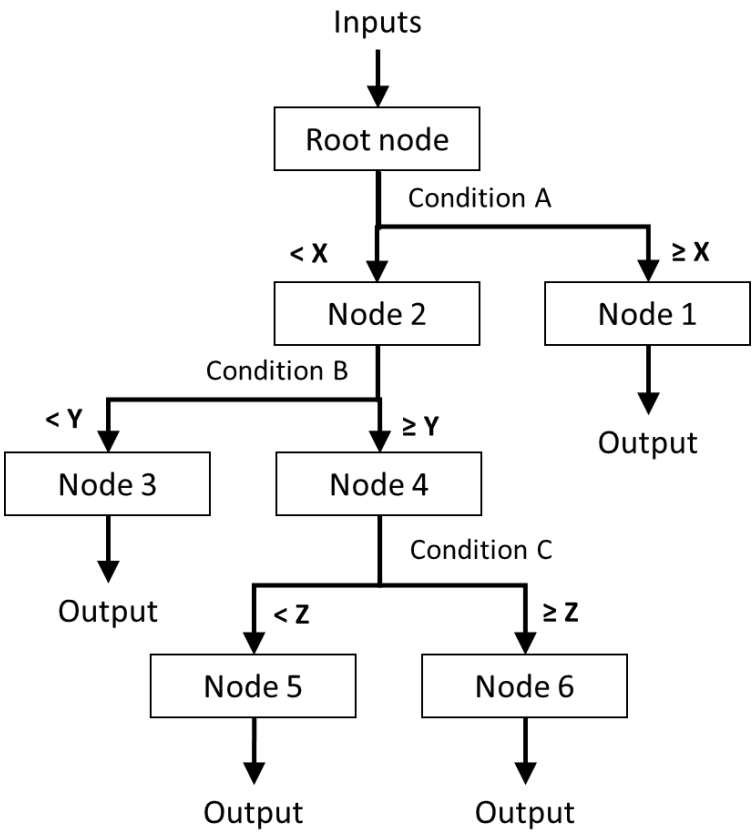

Figure 2.10 The general structure of the CART tree. Modified from Yang et al. (2003)

(d) Random Forest (RF)

The RF classifier is an ensemble classifier that allows a forecast using a set of classification and regression trees. The trees are generated by drawing a subset of exercise samples (a bagging process). Approximately two-thirds of the samples (known as in-bag samples) are

used to develop a model. In contrast, the remaining one-third (referred to as samples outside the bag) of the samples are then used to estimate model performance via majority voting. The algorithm produces trees with high variances and low tendencies, increasing the forest to a user-defined number of trees. Averaging of the class assignment probabilities determined by all the generated trees is the final classification decision, as shown in Figure 2.11.

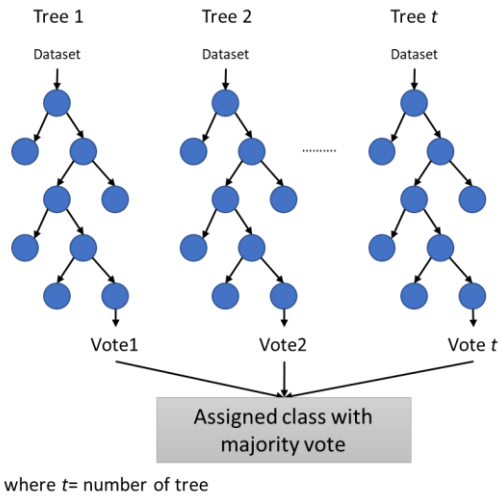

Figure 2.11 The illustration of the random forest algorithm. Adopted from Belgiu and Drăguţ (2016)

2.4 Rice monitoring projects

The United Nations Food and Agriculture Organization (FAO) has initiated monitoring crops globally with the Global Information and Early Warning System (GIEWS). GIEWS uses remotely sensed data from MODIS, METEOSAT, and NOAA-AVHRR to calculate cold cloud duration (CCD) and NDVI images for drought and food insecurity monitoring. It can be explored on http://www.fao.org/giews/en/. Another project to synchronise with trading activities has been incorporated with the Crop Monitor – Agricultural Market Information System (AMIS) project. The system compiles data from MODIS, the Climate

Hazards Center (CHC) InfraRed Precipitation with Station data (CHIRPS), the European Centre for Medium-Range Weather Forecasts (ECMWF), and soil moisture, evapotranspiration rates and runoff from the NASA model. The user can access it on https://cropmonitor.org. Recently ESA has launched the Sentinel-2 for Agriculture (Sen2-Agri) project (http://www.esa-sen2agri.org/) with the aim of continuous monitoring agriculture landscapes at the planetary scale. It provides monthly maps for surface reflectance composites, cropland masks, cultivated crop types, and vegetation indices' status based on NDVI and LAI.

The International Rice Research Institute (IRRI) has collaborated with other institutes to create a rice monitoring system in several countries in Asia and Africa called the 'Eyes in the sky' project. In the first phase, the lowland rice areas were mapped using MODIS images, especially in the South Asia region (Gumma et al., 2011) and the Philippines (Boschetti et al., 2017). The second phase of the project used multitemporal Sentinel-1 to monitor the rice areas and combined this information with a crop model to predict the rice yield. The average accuracy for mapping the rice areas was 89.4% for 12 test sites, and the normalised-RMSE was 13.4% for 24 rice plots which are remarkable results. This programme has been integrated successfully into the Philippine rice monitoring programme. However, it remains challenging to develop a similar system in other developing countries due to limited resources (Setiyono et al., 2019).

China developed another project called 'Cropwatch'. It is specifically intended to use remote sensing data to evaluate the performance of national and international crops and related indicators by the Institute of Remote Sensing and Digital Earth (RADI), Chinese Academy of Sciences (CAS) (Wu et al., 2014). The system provides wheat, maize, rice and soybean growth forecasts and spans 50 countries worldwide. CropWatch (http://www.cropwatch.com.cn) uses high-resolution (Landsat, Radarsat, among others)

and low-resolution (MODIS, NOAA AVHRR, etc.) remote sensing data which are blended with in-situ data. The system can analyse and provide crop-monitoring indicators such as crop conditions, drought, crop acreage, cropping intensity, crop yield predictions, and food production estimations.

The Indonesian Space Agency (LAPAN) and the Ministry of Agriculture have released a rice growth stages map based on MODIS images from 2012. The data are released every eight days or more. A few years later, the Landsat-8 based rice growth stages were launched in 2015 with a 30-meter spatial resolution by both agencies. Both systems can be accessed from http://sipandora.lapan.go.id/site/fasepertumbuhanpadi and http://sig.pertanian.go.id/. In addition to RGS, it also produces other rice products such as productivity maps and flood and drought-prone maps. However, the RGS in the existing system have low spatial resolution since they only relied upon 250-m resolution and a longer revisit time of 16-day.

2.5 Challenges in remote sensing of RGS

The operational use of remote sensing data has increased tremendously in the last few years using several satellite missions have been launched to monitor earth surface dynamics. However, several challenges are associated with RGS assessment. The most important aspect is the lack of freely available high-resolution data. Along with high resolution, high temporal frequency is required for regular monitoring and to extract multitemporal information. Although MODIS and PROBA could provide high temporal coverage, their coarse resolution leads to mixed pixels. The recent Sentinel-2 mission covers high temporal coverage and contains many bands to retrieve detailed information about vegetation. However, Sentinel-2 is constrained by cloud cover; hence no information can be seen. In addition, external environmental factors (rainfall, rice ecosystem, varieties) could impact the classification accuracy. The optical features of different RGS are highly overlapping which consequently hinders the application of remote sensing data to be applied on a large

scale. Due to the ongoing development of Earth observation (EO) technology with the continuous launch of new generation EO satellites, the size of the remote sensing data has been growing tremendously. Such big data poses serious computational challenges when using traditional information systems.

2.6 Keys barriers in implementing RGS monitoring and future scope

Moreover, there are three main barriers to implementing monitoring RGS using remote sensing. The first is that the developing countries mainly located in tropical areas such as Indonesia and the Philippines faced more difficulties using remote sensing data due to extensive cloud cover, especially in the wet season (December – February). The second barrier is that these countries also depend on free satellites dataset to make them operational for providing rice growth stages information in a timely fashion. Some projects have been operational but short due to depending on grants or external funding, such as the International Asian Harvest mOnitoring system for Rice (INAHORT) based on images from the ALOS-2 satellite (Oyoshi et al., 2016). The last is the high uncertainty of implementing SAR-based RS datasets such as Sentinel-1 alone on discriminating RGS using the supervised method since the farmer's planting time can be shifting in Indonesia due to water distribution problems (G. Zhang et al., 2017). Thus, multitemporal and multi-dataset should be used to discriminate the RGS in the near real-time. The supervised classification using machine learning has been investigated in previous studies in different objects, such as detecting damaged buildings and wildfires with acceptable accuracy (Sulova & Jokar Arsanjani, 2020; Valentijn et al., 2020; Wen et al., 2019).

As remotely sensed data becomes more available and more easily accessible, researchers and the community have been developing different methods and techniques to interpret the images into useful information for stakeholders in the rice production business to make better policies more quickly. For example, the rice off-takers can be made more efficient

at finding an area to be harvested in a specific place and time. The government can detect rice production at the national level more accurately because the information is backed by spatial data. Moreover, combining spatial statistics in near-real-time with the mobile application can be more effective for end-users (Bégué et al., 2020).

Alternative to traditional information systems, cloud computing services provides enormous computing power to manage and process big geospatial data with minimal effort. Google Earth Engine (GEE) is a sophisticated geospatial cloud computing platform that consists of petabytes of historical satellite information from multiple satellites at a planetary scale. GEE provides an opportunity for users to retrieve, analyse, display and download remote sensing images from one integrated platform (Gorelick et al., 2017).

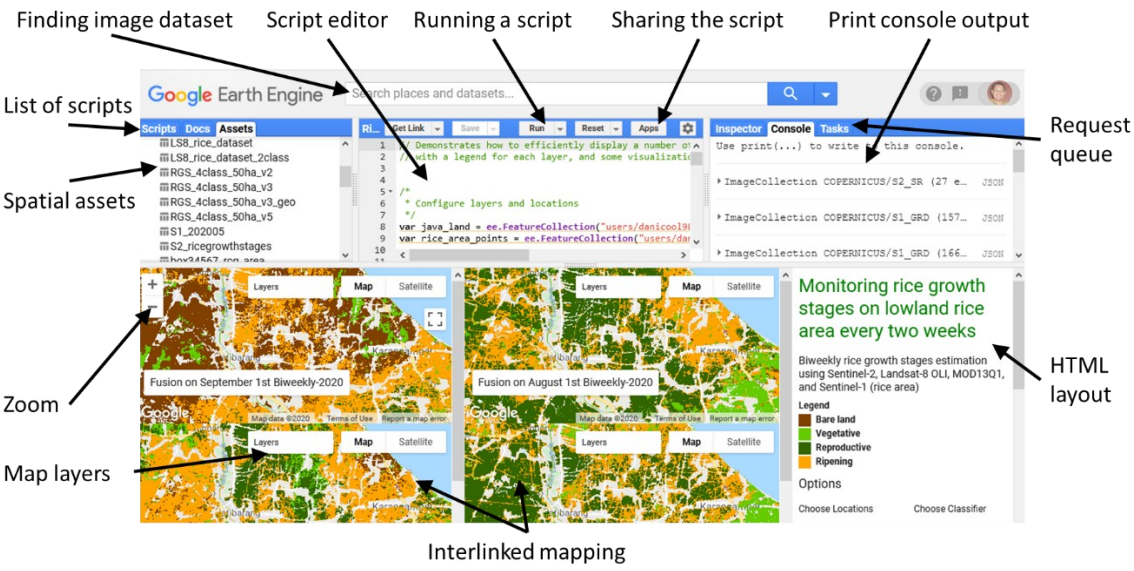

Figure 2.12 The user interface of GEE Code Editor and its functions (https://code.earthengine.google.com).

There are some challenges to be solved when working with GEE. The main limitation is that each user gets limited computational time and storage with the free version. The user needs to pay more to have more calculations and storage. Another limitation is the lack of

access to super high-resolution imagery, including Worldview, Pleiades, RADARSAT-2 or COSMO-SkyMed.

Although GEE has in-built machine learning algorithms in its system, such as SVM, RF, CART, Naïve Bayes classifier, GEE does not support fine-tuning of the model's parameters when building a classification model. Another option for cloud computing is the system for earth observation data access, processing and analysis for land monitoring (SEPAL), supported by the United Nations Food and Agriculture Organization (FAO) which offers land monitoring automatically, especially for the forest carbon stock database under the reducing emissions from deforestation and forest degradation (REDD) programme (Gomes et al., 2020). It consists of more complex elements, advanced processing algorithms, Amazon Web Services (AWS) cloud storage, and AWS computational hardware. Furthermore, the OpenEO initiative enables other researchers to use satellite images independently from the existing platforms such as GEE and AWS. However, OpenEO does not have a user-friendly interface like GEE (Schramm et al., 2021).

2.7 Mapping rice growth stages for near-real-time monitoring

As discussed in Section 2.2, despite a wide range of studies involved in mapping rice areas with high accuracy, studies related to rice phenology are limited. Mapping of RGS using multitemporal images using passive sensors is complex in tropical countries due to the frequent cloud cover. Moreover, the latest study shows that the RGS mapping using Sentinel-1 needs to be a minimum period of 30-day to update the multitemporal dataset using the proposed method (Rudiyanto et al., 2019). MODIS/Landsat-8 OLI images are limited in mapping RGS due to their low spatial resolution and lack of sensitive vegetation bands. A near-real-time monitoring system is required for continuous RGS mapping.

Another research gap is to map RGS by utilising multiple satellites data to increase the prediction accuracy and temporal frequency. With the growth in free satellite images, high prediction accuracy with high temporal frequency is possible by integrating multiple remote sensing data. Another 'unexplored' resource is PROBA-V, which has provided high temporal frequency since 2013.

After generating accurate RGS prediction maps and computing the local rice production statistics, such as the planting and harvested times and the area, sub-monthly image acquisition is required. The information can fill the existing knowledge gap since many studies only focus on the accuracy of the rice area against the existing local statistics.

Cloud computing is a new field that generates informative maps without downloading and managing the data. However, the implementation of GEE for operational monitoring is still limited. Many studies only concentrated on downloading just the GEE data. Quick mapping of RGS using the GEE environment is required to disseminate knowledge of the spatial distribution to agricultural stakeholders.

2.8 Summary points

The timely and accurate spatial information of rice phenology and rice areas is vital for maintaining food security during climate change. This chapter presents the review on remote sensing applications for rice to show the opportunity, gaps, and future direction for further investigations using remote sensing as a tool for food security assessments for near-real-time monitoring. The main points that can be derived from the previous studies are as follows:

(a) A deep discussion about different sensors and methods to map rice areas and their phenology using remote sensing has been presented. The growing trend is to use multiple sensors for mapping rice phenology, to improve the accuracy.

(b) Several studies have used multitemporal vegetation indices for mapping rice areas but it is still difficult to retrieve information related to RGS. The threshold method can be more problematic over a wide area because it requires a local expert to find the threshold values. On the other hand, the machine learning method becomes more interesting due to its simplicity in applying it to a wide area, and reports show a higher level of accuracy (OA >75%).

(c) The growing impact of cloud computing and storage allows the remote sensing community to explore and connect the remotely sense image datasets with other services and mobile applications. Mapping RGS at the operational level needs petabytes of storage and multiple processing pipelines to classify the ready-to-analyse product, so it becomes ready to present to the stakeholders. Moreover, RGS information can be used as an input in crop models to predict yields and to optimise the use of resources.

[intentionally blank]

Chapter 3 Mapping of rice growth phases and bare land using Landsat-8 OLI with machine learning

The objective of chapter 3 is to build a workflow for mapping rice growth stages using Landsat-8 OLI with secondary webcam data. Moreover, it compared several classifiers to ensure that the best classifier was chosen and consistent over the years. This chapter is based on a published paper:

> *Ramadhani, F., Pullanagari, R., Kereszturi, G., & Procter, J. (2020). Mapping of rice growth phases and bare land using Landsat-8 OLI with machine learning. International Journal of Remote Sensing, 41(21), 8428-8452. https://doi.org/10.1080/01431161.2020.1779378*

Supplementary data and software can be downloaded on https://github.com/FadhlullahRamadhani/LS8-OLI-MAPPING

Participating authors:

- Fadhlullah Ramadhani: Conceptualization**,** investigation, data curation**,** formal analysis, methodology, software, visualization, and writing—original draft preparation
- Reddy Pullanagari: Conceptualization, methodology, supervision, and writing—review and editing,
- Gabor Kereszturi: Conceptualization, methodology, supervision, and writing—review and editing,
- Jonathan Procter: Supervision and writing – review & editing

Abstract

Regular monitoring and mapping of rice (Oryza Sativa) growth phases is essential for industry stakeholders to ensure food production is on track and assess the impact of climate change on rice production. In Indonesia, high-cost field surveys have been widely used to monitor the rice growth phases. Alternatively, this research proposes a methodology to retrieve multitemporal rice phenology (vegetative, reproductive, and ripening) and bare land mapping using medium resolution remote sensing imagery obtained from Landsat-8 Operational Land Imager (OLI) combined with machine learning techniques. In this study, we have used extensive ground validation information collected from 2014 to 2016 for training the models. This ground validation information was obtained from pre-installed webcams across Indonesia. Five different machine learning algorithms were used including random forest (RF), support vector machine (SVM) with three kernel functions (linear, polynomial, and radial) and artificial neural networks (ANN) to classify rice growth phases and bare land. This paper also evaluates the temporal evolution of rice phenology and bare land to check the prediction model consistency between two consecutive dates in three years. The results show that the nonlinear SVM algorithm gives the best model accuracy (70.5% with kappa: 0.66) based on the test dataset and the lowest temporal changes (<11%). Spatial-temporal assessment of rice phenology and bare land from Landsat-8 indicated that the models were reliable and robust over different seasons and years. The distribution of rice phenology maps will enable Indonesian management authorities to supply fertiliser, allocate water resources, harvesting, and marketing facilities more efficiently.

Table of contents for Chapter 3

3.1 Introduction

Rice (*Oryza Sativa*) is the primary crop for Asian countries, especially in Indonesia, which contributes 10.6% of the rice produced in Asia (FAOSTAT, 2014). The continuous growth of the Indonesian population places food security under increased pressure. In 2016 approximately 19.4 million people in Indonesia were undernourished (FAOSTAT, 2017). The Indonesian government has been developing many policies to ensure adequate food through supplying subsidized fertilisers, mechanization tools, constructing irrigation projects and educating farmers through extension activities. However, the rice cultivation in Indonesia is vulnerable to climate change with El Niño/Southern Oscillation (ENSO) affecting rice production in 1997-1998 due to drought and flood events (Naylor et al., 2001). To mitigate this, the Indonesian government has established a climate change task force which provides information on cropping patterns and rice production estimates based on climate change models (IAARD, 2011). One of the challenges for increasing the accuracy of prediction is the lack of spatial data of paddy rice growth promptly because the information of rice growth is collected based on "visual estimation" from local workers without any spatial attributes and is challenging to validate.

Remote sensing technology offers a simple operational solution for filling the data gaps with reliable spatial data from regional to global scales. The Earth observation system, comprised of a series of satellite missions, regularly monitors the Earth's surface with various spectral and spatial resolutions aimed at understanding and resolving issues related to food security (Gumma et al., 2019; Kogan et al., 2019), for example, Sentinel missions (Clauss et al., 2018; Nguyen et al., 2016; Skakun et al., 2017; Torbick, Chowdhury, et al., 2017; Veloso et al., 2017), Landsat missions (Dong et al., 2016; McCloy et al., 1987; Sonobe et al., 2017; Tran et al., 2017; Wang et al., 2015; Ye et al., 2018; H. Zhang et al., 2017), Moderate Resolution Imaging Spectroradiometer (MODIS) (Aulia et al., 2016; C.-

F. Chen et al., 2012; C. F. Chen et al., 2012; Clauss et al., 2016; Mondal et al., 2017; G. Zhang et al., 2017), RADARSAT (Chakraborty & Panigrahy, 2000; Chen et al., 2011; Konishi et al., 2007; McNairn et al., 2014; Shao et al., 2001; Wu et al., 2011; Y. Zhang et al., 2017) among others (Koppe et al., 2013; Pan et al., 2015). Subsequently, a number of remote sensing studies have attempted to study rice phenology in different ecosystems, such as irrigated (Conrad et al., 2011) and rainfed areas (Lebrini et al., 2019). For detecting rice phenology, a wide range of broad and narrow-band vegetation indices, including normalized difference vegetation index (NDVI) and enhanced vegetation index (EVI), from different sensors have been proposed. Sakamoto et al. (2005) showed that MODIS data with 500 m resolution combined with wavelet filter was able to estimate growing date with a root mean square error (RMSE) of 12.1 days on planting date. Xiao et al. (2006) have used EVI and Land Surface Water Index (LSWI) derived from MODIS with 8-days composite images to detect transplanting stage in rice in China. Their result is comparable with statistics from a local ground truth database and achieved high accuracy in a flat area, whilst the accuracy seemingly degraded over hilly areas due to mixed pixels with other land use. Dong et al. (2015) have reported that the Landsat-8 OLI sensor is a potential sensor to map paddy fields with better accuracy than MODIS and Landsat-7 in subtropical regions due to its improved performance within radiometric and spectral resolutions. However, the accuracy of Landsat-8 OLI in tropical to sub-tropical areas are affected by rapid land use change due to natural disasters (e.g. tropical cyclones, earthquakes, landslides, floods, volcanic eruptions), weather conditions and urban expansion with recurrent cloud cover (Dong et al., 2015). To overcome weather limitations (e.g. cloud and shadow cover), radar-based imagery such as Synthetic Aperture Radar, Sentinel-1A (Nguyen et al., 2016), and RADARSAT (Chakraborty & Panigrahy, 2000; Chen et al., 2011; Konishi et al., 2007; Oyoshi et al., 2016) was frequently used. However, access to RADARSAT, which could be a financial burden to implement at the operational level in

developing countries. Moreover, the analysis also needs clean and time series data to be clustered by a trained person or using existing knowledge of the study area which leads to high cost and time-consuming activities.

Classifying rice growth phases with Landsat-8 OLI within southeast Asia could be a challenging task due to complex spectral information. Machine learning statistical algorithms alternatively offer a robust solution for classification in high dimensional, nonlinear and complex remote sensing datasets (Boschetti et al., 2017; Campos-Taberner et al., 2017; Campos-Taberner et al., 2016). Several families of machine learning algorithms such as support vector machine (SVM), e.g. (Mountrakis et al., 2011), random forest, e.g. (Belgiu & Drăguţ, 2016), and artificial neural network (ANN), e.g. (Murmu & Biswas, 2015) are widely used in remote sensing applications. SVM has become a common approach in the remote sensing area, especially in classification problems as SVM can generate a robust model and is resistant to the local minima problem (Mountrakis et al., 2011). Campos-Taberner et al. (2016) successfully retrieved leaf area index (LAI) from a rice crop with high accuracy ($R^2 > 0.92$) using Gaussian process regression (GPR). C. F. Chen et al. (2012) attempted to map the rice area in the Mekong basin in China using MODIS data where they achieved high accuracy with a neural network approach.

In Indonesia, ground-based monitoring of rice crops is conducted by a stand-alone camera with an internet connection (webcam). The time-series information from webcam images can depict plant phenology and bare land with more precision than satellite and airborne remote sensing imagery. For example, Liu et al. (2017) have compared vegetation index between the webcam and three different scales of remote sensing imagery and found that the results are comparable to grass savanna with an $R^2 > 0.81$. Hence, the use of ground-based webcam information and remote sensing imagery has a great potential to be used to monitor rice growth phases in a spatial extent from local to global scale using domain

adaptation which has never been explored before in tropical landscape. However, the majority of the studies have used limited data to analyse rice phenology. In addition, these models are associated with poor transferability which impedes the practical application of remote sensing tools.

This study aims to develop a workflow to combine webcam information and remote sensing data (Landsat-8) for mapping rice phenology from 2014 to 2016 using machine learning algorithms such as RF, SVM, and ANN and tested the temporal consistency. This study also tested the transferability of mapping rice phenology and its temporal consistency.

3.2 Data collection

3.2.1 Training dataset

(a) Ground data

Webcam stations are equipped with solar-powered 1.3-megapixel digital cameras and located all around Java Island (Figure 3.1). This study utilizes 35 webcams from the total 55 stations across Java Island as some webcam stations have limited data. The captured photos of these webcams are in the public domain and available at the website: katam.litbang.pertanian.go.id in near real-time. This study used the images between 1 January 2014 and 31 December 2016. The webcams have a field of view of ±200 m on either side of the camera's focal point. Quantum GIS software overlaid with Google Earth layers is applied to ensure the camera focal point is in the middle of the paddy field.

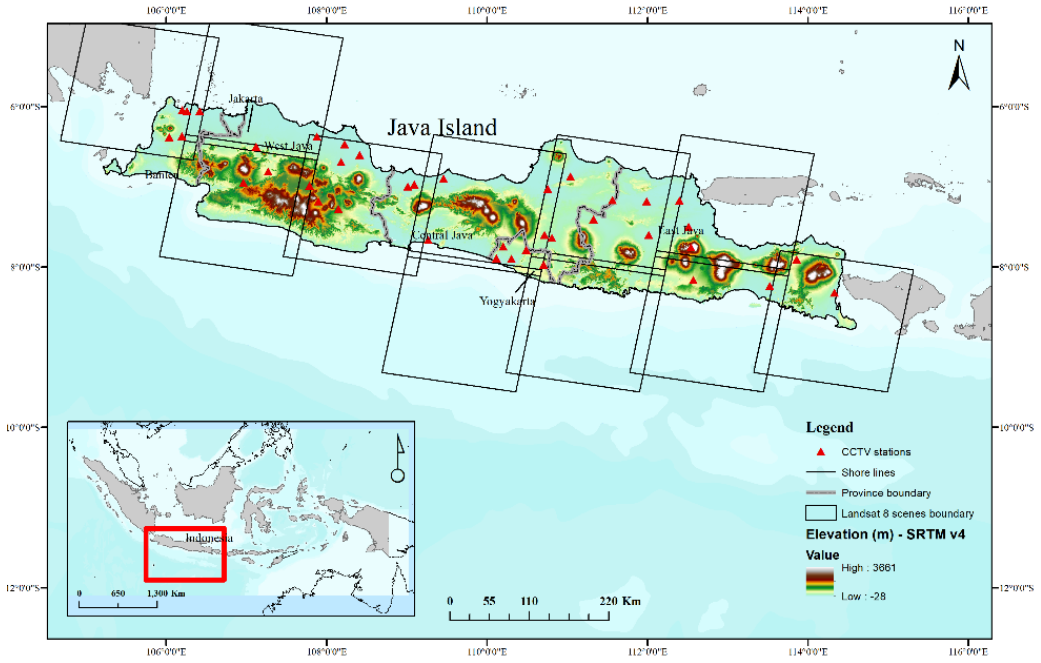

Figure 3.1 Webcam locations on Java Island.

(b) Landsat-8 OLI training dataset

The surface reflectance of Landsat time-series data was downloaded from Google Earth Engine (GEE) repository from 2014-2016 sourced from the United States Geological Survey Earth Resources Observation and Science. The GEE computing platform enables the researcher to process an enormous amount of remote sensing data with unprecedented speed without having difficulties in downloading raw or pre-processed images (Gorelick et al., 2017). The raw Landsat images were orthorectified, radiometrically calibrated and atmospherically corrected using Landsat Surface Reflectance Code (LaSRC) method (USGS, 2017). The six bands which were used in this study are Band 2/ Blue (452 – 512 nm), Band 3/ Green (533 – 590 nm), Band 4/ Red (636 – 673 nm), Band 5/ NIR (0.851 – 879 nm), Band 6/ SWIR1 (1,566 – 1,651 nm), and Band 7/ SWIR2 (2,107 – 2,294 nm) with 30 m resolution. The pixel quality of Landsat images was calculated with CFMASK methods such as clear, water, cloud, snow, and shadows (Foga et al., 2017). The number

of scenes which covered the webcam locations varied from 63-132 scenes for each webcam point with a total of 631 scenes. The scenes derived from 11 paths/rows: 117/66, 118/65, 118/66, 119/65, 119/66, 120/65, 121/64, 121/65, 122/64, 122/65, and 123/64. The satellite images were directly downloaded from Google Earth Engine based on the USGS dataset (USGS Landsat-8 Surface Reflectance Tier 1) with UTM projection and WGS84 datum. Furthermore, the spatial analysis was conducted in the R statistical software with *raster* package (Hijmans, 2016) and the map layout was done by using ArcGIS 10.4.

3.2.2 Applied area

We chose Indramayu as the application area for the best classification model because Indramayu is one of the most significant rice-producing regions in northwest Java Province, Indonesia (Figure 3.2) and also the cropping pattern in Indramayu is dominated by monocultures (Rice). Indramayu consists of 11 sub-districts and borders with the sea to the north and four regencies to the south and northwest. The area is mainly flat with its sloping degree of 0-2 % on altitude 0-100 m above sea level (Siregar & Crane, 2011). The tropical weather and monsoonal climate in this area result in a wet season starting from November to May and a dry season from June to October. The average temperature is 22.9 to 30 °C with an annual average precipitation of 2,213 mm in 2014-2016 (Bontkes & Wopereis, 2003). The regency covers an area of 2,099 km^2 with an irrigated rice/paddy area of 94.94 km^2 and a non-irrigated area of 20.9 km^2 (Bontkes & Wopereis, 2003). The irrigated paddy field is mainly located on Cimanuk – Cisanggarung and Citarum watershed and the planting date are controlled by scheduled water distribution from Jatigede and Rentang Dam (Boer et al., 2012; BPS-Indramayu, 2017; Sianturi et al., 2018).

Cultivation of rice in Indramayu has the first planting season from November to January, with the second planting season from March-July. Some areas to the south of Indramayu are bare land from August to October. Paddy fields near the sea would have the second

planting from July-October as during the rainy season, and they cannot cultivate due to flooding (Fig. 1). In the study area, the farmers commonly utilize the transplanting method of rice cultivation where the farmer grows the seed in a nursery and after 20-25 days the seedling is transplanted to the cultivation area (paddy) and harvested after 100 days (Sari et al., 2013). Transplanting is a widely adopted planting method of weed control in rice cultivation across Asia. The dominant rice varieties in this area are Ciherang, Mekongga, and Situbagendit which are short-duration varieties. The farmers in this area tend to cultivate rice even though water is limited, thus the vulnerability of this area is higher than other areas due to water competition between low stream area and upstream areas, especially during the dry season (Sianturi et al., 2018; Siregar & Crane, 2011).

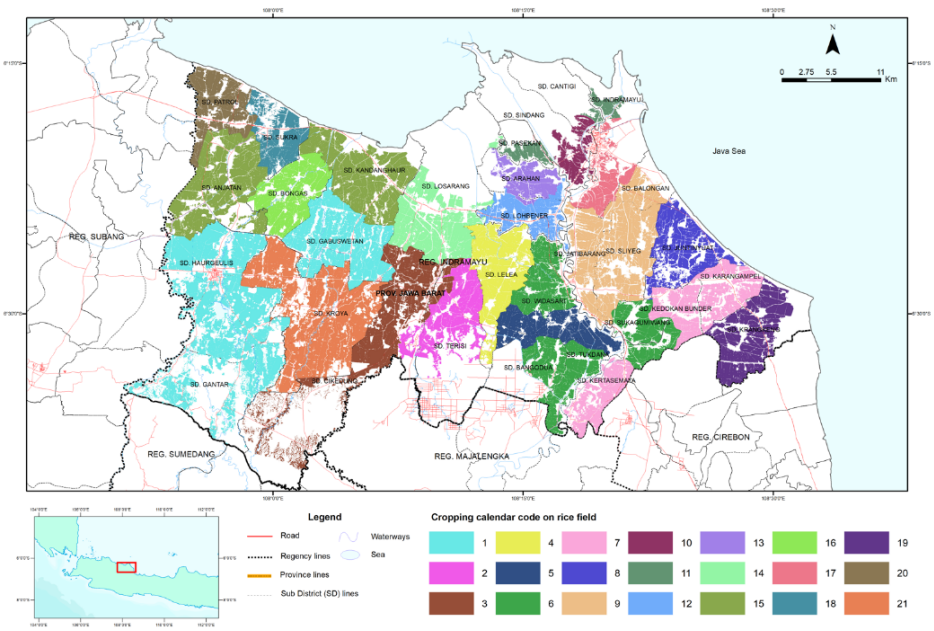

Code	Oct	Nov	Dec	Jan	Feb	Mar	Apr	May	Jun	Jul	Aug	Sep
1	Fallow	Paddy			Harvest	Fallow	Paddy			Harvest	Bareland	
2	Bareland	Fallow	Paddy			Harvest	Fallow	Paddy			Harvest	Bareland
3	Bareland	Fallow	Paddy			Harvest	Paddy			Harvest	Bareland	
4	Bareland		Fallow	Paddy			Harvest	Fallow	Paddy			Harvest
5	Bareland			Fallow	Paddy		Harvest	Bareland	Fallow	Paddy		Harvest
6	Bareland		Fallow	Paddy			Harvest	Fallow	Paddy			Harvest
7	Bareland		Fallow	Paddy			Harvest	Paddy			Harvest	Bareland
8	Bareland		Fallow	Paddy		Harvest	Paddy			Harvest	Bareland	
9	Bareland		Fallow	Fallow	Paddy			Harvest	Paddy			Harvest
10	Bareland		Fallow	Paddy				Harvest	Paddy			Harvest
11	Bareland	Fallow	Paddy			Harvest	Paddy				Harvest	Bareland
12	Bareland		Fallow	Paddy			Harvest	Paddy			Harvest	Bareland
13	Bareland			Fallow	Paddy			Harvest	Paddy			Harvest
14	Bareland		Fallow	Paddy			Harvest	Fallow	Paddy		Harvest	Bareland
15	Bareland			Fallow	Paddy			Harvest	Paddy			Harvest
16	Bareland		Fallow	Paddy			Harvest	Fallow	Paddy		Harvest	Bareland
17	Harvest	Bareland			Fallow	Paddy			Harvest	Paddy		
18	Harvest	Bareland	Fallow	Paddy				Harvest	Paddy			
19	Paddy	Harvest	Bareland		Fallow	Paddy			Harvest	Paddy		
20	Paddy	Harvest	Bareland	Fallow	Paddy			Harvest	Bareland	Paddy		
21	Secondary crops	Paddy			Harvest	Fallow	Paddy			Harvest	Secondary crops	

Figure 3.2 The planting calendar on paddy field map of Indramayu Regency, Indonesia (Compiled from local statistics agency).

The Landsat-8 OLI images to be applied with the best data model and to detect short (e.g. weeks) temporal changes within the applied area were derived from two Landsat-8 OLI set images with path/row 121/64 and 120/65 in a different year. The first set is 6 September 2014 and 22 September 2014, secondly 21 June 2015, and 7 July 2015, and the last set is 7

June 2016 and 23 June 2016, as shown in Figure 3.3. These dates were selected because they are the clearest data in the consecutive order for each year to reduce cloud and shadows interference.

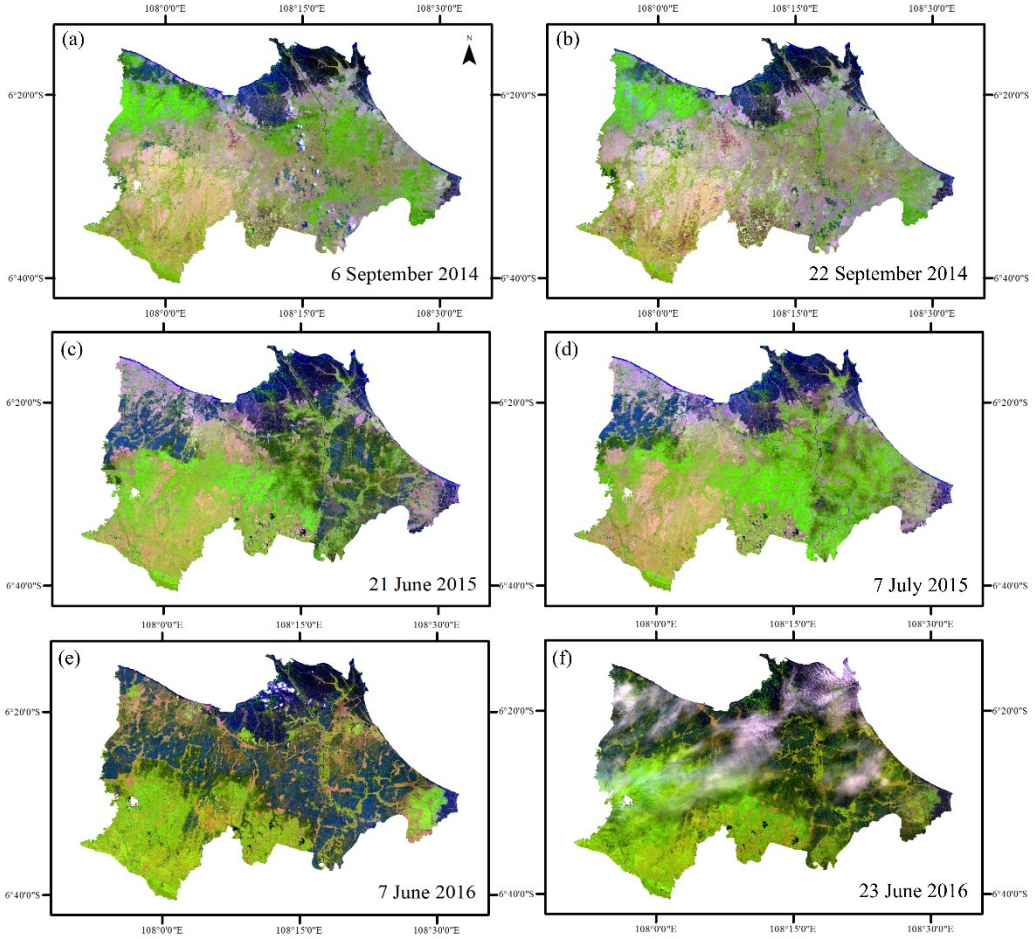

Figure 3.3 The Landsat image of Indramayu Regency with false colour RGB (SWIR1, NIR, and Green) band for scenes: (a) 6 September 2014, (b) 22 September 2014, (c) 21 June 2015, and (d) 7 July 2015, (e) 7 June 2016, and (f) 23 June 2016.

3.3 Methodology

The proposed methodology is composed of three steps, including data pre-processing, model training and testing, and temporal change analysis (Figure 3.4).

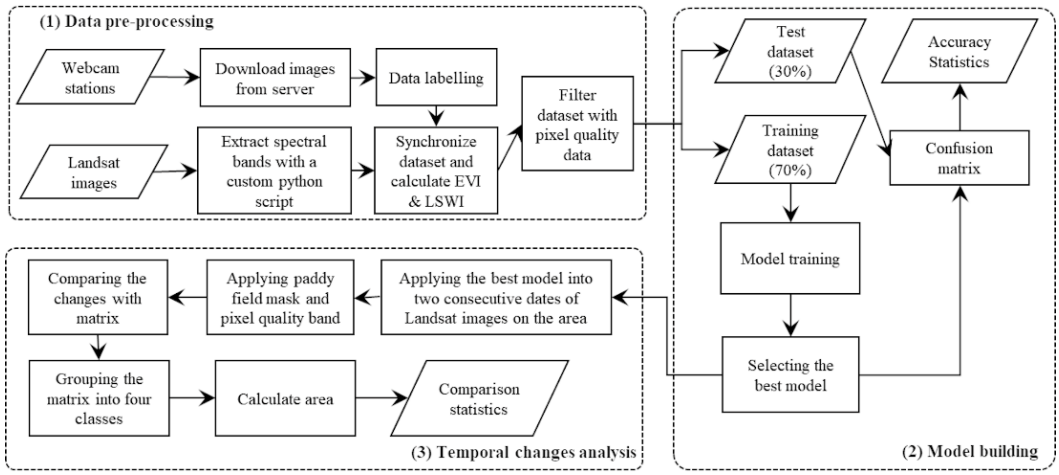

Figure 3.4 The flowchart of the methodology.

3.3.1 Data labelling

Identification of rice growth phases was carried out by visually interpreting webcam images. The significant paddy area activities were recognized as bare land, land preparation, ploughing, inundation, transplanting, vegetative, reproductive, ripening, and harvested stage with a total of 110-125 days of the rice lifecycle (Moldenhauer et al., 2013). However, we have considered three main growth phases and bare land in the analysis. The vegetative stage is started from seedling to tillering within 45-60 days. Afterwards, the reproductive phase is characterized by the emergence of a flag leaf, booting, until flowering. The duration of this phase is ±35 days. The last phase is ripening defined by a 'milk stage' (±30 days) of the grain until it hardens and is ready to harvest. The bare land stages are the land when uncultivated, after harvest, and ratoon; the vegetative stage starts from the transplanting phase after the land has been ploughed and the seed was grown in the nursery bed for 20 – 25 days. The next stage is reproductive from panicle initiation to flowering and ripening stage where vegetation and grains turn yellowish until it has been harvested.

Due to technical difficulties such as network error, the dataset of webcam imagery is not entirely complete. If there are missing images without key phases, these are labelled as no data. In the data analysis, we have considered the cloud-free images (FMASK=322). Table 3.1 shows that the highest frequency of class was bare land since the duration is longer than other phases. Moreover, the masking process eliminated 48.3% from the synchronized data indicating that the areas with webcam stations have high cloud interference.

Table 3.1 Recapitulation of the dataset.

Phase	Synchronized data	Unused data	Used data	Training data (70%)	Test data (30%)
Bare land	424	222	202	142	60
Vegetative	431	184	247	173	74
Reproductive	299	156	143	101	42
Ripening	431	269	162	114	48
Total	1,448	694	754	530	208

The data on rice growth phases were synchronized on the same date with six bands of Landsat-8 OLI from the GEE dataset with a custom python script. We also calculated EVI and LSWI to compare classification performance between three datasets: a) six bands, (b) EVI, c) LSWI. The formula of EVI and LSWI are:

$$EVI=2.5 \times \frac{\rho_{NIR} - \rho_{Red}}{\rho_{NIR} + 6 \times \rho_{Red} - 7.5 \times \rho_{Blue} + 1}$$

$$LSWI=\frac{\rho_{NIR} - \rho_{SWIR1}}{\rho_{NIR} + \rho_{SWIR1}}$$

where ρ is reflectance band, NIR is near-infrared, SWIR1: short-wave infrared 1.

3.3.2 Building the machine learning model

The classification was carried out on a desktop computer using the R package for statistical analysis (Team, 2017), R Studio 1.0.143, and *caret* library (Kuhn, 2008). The *caret* library is a single interface package that allows exploring multiple classifiers in fewer steps and is capable of performing parallel computing (Kuhn & Johnson, 2013). The specific random seed was set before randomly splitting the dataset to ensure the model building was repeatable with the same result. The dataset was randomly divided into 70:30 proportion. The 70% of the dataset was used to train the model with Leave One Out Cross-Validation (LOOCV), a resampling technique to hinder overfitting in the model. LOOCV is the least biased and computationally challenging technique of validation to reduce the variance in model training that one sample is left out, is selected, widely used classification and the rest is used to train the model with specific tuning parameters, and this process is repeated until all samples are used in training. Thus, all the training results are summarized based on the accuracy parameter and the model with the highest accuracy was selected for test analysis with the confusion matrix (Kuhn & Johnson, 2013). In this study, we have evaluated widely using classification algorithms such as random forest, support vector machine and artificial neural network. The parameters of the selected classification algorithms were optimized using a grid search technique.

(a) Random Forest (RF)

RF is an ensemble algorithm based on a decision tree mechanism where each tree is grown independently using a random set of variables and samples and then averages the results of all trees (Belgiu & Drăguţ, 2016; Breiman, 2001). RF technique can run proficiently for the massive dataset (Tatsumi et al., 2015). This analysis was run using *randomForest* library(Liaw & Wiener, 2002) which can be divided into several steps. 1) Creating random decision trees (*ntree*); 2) for each tree, create random bootstrap samples from training

dataset; 3) grow the tree with each internal node using *mtry* predictors (a subset of variables) which are randomly selected and choose the best optimizing split criteria. The last step is selecting the final result of the majority vote from each tree. The previous study shows that higher *mtry* can lead to higher performance by selecting importance predictors(Strobl et al., 2008). The hyperparameters, *ntree,* and *mtry* were optimized with a grid search approach where different combinations of hyperparameters values were evaluated.

(b) Support Vector Machines (SVM)

Support vector machine (SVM) is a popular pattern matching algorithm which constructs optimum hyperplane in a high dimensional space to separate different classes of observations (Verrelst et al., 2015), and requires considerably more computational time than other approaches. In this study, we used three different kernels (Linear, Polynomial, and Radial basis function) with the main parameter Cost (*C*) for smoothing the hyperplane. For polynomial function two parameters, polynomial degree function and scale to determine the normalizing pattern, are required. The radial basis function has one parameter which is Sigma to modify decision boundary. The parameters were tuned within the search window of: for *C* parameter 2^n with n =1 to 10, for Polynomial degree= 1 to 5, scale= 0.001, 0.01, 0, and *C* are 0.01, 0.1, 1 to 20. The last kernel is SVM Radial which was tuned for 2^{-25}, 2^{-20}, 2^{-15}, 2^{-10}, 2^{-5}, 0 and C were set for 2^n with n =1 to 10.

(c) Artificial Neural Networks (ANN)

ANN is a classifier which imitates brain cells to solve complex nonlinear problems (Verrelst et al., 2015). While brain cells contain a collection of neurons, which are connected to each other using a synapse, ANN has nodes and weights, respectively. There are three layers of nodes in the common ANN process. The first layer is the input layer

which is the node that carries out the pixel values of each index in the image. The second layer is a hidden layer, which contains nodes that calculate the sum of logistic function from input nodes in the input layer and the weights of connection to determine node value. The hidden layer becomes the input to specific nodes in the output layer. The output layer calculates the final decision by comparing the values of the nodes from a logistic function with the actual class. This process is run iteratively to minimize the error from input to output layer using a feed-forward propagation algorithm and was used for model training because it provides an adjustable method in the generalization of linear regression (Venables & Ripley, 2013). The tuning parameter is the size of nodes in the hidden layer=1-10, and weight decays are 10^{-4}, 10^{-3}, 10^{-2}, 10^{-1}, and 0. Minimizing weight decay value increases optimization and prevents over-fitting because it can penalize big weights (Venables & Ripley, 2013).

3.3.3 Accuracy statistics

The final classification model was selected based on the average accuracy from iterations of the cross-validation procedure. The performance of the training model was validated with the test dataset. The final results of each classifier were evaluated by the statistics of the performance such as the overall accuracy (OA), producer's accuracy (PA), user's accuracy (UA), and kappa (κ) was calculated using error matrices as shown in Figure 3.5 (Congalton & Green, 2008; Foody, 2002). Landis and Koch (1977) categorized κ into seven classes e.g. 0.81-1.00: almost perfect, 0.61-0.80: substantial, 0.41-0.60: moderate, 0.21-0.40: fair, 0.00-0.21: slight, and <0.00: poor. Thus, these accuracy measurements were analysed with one-way ANOVA and Tukey Honest to test the statistical difference between the classifiers.

		Test data				
		A	B	C	Σ	User's accuracy (%)
Classified data	A	N_{AA}	N_{AB}	N_{AC}	Σ_{AR}	N_{AA}/Σ_{AR} x 100%
	B	N_{BA}	N_{BB}	N_{BC}	Σ_{BR}	N_{BB}/Σ_{BR} x 100%
	C	N_{CA}	N_{CB}	N_{CC}	Σ_{CR}	N_{CC}/Σ_{AR} x 100%
	Σ	Σ_{PA}	Σ_{PB}	Σ_{PC}	N	
	Producers's accuracy (PA) (%)	N_{AA}/Σ_{PA} x 100%	N_{AB}/Σ_{PB} x 100%	N_{AC}/Σ_{PC} x 100%		

$$\text{Overall accuracy (OA)} = \frac{N_{AA} + N_{BB} + N_{CC}}{N} \text{ x } 100\%$$

$$\text{kappa} = \frac{N\sum_{j=1}^{k} N_{jj} - \sum_{j=1}^{k} N_{jR}N_{Pj}}{N^2 - \sum_{j=1}^{k} N_{jR}N_{Pj}}$$

Note: N is total points, k is number of classes, R is test classes, and P is classified class

Figure 3.5 The example of confusion matrix, the formula of producer's, user's, and overall accuracy, and kappa.

3.4 Temporal change analysis

The temporal consistency of the model estimates was investigated on two consecutive Landsat images in the Indramayu Regency. Non-rice growing areas were masked with a high-resolution paddy field map, supplied by the Indonesian Ministry of Agriculture which was developed from very high-resolution satellite images, such as IKONOS and SPOT, and properly validated with field campaigns in 2008-2010.

There are four classes in each date classification map from the best model results from the model building process, such as bare land, vegetative, reproductive, and ripening. The next step was applying a mask of pixel quality band to get two other classes (water and cloud/shadows). Thus, the temporal changes were analysed by creating a matrix between classification with six classes on the current and the previous images. This transitional matrix consists of 36 classes; then it was reclassified into four classes (Table 3.2). The new classes are (1) **Unchanged**: there are no class changes between four rice growth phases; (2) **Changed correctly**: there is a one-step stage change forward between rice growth

phases, and bare land and vegetative into the water, and water into bare land and the vegetative stage (3) **Changed incorrectly**: there is a two-step and more stage changes forward between rice growth phases or a stage change backward between rice growth phases. For example, water changes into a reproductive and ripening stage or a change from the vegetative and reproductive stage into bare land or reproductive and ripening stage into the water, and there is no change in water class; 4) **Cloud and shadow**: there is a shadow or cloud class on one or two dates. The sum of the area of four classes was summarized with spatial analysis, and the mean difference percentage of the area between classes for all classifiers was calculated for each year. Especially for changed incorrectly class, the mean of absolute differences (MAD) was calculated over the three years to compare performance between the classifiers.

Table 3.2 An example of a transitional matrix and reclassifying scheme in 2015.

		Classification on 7 July 2015 (current)					
	Code	**1**	**2**	**3**	**4**	**11**	**12**
Classification on 21 June 2015 (previous)	**1**	1 → 1	1 → 2	1 → 3	1 → 4	1 → 11	1 → 12
	2	2 → 1	2 → 2	2 → 3	2 → 4	2 → 11	2 → 12
	3	3 → 1	3 → 2	3 → 3	3 → 4	3 → 11	3 → 12
	4	4 → 1	4 → 2	4 → 3	4 → 4	4 → 11	4 →12
	11	11 → 1	11 → 2	11 → 3	11 → 4	11 → 11	11 → 12
	12	12 → 1	12 → 2	12 → 3	12 → 4	12 → 11	12 → 12

Note: The colour-coded temporal changes classification matrix. The number codes are (1) Bare land; (2) Vegetative; (3) Reproductive; (4) Ripening; (11) Water; (12) Cloud/ shadow. The colour codes are Yellow: Unchanged; Green: Change correctly; Red: Change incorrectly; and Grey: Cloud and shadow.

3.5 Results

3.5.1 Spectral signature analysis

The spectral signatures of three rice growth phases and bare land in our study were calculated using all training samples. Figure 3.6 (a) shows the mean spectral reflectance and the corresponding rice growth phase. The bare land stage has a different pattern as it has the highest reflectance on the red and SWIR1. On the other hand, vegetative, reproductive, and ripening phases pose an almost identical pattern where the surface reflectance was low at the red band and high at the NIR band. The highest reflectance value of the reproductive stage on the NIR band indicates that the interpretation of the growth phase using secondary data correlates with the greenness of rice growth which has a high mean reflectance on the NIR band. However, the ripening phase is almost identical to the reproductive stage, except it is lower on the NIR band which indicates that the accuracy of identification of the ripening stage would also be lower. The webcam images on selected dates indicate four phases of paddy growth phases (Figure 3.6(b)) highlighting that the reproductive and ripening stages have almost identical visual appearances and spectral curves.

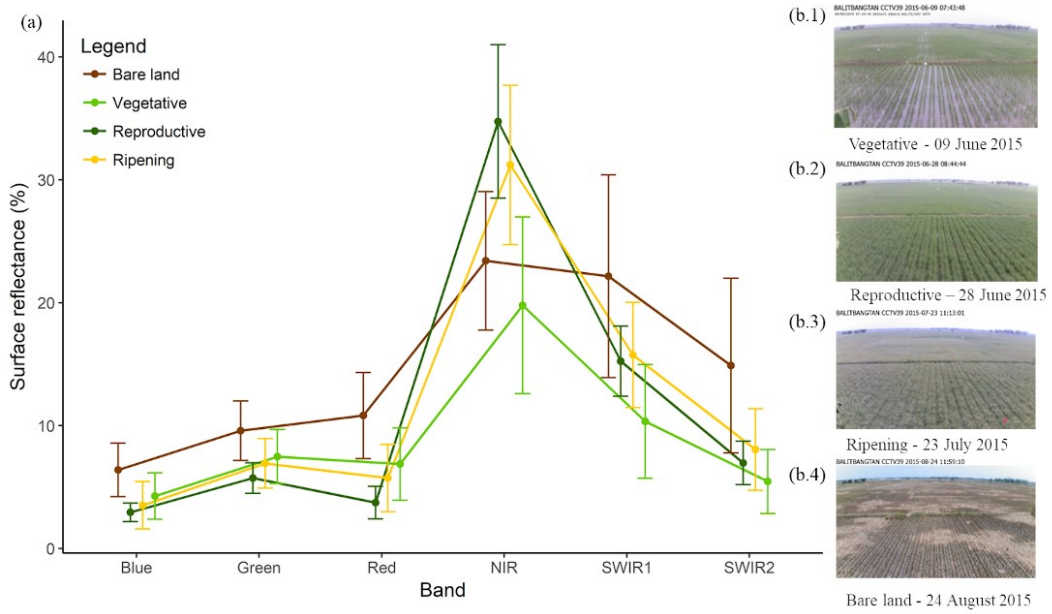

Figure 3.6 (a) Spectral signatures of rice growth phases in mean surface reflectance based on training and test dataset. (b) The example images from webcam station with coordinate: 6°28'18.0"S, 108°13'35.0"E with vegetative (b.1), reproductive (b.2), ripening (b.3), and bare land (b.4).

3.5.2 Accuracy assessment

The accuracy measurement using the confusion matrix of different predictors has been done to investigate the best predictors used to classify the rice growth stages. Table 3.3 shows that the accuracy of using EVI as a sole predictor is 49.6% with SVM Polynomial, and for LSWI and EVI as predictors are 62.5%. Moreover, the highest accuracy (68.3 – 70.5%) was achieved by using six Landsat-8 bands as predictors in all classifiers which outperformed EVI's accuracy by>20%.

Table 3.3 The list of the accurate measurements based on Landsat-8's test data for rice growth stage classification with different predictor datasets.

#	Classifier	Predictors	Overall accuracy	kappa
1	ANN	LSWI and EVI	60.3%	0.45
2	ANN	EVI	49.1%	0.32
3	ANN	Blue, Green, Red, NIR, SWIR1, and SWIR2	70.1%	0.59
4	Random Forest	LSWI and EVI	61.6%	0.48
5	Random Forest	EVI	43.8%	0.24
6	Random Forest	Blue, Green, Red, NIR, SWIR1, and SWIR2	68.3%	0.57
7	SVM Linear	LSWI and EVI	62.9%	0.50
8	SVM Linear	EVI	46.4%	0.26
9	SVM Linear	Blue, Green, Red, NIR, SWIR1, and SWIR2	70.1%	0.59
10	SVM Polynomial	LSWI and EVI	62.5%	0.49
11	SVM Polynomial	EVI	49.6%	0.33
12	SVM Polynomial	Blue, Green, Red, NIR, SWIR1, and SWIR2	70.1%	0.59
13	SVM Radial	LSWI and EVI	60.3%	0.46
14	SVM Radial	EVI	49.1%	0.32
15	SVM Radial	Blue, Green, Red, NIR, SWIR1, and SWIR2	70.5%	0.60

The confusion matrix indicates that all classifiers have the highest producer's accuracy (PA) in the vegetative stage (Table 3.4). On the other hand, the highest UA (user's accuracy) is a bare land stage. It indicates that SWIR1 is more dominant than the NIR band prediction. However, the reproductive stage has the lowest PA and UA because of the availability of a limited amount of data over a short time (Table 3.4).

Overall, the classifiers has significantly different accuracies F at the $p < 0.001$ for [F(4,120), $p <$ 1.01e-07] of classifiers. The pairwise test shows that there is no significant difference in accuracy and kappa between SVM based classifiers and ANN except the pair with RF (Figure 3.7).

.

Table 3.4 The confusion matrix performance on the test dataset.

		Test data					
	Growth phases	Bare land	Vegetative	Reproductive	Ripening	Total	UA (%)
			(a) Artificial Neural Networks				
Classified data	Bare land	**42**	4	0	8	54	**77.8**
	Vegetative	13	**57**	2	3	75	76.0
	Reproductive	0	8	**23**	2	33	69.7
	Ripening	5	5	17	**35**	62	56.5
	Total	60	74	42	48	224	
	PA (%)	70.0	**77.0**	54.8	72.9		
	OA (%)	70.1					
	kappa	0.59					
			(b) Random Forest				
Classified data	Bare land	**44**	4	0	8	56	**78.6**
	Vegetative	13	**56**	2	3	74	75.7
	Reproductive	0	7	**23**	7	37	62.2
	Ripening	3	7	17	**30**	57	52.6
	Total	60	74	42	48	224	
	PA (%)	73.3	**75.7**	54.8	62.5		
	OA (%)	68.3					
	kappa	0.57					
			(c) SVM Linear				
Classified data	Bare land	**41**	3	0	8	52	**78.8**
	Vegetative	15	**60**	2	5	82	73.2
	Reproductive	0	9	**26**	5	40	65.0
	Ripening	4	2	14	**30**	50	60.0
	Total	60	74	42	48	224	
	PA (%)	68.3	**81.1**	61.9	62.5		
	OA (%)	70.1					

	kappa	0.59					
			(d) SVM Polynomial				
Classified data	Bare land	**45**	2	0	8	55	**81.8**
	Vegetative	12	**57**	2	4	75	76.0
	Reproductive	0	9	**23**	4	36	63.9
	Ripening	3	6	17	**32**	58	55.2
	Total	60	74	42	48	224	
	PA (%)	75.0	**77.0**	54.8	66.7		
	OA (%)	70.1					
	kappa	0.59					
			(e) SVM Radial				
Classified data	Bare land	**43**	1	0	10	54	**79.6**
	Vegetative	13	**60**	2	3	78	76.9
	Reproductive	0	8	**24**	4	36	66.7
	Ripening	4	5	16	**31**	56	55.4
	Total	60	74	42	48	224	
	PA (%)	71.7	**81.1**	57.1	64.6		
	OA (%)	70.5					
	kappa	0.60					

3.5.3 Temporal model consistency

Multitemporal maps of the study area extracted during the times of 2014 (September), 2015 (July), and 2016 (July) show the distribution of rice phenology and bare land. The images in 2014 show that almost all the area is in a bare land stage after the second planting season (Figure 3.8). The northern part of the image was misclassified, indicated by red colour. In contrast to 2014, the majority of 2015 was dominated by the vegetative stage due to a second planting season (Figure 3.9). Figure 3.10 shows that the dataset images have more cloudy areas than the previous year. The date was 16-days earlier than dataset images in 2015, which show the peak of the vegetative stage in most areas for the second planting season. Overall, the classification shows a good agreement with the cropping pattern (Sianturi et al., 2018). Over the three years within this study, only a small proportion of the area was misclassified. The topographic effect also contributed to lesser accuracy since the optical sensor depends on a homogenous indicated angle on a flat area (Proy et al., 1989). Therefore, all small parcel rice areas in the hilly area would give inconsistent surface reflectance which the model could not predict.

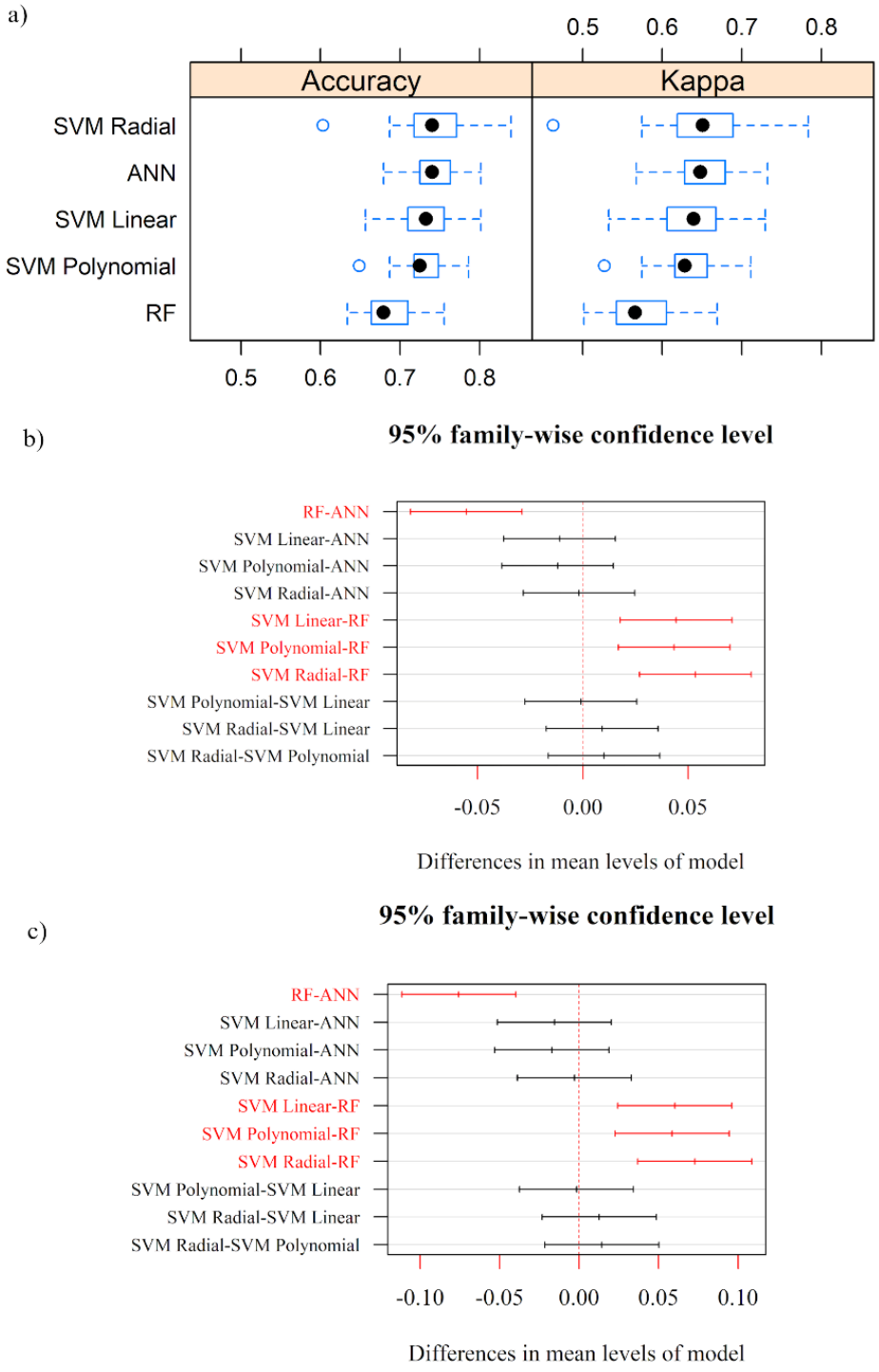

Note: ANN: Artificial Neural Network, RF: Random Forest, SVM: Support Vector Machine. Red lines show highly significant differences between the two classifiers.

Figure 3.7 (a) The boxplot of overall accuracy (OA) and kappa (κ), (b) Tukey test result of confidence level of OA, and (c) Tukey test result of confidence level of kappa.

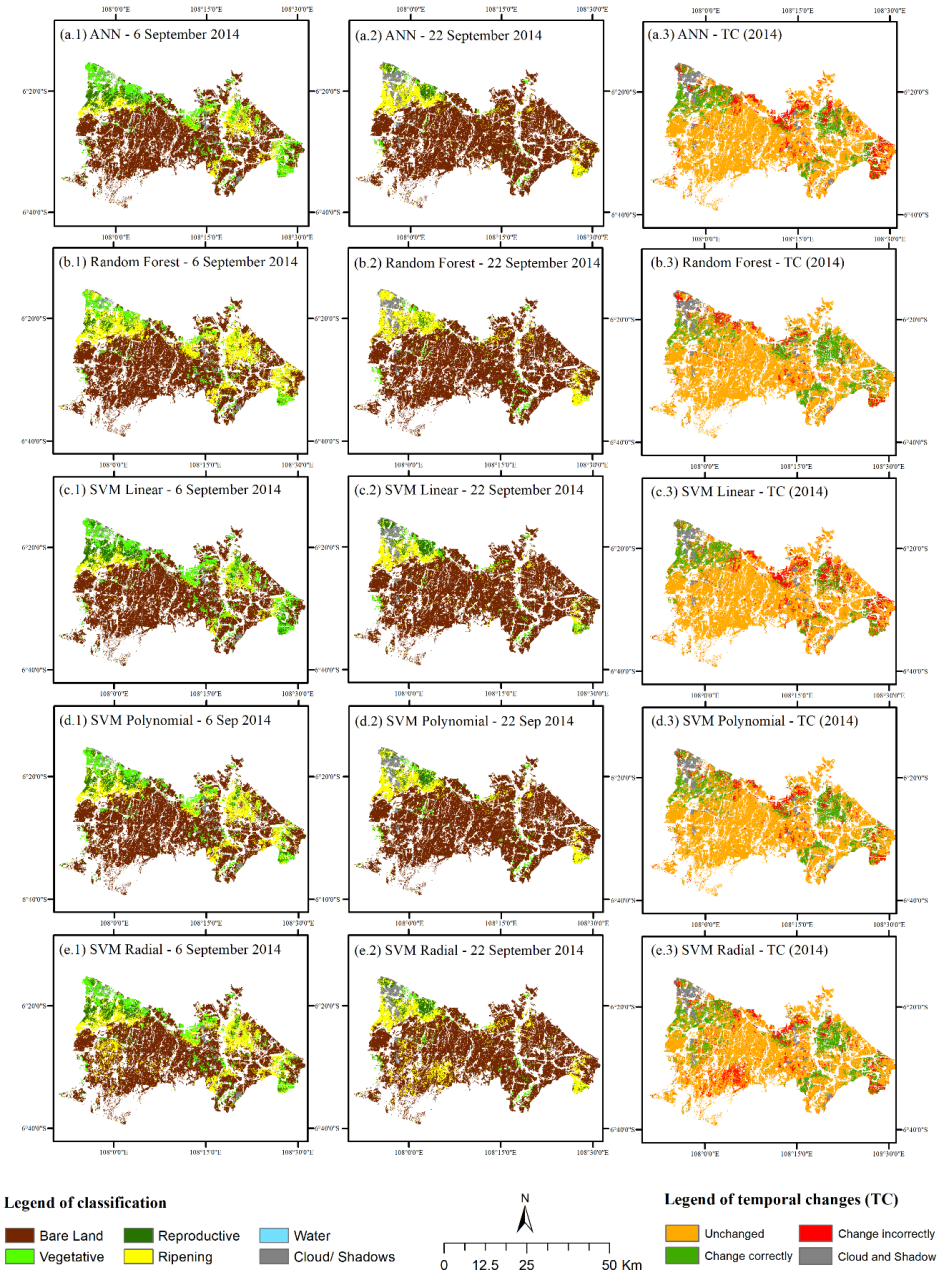

Figure 3.8 The classification maps based on Landsat image on 6 September 2014 for (a.1) ANN, (b.1) Random forest, (c1) SVM Linear, (d.1) SVM Polynomial, and (e.1) SVM Radial and on 22 September 2014 for (a.2) ANN, (b.3) Random forest, (c.4) SVM Linear, (d.5) SVM Polynomial, and (b.6) SVM Radial. The temporal changes in 2014 for (a.3) ANN, (b.3) Random Forest, (c.3) SVM Linear, (d.3) SVM Polynomial, and (e.3) SVM Radial.

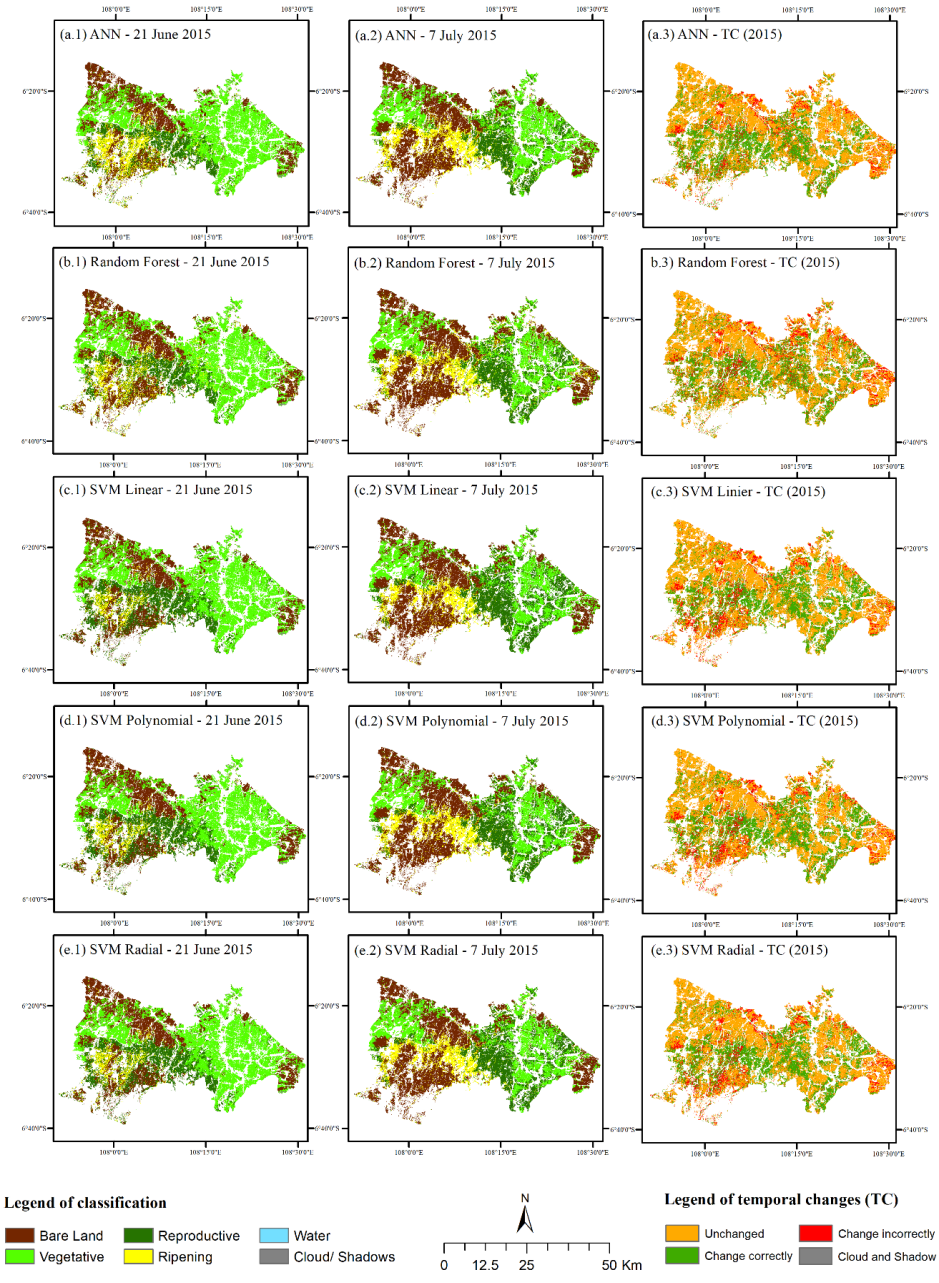

Figure 3.9 The classification maps based on Landsat image on 21 June 2015 for (a.1) ANN, (b.1) Random forest, (c1) SVM Linear, (d.1) SVM Polynomial, and (e.1) SVM Radial and on 7 July 2015 for (a.2) ANN, (b.3) Random forest, (c.4) SVM Linear, (d.5) SVM Polynomial, and (b.6) SVM Radial. The temporal changes in 2014 for (a.3) ANN, (b.3) Random Forest, (c.3) SVM Linear, (d.3) SVM Polynomial, and (e.3) SVM Radial.

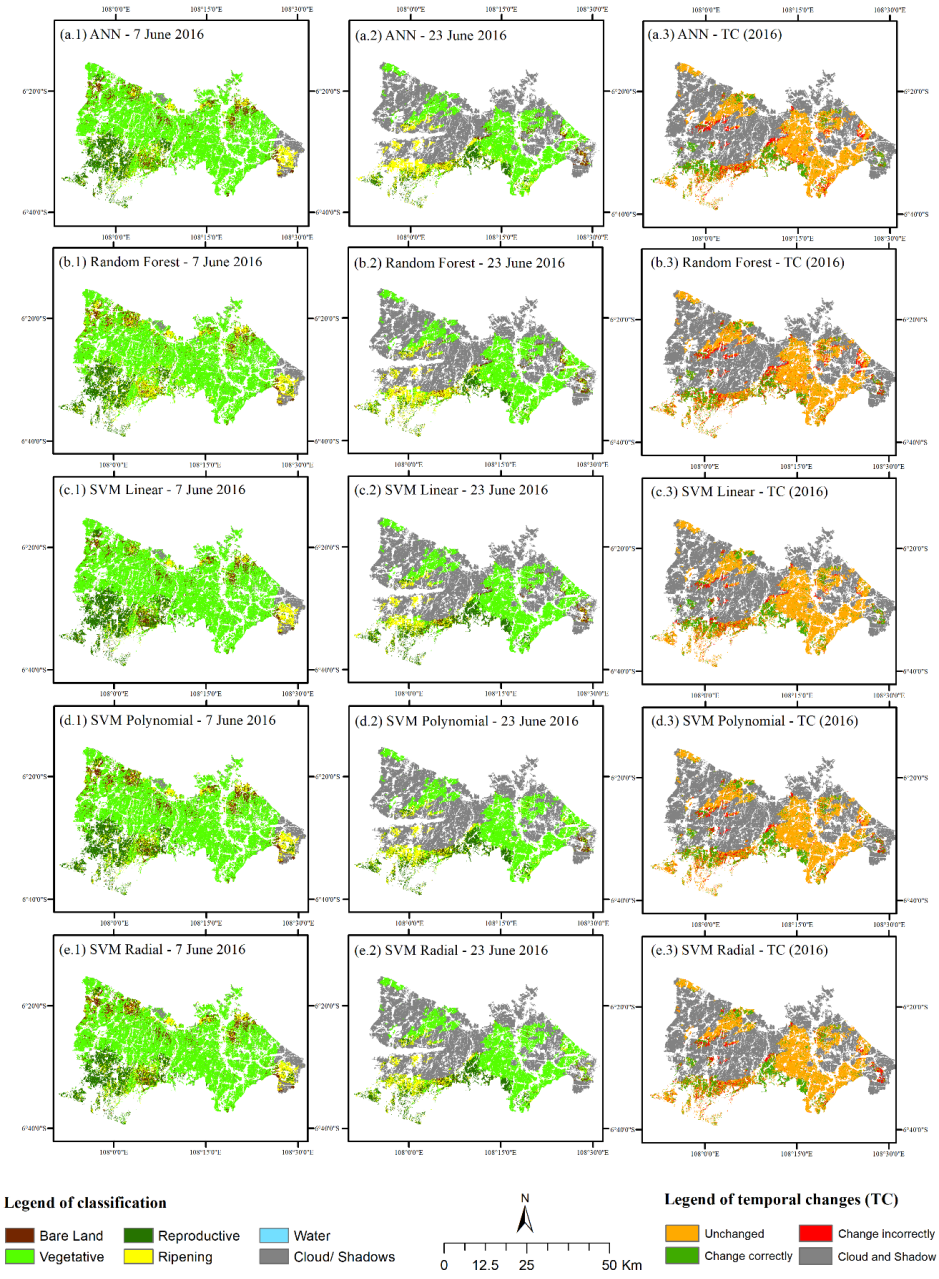

Figure 3.10 The classification maps based on Landsat image on 7 June 2016 for (a.1) ANN, (b.1) Random forest, (c1) SVM Linear, (d.1) SVM Polynomial, and (e.1) SVM Radial and on 23 June 2016 for (a.2) ANN, (b.3) Random forest, (c.4) SVM Linear, (d.5) SVM Polynomial, and (b.6) SVM Radial. The temporal changes in 2014 for (a.3) ANN, (b.3) Random Forest, (c.3) SVM Linear, (d.3) SVM Polynomial, and (e.3) SVM Radial.

3.5.4 Spatio-temporal changes

The temporal changes were completed by classifying two consecutive Landsat images to explore the consistency of the surface changes during the 16-day interval for three consecutive years. In Figure 3.8-3.10 (a-f.3), the performance of all classifiers was consistent except Random Forest. Random Forest mostly misclassified transitions from bare land and vegetative phase to ripening phase. Moreover, nonlinear SVM has the least difference than other classifiers (7.83% and 10.19%) due to the flexibility of hyperplane for determining class separation in high dimensional space, as shown in Table 3.5.

3.6 Discussion

In this study, we have presented a workflow of mapping rice growth phases in Indramayu Regency using Landsat-8 and ground webcam data using machine learning algorithms which dataset and code can be downloaded at https://github.com/FadhlullahRamadhani/LS8-OLI-MAPPING. In order to create a robust model, extensive data were collected between 2014 and 2016. Since rice phenology is associated with seasonal dynamics due to different cultivation practices (upland and lowland), cropping patterns, environmental changes, a wide range of remote sensing datasets such as Landsat-8, Sentinel-2, and Sentinel-1 are essential to characterise rice crops as stressed by Rudiyanto et al. (2019) regarding the importance of time-series remote sensing data for characterising rice phenology. Although many researchers restrict experiments to limited timeframes (Parsa & Dirgahayu, 2013), this study accounted for different seasons throughout multiple years and environments for modelling the rice phenology.

Table 3.5. The recapitulation of temporal changes in mean absolute difference (MAD) for each classifier and year.

Classifiers	Unchanged			Changed correctly			Changed incorrectly			
	2014	2015	2016	2014	2015	2016	2014	2015	2016	MAD
ANN (%)	-0.59	2.21	-2.72	-6.77	0.07	2.61	15.59	**-11.62**	10.82	11.03
RF (%)	2.05	-0.70	-2.81	9.57	-3.97	-8.22	**-31.64**	14.47	32.30	24.46
SVM Linear (%)	0.95	0.09	4.35	-18.06	0.61	-1.68	21.62	-2.14	**-22.10**	14.99
SVM Polynomial (%)	2.25	-1.64	0.14	2.47	2.51	-10.00	-21.80	1.61	-10.00	**7.83**
SVM Radial (%)	-4.65	0.04	1.05	12.79	0.78	-11.02	16.24	-2.33	-11.02	**10.19**

Note: MAD: mean of absolute differences

This study indicates the use of six bands of Landsat imagery rather than the information of vegetation indices and significantly improved the accuracy for mapping rice phenology and bare land. In general, vegetation indices carry limited information and have less capability to classify rice growth phases because of similarities between spectral signatures. For example, in Figure 3.6, we note that the spectral pattern of vegetative and reproductive phases seems similar. Similar responses have been seen by K. W. Chang et al. (2005). Moreover, the majority of the vegetation indices such as EVI and NDVI, Soil-adjusted vegetation index (SAVI) typically use spectral bands from visible and NIR regions which are highly influenced by soil background and vegetation structure.

Although rice phenology was classified with moderate accuracy, the error could be caused by many reasons such as spectral heterogeneity of pixels within each class, broad spectral and spatial resolution and availability of a limited number of bands in the sensor. As a consequence of different soil backgrounds and different types of rice cultivation (e.g. upland and low land) present in Indramayu Regency, high variability occurred in spectral data which results in classification errors. Although the training data being attempted to cover a wide range of rice varieties and soil types, some information could be missed. Moreover, the paddy field in the study area is highly fragmented by small roads to ease access between the main road into paddy fields, resulting in misclassification within the model. We assumed that the farmer only plants rice on the paddy field as suggested on the cropping calendar. However, there is a small proportion of mixed cropping where farmers grow other crops such as soybean and maize along with rice during the dry season in small-scale areas. Since Landsat-8 has a coarse resolution (30 m), some mixed pixels and misclassification can be expected in mixed cropping regions. The mixture effect could be minimized by unmixing approaches as Lu et al. (2017) reported that an unmixing approach with integration Theil-Sen (TS) was able to differentiate between vegetation over the urban environment.

We propose machine learning approaches to retrieve rice phenology from Landsat-8, and machine learning algorithms have provided encouraging results. The algorithm SVM with radial function outperformed RF, SVM linear, SVM polynomial and ANN and showed robust performance on the test results. The performance was consistent on spatio-temporal maps over different times and regions. However, some parts of the study area were classified incorrectly, particularly in bare land and vegetative phases. The incorrect classification could be caused by different agronomic practices and topographic variations, which influence the spectral signatures (Campos-Taberner et al., 2017).

Further study is required to investigate the recent availability of high spatial resolution (10-20 m) Sentinel-2 data for rice phenology across Asian countries. Sentinel-2 provides valuable spectral information for monitoring rice growth stages with a potential higher accuracy than Landsat 8 OLI (Vuolo et al., 2018). Since cloud cover affects optical imagery in Indonesia, integrating information from multiple satellite sensors (MODIS, PROBA-V, Landsat-8, and Sentinel-2) could be a useful alternative for enhanced spatio-temporal coverage. Moreover, additional spectral information can be expected from multiple satellites which could provide detailed physiological information of different rice growth phases.

Radar imagery, such as Sentinel-1, is one of the other alternative solutions to overcome the cloud and shadows problem. Using smartphones by local extension workers or the farmers themselves can be a reliable secondary data source to build up an automated classification model if computer vision is enabled with active learning concept (Alajlan et al., 2014; Baumann et al., 2017; Brown et al., 2016; Chung et al., 2018; Knox et al., 2017; Liu et al., 2017; Rousselet et al., 2013). In future work, the integration of multiplatform remote sensing data for monitoring rice production and climate data could offer a solution for

developing countries to supply and apply subsidized agriculture inputs with better precision and enable trackable distribution of crops to support improved accountability.

3.7 Conclusion

Java Island is Indonesia's largest rice producer, primarily Indramayu's paddy fields. Along with the adverse effects of climate-related disasters, such as floods, drought, it is crucial to track the rice growth stage dynamically with a fast and reliable method. This paper provides a machine learning framework to classify rice growth phases using Landsat-8 data. The near real-time monitoring of paddy areas enables governments to make effective decisions on food security issues in developing countries.

From this research, we conclude that the Landsat-8 data can be used along with ancillary data from webcams to build a predictive model for rice growth phases with adequate accuracy. Moreover, the accuracy was improved significantly using all bands compared to vegetation indices. The results of spatio-temporal maps using transfer learning demonstrate the consistency and reliability of this approach for mapping rice phenology. However, this model shows some inconsistencies due to mixed pixels, seasonality, and shifting planting time that require further investigation and additional training datasets.

3.8 Acknowledgement

The first author acknowledges the Indonesian Agency for Agricultural Research and Development (IAARD) for providing the scholarship on Sustainable Management of Agricultural Research and Technology Dissemination (SMART-D) project. Indonesian Agro climate and Hydrology Research Institute (IAHRI) for maintaining webcam data. U.S. Geological Survey and Google Earth Engine for providing Landsat data. All R developers and community for developing free R software and packages.

Chapter 4 Automatic Mapping of Rice Growth Stages Using the Integration of SENTINEL-2, MOD13Q1, and SENTINEL-1

The objective of chapter 4 is to build a workflow for mapping rice growth stages using the fusion from SENTINEL-2, MOD13Q1, and SENTINEL-1. Moreover, the rice cultivation detection was applied to make it better accuracy. This chapter is based on a published paper:

> *Ramadhani, F., Pullanagari, R., Kereszturi, G., & Procter, J. (2020). Automatic Mapping of Rice Growth Stages Using the Integration of SENTINEL-2, MOD13Q1, and SENTINEL-1. Remote Sensing, 12(21), 3613. https://www.mdpi.com/2072-4292/12/21/3613*

Supplementary data and source code can be downloaded on https://github.com/FadhlullahRamadhani/S2-PADDY-MAPPING

Participating authors:

- Fadhlullah Ramadhani: Conceptualization**,** investigation, data curation**,** formal analysis, methodology, software, visualization, and writing—original draft preparation
- Reddy Pullanagari: Conceptualization, methodology, supervision, and writing—review and editing,
- Gabor Kereszturi: Conceptualization, methodology, supervision, visualization, and writing—review and editing,
- Jonathan Procter: Supervision, and writing – review & editing

Abstract

Rice (*Oryza sativa* L.) is a staple food crop for more than half of the world's population. Rice production is facing a myriad of problems, including water shortage, climate, and land-use change. Accurate maps of rice growth stages are critical for monitoring rice production and assessing its impacts on national and global food security. Rice growth stages are typically monitored by coarse-resolution satellite imagery (250 x 250 m). However, it is difficult to accurately map due to the occurrence of mixed pixels in fragmented and patchy rice fields, as well as cloud cover, particularly in tropical countries. To solve these problems, we developed an automated mapping workflow to produce near real-time multitemporal maps of rice growth stages at a 10-m spatial resolution using multisource remote sensing data (Sentinel-2, MOD13Q1, and Sentinel-1). This study was investigated between 1 June and 29 September 2018 in two (wet and dry) areas of Java Island in Indonesia. First, we built prediction models based on Sentinel-2 and fusion of MOD13Q1/Sentinel-1 using the ground truth information. Second, we applied the prediction models on all images in area and time and separated between the non-rice planting class and rice planting class over the cropping pattern. Moreover, the model's consistency on the multitemporal map with a 5–30-day lag was investigated. The result indicates that the Sentinel-2 based model classification gives high overall accuracy of 90.6% and the fusion model MOD13Q1/Sentinel-1 shows 78.3%. The performance of multitemporal maps was consistent between time lags with an accuracy of 83.27–90.39% for Sentinel-2 and 84.15% for the integration of Sentinel-2/MOD13Q1/Sentinel-1. The results from this study show that it is possible to integrate multisource remote sensing for regular monitoring of rice phenology, thereby generating spatial information to support local-, national-, and regional-scale food security applications.

Table of contents for Chapter 4

4.1 Introduction

Regular monitoring of the paddy area is vital as rice production supports rural livelihoods in Asia, where more than 1.21 billion tonnes of rice were harvested to feed 4.56 billion people in 2018 (FAOSTAT, 2019; Lowder et al., 2016). The rice production often struggles with the effects of climate change (Arévalo et al., 2019; Hazaymeh & Hassan, 2017), water shortage (Elagouz et al., 2019; Surmaini et al., 2015), inadequate machinery supplies in developing countries (Van Ittersum et al., 2013), and soil degradation (Guo et al., 2018), which in turn requires intensified monitoring to ensure sustained food production. The common practice of monitoring rice crops in Indonesia is by using local government officers at a sub-district level to collect data based on field visits and information provided by the farmers. This data is expensive to collect, non real-time, and inefficient to handle spatio-temporal changes in rice-producing areas (Lewis et al., 2008; Raedeke & Rikoon, 1997; Wood et al., 1999). Moreover, the paddy area needs to be monitored in near-real-time due to the need for a continuous water supply from irrigation canals and fertiliser inputs at critical stages (Castillo et al., 2006). Thus, timely and accurate information on rice growth stages is vital for planning and managing the rice farming system, which is critical for sustainable food security at the regional and national scale (Vermeulen et al., 2012; Wassmann et al., 2009).

Remote sensing can offer cost-effective near real-time solutions to analyse land-use changes (Bruzzone, 2014; Joshi et al., 2016; Liu et al., 2010), cropping patterns (Fatikhunnada et al., 2020; Minh et al., 2019; Nguyen et al., 2012; Rudiyanto et al., 2019; Sianturi et al., 2018), growth stages (Gao et al., 2017; Ramadhani et al., 2020b; Rudiyanto et al., 2019), and crop detection over large areas (Boschetti et al., 2017). Previous studies have widely used coarse resolution multitemporal optical imagery, such as Moderate Resolution Imaging Spectrometer (MODIS) (Clauss et al., 2016; Sakamoto et al., 2005;

Setiawan et al., 2014; Xiao et al., 2006; Zhang et al., 2015), for rice monitoring. MODIS has a significant advantage of daily revisited time and is able to generate vegetation indices, such as enhanced vegetation index (EVI) and normalized difference vegetation index (NDVI). These indices can be used to quantify rice growth stages accurately and recreate a temporal evolution of rice production. This data can be fed to establish regional and national productivity of rice yield inventories (Sakamoto et al., 2006; Xiao et al., 2005; Zhang et al., 2015). However, most of the other optical satellites (e.g. Landsat-8, SPOT-5 and ASTER) have less frequent visit times, and they are prone to cloud cover and shadow, resulting in gaps in the temporal data, particularly in monsoon season (Onojeghuo et al., 2018). Additionally, their medium to coarse spatial resolution (> 250 m) hampers the capability to discriminate the rice growth stages within paddy fields. Moreover, paddy rice fields are often highly fragmented, resulting in mixed pixels. Some prior studies show that single-date rice monitoring with Landsat 7/8 can be done with better accuracy (Campos-Taberner et al., 2016; Kontgis et al., 2015; Ramadhani et al., 2020b) with a revisited time of 16 days, which is challenging to get precise data which is useful at the operational level.

To avoid the cloud interference, microwave or synthetic aperture radar (SAR) data from RADARSAT (Li et al., 2003; Zhang et al., 2014), ALOS-PALSAR (Wang et al., 2009; Zhang et al., 2009), and Sentinel-1 (Bazzi et al., 2019; Dirgahayu & Made Parsa, 2019; Jo et al., 2020; Lasko et al., 2018; L. R. Mansaray et al., 2017; Singha et al., 2019), have been explored for rice mapping. The backscattering of the microwave radiation can be used to detect the rice cropping pattern due to phenological changes of the rice canopy structure having characteristic microwave scattering properties (Yin et al., 2019). The previous studies on the mapping of rice growth stages are limited to identifying rice/non-rice areas (Clauss et al., 2018; Gumma et al., 2011; Mosleh et al., 2015) and the cropping pattern using various sensors (Chandna & Mondal, 2020). Rudiyanto et al. (2019) demonstrated the detection of rice phenology in Indonesia and Malaysia rice fields, using hierarchical

clustering with vertical-horizontal backscatter from Sentinel-1. On the other hand, Phung et al. (2020) were able to correlate between incident angles of backscattering and day of rice planting based on smoothed VH backscattering intensity images. These studies have utilised the fact that the inundation and vegetative rice growth stages typically have the lowest backscattering intensity due to the flooded soil that reflects the radar energy specularly away from the sensor. As the rice grows, the backscattering intensity becomes higher when the rice canopy is established (e.g., reproductive phase) as the canopy can give double-bounce scattering (Liu et al., 2016; Pham-Duc et al., 2017). Finally, the backscattering intensity becomes lower again after harvesting due to a loss of biomass (Ndikumana, Ho Tong Minh, Dang Nguyen, et al., 2018). The utility of RADAR for rice growth stage monitoring can also benefit from the frequent satellite revisit times and penetration through cloud cover affected by many tropical countries. The only global and free RADAR dataset is provided by Sentinel-1 satellite imagery. Other RADAR-capable satellites, such as ALOS-PALSAR and TerraSAR-X, are limited in uses or available via paid subscriptions. Moreover, the speckle noise issue can be a problem in complex land-use (Lee et al., 1994) and can be minimized with the deep learning approach (Kang et al., 2020; Sica et al., 2020). Importantly, microwave remote sensing has a significant time lag to be analysed near-real-time due to its slow processing time and high demand for local knowledge to classify the rice growth stages (Rudiyanto et al., 2019). Moreover, the short time (< 16 days) is vital for rice mapping for validating the rice production prediction on a national or local scale.

Considering the advantages from both optical and radar images, combining multiple remote sensing data (data fusion) can improve accuracy with high temporal coverage. The fusion between active and passive remote sensing have been adopted (Belgiu & Stein, 2019; Ding et al., 2020; Ghassemian, 2016; Waske & Benediktsson, 2007) to overcome the missing data, and have higher accuracies due to the ability to distinguish specific crop area,

especially near water bodies. According to Schmitt and Zhu (2016), there are three types of data fusion: 1) raw data fusion, 2) feature extraction fusion, and 3) decision-making level. Feature extraction fusion is more attractive than the others because the fusion process can be carried out with multiple images with different temporal and spatial resolutions. The feature fusion uses similar objects from multiple sources that are combined for further assessment. For example, Park et al. (2018) developed a method by combining the data of Landsat, MODIS, and ALOS-PALSAR to map paddy areas in South Korea, which increased the accuracy by 6–9%, compared to individual sensor information. Similarly, Cai et al. (2019) reported high accuracy for mapping rice paddy areas in China with multiple sensors (Sentinel-1/Sentinel-2/MODIS). The resultant high accuracy is due to the strong correlation between the leaf area index (LAI) and biomass with cross-polarization of microwave backscattering (Inoue et al., 2002). To date, the study of integration between optical and radar-based imagery on rice growth stages classification is not investigated thoroughly on the feature extraction and decision-making fusion level to increase accuracy.

Considering some limitations of previous studies, such as course spatial resolution, single-source dataset, and manual interpretation, the actual demand for near-real-time rice growth stage prediction models using remote sensing is high. Thus, this study aimed to develop an automatic workflow for generating 10-m-resolution multitemporal maps of rice growth stages by combining Sentinel-2, MOD13Q1, and Sentinel-1 imagery. The result of this study, both the method and the map products, can be used for mapping at national and regional scales to ensure food security and production with timely and accurate spatial information using multiple remote sensing data sources.

4.2 Background, study area, and data

4.2.1 Rice growth stages

The growth stage of paddy rice in Asia, particularly Indonesia, can be split into five classes, which reflect the rice cultivation practices in any given time (Bouman, 2019; Fageria, 2007; Hardke, 2013). First, the bare land area is filled by water (flooding) and ploughed for (15–25 days) depending on the water irrigation schedule (Figure 4.1). The second stage is the vegetative stage, which the rice grows from seedling emergence until panicle development (55–65 days; Figure 4.1). The third stage is the reproductive stage where the leaf stem bulges with the panicle, also known as the booting stage (20–25 days; Figure 4.1). Flowering and pollination also occur in this stage. The final stage is the ripening stage, which includes fertilisation, the grain is filling/expanding, and the paddy grain becomes dry-brown (30–35 days; Figure 4.1). The total cultivation time is 120–150 days, depending on the varieties. Intercrops, growing other crops (maize, soybean, green beans) between the rice crop, is also adopted in some areas. The size of parcels is varied between 0.2 – 2 ha).

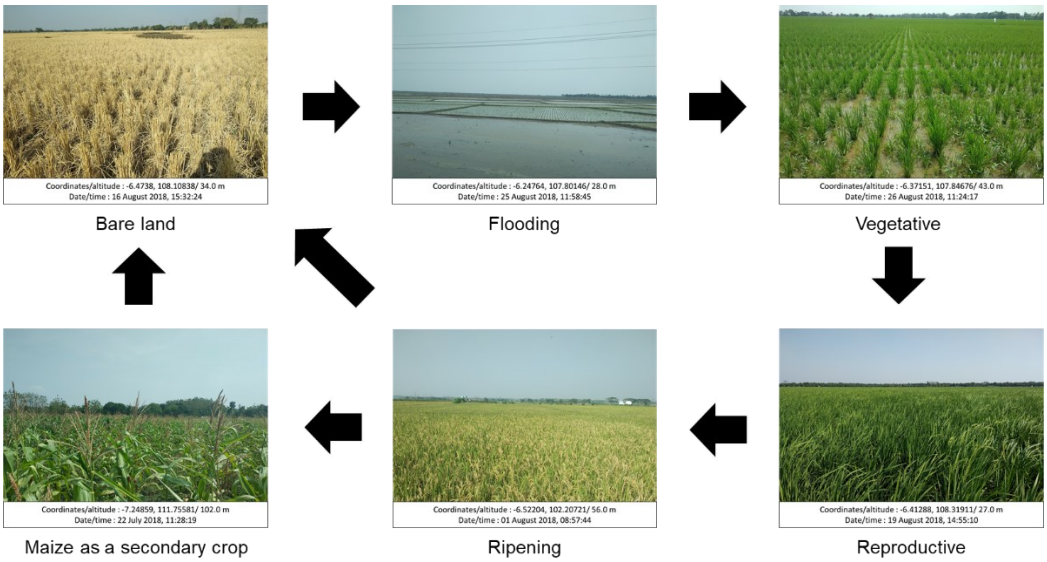

Figure 4.1 The example of rice growth stages and other rice field conditions in the paddy field area. The geolocation and date are stamped on the photos.

4.2.2 Study area

In this study, we chose two distinctive regions with different climates (wet and dry area) and fragmented paddy areas from Java Island, Indonesia (Figure 4.2). The West Area is located on West Java, representing the paddy area, mainly irrigated area and low land, while the East Area is located with a larger rain-fed paddy field and has a high fragmented area. Both areas have a monsoon climate with two seasons: the wet and dry seasons (Kottek et al., 2006). The wet season is from October to March, and the dry season is from April to September (Figure 4.3). Typically, short-duration varieties (~ 120 days), such as IR64, Ciherang, of glutinous rice are widely adopted in this area (Rudiyanto et al., 2019; Sianturi et al., 2018).

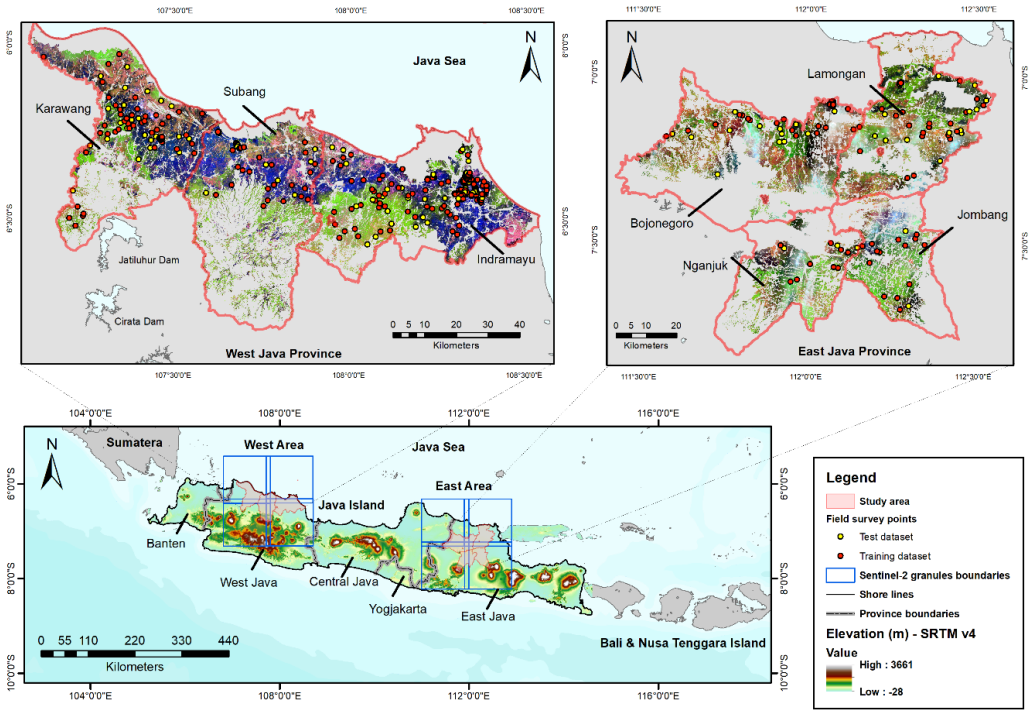

Figure 4.2 Map of the study area for West Area and East Area and overlay with the false colour (NIR/SWIR/Green) of Sentinel-2 image, which has been masked to show only the paddy rice fields for the West Area on 11 and 14 June 2018 and for the East Area on 13 June 2018.

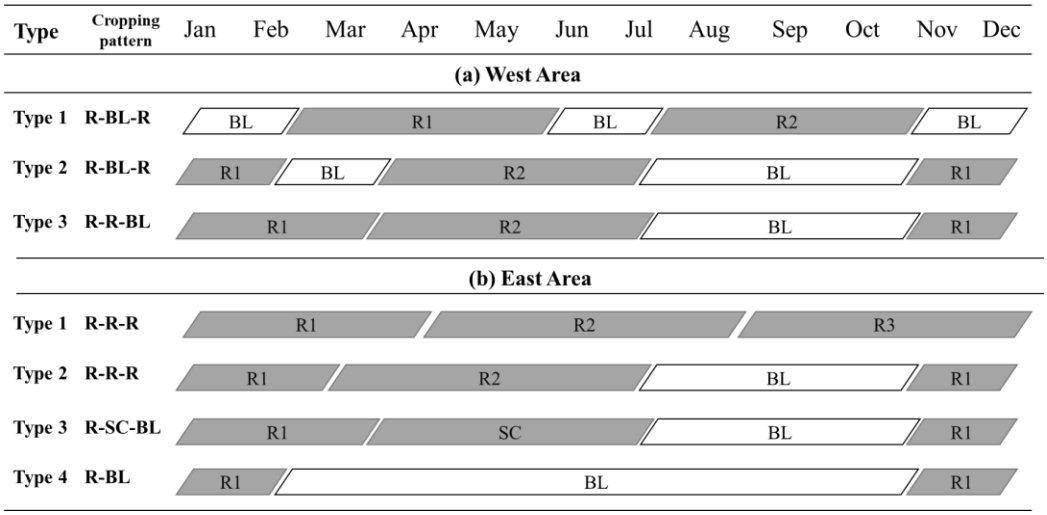

Note: R1: Rice 1st cultivation, R2: Rice 2nd cultivation, R3: Rice 3rd cultivation, SC: Secondary crops, and BL: Bare land.

Figure 4.3 The simplified cropping pattern of the West Area and East Area.

(a) West Area

West Area consists of paddy area in three regencies, which are Karawang (96,482 ha), Subang (84,228 ha), and Indramayu (115,555 ha), with a total area of 310,265 ha (BPS-West-Java, 2018) (Figure 4.2). Most of the area is irrigated paddy field from the Jatiluhur area (258,633 ha), established on alluvial and lithosol soil. The water distribution is maintained by the state-owned company easing water requirements. However, further issues arise from sedimentation, breaking drainage, and land-use change, especially in the dry season. The season comprises two rice planting cycles, separated by 1-3 months of bare land. This bare land period is intended to rest the soil and stop the crop pest life cycle (Figure 4.3). The planting time changes based on the catchment location, with the first planting season, starting from November and the second in March in the upper catchment areas. The downstream areas start their season in February due to constant floods during the rainy season, while the second planting is in July.

(b) East Area

East Area is located on West Java Province consists of four regencies, including Bojonegoro (78,677 ha), Lamongan (87,336 ha), Jombang (48,704 ha), and Nganjuk (42,918 ha), totalling an area size of 257,635 ha (BPS-East-Java, 2018) (Table 4.1). The soil types of this region are much more diverse, including alluvial soils, grumusol, and regosol. The main cropping pattern can be divided into four types. The first cropping pattern is rice planted three times throughout the year with planting times in December, April, and August with water pumping from the Bengawan Solo river for year-round irrigation. This cropping pattern is only found in this one area near the Bengawan Solo river facilitating the farmer to cultivate during the dry season by pumping water. The second cropping pattern is planting rice twice annually with the first planting season in December and the second in April. The third cropping pattern utilises one rice planting period and a secondary crop planted in the dry season, such as maize, soybean, and shallots. The fourth cropping pattern consists of rice cultivation during the rainy season (Figure 4.3).

Table 4.1 Comparison between the West Area and East Area.

Study Area	West Area (WA)	East Area (EA)
Topography	broad coastal plain on the north and hills the south	Most of the area is a flat area in the north and hilly on the south.
Height	0 –1500 m, 0 – 2 %.	150 –1500 m, 0 – 2 %.
Climate	Total annual rainfall: 1849 mm with the number of rainy days: 95 days (2018)	Total annual rainfall: 1,860 mm with the number of rainy days: 102 days (2018)
Soil type	Alluvial, Lithosol	Alluvial, Grumusol, Regosol
Irrigation	Cimanuk, Cipanduy, Citarum, Ciliwung Irrigations area	Brantas, and Solo irrigations area
Irrigated paddy field	272,633 ha	166,286 ha
Non-irrigated paddy field	37,632 ha	91,349 ha
Total paddy field	310,265 ha	257,635 ha

4.3 Satellite Imagery

This study is based on three satellite datasets from 1 June to 29 September 2018. The first dataset comes from Sentinel-2 A/B in Level-1C (L1C) format, which is a Top-Of-Atmosphere product from Copernicus Open Access Hub (Gascon et al., 2017). Sentinel-2 satellites provide five days of revisited time over the study area. The scenes of Level-1C were subjected to atmospheric corrections into Level-2A by using Sen2Cor (Louis et al., 2016). The Sen2Cor produces surface reflectance, which includes seven bands with a 10-m resolution, four bands with a 20-m resolution, six bands with a 60-m resolution, and Scene Land Classification (SCL) with a 20-m resolution. Here, we used 11 bands as the predictors for the Sentinel-2 model (Table 4.2). Moreover, bands 5, 6, 7, 8A, 11, and 12 were resampled into a 10×10 m pixel size to match with high-resolution bands.

Table 4.2 Remote sensing data

Sentinel-2 L2A (5 Days Revisit Time)			MOD13Q1 (16 Days Composite Period)		Sentinel-1 (12 Days Revisit Time)		
Band	Central Wavelength (nm)	Resolution (m)	Band	Resolution (m)	Band	Resolution (m)
Band 2 – Blue	490	10	NDVI	250	VH	10
Band 3 – Green	560	10	EVI	250		
Band 4 – Red	665	10	Quality indicator	250		
Band 5 – Red edge 1	705	20				
Band 6 – Red edge 2	740	20				
Band 7 – Red edge 3	783	20				
Band 8 – Near-infrared	842	10				
Band 8A – Red edge 4	865	10				
Band 11 – Shortwave infrared 1	1610	20				
Band 12 – Shortwave infrared 2	2190	20				
Scene land classification (SCL) band	-	20				

The second dataset was MOD13Q1 from Terra sensor with a 250-m resolution from Google Earth Engine (GEE), which was pre-processed to surface reflectance (Abdi & Ardiansyah, 2017; Gorelick et al., 2017) and resampled in a 10×10 m pixel size. We used this dataset for filling the gap of Sentinel-2 imagery because it is a composite 16-day period of daily MODIS observation. MOD13Q1 consists of the normalized difference vegetation index (NDVI) and enhanced vegetation index (EVI), which are chosen with the highest NDVI value in the 16-day period. The calculation of NDVI and EVI is based on MODIS/Terra bands with the formula as follows:

$$NDVI = \frac{\rho_{NIR} - \rho_{Red}}{\rho_{NIR} + \rho_{Red}}, \quad (1)$$

$$EVI = 2.5 \times \frac{\rho_{NIR} - \rho_{Red}}{\rho_{NIR} + 6 \times \rho_{Red} - 7.5 \times \rho_{Blue} + 1}. \quad (2)$$

The third dataset was Sentinel-1A, which was downloaded from GEE and pre-processed with Sentinel-1 toolbox to remove thermal noise, calibrating radiometric and terrain correction (https://developers.google.com/earth-engine/sentinel1). The Sentinel-1 has 12 days of revisited time on the study area due to the location on the equator. We used vertical-horizontal backscattering (VH) descending data and Minimised Interferometric Wide Swath (IW) mode, which consists of vertical-horizontal (VH), vertical-vertical backscattering (VV), and angle bands (Table 4.3). Thus, the speckle noise of VH values was reduced using the refined-Lee filter with a 7 × 7 window size (Lavreniuk et al., 2017; Lee, 1981; Lee et al., 1994; Plank et al., 2017). This dataset has already been used for mapping the paddy area due to the high sensitivity of water presence in rice cultivation area globally (Bazzi et al., 2019; Lasko et al., 2018; L. R. Mansaray et al., 2017; Onojeghuo et al., 2018; Singha et al., 2019). In this study, we used VH as predictors because the VH is more consistent and sensitive in the detection of rice research works than VV backscattering, as suggested in previous works (Nguyen et al., 2016; Son et al., 2017).

The total number of acquisitions used in this study were 200 scenes for Sentinel-2, 28 scenes for Sentinel-1, and 17 composite scenes for MOD13Q1 (Table 4.3). All of the datasets was masked with a high-resolution paddy field area from the Indonesia Ministry of Agriculture to reduce complexity with other land use before further processing.

Table 4.3 List of the acquisition date of Sentinel-2, MOD13Q1, and Sentinel-1.

Sensor	Acquisition Date (Day of the Year) in 2018	Total
Sentinel-2	T48MZU and T48MZT: 152, 157, 162, 167, 172, 177, 182, 187, 192, 197, 202, 207, 212, 217, 222, 227, 232, 237, 242, 247, 252, 257, 262, 267, and 272 T48MYU and T48MYT: 155, 160, 165, 170, 175, 180, 185, 190, 195, 200, 205, 210, 215, 220, 225, 230, 235, 240, 245, 250, 255, 260, 265, and 270 T49MFM, T49MEM, T49MEM, T49MEN, and T49MFN: 154, 159, 164, 169, 174, 179, 184, 189, 194, 199, 204, 209, 214, 219, 224, 229, 234, 239, 244, 249, 254, 259, 264, and 269	200 scenes
Sentinel-1	IW mode, VV-VH band: 159, 161, 171, 173, 183, 185, 195, 197, 200, 207, 209, 219, 221, 231, 233, 236, 243, 245, 248, 257, 267, 269, 279, 281, 291, 293, 296, and 303	28 scenes
MOD13Q1	1, 17, 33, 49, 65, 81, 97, 113, 129, 145, 161, 177, 193, 209, 225, 241, and 257	17 composite scenes

4.4 Methods

The workflow of analysing multisource remote sensing data for multitemporal mapping of rice growth stages from June–September 2018 is illustrated in Figure 4.4. First, we labelled and synchronised data from multiple satellites (Sentinel-2, MOD13Q1, and Sentinel-1) with the collected field data. The next step is to build two separate prediction models for rice growth stages using the support vector machine methodology for the Sentinel-2 and another for fusion between MOD13Q1 and Sentinel-1 (MOD13Q1/Sentinel-1). After assessing the accuracy of both models (Sentinel-2 and MOD13Q1/Sentinel-1), the image data were combined into one time series to fill the cloud-obscured pixels of Sentinel-2. Additionally, rice planting detection was applied to separate rice cultivation and non-rice

cultivation activity on the rice fields. The final rice growth stages map is the integration of the Sentinel-2/MOD13Q1/Sentinel-1 maps. Finally, we calculated the consistency percentage of the Sentinel-2 and Sentinel-2/MOD13Q1/Sentinel-1 maps over time. In the following subsection, the data conversion steps are described in detail.

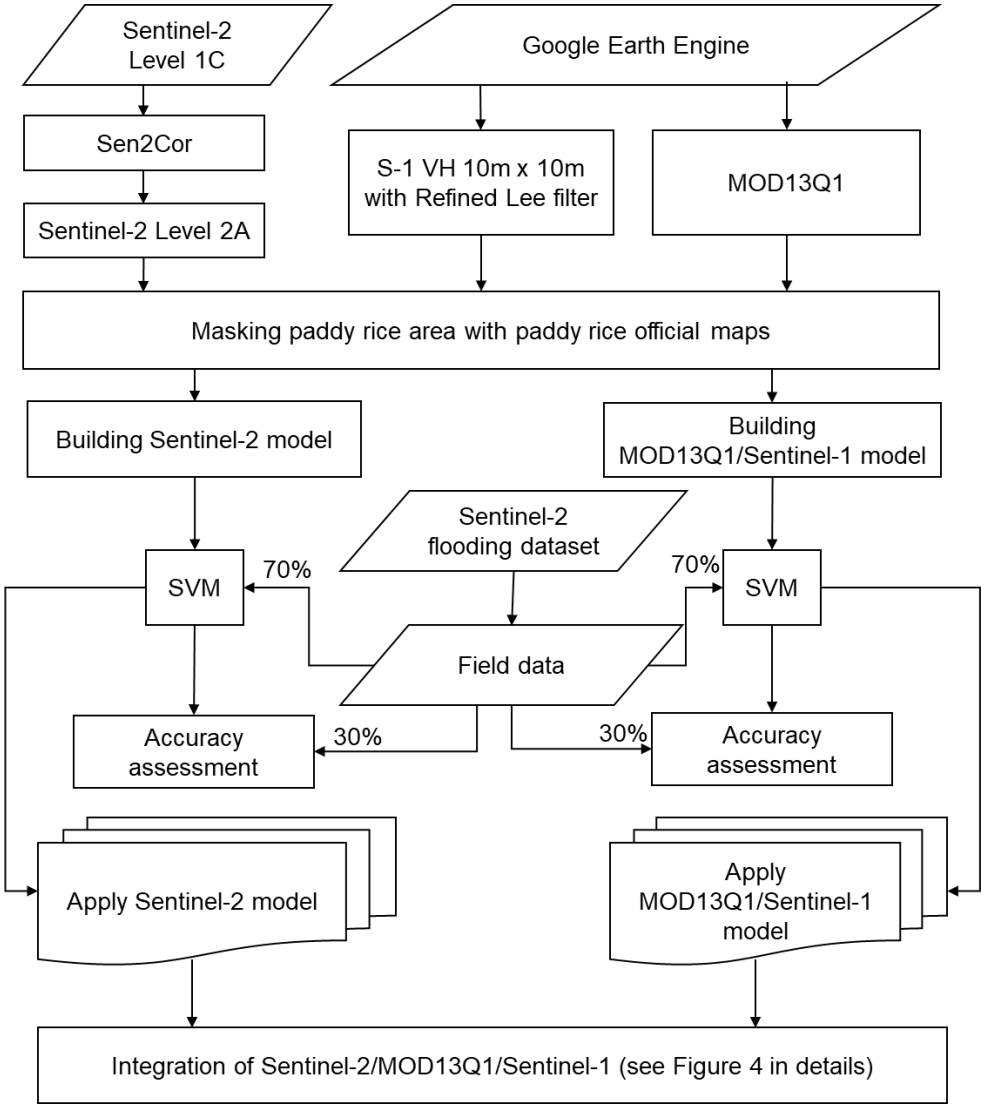

Figure 4.4 The workflow of the integration of Sentinel-2/MOD13Q1/Sentinel-1.

4.4.1 Field data and dataset labelling

The field data was collected as purposive and random sampling with a Global Positioning System (GPS)-enabled mobile phones and synchronised with a pocket GPS receiver

between 20 July and 4 September 2018. The sampling points were selected randomly with a 500-m buffer distance using the official paddy area as the base map, which returned 227 points in the West Area and 171 points in the East Area in total. These sites were then visited in the field. The enumerator of the field data made sure that the sampling area had a dimension at least 50×50 m and contained the same rice growth stage throughout to reduce impacts of mixed pixels. Each field site has associated field photos that were used for labelling. The field observations were then matched up with the closest and cloud-free satellite dataset's date for extraction.

The flooding class has been underrepresented due to fieldwork conducted in the dry season. To ensure the field dataset was balanced, 70 flooding locations were manually extracted from a Sentinel-2 false colour composite image taken on 6 June 2018. The total number of Sentinel-2 datasets utilised was 426 observations, and MOD13Q1/Sentinel-1 had 468 observations. The difference is due to the changes in cloud cover within the datasets.

4.4.2 Prediction models for the rice growth stages

In this study, we used SVM because of its suitability in remote sensing data applications and its capacity to handle complex classification problems (Cortes & Vapnik, 1995; Guyon et al., 1992). SVM maps the data points in high-dimensional feature space and separates the class using hyperplane with a kernel function, linear, polynomial, sigmoid, and radial functions. The closest data points of the hyperplane become the support vectors, which determine the position and orientation of the hyperplane to find the maximum margin (the distance between the support vectors with the hyperplane) (Raghavendra & Deka, 2014). Here, we used the radial basis function (RBF) because of the high variability and complex predictors for rice conditions (Onojeghuo et al., 2018; Son et al., 2017). Moreover, Kavzoglu and Colkesen (2009) suggested that SVM with RBF has advantages, such as training pixels being needed less than with other classifiers and being flexible with a

statistical distribution range in remotely sensed data. Moreover, SVM with RBF has been applied successfully for rice growth stage mapping before and outperformed other classification methods, such as random forest and neural networks (Ramadhani et al., 2020b). There are two kernel parameters of SVM RBF that can increase the accuracy, i.e., cost penalty (C) was used to define trade-off between model complexity and error and Sigma for smoothing the vector (Mountrakis et al., 2011).

Two SVM models were built in this study, using the R programming language with the *caret* package (Kuhn, 2008), as follows:

(a) Sentinel-2 model: this prediction model was based on Sentinel-2 input bands (Table 4.2) as predictors labelled based on the field data temporally closest to the Sentinel-2 imagery acquisition. The Sentinel-2 model to predict rice growth stages was trained using the field dataset with a 70:30% random split (i.e., 299 and 127 observations from the field dataset). The relationship between the bands of Sentinel-2 and the rice growth stages can be expressed as follows:

$$Rice\ growth\ stages\ (Sentinel2) \sim B02 + B03 + B04 + B05 + B06 + B07 + B08 + B11 + B12 + B8A. \quad (3)$$

(b) MOD13Q1/Sentinel-1 model was developed by combining MOD13Q1 and Sentinel-1 with predictors of NDVI and EVI from MOD13Q1 and VH for three consecutive three-time lag series (e.g., Sentinel-1 image of VH on t day (T0), t-12 days (T1), and t-24 days (T2) in decibel (dB)). We found that using three consecutive VH values had better accuracy, which can be explained by the typical length of each rice growths stage of around 24 days. We used 330 points for the training dataset and 138 points for the test dataset. The relationship of the MOD13Q1 indices and multitemporal backscattering data of Sentinel-1 and the rice growth stages can be expressed as follows:

$$Rice\ growth\ stages\ (MOD13Q1/Sentinel1) \sim NDVI + EVI + T0 + T1 + T2. \quad (4)$$

The two models were trained with the parameter cost penalty (2^n with n = 1 to 10) to define trade-offs between model complexity and error and Sigma (2^{-25}, 2^{-20}, 2^{-15}, 2^{-10}, 2^{-5}, 0) for smoothing the vector (Mountrakis et al., 2011). Moreover, the resultant models were cross-validated with the *leave-one-out cross-validation* method to ensure an unbiased result. The highest accuracy model was selected to be used to classify rice growth stages on the satellite dataset.

4.4.3 Generating multitemporal maps for rice growth stages by integrating Sentinel-2/MOD13Q1/Sentinel-1

The final paddy growth stage maps were preferred to be based on Sentinel-2 classification results due to their better resolution than MOD13Q1. However, temporal gaps in the Sentinel-2 data frequently occur due to cloud coverage and shadows. These gaps were filled with the prediction maps generated from the integration of MOD13Q1 and Sentinel-1, which has the same spatial resolution using the resampling technique. The Sentinel-2-based rice growth stage classification was filtered for pixels that had not been bare land for a period 120 days (t_1) and 150 days (t_2) for the East Area and West area, respectively (Figure 4.5). The timeline of each processing multitemporal map for a 16-day period from 10 June – 29 September 2018 can be seen in Table 4.4.

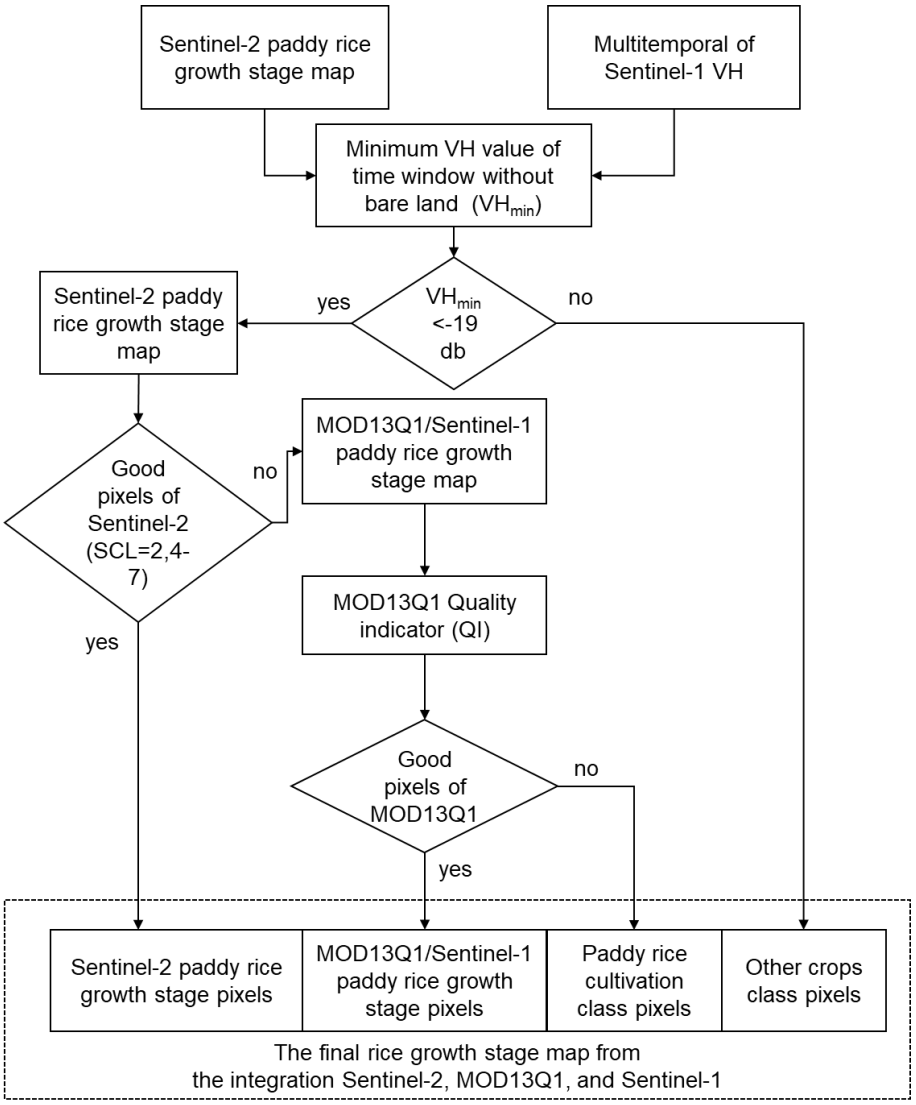

Figure 4.5 The flowchart of rice detection and the integration of Sentinel-2/MOD13Q1/Sentinel-1.

The differences between time windows were due to different rice cultivation between those areas during the dry season. The East Area has limited time to flood the rice field (<20 days) compared to the West Area (20–40 days). Cloud and shadow were removed using the scene classification band. The Sentinel-1 VH was stacked up to find the lowest VH value (VH_{min}) over the time window *t1* and *t2* (Liu et al., 2016). Low radar backscatter signal can be associated with both the water/vegetative stage due to radar energy reflected off and bare land due to penetration radar energy on dry land (Rudiyanto et al., 2019),

making classification using only backscattering sensor data challenging. This confusion can be reduced by utilizing Sentinel-2-based rice growth stage classification. If the VH_{min} was higher than −19 *dB* and the rice growth stages are reproductive or ripening, then the pixel value will be replaced by a non-rice planting class, and others would have the rice growth stages value from Sentinel-2 maps. This step separates the maize or soybean in the reproductive or ripening phase because the spectral profile is nearly the same as rice's profile, as illustrated in Figure 4.6 (Liu et al., 2016; Rudiyanto et al., 2019).

Table 4.4 Timeline of remote sensing images processed in 2018.

No	Period	Sentinel-2	MOD13Q1	Sentinel-1 (T0)	Sentinel-1 (T-1)	Sentinel-1 (T-2)	Rice Planting Detection
1	10 – 25 June	11 – 14 June	10 – 25 June	10 – 20 June	25 May – 4 June	9 – 19 May	11 February – 11 June
2	26 June – 11 July	26 – 29 June	26 June – 11 July	26 June – 6 July	10 – 20 June	25 May – 4 June	26 February – 25 June
3	12 – 27 July	13 – 16 July	12 – 27 July	12 – 22 July	26 June – 6 July	10 – 20 June	15 March – 12 July
4	28 July – 12 August	28 July – 12 August	28 July – 12 August	28 July – 7 August	12 – 22 July	26 June – 6 July	30 March – 27 July
5	13 – 28 August	13 – 16 August	13 – 28 August	13 – 23 August	28 July – 7 August	12 – 22 July	15 Apr – 12 August
6	29 August – 13 September	30 August – 2 September	29 August – 13 September	29 August – 8 September	13 – 23 August	28 July – 7 August	2 May – 29 August
7	14 – 29 September	14 – 16 September	14 – 29 September	13 – 23 September	29 August – 8 September	13 – 23 August	17 May – 13 September
Total	10 June – 29 September	11 June – 16 September	10 June – 29 September	10 June – 23 September	25 May – 8 September	9 May – 23 August	11 February – 13 September

In some instances, we found that even the complete Sentinel-2 and MOD13Q1/Sentinel-1 was unable to have cloud-free data every 16-day period. Thus, we used rice's detection result to replace the cloud pixels. If the VH_{min} was lower than −19 *dB*, the pixel would be marked as the rice planting class. Otherwise, the cloud pixels were marked as another crop class. This resulted in a seven-class map, including bare land, flooding, vegetative, reproductive, ripening, rice planting, and other crops. The integration of Sentinel-2/MOD13Q1/Sentinel-1 will have more rice growth stages data than the Sentinel-2 rice growth stage model alone.

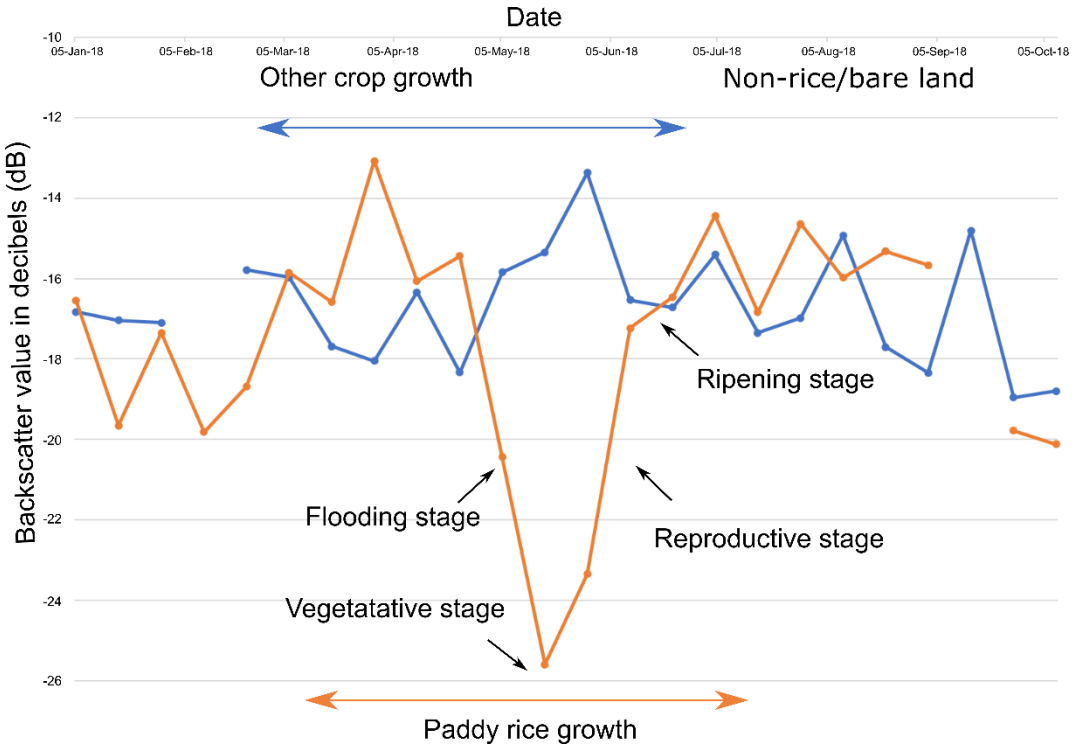

Figure 4.6. The example of rice detection workflow for each pixel with vertical-horizontal backscattering (VH) values. The blue line is the example of a non-rice cultivation class (-7° 10' 34.9",111° 52' 55.42"), and the orange line is the example of a rice cultivation class (-6° 27' 57.27",108° 8' 56.64").

4.4.4 Accuracy assessment and temporal changes

The accuracy of the Sentinel-2, MOD13Q1/Sentinel-1 model, and rice planting detection were tested using the comparison of predicted values and ground-reference data. By using

the confusion matrix, the overall accuracy, user's accuracy (UA), and producer's accuracy (PA) can be calculated as suggested by (Foody, 2002; Olofsson et al., 2014; T. Sun et al., 2017). The test data for the Sentinel-2 model is 127 points, and MOD13Q1/Sentinel-1 is 138 points.

The temporal changes of predictions maps were reclassified into four classes: (1) No Change, there is no change between stages; (2) change correctly, the stages change into progressively according to the common practices of rice cultivation in Figure 4.1; (3) change incorrectly, the stages change into two stages forward or back to previous stages; and (4) cloud and shadows, one of the images have cloud/shadows. Thus, the average of no change, change correctly, and change incorrectly can be calculated. The consistency of the map of Sentinel-2 was tested by comparing two images of different 5, 10, 15, 20, 25, and 30 lag-days, and the Sentinel-2 / MOD13Q1 / Sentinel-1 maps were 16-day lag-days, respectively. The formulas of consistency and inconsistency as follows:

$$\text{No change (\%)} = \frac{\sum \text{Area of no change}}{\sum \text{All area}} \text{x}100\%, \tag{5}$$

$$\text{Change correctly (\%)} = \frac{\sum \text{Area of changed correctly}}{\sum \text{All area}} \text{x}100\%, \tag{6}$$

$$\text{Consistency (\%)} = \frac{\sum \text{Area of no change} + \sum \text{Area of changed correctly}}{\sum \text{All area}} \text{x}100\%, \tag{7}$$

$$\text{Inconsistency (\%)} = \frac{\sum \text{Area of changed incorrectly}}{\sum \text{All area}} \text{x}100\%. \tag{8}$$

A high consistency value is better since the prediction model can accurately predict the growth stages in current and previous times.

4.5 Results

4.5.1 Spectral bands

Figure 4.7 (a) provides the mean and deviation of reflectance values for different rice growth stages based on the ground truth dataset. The result indicates that five classes have distinctive spectral features with significant variability. The reflectance profiles of bare land and flooding are different from rice growth stages (vegetative, reproductive, and ripening) as the rice growth stages have the higher mean value on Red Edge 3, NIR, and SWIR1 band. The flooding class displays the lowest reflection on the NIR band due to almost no reflection off from the vegetation. Moreover, the spectral bands of rice growth stages are concurrent with a multi-angle spectrometer from Sun et al. (T. Sun et al., 2017), except for the flooding phase because of the different rice management in the study area. The spectral trend in vegetative and reproductive phases followed a similar pattern.

The averages of NDVI and EVI values can be seen in Figure 4.7 (b). It shows that bare land and flooding have similar NDVI values on average but are different on EVI, which indicates that EVI has a more significant role in separating bare land and flooding (Xiao et al., 2003). The NDVI and EVI values for rice growth stages follow the common rice growth stages values where the vegetative stage has the lowest values and the highest values are the reproductive stage due to the dense canopy. Lastly, the ripening stage is in the middle as it changes the vegetation to golden colour (Qiu et al., 2014).

Figure 4.7 (c) shows the relationship between rice growth stages in three consecutive acquisition dates. It shows that the bare land, ripening, and reproductive stages have backscattering values >-19 *dB,* meaning the surface has relatively dense biomass over 24 days. The bare land is decreasing, and otherwise, ripening and reproductive

is decreasing. The main feature is the flooding class, which shows the lowest backscattering value on the previous 24 days and increases afterwards. The backscattering values on the vegetative stage were stable <19 *dB,* which shows the low scattering due to specular reflection (Hoang et al., 2016).

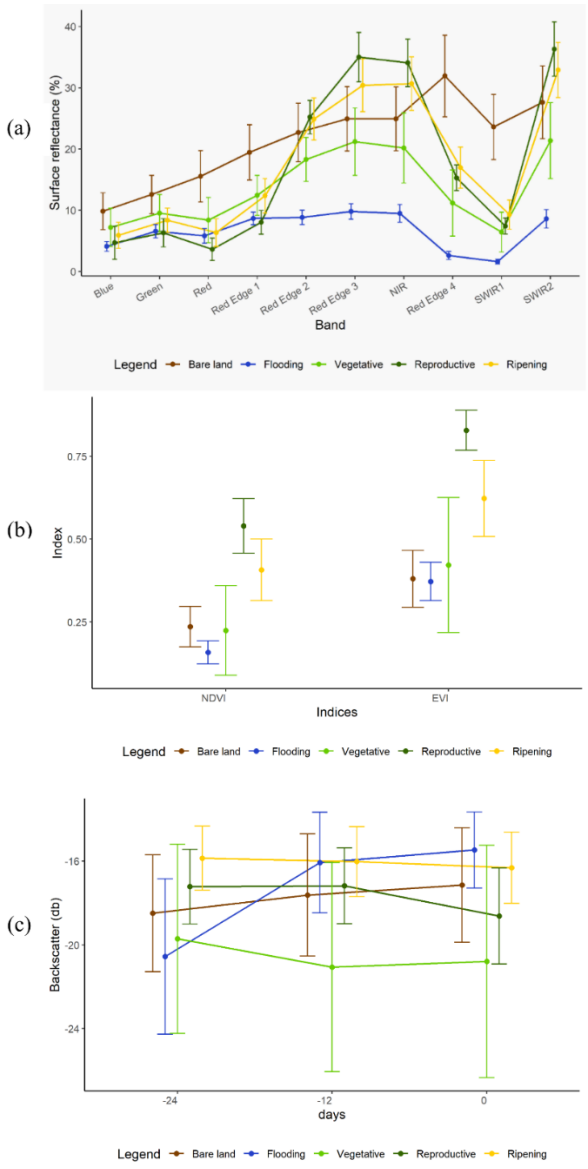

Figure 4.7 (a) The means of spectral bands from Sentinel-2 values, (b) the means of NDVI and EVI values from MOD13Q1, and (c) the means of Sentinel-1 VH values regarding bare land, flooding, and rice growth stages. The bands are offset for visualization and error bars represent standard error.

4.5.2 Accuracy assessment of rice growth stages model

Overall, the accuracy of the Sentinel-2-based model is higher than the combined MOD13Q1/Sentinel-1 model (Table 4.5). The former can reach a high overall accuracy of 90.6% for all rice growth stages (except ripening) from the producer's accuracy. The ripening stage is often misclassified with vegetative and reproductive stages. On the other hand, the MOD13Q1/Sentinel-1 model has an overall accuracy of 78.3%, which is lower due to confusion between the ripening class and the bare land stage. However, the MOD13Q1/Sentinel-1 model can predict the reproductive stage with high accuracy (97.1% for PA and 84.6% for UA).

Table 4.5 The confusion matrix performance on the test dataset on Sentinel-2 and MOD13Q1/Sentinel-1.

		Reference Data						
	Classes	Bare Land	Flooding	Vegetative	Reproductive	Ripening	Sum	UA (%)
		(a) Sentinel-2						
Predicted data	Bare land	32	0	0	0	1	33	97.0
	Flooding	0	21	0	0	0	21	100.0
	Vegetative	1	0	16	0	4	21	76.2
	Reproductive	0	0	2	35	3	40	87.5
	Ripening	0	0	0	1	11	12	91.7
	Sum	33	21	18	36	19	127	
	PA (%)	97.0	100.0	88.9	97.2	57.9		
	OA (%)	90.6						
		(b) MOD13Q1/Sentinel-1						
Predicted data	Bare land	31	1	5	0	5	42	73.8
	Flooding	0	18	3	0	0	21	85.7
	Vegetative	2	2	15	0	0	19	78.9
	Reproductive	0	0	3	33	3	39	84.6
	Ripening	4	0	1	1	**11**	17	64.7
	Sum	37	21	27	34	19	138	
	PA (%)	83.8	85.7	55.6	97.1	57.9		
	OA (%)	78.3						

Note: OA= Overall accuracy, UA = User's accuracy, and PA = Producer's accuracy.

The Sentinel-2 rice growth stage model was able to capture the variation of different rice growth stages, as shown in Figure 4.8. The map of a particular area on the West Area shows that the vegetative stage was recorded on 1–26 June 2018, followed by the reproductive stage on 1 – 21 July 2018, and then the ripening stage until 10 August 2018. The models show that the land was harvested on 15 August 2018.

Figure 4.9 shows that the paddy area was surrounded by a non-paddy class as in the East Area, and the irrigation becomes scarce on second rice planting. The vegetative stage was captured on 3–23 June 2018. Then, the reproductive stage was 28 June – 23 July 2018. The process of ripening happened between 2 and 17 August 2018. Afterwards, the paddy area becomes bare land or host to other crop types.

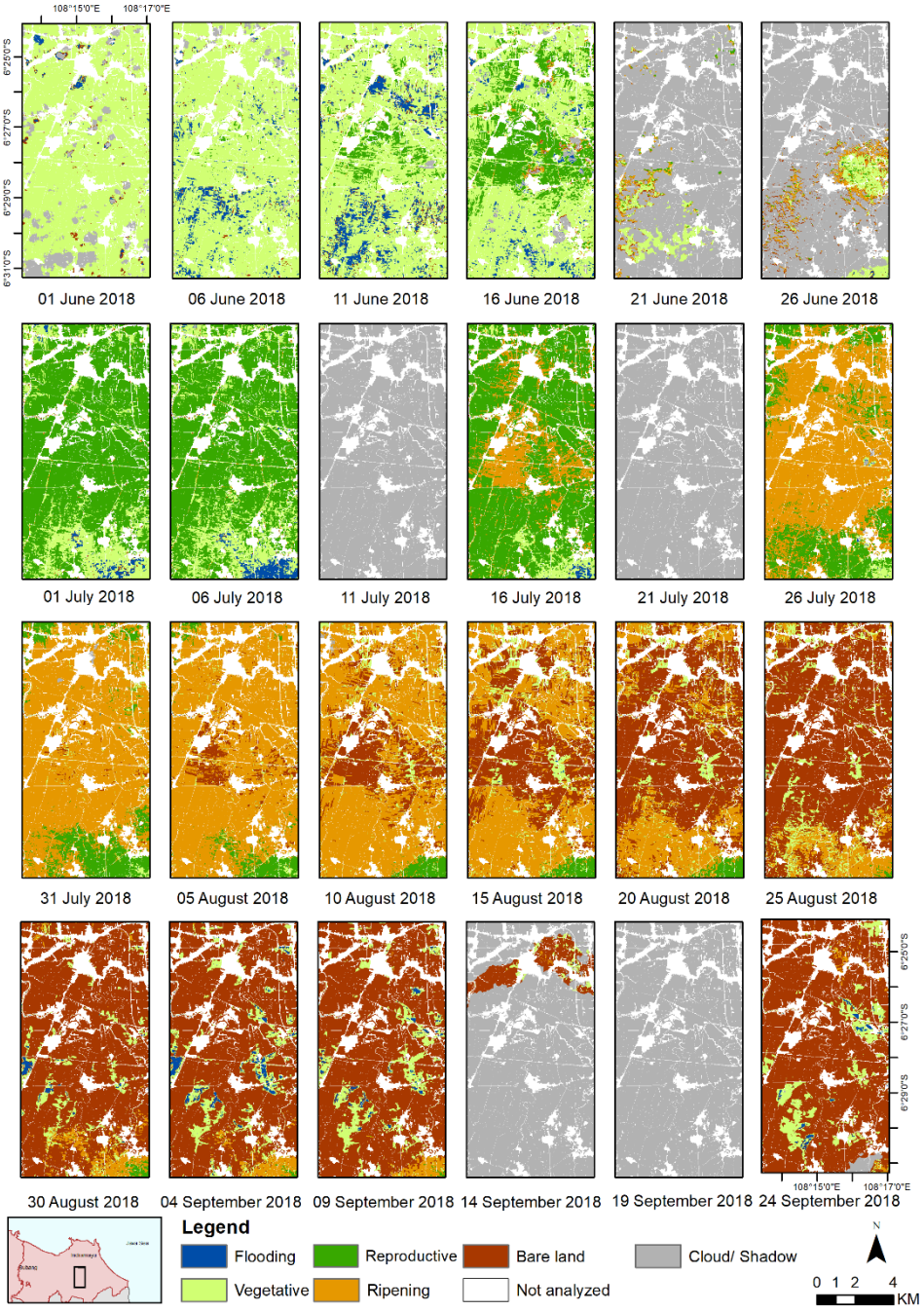

Figure 4.8 Example of a small area of temporal rice growth stage maps based on the Sentinel-2 model on the West Area between 1 June and 24 September 2018 every five days.

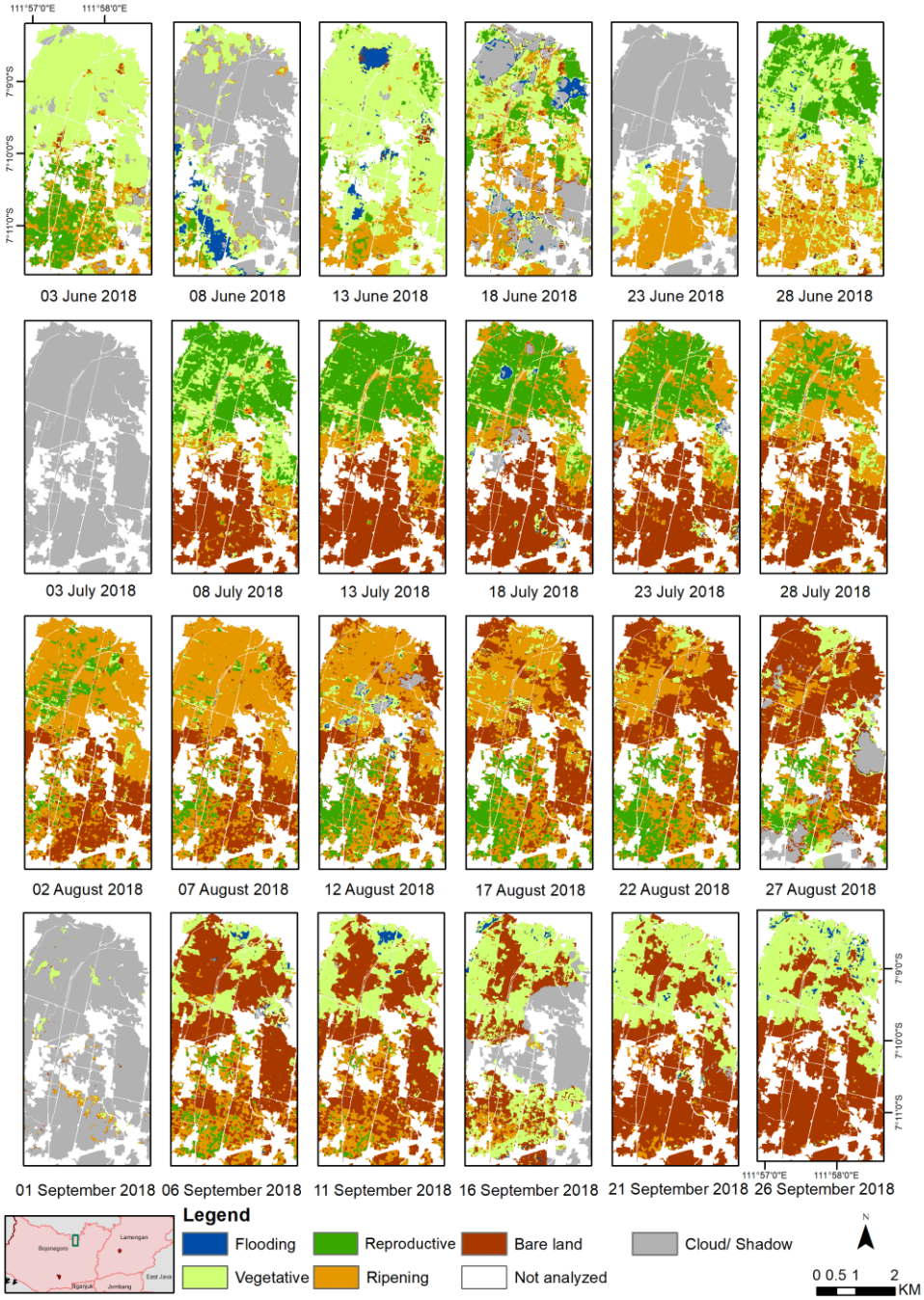

Figure 4.9 Example of a small area of temporal rice growth stages maps based on the Sentinel-2 model on the East Area between 3 June and 26 September 2018 every five days.

4.5.3 Temporal changes

The temporal analysis of Sentinel-2 shows that the model was able to capture the change classes with correct ranges of 83 – 90% (Table 4.6) of the time. The temporal consistency decreases with the time lag increase. The gradual decrease of the non-change area from 5 to 16 days also confirms that the model can classify the change of rice growth, as shown in Figures 4.10 and 4.11. The West Area has a better consistency result since the irrigation schedule is stable, unlike the East Area where irrigation depends on rain.

On the other hand, the temporal analysis of Sentinel-2/MOD13Q1/Sentinel-1 proves that consistency is high (84.15%), which is comparable with the Sentinel-2 consistency on the 15-day period (87.91%). Table 4.6 also indicates that high consistency was achieved from the West Area and East Area, which suggests that the detection of the non-rice planting class is working well in the East Area. Moreover, Figures 4.7 and 4.8 show that final classification images from the integration of the Sentinel-2/MOD13Q1/Sentinel-1 model can deliver a rice growth stage map without cloud and shadows at a 10-m resolution. The Sentinel-2 model was able to fill in >80% of the study area except on 26 June, 28 July, and 14 September 2018 in the West Area (Figure 4.7). Moreover, the East Area map shows that the rice field area is dominantly on bare land and non-rice planting except on the area on the north of the East Area, where rice planting can be irrigated with pumping water from the near river (Figure 4.8).

Table 4.6 List of the average of performance from temporal changes analysis of (a) Sentinel-2 and (b) Sentinel-2/MOD13Q1/Sentinel-1.

Time Lag	N	No Change (%)			Change Correctly (%)			Consistency (%)			Inconsistency (%)		
(a) Sentinel-2													
		WA	EA	Avg.	WA	EA	Avg.	WA	EA	Avg.	WA	EA	Avg.
5	23	58.72	69.22	63.90	34.00	18.82	26.48	92.72	88.04	90.39	7.28	11.96	9.61
10	22	50.49	68.33	59.35	40.80	18.97	29.96	91.29	87.30	89.31	8.71	12.70	10.69
15	21	44.06	63.41	53.68	46.47	21.86	34.23	90.53	85.27	87.91	9.47	14.73	12.09
20	20	40.57	62.24	51.40	48.79	22.26	35.53	89.36	84.50	86.93	10.64	15.50	13.07
25	19	39.02	55.41	47.22	48.36	26.05	37.21	87.39	81.47	84.43	12.61	18.53	15.57
30	18	35.09	55.77	45.43	50.74	24.92	37.83	85.83	80.70	83.27	14.17	19.30	16.73
(b) Sentinel-2/MOD13Q1/Sentinel-1													
16	6	60.27	65.1	62.64	24.26	18.75	21.50	84.52	83.77	84.15	15.48	16.23	15.85

Note: WA= West Area, EA = East Area, and Avg.=Average.

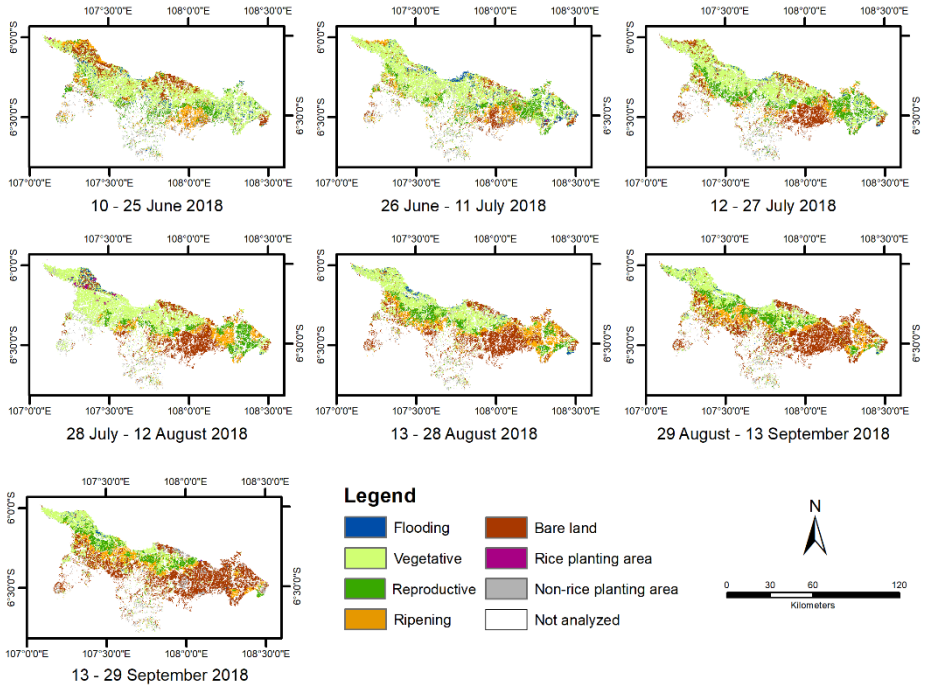

Figure 4.10 Temporal map of rice growth stages based on Sentinel-2/MOD13Q1/Sentinel-1 on the West Area.

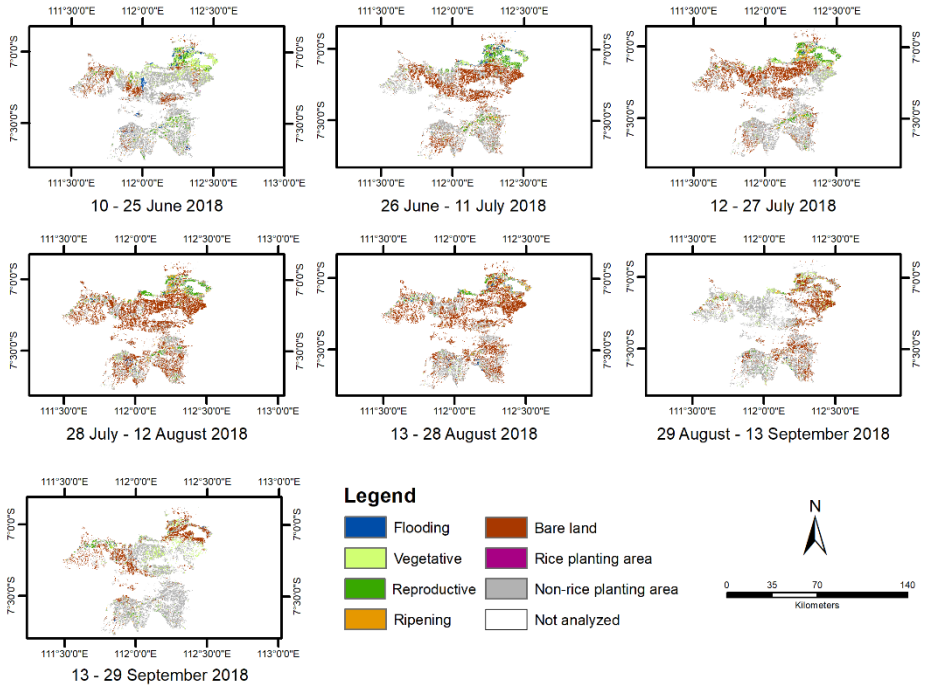

Figure 4.11 Temporal map of rice growth stages based on Sentinel-2/MOD13Q1/Sentinel-1 on the East Area.

4.6 Discussion

4.6.1 The Performance of integrating Sentinel-2/MOD13Q1/Sentinel-1 for mapping rice growth stages

High-resolution multitemporal images of rice growth stages are essential to improve rice production. Although optical images are less favourable for providing continuous images in tropical regions, this research developed a new method to generate multitemporal maps for rice growth stages across Java Island using multisource remote sensing data (Sentinel-2/MOD13Q1/Sentinel-1). This method outperforms a single source of remote sensing information in a real-world application level on rice growth stage mapping as confirmed with previous results, especially to fill the missing data, increasing the overall accuracy by 2–5% (Cai et al., 2019; Lopes et al., 2020; Orynbaikyzy et al., 2019). Previous research reported that using single-date data for creating rice maps is not an adequate strategy for mapping multitemporal implementation. These rice growth stage maps showed temporal consistency even without using the extended temporal composite vegetation index or backscattering profile series. This workflow works best on the paddy rice area, which is often flat and water covered. The water cover can be picked up by the Sentinel-1 VH signal and improve the temporal frequency of observation, and thus the overall rice growth stage models. Other advantages of this model are that it can be rolled out to cover larger areas (i.e., entire Southeast Asia) with the same farm practices and without depending on a clean time series of the vegetation index.

Increasing the temporal frequency of Sentinel-1 images can improve the accuracy of rice growth stages since the backscattering profiles were more accurately determined, particularly on the vegetative stage during the dry season, such as the East Area, where water is scarce. Moreover, Ndikumana, Ho Tong Minh, Baghdadi, et al. (2018) reported that Sentinel-1 with a 6-day revisit cycle can produce a rice map with an 88% accuracy for rice fields in France, which better compares with the 12-day revisit cycle from the study from Clauss et al. (2018) with an 83% accuracy.

It is not surprising that the Sentinel-2 based model produced higher accuracy than the fusion of MOD13Q1 and Sentinel-1 due to the red edge bands with high spatial resolution. These bands can enhance the detection of capturing canopy chlorophyll content better, as suggested by Frampton et al. (2013) and (Zhou et al., 2017), which enables separation of

the rice growth stages. The accuracy from the fusion of MOD13Q1 and Sentinel-1 was higher than MODIS information alone, which indicates the complementary information from Sentinel-1. This high accuracy is prominent for the flooding class due to the coarse resolution of the MOD13Q1 data, allowing a more significant portion of mixed pixels to occur compared to the 10-m Sentinel-2 data. The prediction maps from MOD13Q1 and Sentinel-1 were used to fill the missing data or for cloudy pixels of the Sentinel-2.

The consistency of Sentinel-2 has a negative correlation between lag days. The 5-day lag showed the highest consistency percentage and slowly decreased to the 30-day lag-time due to the unchanged stages. Moreover, the correct changes became lower and less consistent over the lag days. This result demonstrated that the models could detect the changes in growth stages over time and still have the increased consistency (83.27%) over 30 consecutive days. Moreover, the integration of Sentinel-2/MOD13Q1/Sentinel-1 shows an increase the consistency (2.54%) compared with the 5-day lag consistency percentage.

4.6.2 The implication of satellite-based monitoring in tropical countries

The tropical regions are challenging for optical satellite-based remote sensing due to persistent cloud coverage. Most of the study relies on high-frequency temporal remote sensing data to capture rice growth changes, which are hampered by observation gaps, which can be filled using radar-based imagery (e.g., S1). However, radar-based data also has some limitations, such as geometric distortion and a different response to bare land (Perbet et al., 2019). Our finding shows that by merging three sensors, we can deliver information on rice growth stages for near real-time monitoring for the Sentinel-2 model, and better accurate information in periodical data for Sentinel-2/MOD13Q1/Sentinel-1 data. Furthermore, this study successfully filled the missing data up to 28.2% in the West Area and 8.8% in the East Area (Figure 4.12).

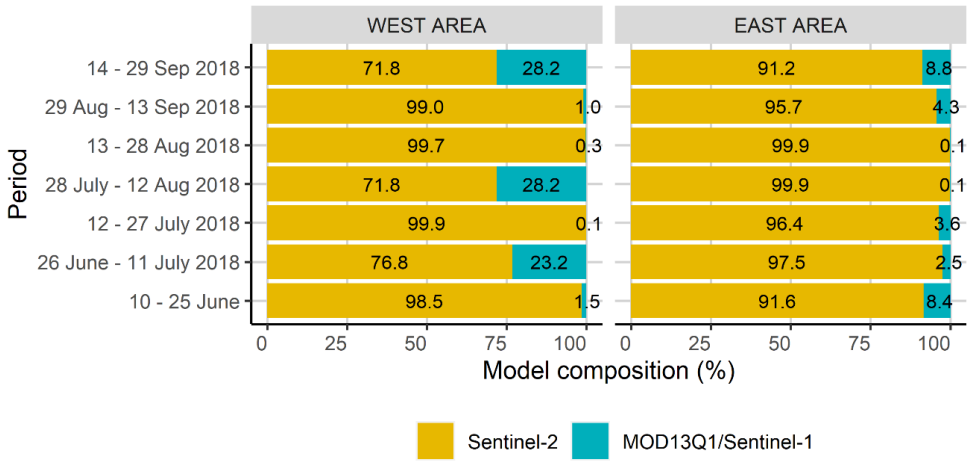

Figure 4.12 Pixel-based model compositions of temporal rice growth stages map of Sentinel-2/MOD13Q1/Sentinel-1 on final paddy condition map on 10 June – 30 September 2018.

Our methodology focuses on developing a groundwork for mapping rice growth stages for near-real-time monitoring, which is challenging to accomplish in an operational level due to the short duration of rice cultivation. Moreover, we focused on making it feasible to incorporate with cloud-based computing or stand-alone workstations and less human interference. Our study is in line with the works of Rudiyanto et al. (2019). They have succeeded in mapping rice growth stages from multitemporal Sentinel-1 images with unsupervised classification for one month with the same area with cropping pattern information. Significantly, our methodology outperformed the established rice monitoring systems in Indonesia based on MODIS (LAPAN, 2019) or Landsat rice monitoring (PUSDATIN, 2019), as our results created rice growth stage maps at a 10-m spatial resolution with a 16-day period, less cloudy data, and providing present cultivation crop.

Future research should be focused on fusing the multitemporal and multiresolution of satellite observation to increase data availability and accuracy with <100-m spatial resolution. Our study shows that it is possible to fuse the information of the feature level using machine learning. Our experiment showed that the desktop personal computer with 16 GB RAM could classify the image with high speed (17,770 ha/min). This method can also be employed for other remote sensing data, such as PROBA-V or WorldView missions.

This technology enables users to compile information interactively via a user interface on a dedicated website or mobile application, resulting in significantly reduced wait times.

Moreover, the classifier of machine learning can be chosen easily with other open-source machine learning packages, such as TensorFlow (Abadi et al., 2016) with Keras (Ketkar, 2017) or Scikit-learn (Pedregosa et al., 2011). Importantly, the integration of rice growth stages with other information, such as the recommended cropping calendar, climate predictions, weather reports, price trend maps, insurance risk maps, and other in situ knowledge, will improve the rice productivity supporting regional food security.

4.6.3 Limitation of satellite remote sensing for rice mapping

This research has some limitations, such as the availability of cloud-free images. These limitations are further hampered by the fact that there is a bias between the seasons. For example, most optical observations concentrate on the dry season, while only coarser resolution data are available (MODIS and RADAR) on the wet season. Accordingly, some areas with different surface reflectance may be misclassified if it is applied to images in the wet season, such as a wetland. Some traditional farmers switch flooding and drying again, and conduct final flooding before transplanting. This study's accuracy is highly dependent on the existing rice field map, and, over time, some area could be converted into an urban or industrial area. Long-term rice mapping using multitemporal satellite images has been explored in some studies (Dong et al., 2016; Onojeghuo et al., 2018; Zhou et al., 2016) with high accuracy, which can be used to correct existing rice field maps every five years.

The East Area has high fragmentation of different crops on the rice field area especially on the north area of Nganjuk Regency (Ramadhani et al., 2020a), which caused problems in classifying between the vegetative stage of rice and shallot cultivation since both crop types need a significant time of water cover to keep the soil moisture. Hence, they are spectrally similar at a specific time, mostly in the early second planting season. Moreover, the fragmented rice field paddocks with an area <0.5 ha made it difficult to be separated automatically in a large area. Thus, additional information is required, including the use of unmanned aerial vehicles (UAVs) (Zhou et al., 2017), ongoing and planned hyperspectral satellite missions (e.g., *PRecursore IperSpettrale della Missione Applicativa* (Cogliati et al., 2021; Pignatti et al., 2013)- PRISMA and Environmental Mapping and Analysis Program - EnMAP (Guanter et al., 2015), and webcams (Lebourgeois et al., 2008), for a more apparent separation between such classes.

4.7 Conclusion

There is a need for timely and accurate spatial information on rice growth stages. This paper has provided an automatic process to build multitemporal maps for rice growth stages with a 10-m spatial resolution, which is sufficient for crop monitoring at the local and national levels in developing countries. This information is useful for stakeholders using a combination of Sentinel-2, MOD13Q1, and Sentinel-1 for a near real-time and high accuracy, consistency and temporal frequency (16-day period). Furthermore, the Sentinel-2 model in this study was implemented in Indonesia, with 7.4 million hectares of autonomous data retrieving, analysis, and dissemination, which are available on a website (http://katam.litbang. pertanian.go.id/sc/).

The research presented here is based on open-access satellite data and software, improving its accessibility and uptake by end-users in developing countries. Improving the speed of the mapping process can provide an effective tool for stakeholders and decision-makers to coordinate the distribution of machinery, fertiliser, and water more efficiently. The estimation of rice production can be predicted with better accuracy to control the export and import of rice trade. In addition to the climate change issue, the result is applied as an input of prediction of production and food security in a fragile area, such as drought and flooding, using the temporal analysis or becoming a part of the ASIA Rice project (asia-rice.org) to support the dissemination among its members.

[intentionally blank]

Chapter 5 Mapping a Cloud-Free Rice Growth Stages Using the Integration of PROBA-V and Sentinel-1 and Its Temporal Correlation with Sub-District Statistics

The objective of chapter 5 is to investigate a new method for mapping cloud-free rice growth stages using the integration of PROBA-V and Sentinel-1 and its temporal correlation with sub-district statistics. This chapter is based on a published paper:

> *Ramadhani, F., Pullanagari, R., Kereszturi, G., & Procter, J. (2021). Mapping a Cloud-Free Rice Growth Stages Using the Integration of PROBA-V and Sentinel-1 and Its Temporal Correlation with Sub-District Statistics. Remote Sensing, 13(8), 1498. https://www.mdpi.com/2072-4292/13/8/1498*

Supplementary data and source code can be downloaded on https://github.com/FadhlullahRamadhani/Remote-sensed-correlation-statistics.

Participating authors:

- Fadhlullah Ramadhani: Conceptualization**,** investigation, data curation**,** formal analysis, methodology, software, visualization, and writing—original draft preparation
- Reddy Pullanagari: Conceptualization, methodology, supervision, and writing—review and editing,
- Gabor Kereszturi: Conceptualization, methodology, supervision, visualization, and writing—review and editing,
- Jonathan Procter: Supervision, and writing – review & editing

Abstract

Monitoring rice production is essential for securing food security against climate change threats, such as drought and flood events becoming more intense and frequent. The current practice to survey an area of rice production manually and in near real-time is expensive and involves a high workload for local statisticians. Remote sensing technology with satellite-based sensors has grown in popularity in recent decades as an alternative approach, reducing the cost and time required for spatial analysis over a wide area. However, cloud-free pixels of optical imagery is required to produce accurate outputs for agriculture applications. Thus, in this study, we propose an integration of optical (PROBA-V) and radar (Sentinel-1) imagery for temporal mapping of rice growth stages, including bare land, vegetative, reproductive, and ripening stages. We have built classification models for both sensors and combined them into 12-day periodical rice growth-stage maps from January 2017 to September 2018 at the sub-district level over Java Island, the top rice production area in Indonesia. The accuracy measurement was based on the test dataset and the predicted cross-correlated with monthly local statistics. The overall accuracy of the rice growth-stage model of PROBA-V was 83.87%, and the Sentinel-1 model was 71.74% with the Support Vector Machine classifier. The temporal maps were comparable with local statistics, with an average correlation between the vegetative area (remote sensing) and harvested area (local statistics) is 0.50 and lag time 89.5 days (n = 91). This result was similar to local statistics data, which correlate planting and the harvested area at 0.61, and the lag time as 90.4 days, respectively. Moreover, the cross-correlation between the predicted rice growth stage was also consistent with rice development in the area ($r > 0.52$, $p < 0.01$). This novel method is straightforward, easy to replicate and apply to other areas, and can be scaled up to the national and regional level to be used by stakeholders to support improved agricultural policies for sustainable rice production.

Keywords: rice growth stages; machine learning; monitoring; PROBA-V; Sentinel-1; SVM

Table of contents for Chapter 5

5.1 Introduction

Rice (*Oryza sativa* L.) is one of the main crops grown in the tropical and subtropical area, with more than half the world population depending on rice as a staple food (Normile, 2008). However, global production is close to its limits while the dependent population is expected to grow up to 9.26 billion by 2050 (FAO, 2020). Moreover, urbanization, depleting water resources, climate change, and natural disasters have been threatening the sustainable production of rice despite its increased production by introducing new cultivars, chemical fertiliser, and better irrigation. Near-real-time and accurate information about rice growth stages is vital to support stakeholders to make better decisions to maximize production volumes and secure food production.

Rice fields have been traditionally monitored by a local field statistician to calculate the planting and harvesting area from the local to a national scale. However, this is a long and exhausting field-sampling process that may not be compatible with the current and future situation where climate change may cause reduced agricultural productivity in developing countries by 2080 (based on emissions-forecasting worst-case scenarios) (Parry et al., 2005).

Remote sensing has been widely used to monitor crops, including projects such as Monitoring Agricultural ResourceS (MARS) by the EU (De Boissezon, 1995; Van der Velde & Bareuth, 2015). They have developed an automated system for rice monitoring for Europe, which has limited portability for tropical countries with limited free satellite image sources and high cloud occurrences. Other rice monitoring projects exist, such as Geo Global Agricultural Monitoring by multiple international organizations (Whitcraft et al., 2015) and CropWatch by China (Wu et al., 2014). However, the monitoring system only works for dedicated countries, making it difficult to be developed and replicated to other countries, especially for developing ones.

In recent years, many attempts have been made for mapping rice areas using multitemporal Synthetic-aperture radar (SAR) images based on backscattering profiles (Bazzi et al., 2019; Inoue et al., 2020a; Jo et al., 2020; Lasko et al., 2018; Mansaray et al., 2020; Nguyen et al., 2016; Phung et al., 2020; Satalino et al., 2012; Wakabayashi et al., 2019). Compared to optical sensors, the SAR sensors such as Sentinel-1 (Lasko et al., 2018; Mandal et al., 2018), TerraSAR-X (Koppe et al., 2013; Yuzugullu et al., 2015) and Radarsat-2 (Li et al.,

2012; Wu et al., 2011; Y. Zhang et al., 2017) have the advantage of penetrating through the clouds, which is the major obstacle in monitoring efforts. The previous studies reported that backscattering profiles could detect rice area (Bazzi et al., 2019; Mascolo et al., 2019; Son et al., 2017; G. Zhang et al., 2020), rice cropping pattern (Rudiyanto et al., 2019; Sianturi et al., 2018; Son et al., 2017), and rice growth stages (Phung et al., 2020; Rudiyanto et al., 2019) with high precision. Based on these results, Remote sensing-based Information and Insurance for Crops in Emerging economies (RIICE) has been developing a method with Sentinel-1 to map rice areas in six Asian countries (Holecz et al., 2013; Nelson et al., 2014).

Several studies highlighted that multiple-sensor data could increase the accuracy by 3–9% of rice mapping under different landscapes (Cai et al., 2019; Luo Liu et al., 2020; Perbet et al., 2019; X. Yang et al., 2020). For example, optical sensors can enhance or confirm the rice-specific backscattering profile with SAR data challenging to interpret in a complex area (Rudiyanto et al., 2019). Furthermore, the vertical-horizontal/vertical-vertical (VH/VV) backscatter images can detect inundating of rice area using the spikes of backscatter values (Cai et al., 2019; L. Mansaray et al., 2017). On the other hand, vegetation indices such as Enhanced Vegetation Index (EVI) and Normalized Difference Vegetation Index (NDVI) from Sentinel-2 or Landsat-8 can also detect changes by using a phenology method for rice cultivation by capturing the increase and decrease in indices values (L. Mansaray et al., 2017; Tian et al., 2018). However, the phenology method requires long temporal data (>3 months), which may challenge building automated rice growth-stage detection methods. The Project for On-Board Autonomy-Vegetation (PROBA-V) is a satellite mission to monitor vegetation globally with a 2–5 days revisit time and 100 m spatial resolution. It has been used for mapping land use classification using vegetation indices with better spatial resolution than the Moderate-Resolution Imaging Spectroradiometer (MODIS) based products (Bórnez et al., 2020; Shimabukuro et al., 2020). Despite the advantages of PROBA-V, the application of this technology for rice growth stages is limited.

The Indonesian Ministry of Agriculture has been developing several rice monitoring projects utilizing remote sensing technology to update food production statistics. The first project they supported undertook rice monitoring with the MODIS with Terra sensor with a spatial resolution of 250 m to map rice growth stages in 2012 (https://sipandora

.lapan.go.id/site/fasepertumbuhanpadi, accessed date: 11 November 2020) with accuracy <70% (PUSDATIN, 2019). In 2016, another project was undertaken using Landsat-8 Operational Land Imager (OLI) using NDVI threshold (http://sig.pertanian.go.id/, accessed date: 21 December 2020) with accuracy <60% without cloud masking (PUSDATIN, 2019). However, both projects have one major limitation; cloud occurrence causes uncertainty over a specific timeframe.

The Indonesian Agency for Agricultural Research and Development has recently launched a rice monitoring system using Sentinel-2, allowing users to have detailed information about rice conditions in 10 m resolution (S-2 RGS). The S-2 RGS uses a machine learning model to classify rice conditions using ten bands of Sentinel-2 as a predictor (Ramadhani et al., 2020a). The information can be accessed freely online and on android with an interactive map (http://katam.litbang.pertanian.go.id/sc/, accessed date: 15 January 2021). However, the existing monitoring approach is incapable of temporal tracking using local statistics due to missing data in some periods due to cloud and shadows, and the results are not consistent because they are unable to produce time-series data.

This study aims to overcome these challenges by proposing a new workflow to integrate ground observations and high-frequency revisit optical sensors with PROBA-V and radar sensors such as Sentinel-1. Furthermore, images from both sensors are available on the Google Earth Engine (GEE), which is freely accessible for public use. Thus, the objectives of this study are as follows: building classification models for mapping the rice growth stages using the integration of PROBA-V and Sentinel-1; and measuring the correlation between the area of rice growth stages with local statistics at sub-district levels. This study will provide a foundation for mapping the rice growth stages accurately and making these available to the stakeholders for making better decisions when manual observations are limited.

5.2 Background, study area, and data

5.2.1 Rice growth stages

The rice production cycle usually takes about 3–4 months, depending on the variety and environmental conditions, to grow from seed to mature plants. They experience three general phases of growth: vegetative, reproductive, and ripening (Bouman, 2019). Figure 5.1 illustrates the rice growth phases and surface conditions in the rice fields (Kawamura

et al., 2018). First, the seed is planted in a small bed and, after 25 days, is transplanted into the main rice field to produce a higher yield and reduce weed occurrences. The vegetative stage spans from seed germination to maximum tillering. The next stage is the reproductive stage, where the plant grows from panicle initiation to heading. The last phase is ripening. The young grain in the panicle starts to develop starch. The grain colour becomes gold and then it is harvested. Within this study, we added a bare land class to capture the dynamics of the changing land surface within rice fields.

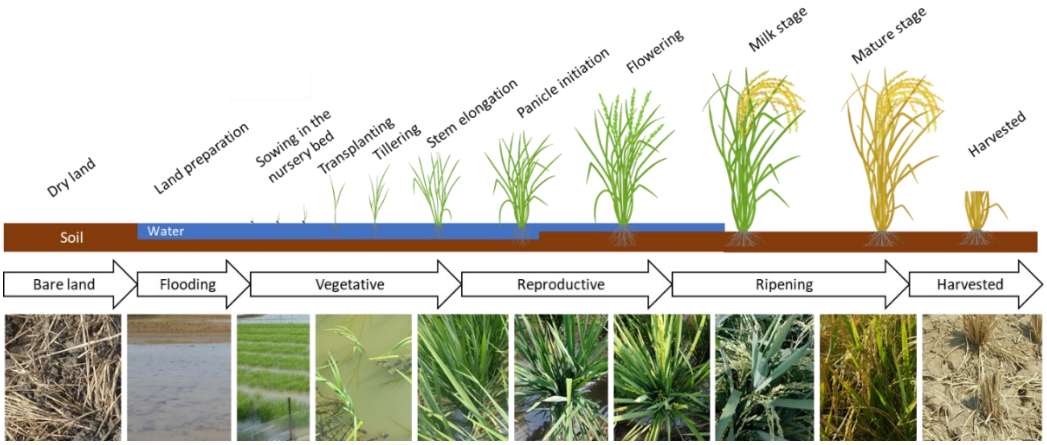

Figure 5.1 The rice growth stages with actual images from the field campaign.

5.2.2 Study area

The study area is located on Java Island, the leading rice producer in Indonesia, with a combination of irrigated and low land areas. The area consists of three regencies: Karawang, Subang, and Indramayu, with 309,046 ha in West Java Province (Figure 5.2), which is split into 91 sub-districts administratively (BPS-West-Java, 2018). The leading rice production areas are usually within the sub-districts in Indramayu (116,869 ha) and Subang (90,474 ha). Karawang (101,703 ha) is a regency with high land-use change rates due to industrialization and housing construction. The most significant paddy field area is Losarang, Indramayu, with 7244 ha, and the smallest is Cikampek, Karawang (416 ha). The average rice field area, over 91 sub-districts, is 3373 ha.

The majority of the land area is irrigated and dominated by alluvial soils which are most suitable for rice cultivation. This comes from deposition from the Cimanuk, Citarum, and Cilamaya rivers. A state-owned company maintains the water distribution from the Jatiluhur dam in the south of the study area. The climate is monsoon with two seasons: the

wet and dry seasons, and is classified as tropical rainforest based on Köppen–Geiger climate classifications (Kottek et al., 2006). Paddy cultivation includes the use of short-duration rice varieties such as IR64, Ciherang, glutinous rice, and other varieties (Rudiyanto et al., 2019; Sianturi et al., 2018). Fertiliser is applied twice during the vegetative stage, and chemical pesticides are used to remove pests. Crops are harvested using manual tools and labour. The rice crop is typically cultivated twice a year, with farmers starting sowing during the rainy season in November–December and harvested in January–February. The second sowing is undertaken in March–April and harvest from June to July. However, some areas have scheduled water irrigation which allows rice cultivation even in the dry season. The complete cropping pattern of the study area is well described in the previous study (Sianturi et al., 2018).

5.2.3 Satellite imagery

This study uses two multitemporal imagery sources: Project for On-Board Autonomy-Vegetation (PROBA-V) and Sentinel-1 satellite imagery was downloaded directly from GEE storage within the period from January 2017 to August 2018. PROBA-V Top of Canopy dataset comes from Flemish Institute for Technological Research/European Satellite Agency (GEE id: VITO_PROBAV_C1_S1_TOC_100M). The product contains five bands, e.g., red (658 nm), near-infrared (NIR) (834 nm), blue (460 nm), short-wave infrared (SWIR) (1610 nm), and the NDVI values were calculated from the red band and NIR band (Meroni et al., 2016). This dataset comes from a composite of 300 m spatial resolution every two days and 100 m every five days, which has been corrected at the atmospheric and radiometric level (Sterckx et al., 2014).

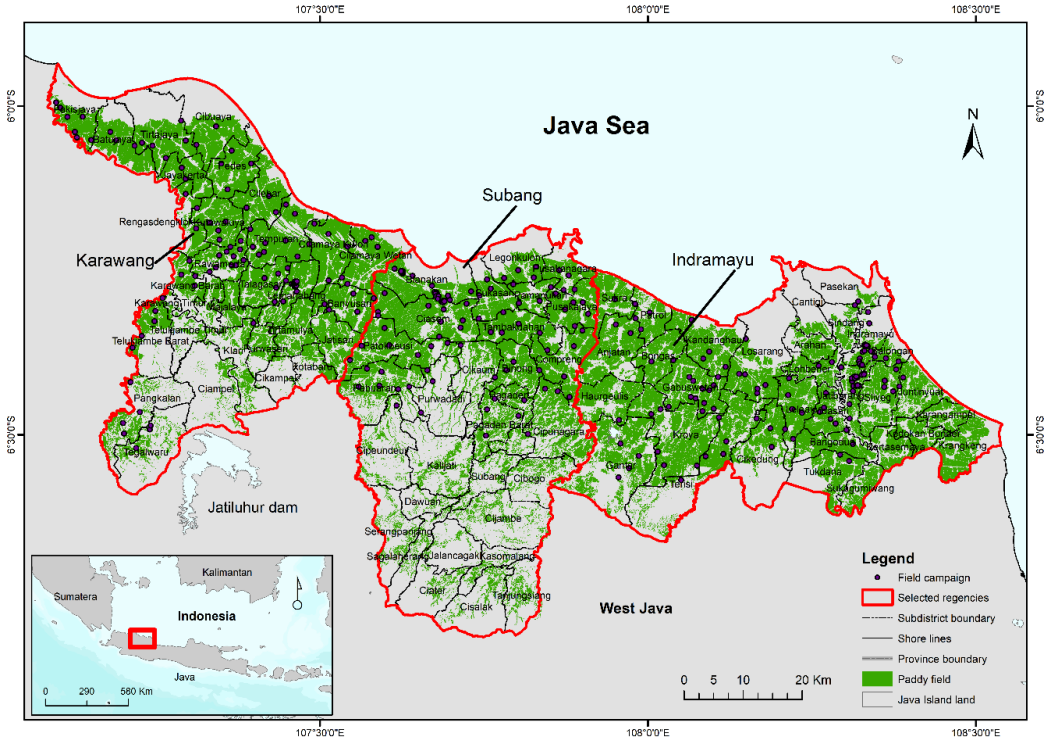

Figure 5.2 The map of the rice area on the study area for Karawang, Subang, and Indramayu Regency.

The Sentinel-1 dataset comes from the Copernicus project by the European Space Agency (ESA) as one of the space missions to monitor land on a global scale. Sentinel-1 has a dual-polarization C-band Synthetic Aperture Radar (SAR) with two satellites in the same orbit to have shorter revisit times (6–12 days). The dataset has been processed with the Sentinel-1 toolbox to remove thermal noise, calibrate radiometric problems, and correct the terrain (GEE id: COPERNICUS_S1_GRD). The dataset contains vertical-horizontal (VH) and vertical–vertical (VV) cross-polarization with Interferometric Wide Swath mode in order to have the largest area in one swath with 10 m resolution from a descending orbit dataset. A revised Lee filter was run to decrease speckle noise (Lee, 1981). In the next step, the Sentinel-1 (VH only) images were resampled to 100 m to match the PROBA-V's resolution.

The total number of images of PROBA-V and Sentinel-1 processed from 1 January 2017 to 23 July 2018 were 598 and 132 images, respectively. All the PROBA-V and Sentinel-1 processed images were masked with existing rice field maps from the official Indonesian Ministry of Agriculture, which come from high-resolution images obtained in 2010. The masking process was carried out to ensure that only rice fields remained within the image.

5.2.4 Local statistics

The agriculture agencies at the regency level have been collecting rice statistics, including planting area, harvesting area, and productivity for each month at the sub-district level since the 1980s. The planting and harvesting data are from farmer-provided information to the local agriculture statistics group. The collated data report would be sent to the agricultural division at the regency, province, and national level for the Indonesian Central Bureau of Statistics and the Indonesia Ministry of Agriculture.

The overall statistics of rice planting and harvested area are illustrated in Figure 5.3. The highest rice planting area between January 2017 to July 2018 was 94,428 ha in December 2017, and the harvested area was 76,300 ha in March 2018 for all three regencies (K. I. Dinas Pertanian, 2018; K. K. Dinas Pertanian, 2018; K. S. Dinas Pertanian, 2018).

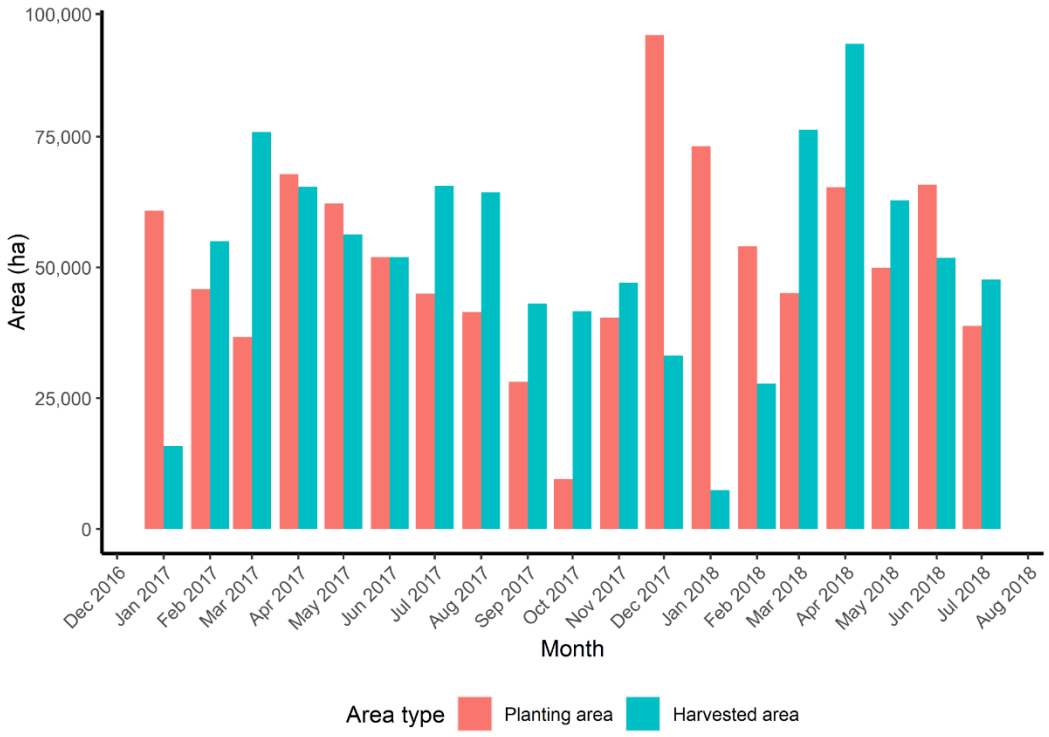

Figure 5.3 The fluctuations between the rice planting and rice harvested area on Karawang, Subang, and Indramayu Regency from January 2017 to July 2018.

5.3 Methods

There are four steps to find the cross-correlation between rice growth stages and rice planting and harvested areas. The first step was collecting data from the field campaign to

generate the ground-truthing dataset. The second step is to build a statistical learning model to classify rice growth stages using images from PROBA-V and Sentinel-1 and ground-truthing datasets. In the third step, the time-series rice growth stages prediction maps were generated, and sub-district level maps were calculated. The last step was to calculate cross-correlation and map the correlation value to each sub-district to generate a correlated and lag-day distribution map, as shown in Figure 5.4.

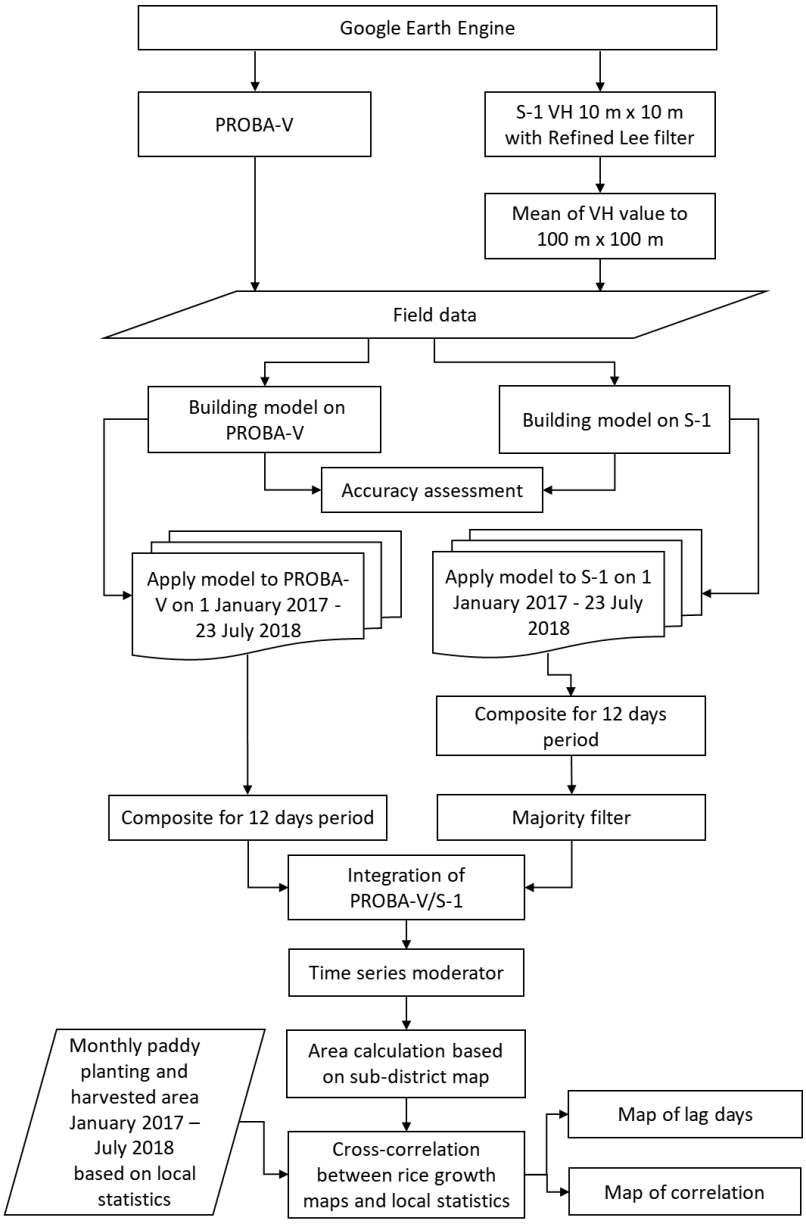

Figure 5.4 The workflow of methodology for rice growth stages mapping using PROBA-V and Sentinel-1.

5.3.1 Data sampling

The purposive random sampling was undertaken during a field campaign based on rice field area from Indonesia Ministry of Agriculture from 4 July to 31 July 2018, yielding 316 points. The surveyor visited the designated points to take field photos and record the rice field surface conditions such as land preparation, bare land, flooding, vegetative, reproductive, ripening, or harvested using a GPS-enabled smartphone. The designated points should be uniform and wide enough to represent the distribution of the area for reducing the mixed pixel effect (Pi-Fuei et al., 2001). An example of a field survey under various conditions is shown in Figure 5.5.

Figure 5.5 The examples of rice conditions in the field campaign.

5.3.2 Building classification models

The resulting data from the field surveys were labelled into four classes: bare land, vegetative, reproductive, and ripening, and then synchronized with the PROBA-V and Sentinel-1 dataset to the closest date. Thus, the dataset was used to build a prediction model using a machine learning classifier with the *caret* package in the R statistical program (Kuhn, 2008; Team, 2017) with leave-one-out cross-validation (LOOCV). The total dataset was divided into training (70%) and test (30%) datasets for building a training model and testing, respectively. Here, we used the Support Vector Machine (SVM) with the radial basis function kernel (SVM-RBF) classifier, which is one of the most used classifiers for solving multi-class problems developed by Vapnik (Cortes & Vapnik, 1995; Guyon et al., 1992) and suitable for this application due to its flexibility of high variability and complex dataset (Onojeghuo et al., 2018; Son et al., 2017). Additionally, Griffiths et al. (2010) suggested that SVM have high accuracy when used with a small dataset. Moreover, the previous study shows that SVM has better performance than the neural network and random forest classifier (Ramadhani et al., 2020b). It could be used to create the automatization of rice growth stages map (Ramadhani et al., 2020a). The SVM-RBF has

two hyperparameters to increase separability between classes: Cost and Gamma, which need to be found using a grid search with initial values.

A classification model was built using the five predictors of PROBA-V bands with 223 points as a training dataset and 93 points as the test dataset. Another classification model was built using time series Sentinel-1 images. In contrast to the PROBA-V model, S-1 VH1, VH2, and VH3 images were collected from three consecutive dates as predictors to build the S-1 model. The predictor VH1 refers to the sampling date, VH2 is the previous 12-days VH data, and VH3 is the previous 24-days of VH data from the sampling date, respectively. The VH has better sensitivity to detect rice phenology than vertically emitted and vertically receiving (VV) due to cross-polarization having more signal depolarization in the rice canopy with multiple reflections (Nguyen et al., 2016; Son et al., 2017).

5.3.3 Accuracy assessment

The accuracy of PROBA-V and Sentinel-1 models were assessed using the comparison of predicted values from the training dataset and test dataset within pixels using the confusion matrix. The overall accuracy (OA), user's accuracy (UA), producer's accuracy (PA) can be calculated as suggested by Foody (2002).

5.3.4 Integration map of PROBA-V and Sentinel-1, and time series modulator

Initially, rice growth stage maps were generated using PROBA-V, and then cloud pixels were filled with the S-1 prediction map. Consequently, time series maps were generated from the integration of both images. To increase the consistency of time series maps, a time series modulator was applied. The modulator's work is to check whether the current map is consistent with the previous period map and correct it automatically. For example, if the previous map had a bare land class and the current map shows a ripening class, which is not consistent, the current map's value was changed into a bare land class. This modulator also applied with ripening (the previous map)—reproductive class (the current map) and vegetative (the previous map)—ripening class (the current map).

The prediction maps for rice growth stages were overlayed with sub-district maps. The intersect maps were calculated to obtain an area of rice growth stages over a 12-day period for each sub-district (using Geographic Information System software) to compare with the local statistical records.

5.3.5 Cross-correlation

The similarity between rice growth stages and rice planting and harvesting area in time series was calculated using cross-correlation. Cross-correlation allows finding the best correlation and lag days between two-time series data. The time series pair datasets are from the generated rice growth-stage maps (vegetative, reproductive, and ripening) and time series from monthly locally collected statistics (planting area and harvested), as shown in Table 5.1. The lag days information with correlation index shows how strong the relationship between the two classes has the same temporal pattern but at different times.

Table 5.1 The five time-series pair datasets.

#	Pair Name	Time-Series 1	Time-Series 2
1	Vegetative – Planting	Vegetative area based on remote sensing	Planting area based on local statistics
2	Vegetative – Harvested	Vegetative area based on remote sensing	Harvested area based on local statistics
3	Reproductive – Harvested	Reproductive area based on remote sensing	Harvested area based on local statistics
4	Ripening – Harvested	Ripening area based on remote sensing	Harvested area based on local statistics
5	Planting – Harvested	Planting area based on local statistics	Harvested area based on local statistics

The cross-correlation (r) on five pair datasets can be calculated as follows (Holmes & Ward, 2019):

$$r_k^{xy} = \frac{\frac{1}{n}\sum_{t=1}^{n-k}(y_t - \bar{y})(x_{t+k} - \bar{x})}{\sqrt{SD_x SD_y}} \quad (1)$$

where r_k^{xy} = cross-correlation coefficient for a k period lag for x and y time series, $\bar{y}$ = mean of y time series, y_t = value of time series y on period t, x_{t-k} = value of time series k periods before period t $\bar{x}$ = mean of x time series, SD_x and SD_y are the standard deviation of the x and y time series, respectively. The p-value with the two-tailed test was also calculated using the highest correlation value on a specific range for each pair of time series.

In addition, distribution maps of the correlation and the lag time among sub-districts to show the spatial information were created to understand the spatial distribution. Moreover, the classification of correlation value can be grouped as follows: 1) high ($0.6 < r \leq 1.0$), medium ($0.4 < r \leq 0.59$), and low ($r \leq 0.39$).

5.4 Results

5.4.1 Spectral bands of PROBA-V and VH backscattering

Figure 5.6 (a) illustrates the distribution of surface reflectance of different rice growth stages. The graph shows that bare land and rice growth stages have distinctive spectral features. The bare land is significantly different from rice growth stages in the SWIR region due to its high surface reflectance, while the vegetative stage has lower values. On the other hand, reproductive and ripening phases have overly similar reflectance values.

The backscattering of VH signatures over three consecutive acquisitions show that the vegetative stage has the lowest value (<−22 dB) due to water scattering from wet soil (Liu et al., 2016) (Figure 5.6 (b)). The reproductive stage tends to decrease from −18 to −21 dB, which is the same as the ripening phase but in the higher value range from −16 to −23 dB. Additionally, the bare land has a steady increase in backscattering value from −19 to −16 dB due to less biomass on the ground (Soo Chin et al., 1998). The SAR data show a more significant separation between the reproductive and ripening phases than the optical data.

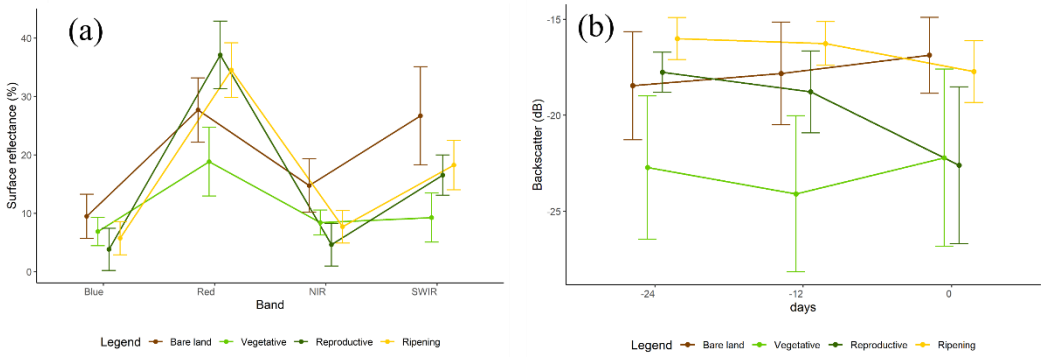

Figure 5.6 (a) Spectral band of PROBA-V related to rice growth stages and (b) backscattering of VH on three consecutive dates.

5.4.2 Accuracy of the machine learning model

Table 5.2 shows the accuracy of rice growth stages of the PROBA-V model has higher OA (83.87%) than the Sentinel-1 model (71.74%). The majority of rice growth stages were predicted with high accuracy (>80%), except for the ripening stage with PA (50.00%) for the PROBA-V model. The UA of the ripening class shows the least accuracy than other classes.

On the other hand, the rice growth stages of the Sentinel-1 model shows an acceptable PA and UA (>66%) for all classes except the ripening class. The highest PA was noticed with the bare land (75.00%) and the highest UA with the reproductive stage (80.77%). The vegetative stages are more likely to overlap with bare land due to the limitations of Sentinel-1 detecting the wet soil from land preparation and vegetative stage.

Table 5.2 The confusion matrix performance on the test dataset on PROBA-V and Sentinel-1.

	Rice Condition	**Bare Land**	**Vegetative**	**Reproductive**	**Ripening**	**Sum**	**UA (%)**
			Test data for PROBA-V with five predictors				
Predicted data	Bare land	26	0	2	2	30	86.67
	Vegetative	2	19	0	1	22	86.36
	Reproductive	0	2	26	4	32	81.25
	Ripening	1	0	1	7	9	77.78
	Sum	29	21	29	14	93	
	PA (%)	89.67	90.61	89.67	50.00		
	OA (%)	83.87					
			Test data for Sentinel-1 with three predictors				
Predicted data	Bare land	21	6	2	2	31	67.74
	Vegetative	1	14	3	0	18	77.78
	Reproductive	2	1	21	2	26	80.77
	Ripening	4	0	3	10	17	58.82
	Sum	28	21	29	14	92	
	PA (%)	75.00	66.67	72.47	71.43		
	OA (%)	71.74					

Note: PA = Producer's accuracy, UA = User's accuracy, and OA = Overall accuracy.

5.4.3 Rice growth stages maps from the integration of PROBA-V and Sentinel-1

Figure 5.7 displays the predicted maps of different rice growth stages using PROBA-V alone and Sentinel-1 alone and the integration of both sensors data. The imaging dates are 5–16 August, 17–28 August, and 29 August–9 September 2017. The PROBA-V in 5–16 August 2017 is affected by cloud cover. Thus, the rice growth stage map of Sentinel-1 can be used to fill the gap (Figure 5.7). The Sentinel-1 based maps have a high similarity of PROBA-V on 17–28 August 2017, which show the prediction model can estimate the rice growth stages with acceptable accuracy. However, the downside of the Sentinel-1 rice growth stage map is less sensitive to the ripening phase (Figure 5.S4, *See Supplementary material section*). Nonetheless, the integration of two satellites data can significantly improve data continuity of the rice growth stages every 12-days (more maps are available on Supplementary material (Figures 5.S1–5.S16)).

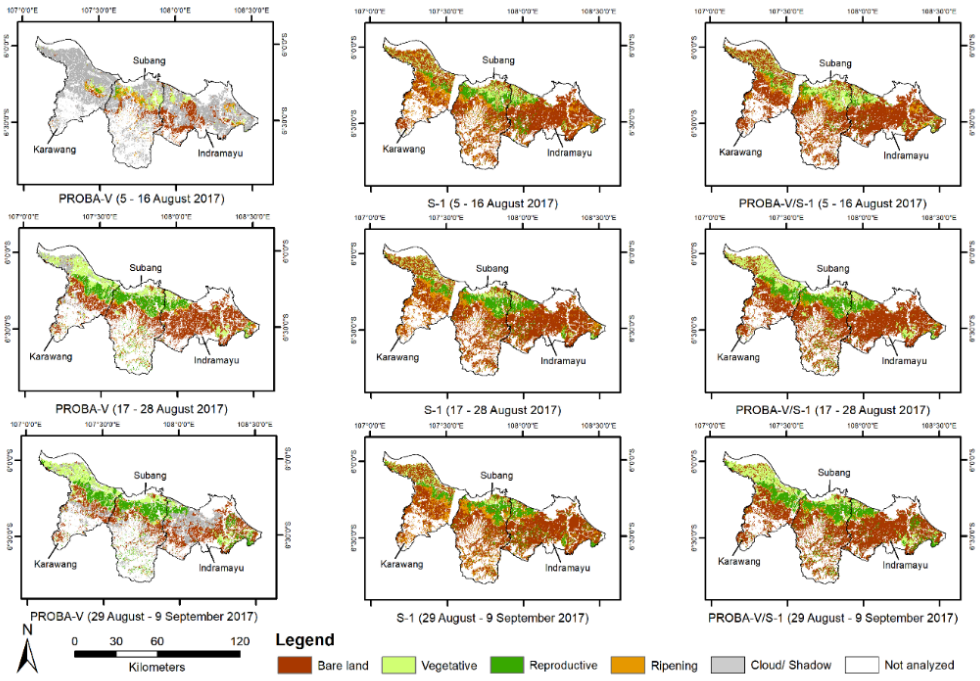

Figure 5.7 Example of integration PROBA-V and Sentinel-1 image on 5–16 August 2017, 17–28 August, and 29 August–9 September 2017.

5.4.4 Time-series rice growth stages area

Figure 5.8 shows the temporal pattern of the rice growth stage area predicted from remote sensing images. In the Indramayu Regency, the bare land area increased steadily until April

2017 and then decreased. The second planting time was also captured in April–May 2017 as the vegetative stages area increased on Indramayu and Subang Regency. Conversely, the Karawang Regency had a different peak of planting time in July 2017 (Figure 5.8). The harvested area in the three regencies also fluctuates and is lower than the vegetative area, except for Indramayu on April–May 2018.

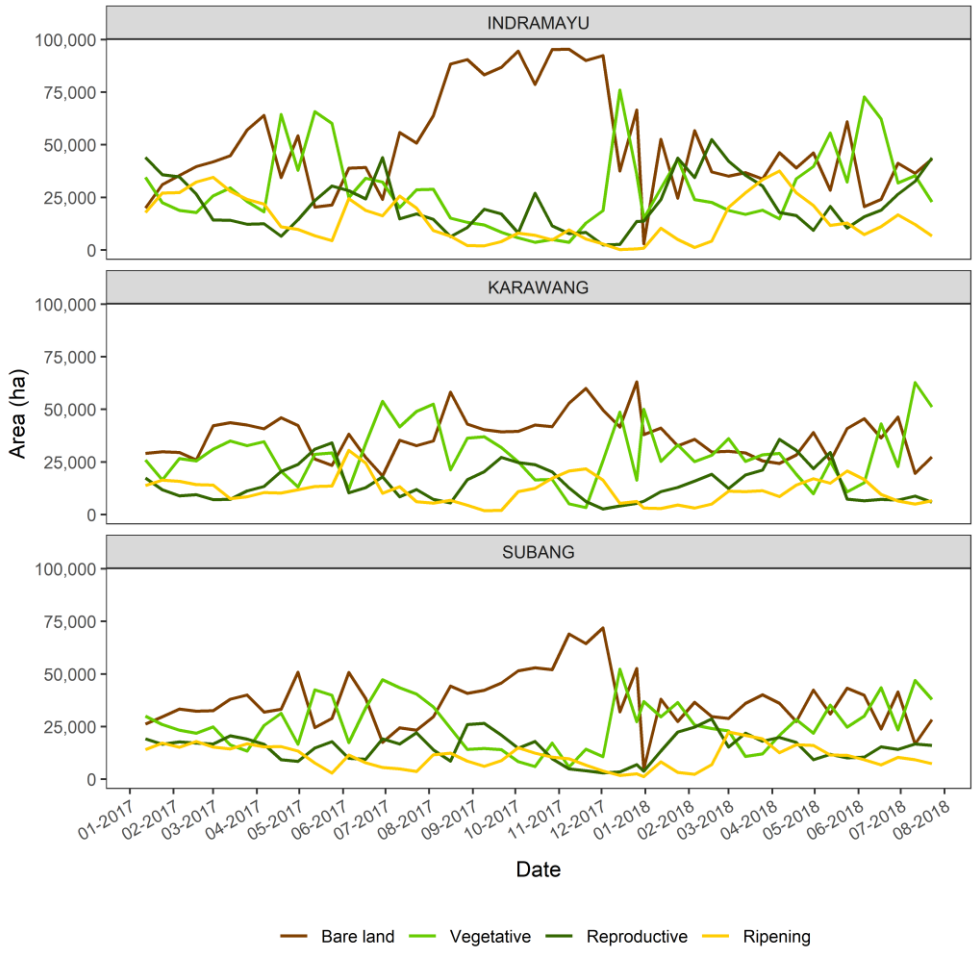

Figure 5.8 The temporal area of rice growth stages for Indramayu, Karawang, and Subang Regency from 1 January–23 July 2017.

Figure 5.9 shows the planting and harvested area calculated from local statistics and remote sensing data (vegetative and ripening regions). The temporal trend was closely aligned with both methods. However, remote sensing data overestimated the vegetative area, which was almost double the actual rice planting area. This phenomenon is due to double counting of the vegetative stage from flooding to maximum tillering, lasting for four months. The ripening phase also has a similarity of paddy harvested area in three regencies in February

2017, August 2017, March 2018, and May 2018. However, it has less area than the paddy harvested area due to the ripening stage during the last 30 days.

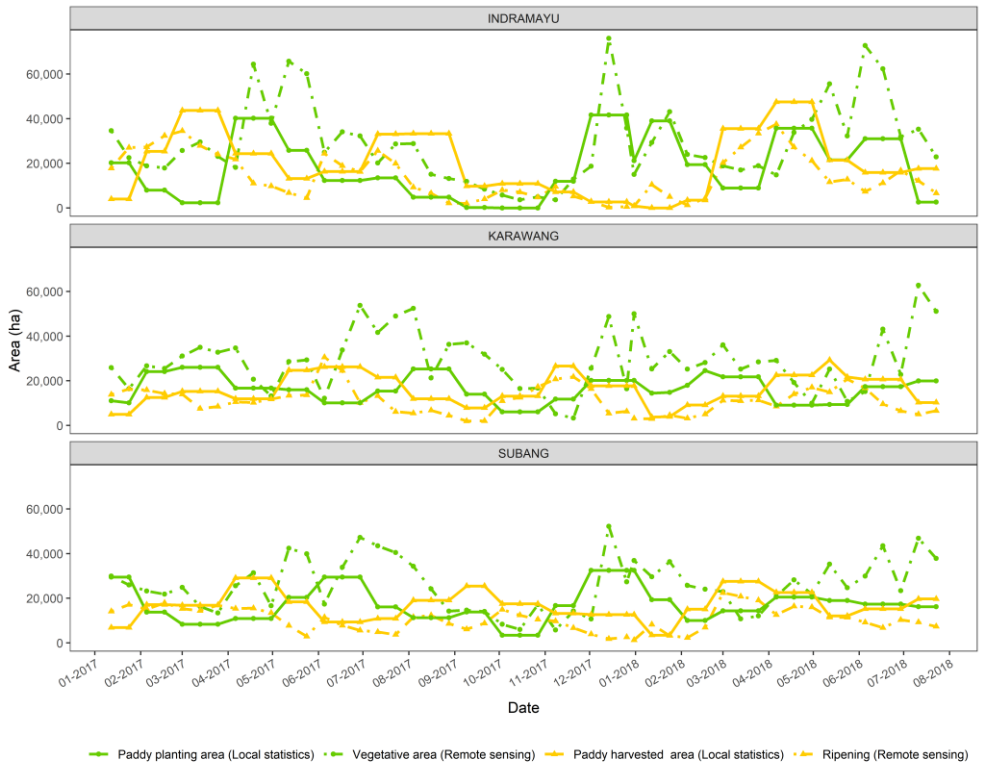

Figure 5.9 The comparison of temporal rice growth stages (vegetative and ripening) with local statistics (planting and harvested area) for Indramayu, Karawang, and Subang Regency from 1 January 2017–23 July 2018.

Figure 5.10 compares rice growth stages in temporal at the six sub-districts with >7000 ha. It shows that every sub-district has its unique temporal data, but some sub-districts had similar trend and cropping patterns, such as Gantar, Kroya, and Terisi in the Indramayu Regency. Those areas had a peak of planting time in April 2017, December 2017, and May 2018. On the other hand, sub-districts in Subang, such as Ciasem and Patokbeusi, had later planting times in February 2017, June 2017, January 2018, and June 2018.

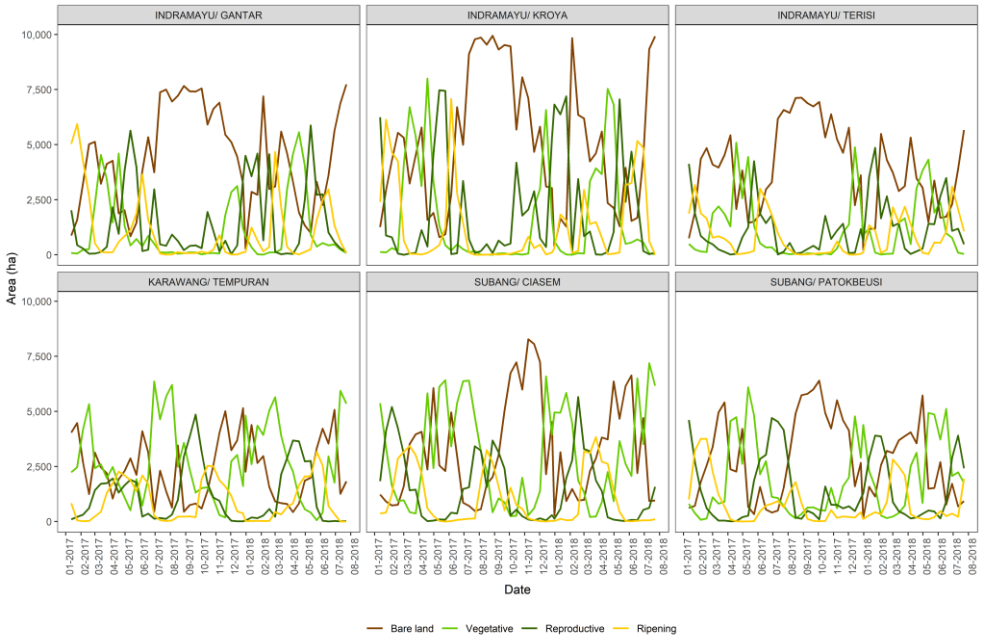

Figure 5.10 The comparison of temporal rice growth stages area for six sub-districts with rice area >7000 ha on Indramayu, Karawang, and Subang Regency from 1 January 2017–23 July 2018.

Figure 5.11 shows the temporal comparison between vegetative and ripening stages and rice planting and harvested area in the sub-districts level. Most of the sub-district indicates that there is a temporal relationship between predicted data and observation data. There was some overlap between the rice planting area and vegetative stage in March–April 2017 on sub-districts such as Gantar, Kroya, and Terisi. Moreover, the vegetative stage peak was higher than the rice planting area, and the ripening stage also less than the rice harvested area such as Ciasem, Subang Regency. More details of each sub-district temporal plots can be seen on https://github.com/FadhlullahRamadhani/Remote-sensed-correlation-statistics/tree/master/Results_PROBA_S1/sd, accessed date: 13 April 2021.

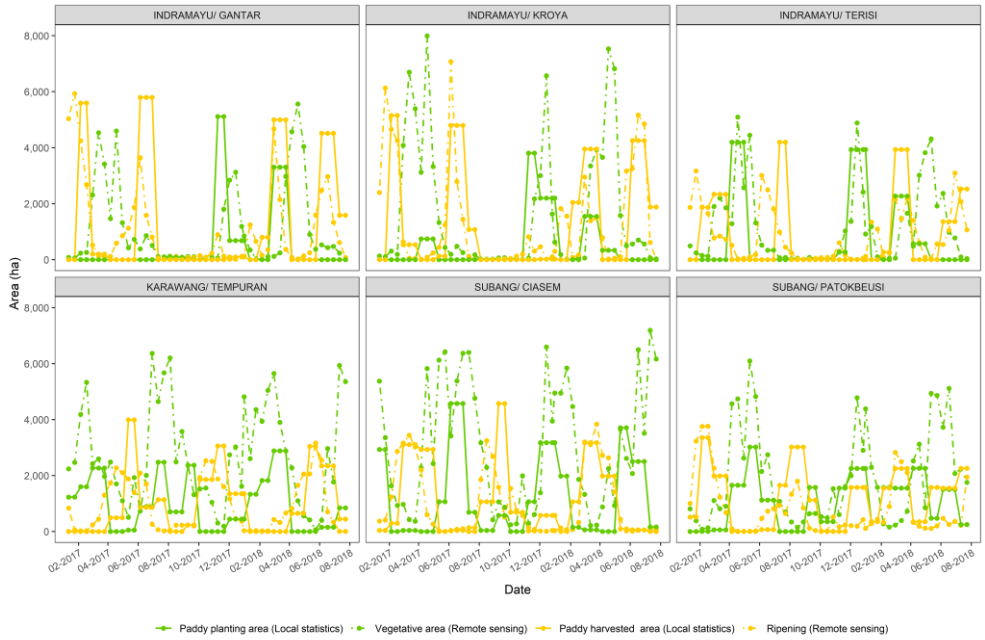

Figure 5.11 The comparison of temporal rice growth stages area (vegetative and ripening) with local statistics area (planting and harvested) for six sub-districts with rice area >7000 ha on Indramayu, Karawang, and Subang Regency from 1 January 2017–23 July 2018.

5.4.5 Results of cross-correlation analysis

Multitemporal rice growth stage maps were compared with local statistics, especially at the sub-districts level ($n = 91$). Figure 5.12 (a) shows the correlation values of predicted values to the local statistics. The paired comparison between rice growth stages have a high correlation (>0.6), and the lag time is similar to rice cultivation time (Figure 5.12 (b)). The vegetative stage area has a 5.27 day lag time with rice planting ($r = 0.52$, $p < 0.01$) and 89.47 day lag time with the harvested area ($r = 0.50$, $p < 0.01$), which is similar to the rice planting area and harvested area (Table 5.S1, *See Supplementary material section*). The correlation between reproductive and harvested area has a medium relationship ($r = 0.57$, $p < 0.01$) and the lag day (44.04 days), also consistent with the rice farming in the study area. However, the lag time for ripening and harvested pair is 12 days ($r = 0.60$, $p < 0.01$), which is less than the 30 days for ripening stages, indicating that the model only predicted half of the period of ripening.

Most of the sub-districts have high correlation values, such as Cikedung, Cilamaya Wetan, and Cipunagara ($r > 0.7$, $p < 0.01$). Nevertheless, some sub-districts have the least correlation value, such as Gantar, Klari, and Cipeundeuy ($r < 0.3$, $p > 0.05$) (Table 5.S1).

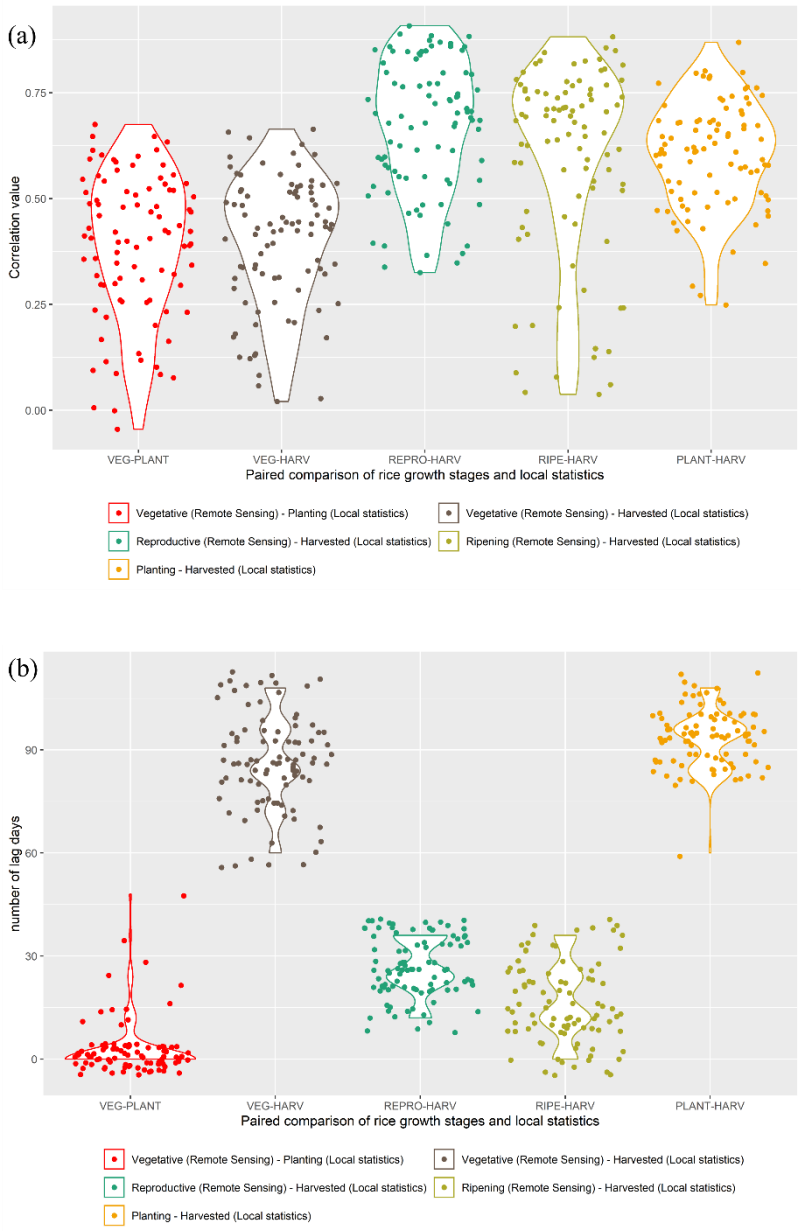

Figure 5.12 The distribution of correlation value (a) and lag (b) from temporal analysis of rice growth stages and local statistics with jitters position.

Figure 5.13 shows the map of the correlation coefficient's distribution in the study area from cross-correlation analysis. It shows that most of the north of the study area has a high to medium correlation for five paired time-series, especially reproductive–harvested and ripening–harvested pairs. Moreover, many sub-districts have more high correlation values on the three pair dataset, such as the reproductive–harvested, ripening–harvested, and planting–harvested dataset. However, the south part of Subang Regency has the lowest

correlation for all comparisons except the planting–harvested stage area, especially Cijambe, Cisalak, Ciater, Kasomalang, Jalancagak, Sagalherang, and Serapanjang sub-district.

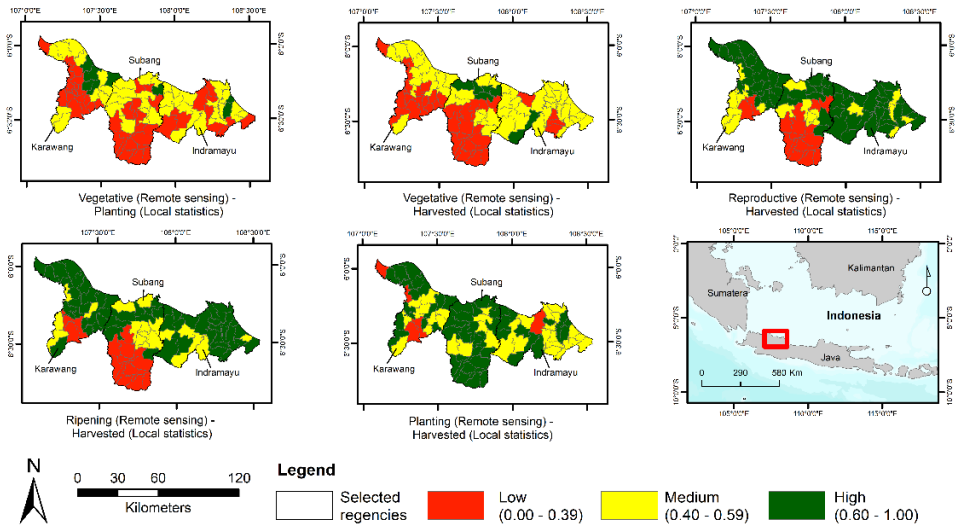

Figure 5.13 Distribution map of correlation value from cross-correlation analysis in sub-district level for Indramayu, Karawang, and Subang Regency.

The distribution map of lag time for three regencies is illustrated in Figure 5.14. The lag time for vegetative–planting is well distributed through three regencies with a lag time of 0–12 days. The distribution of lag days on vegetative–the harvested area is also similar to the distribution of local statistics (96–108 days). Only seven sub-districts are less than 72 days, particularly the Cikampek sub-district.

However, other comparisons have varied lag days, indicating the relationship variability between rice growth stages and local statistics tabulation. For example, the reproductive stage—harvested area pair has a varied lag time (24–60 days), which should be around 45–60 days. Moreover, some inconsistency in lag time (0–12 days) in the reproductive stage—the harvested area should be 24–36 days in 15 subdistricts, mainly located north of Karawang and Subang.

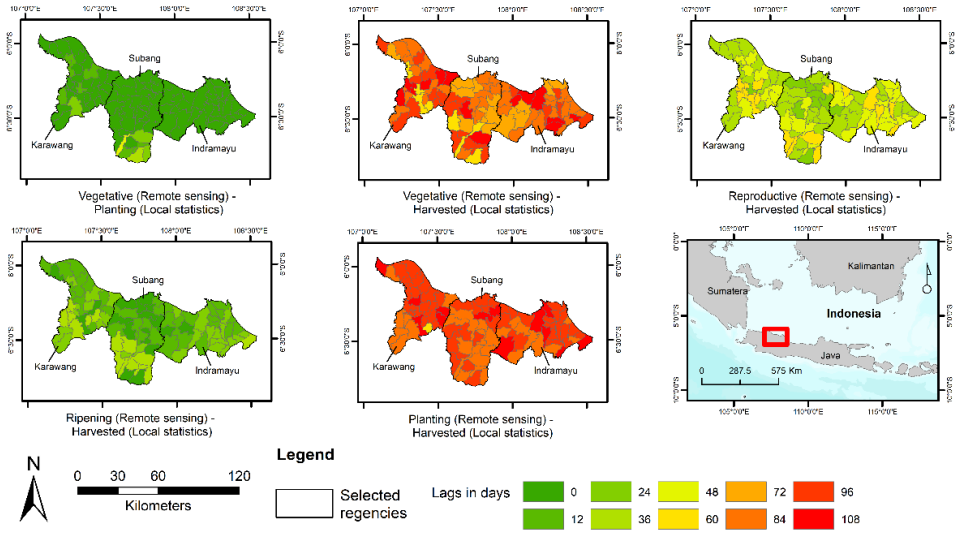

Figure 5.14 Distribution map of lag time from cross-correlation analysis in sub-district level for Indramayu, Karawang, and Subang Regency.

5.5 Discussion

This study has demonstrated the capability to integrate PROBA-V and Sentinel-1 satellite images to produce a cloud-free multitemporal map from 1 July 2017–23 July 2018. The approach was one solution to increase data availability, certainty, and consistency compared with the locally derived statistics. The integration approach between optical and radar sensors has been demonstrated to increase the accuracy and data accessibility in other studies (Ramadhani et al., 2020a; Roy et al., 2019). The radar sensor can generate maps in the wet season when the optical sensor fails to provide the required information. However, the accuracy of the Sentinel-1 model in the dry season is lower than the wet season due to scattering on dry land being indistinct from the vegetative stage, especially in July–August on the north of Subang and Indramayu regencies. Conversely, the PROBA-V model will give a more accurate result on the dry season, which has less cloud.

The results of this study show that the integration of PROBA-V and Sentinel-1 can be one alternative to deliver rice growth stage maps in the near-real-time with high accuracy of each rice growth stage models with cloud-free data, compared with a previous study (Ramadhani et al., 2020b). Figure 5.15 shows the fluctuation of the composition of the integration of two sensors. It illustrates that PROBA-V based maps have >60% in the dry season (April–September), and Sentinel-1's rice growth stages maps are more dominant in

the wet season (January–February, and October–December). The advantage of fusion at the decision level is an easily implemented monitoring system than pixel-level or features-level fusion, which requires pixel co-registration and high memory requirements (Ghassemian, 2016).

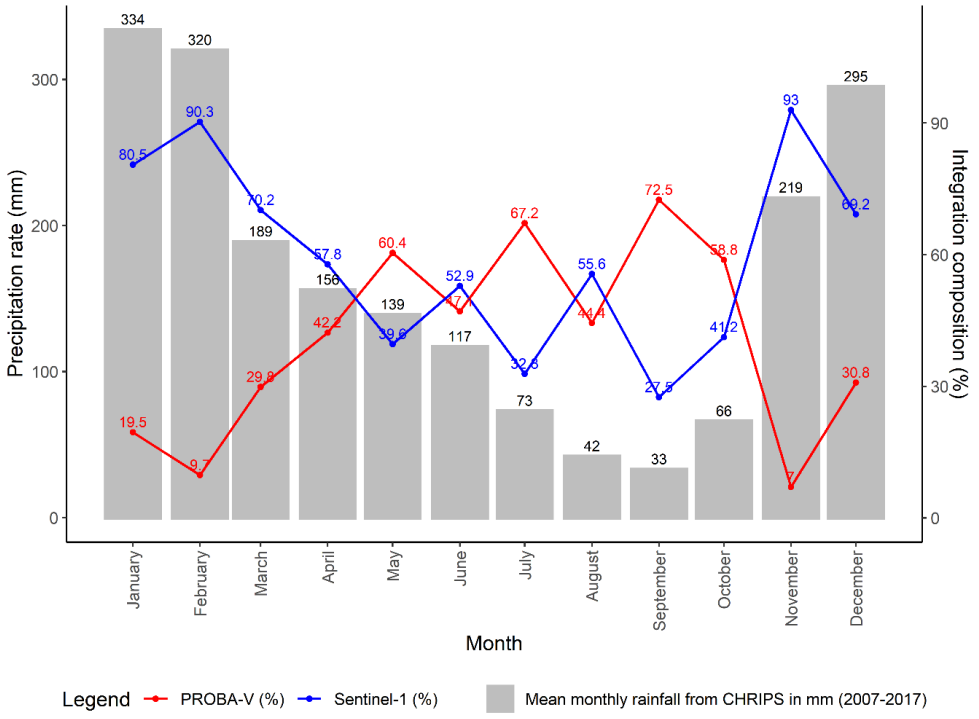

Figure 5.15 The monthly average sensor's composition is based on clear images from 1 January 2017–23 July 2018.

The correlation analysis on the sub-districts level shows a high similarity of the vegetative—harvested area from generated maps with planting—harvested area (Figure 5.12b). Other similarities also applied to vegetative—planting area and reproductive—harvested area. However, the pair of ripening and harvested areas with low similarity may be due to remote sensing maps failing to capture the harvested area in a specific time. The other explanation is that many farmers are still harvested with manual labour, only cutting half of the rice canopy to get the grain rather than all rice stem with a combined harvester, leading to false classification to ripening class in the model.

Moreover, the correlation value distribution map shows that the south of Subang Regency has low correlation values (Figure 5.13). The low correlation between those areas is due to different irrigation schemes with the north Subang Regency based on the ground truth. The

south of Subang Regency is mostly a rainfall-dependent area where the model can have false classification predominantly vegetative with bare land class and ripening to bare land. Moreover, the rice area on those areas is small patches in the valley or hillside where remote sensing is difficult to capture due to interference with other canopies, such as trees on Sentinel-1 and limited pixel resolution PROBA-V.

Nevertheless, our rice growth stage maps are similar to previous studies on the north of West Java island, where rice cultivation season starts from the south of the Indramayu region in September and end on the north of Karawang Regency in February (Rudiyanto et al., 2019). Moreover, Sianturi et al. (2018) investigated that the north of the study area is prone to flood due to sea-level rise every wet season.

Our study can be compared with the work of Rudiyanto et al. (2019) using time-series Sentinel-1 data with the unsupervised method to produce rice area and monthly rice growth stages area in the same study location. The advantage of their work on rice growth stage maps is the ability to distinguish secondary non-rice patterns where our study assumed that all crop cultivation on the area is rice cultivation. However, this proposed method indicates the simplicity of the implementation classification procedure. It can be used for the near-real-time application due to high accuracy in two rice growth stage models where their work depends on local knowledge expertise. The temporal resolution of our study is 12-days, representing a significant improvement compared to Rudiyanto et al. (2019), which have a monthly period. A shorter period is preferred by stakeholders as the rice cultivation period is a short duration farming, and where the change of rice growth stages is imminent and easy to verify, it can also be complemented with crop modeling to produce rice production estimation (Arumugam et al., 2020).

The overall result of the present work shows that a 100 m spatial and 12-day temporal resolution period can be one of the methods for filling the data gap with other information that has been available from MODIS (250 m, 16 days revisited time), Landsat-8 OLI (30 m, 16 days revisited time), and Sentinel-2 (10 m, five days revisited time). The three mentioned methods have difficulties compared with the existing local statistics data due to cloud interference in temporal space.

This study proved that remote sensing data obtained from multiple platforms could have a beneficial impact on the prediction model accuracies (Table 5.2). Therefore, it can be

integrated into rice growth stage mapping efforts from regional to country scales. Our methodology can be evaluated and deployed elsewhere, with other crops using new training and test datasets. The source code can be viewed on https://github.com/FadhlullahRamadhani/Remote-sensed-correlation-statistics, accessed date: 01 April 2021. Additionally, the machine learning classifier can be changed to deep learning classifiers where previous studies may increase the accuracy and the speed of image processing (Cao et al., 2020; Y. Chen et al., 2017; Ndikumana, Minh, et al., 2018; Zhu et al., 2020).

Despite the positive result of this study, some limitations need to be acknowledged in the future. The overall accuracy still depends on the capability and size of the ground-truthing data. The classification error could be caused by the presence of mixed pixels, where some regions commonly grow two-three crops at a time. Another limitation is that the official rice field area which we used as the masking area, may not be accurate in some areas, especially in the Karawang Regency, where it has a high land-use change frequency (Franjaya et al., 2017). In the future, this study can be combined with a scene-based classification of rice areas using an area sampling framework to increase the accuracy of the machine learning model, thus increasing the consistency over time (Gandharum et al., 2021). Furthermore, the climate can shift the cropping pattern to some extent where the farmer is unable to cultivate rice in a few years, especially in the strong El-Nino season (Surmaini et al., 2015).

5.6 Conclusions

The rice production stakeholders for the public and private sectors need accurate information to provide supply and trade information efficiently. In this paper, we have developed a cloud-free method of mapping rice growth stages with a spatial resolution of 100 m and a 12-day periodic time with a high correlation with local statistics, making the outputs more likely to be utilized by the agriculture stakeholder due to acceptable accuracy. Additionally, this method can be implemented or combined in near-real-time and automatic rice monitoring systems such as S-2 RGS to fill the missing information.

This project was developed to increase the crop information availability of the Indonesian Ministry of agriculture to provide better information for more reliable policy, especially for climate change adaptation and mitigation action planning. In the future, the integration of multiple sensors (MODIS, PROBA-V, Landsat-8 OLI, Sentinel-1, Sentinel-2, or Sentinel-

3) with different resolution data can be applied to provide a cloud-free map for rice production or other crops. Moreover, the application development in the GEE environment is a preferable option due to the free, fast, and less infrastructure needed to download the images, analyses processing, and information dissemination. The future launch of Landsat 9, Sentinel-1 C and D, and freely available satellite data such as Hyperspectral Precursor of the Application Mission (PRISMA) can be used to increase data volume and variety, especially for the countries prone to crop failure due to natural climate variability and extreme weather events.

5.7 Acknowledgements

Indonesia Ministry of Agriculture through the Indonesian Centre for Agri-cultural Land Resources Research and Development (ICALRRD) to provide high resolution of the official rice area on the study area. The authors also acknowledge the local agriculture data from Agriculture Division on Karawang, Subang, and Indramayu, Misnawati for data tabulation, and M. Ronal Koswara for fieldwork.

5.8 Supplementary material

Table 5.S1 The cross-correlation between rice growth stages area (vegetative, reproductive, and ripening) and local statistics (rice planting and harvested area).

No	Sub-district	Area (ha)	Veg – Plant		Veg – Harv		Repro – Harv		Ripe – Harv		Plant – Harv	
			Corr.	Lag	Corr.	Lag	Corr.	Lag	Corr.	Lag	Corr.	Lag
						Indramayu						
1	Anjatan	6,419	0.68**	0	0.66**	84	0.75**	48	0.86**	0	0.61**	90
2	Arahan	1,958	0.58**	0	0.56**	90	0.67**	48	0.79**	12	0.66**	90
3	Balongan	1,085	0.58**	0	0.59**	84	0.62**	48	0.75**	12	0.64**	84
4	Bangodua	3,601	0.69**	0	0.65**	90	0.65**	48	0.77**	0	0.57**	90
5	Bongas	3,831	0.62**	0	0.55**	90	0.81**	48	0.85**	0	0.51**	84
6	Cantigi	697	0.69**	0	0.52**	90	0.55**	36	0.68**	12	0.48*	108
7	Cikedung	4,120	0.76**	0	0.58**	84	0.66**	48	0.52**	12	0.71**	84
8	Gabuswetan	6,241	0.63**	0	0.64**	84	0.68**	36	0.58**	0	0.72**	84
9	Gantar	8,059	0.1	0	0.67**	84	0.64**	36	0.68**	12	0.46*	108

10	Haurgeulis	4,403	0.57**	0	0.64**	84	0.75**	36	0.57**	0	0.68**	84
11	Indramayu	1,711	0.55**	0	0.51**	90	0.66**	48	0.72**	12	0.69**	90
12	Jatibarang	2,609	0.52**	0	0.55**	90	0.61**	48	0.78**	24	0.61**	90
13	Juntinyuat	3,697	0.65**	0	0.53**	84	0.73**	36	0.81**	0	0.57**	90
14	Kandanghaur	5,941	0.64**	0	0.39*	90	0.69**	36	0.72**	0	0.47*	90
15	Karangampel	2,066	0.57**	0	0.63**	90	0.62**	48	0.64**	12	0.59**	90
16	Kedokan Bunder	2,301	0.65**	0	0.54**	90	0.57**	60	0.65**	12	0.45*	84
17	Kertasemaya	2,485	0.35*	0	0.56**	90	0.74**	48	0.72**	12	0.47*	90
18	Krangkeng	4,623	0.47*	0	0.64**	108	0.75**	48	0.72**	12	0.43*	108
19	Kroya	10,064	0.42*	0	0.66**	84	0.67**	36	0.64**	0	0.42*	90
20	Lelea	4,709	0.65**	0	0.61**	90	0.62**	60	0.61**	24	0.49*	108
21	Lohbener	2,479	0.63**	0	0.61**	90	0.68**	48	0.70**	12	0.58**	90
22	Losarang	5,066	0.38*	0	0.62**	108	0.72**	60	0.73**	24	0.35*	108
23	Pasekan	597	0.63**	0	0.48*	90	0.65**	48	0.8**	12	0.54**	90

24	Patrol	2,523	0.6**	0	0.65**	84	0.76**	48	0.77**	12	0.65**	90
25	Sindang	1,381	0.69**	0	0.51**	108	0.65**	48	0.8**	12	0.51**	90
26	Sliyeg	4,607	0.63**	0	0.6**	90	0.75**	48	0.79**	12	0.62**	90
27	Sukagumiwang	2,245	0.51**	0	0.48*	108	0.50**	48	0.64**	12	0.51**	108
28	Sukra	3,351	0.41*	0	0.53**	84	0.77**	48	0.79**	12	0.65**	90
29	Terisi	7,297	0.65**	0	0.71**	84	0.75**	48	0.56**	12	0.73**	84
30	Tukdana	3,692	0.58**	0	0.62**	90	0.65**	48	0.82**	12	0.50**	84
31	Widasari	3,011	0.69**	0	0.55**	90	0.54**	48	0.72**	12	0.56**	90
						Karawang						
32	Banyusari	4,332	0.75**	0	0.66**	90	0.82**	60	0.72**	12	0.58**	108
33	Batujaya	4,881	0.56**	0	0.48*	84	0.82**	36	0.81**	0	0.84**	90
34	Ciampel	1,213	0.37**	0	0.14	84	0.33*	48	0.49*	36	0.29**	84
35	Cibuaya	4,772	0.68**	0	0.55**	90	0.80**	36	0.86**	0	0.79**	90
36	Cikampek	341	0.5**	24	0.55**	108	0.59**	36	0.68**	12	0.44*	60

37	Cilamaya Kulon	5,424	0.73**	12	0.62**	90	0.71**	36	0.81**	0	0.78**	90
38	Cilamaya Wetan	5,031	0.73**	12	0.64**	90	0.75**	48	0.80**	0	0.63**	84
39	Cilebar	5,243	0.7**	0	0.60**	90	0.82**	36	0.81**	0	0.80**	90
40	Jatisari	3,968	0.76**	0	0.61**	90	0.70**	60	0.70**	24	0.47*	108
41	Jayakerta	3,393	0.54**	0	0.43*	90	0.59**	48	0.68**	24	0.74**	90
42	Karawang Barat	2,248	0.59**	12	0.50**	108	0.54**	60	0.72**	12	0.63**	90
43	Karawang Timur	1,358	0.59**	0	0.45*	90	0.55**	48	0.67**	12	0.68**	90
44	Klari	2,509	0.29	0	0.35*	60	0.14	36	0.20	0	0.25	108
45	Kotabaru	1,416	0.71**	0	0.63**	108	0.59**	36	0.73**	12	0.62**	90
46	Kutawaluya	4,440	0.40*	0	0.55**	90	0.54**	48	0.75**	0	0.65**	90
47	Lemahabang	4,034	0.65**	0	0.59**	90	0.59**	36	0.59**	0	0.61**	90
48	Majalaya	2,417	0.64**	12	0.42*	90	0.61**	36	0.66**	12	0.52**	90
49	Pakisjaya	3,013	0.23	0	0.46*	84	0.75**	48	0.79**	12	0.48*	108
50	Pangkalan	3,025	0.6**	0	0.48*	84	0.59**	36	0.48*	12	0.71**	84

51	Pedes	5,342	0.65**	0	0.59**	90	0.68**	36	0.78**	12	0.8**	90
52	Purwasari	1,768	0.62**	0	0.51**	108	0.73**	60	0.78**	24	0.62**	90
53	Rawamerta	3,516	0.48*	12	0.68**	90	0.66**	48	0.79**	12	0.44*	108
54	Rengasdengklok	2,469	0.19	24	0.35*	108	0.47**	36	0.32*	0	0.27	90
55	Talagasari	4,144	0.74**	12	0.63**	108	0.64**	60	0.61**	12	0.50**	90
56	Tegalwaru	1,968	0.69**	0	0.48*	84	0.61**	36	0.71**	24	0.58**	84
57	Telukjambe Barat	2,625	0.31*	0	0.15	90	0.55**	36	0.67**	0	0.62**	84
58	Telukjambe Timur	1,029	0.31*	24	0.26	108	0.48*	60	0.53**	36	0.47*	84
59	Tempuran	7,215	0.66**	24	0.61**	108	0.67**	48	0.76**	12	0.50**	90
60	Tirtajaya	5,061	0.61**	0	0.63**	90	0.79**	48	0.81**	12	0.79**	90
61	Tirtamulya	3,508	0.72**	0	0.63**	108	0.61**	48	0.65**	24	0.58**	90
						Subang						
62	Binong	4,014	0.52**	0	0.31*	72	0.37*	48	0.44*	0	0.59**	84

63	Blanakan	5,234	0.65**	0	0.64**	84	0.66**	24	0.64**	0	0.68**	90
64	Ciasem	8,817	0.54**	0	0.51**	84	0.76**	36	0.82**	0	0.68**	84
65	Ciater	951	0.15	24	0.14	108	0.02**	60	-0.10	36	0.74**	84
66	Cibogo	1,990	0.48*	0	0.56**	72	0.54**	36	0.63**	0	0.61**	84
67	Cijambe	2,316	0.39*	24	0.27	108	0.36*	60	0.16	36	0.76**	84
68	Cikaum	2,723	0.45*	0	0.41*	84	0.52**	48	0.53**	0	0.67**	84
69	Cipeundeuy	1,933	0.13	24	0.20	72	0.24	48	0.04**	36	0.51**	90
70	Cipunagara	5,974	0.73**	0	0.69**	84	0.74**	48	0.57**	12	0.57**	84
71	Cisalak	1,328	0.20	48	0.11	60	0.01	48	-0.07	12	0.66**	90
72	Compreng	5,492	0.21	0	0.41*	84	0.39*	36	0.40*	0	0.69**	90
73	Dawuan	597	0.20	24	0.23	72	0.42*	36	0.20	24	0.74**	90
74	Jalancagak	582	0.39*	24	0.41*	108	0.24	60	0.23	36	0.65**	90
75	Kalijati	2,549	0.57**	12	0.29	108	0.29	48	0.38*	36	0.48*	84
76	Kasomalang	695	0.32*	12	0.27	90	0.39*	48	0.18	36	0.77**	84

77	Legonkulon	2,694	0.58**	0	0.57**	90	0.50**	24	0.65**	0	0.87**	90
78	Pabuaran	5,441	0.64**	0	0.46*	84	0.60**	36	0.66**	12	0.66**	90
79	Pagaden	2,691	0.45*	0	0.51**	72	0.58**	36	0.48*	0	0.76**	84
80	Pagaden Barat	3,151	0.48*	0	0.55**	72	0.39*	36	0.52**	0	0.68**	90
81	Pamanukan	2,127	0.54**	0	0.72**	84	0.65**	36	0.72**	0	0.56**	90
82	Patokbeusi	7,066	0.52**	0	0.47*	84	0.60**	36	0.62**	12	0.72**	84
83	Purwadadi	1,418	0.05**	24	0.1	60	0.22	24	0.07**	24	0.60**	90
84	Pusakajaya	4,529	0.74**	0	0.67**	90	0.72**	60	0.74**	12	0.61**	108
85	Pusakanagara	2,399	0.66**	0	0.56**	90	0.68**	36	0.81**	12	0.80**	90
86	Sagalaherang	939	0.17	0	0.13	84	0.08**	24	0.26	0	0.79**	84
87	Serangpanjang	1,599	0.34*	24	0.15	108	0.16	48	0.11	36	0.76**	90
88	Subang	1,312	-0.01	48	0.21	60	0.03	24	-0.05	24	0.64**	84
89	Sukasari	3,298	0.46*	0	0.71**	84	0.63**	24	0.7**	0	0.7**	90
90	Tambakdahan	5,334	0.52**	0	0.66**	84	0.71**	36	0.73**	0	0.54**	108

91	Tanjungsiang	1,281	0.26	24	0.17	108	0.21	60	0.19	36	0.68**	84
Total/ Average		309,046	0.52**	5.27	0.50**	89.47	0.57**	44.04	0.60**	12.00	0.61**	90.40

Note: Corr = Correlation, Veg = Vegetative stage area (remote sensing), Repro = Reproductive stage area (remote sensing), Ripe = Ripening stage area (remote sensing), Plant = Paddy planting area (local statistics), Harv = Paddy harvested area (local statistics),, unit in Lag is day (s), ** = $p<0.01$ (highly significant) and * = $p<0.05$ (statistically significant)

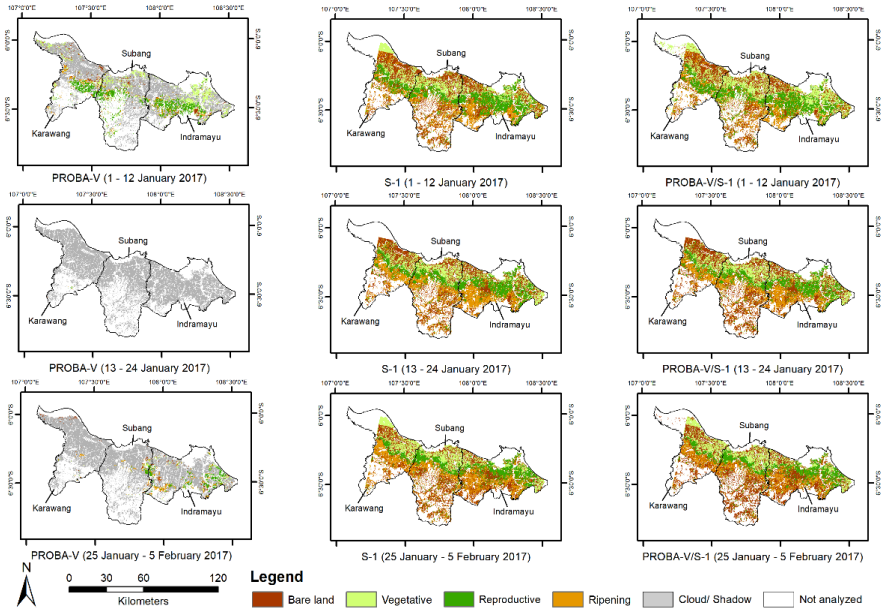

Figure 5.S1 The rice growth stages map from PROBA-V, Sentinel-1, and the integration of PROBA-V and Sentinel-1 on three periods (1 – 12 January 2017, 13 – 24 January 2017, and 25 January – 5 February 2017).

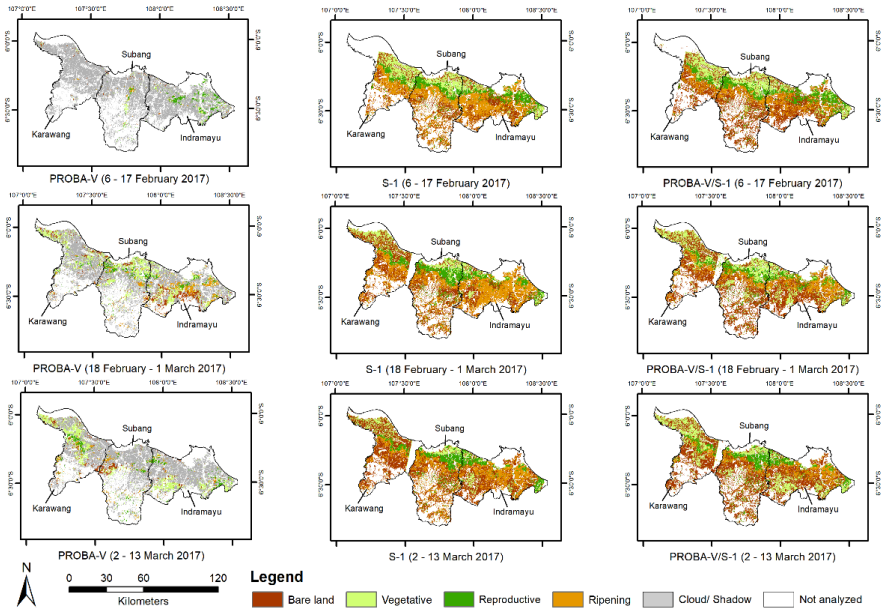

Figure 5.S2 The rice growth stages map from PROBA-V, Sentinel-1, and the integration of PROBA-V and Sentinel -1 on three periods (6 – 17 February 2017, 18 February – 1 March 2017, and 2 – 13 March 2017).

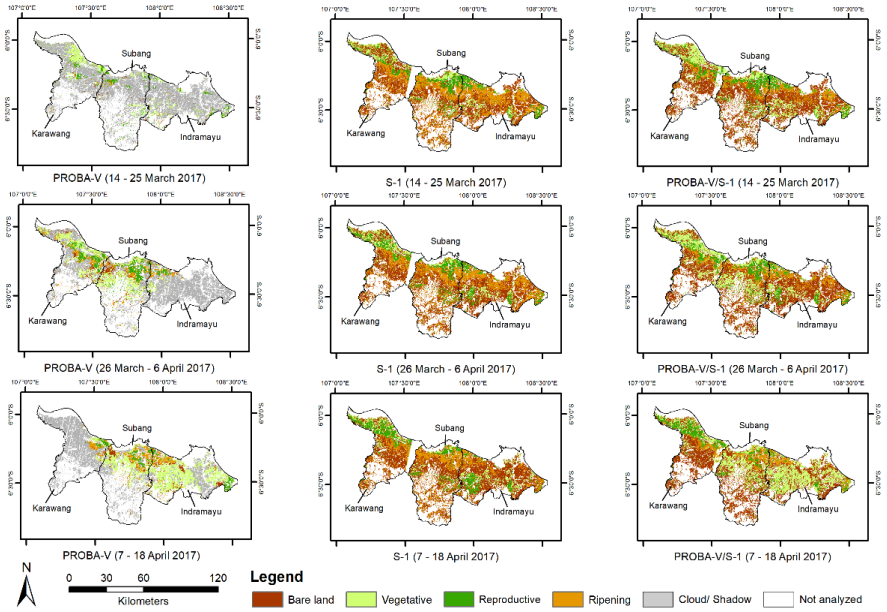

Figure 5.S3 The rice growth stages map from PROBA-V, Sentinel-1, and the integration of PROBA-V and Sentinel -1 on three periods (14 – 25 March 2017, 26 March – 6 April 2017, and 7 – 18 2017)

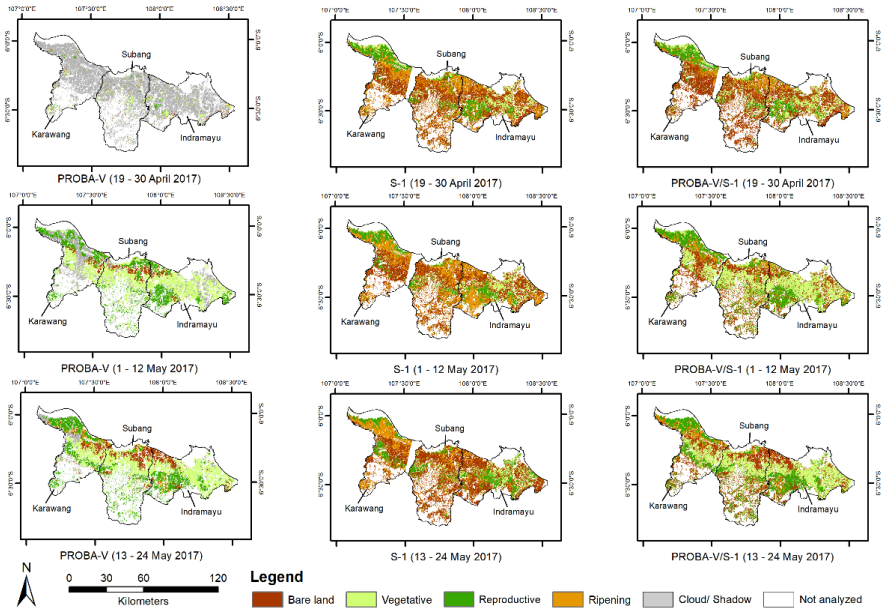

Figure 5.S4 The rice growth stages map from PROBA-V, Sentinel-1, and the integration of PROBA-V and Sentinel -1 on three periods (19 – 30 April 2017, 1 – 12 May 2017, and 13 – 24 May 2017).

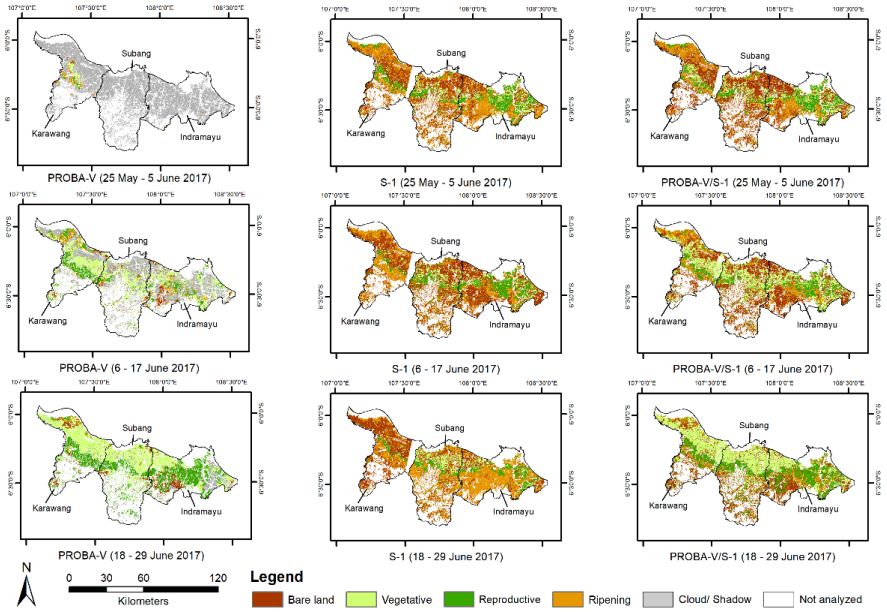

Figure 5.S5 The rice growth stages map from PROBA-V, Sentinel-1, and the integration of PROBA-V and Sentinel -1 on three periods (25 May – 5 June 2017, 6 – 17 June 2017, and 18 – 29 June 2017).

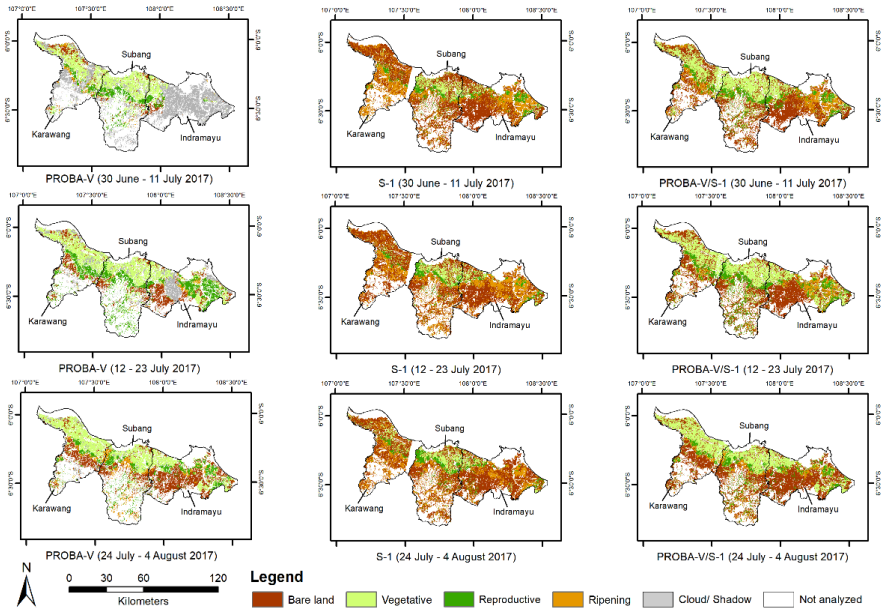

Figure 5.S6 The rice growth stages map from PROBA-V, Sentinel-1, and the integration of PROBA-V and Sentinel -1 on three periods (30 June – 11 July 2017, 12 – 23 July 2017, and 24 July – 4 August 2017).

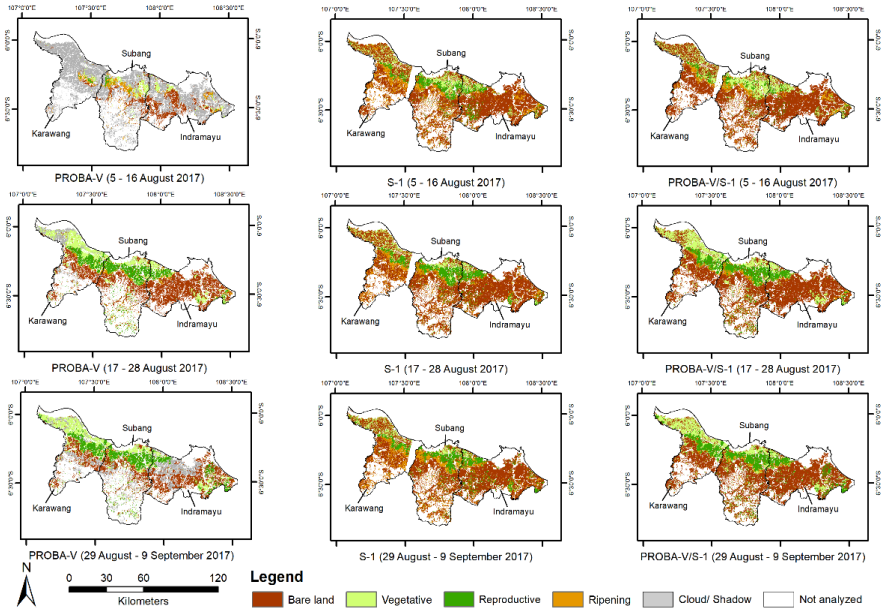

Figure 5.S7 The rice growth stages map from PROBA-V, Sentinel-1, and the integration of PROBA-V and Sentinel -1 on three periods (5 – 16 August 2017, 17 – 28 August 2017, and 29 August – 9 September 2017).

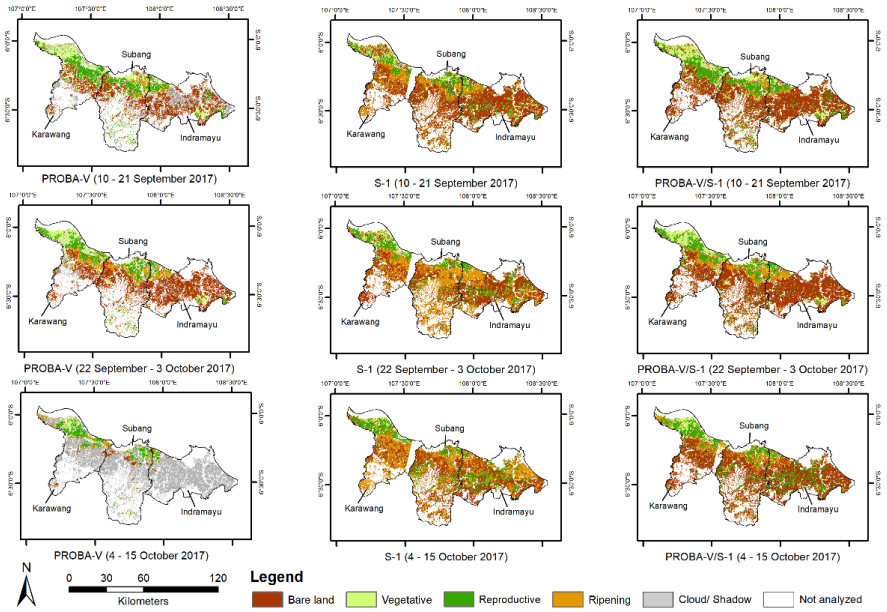

Figure 5.S8 The rice growth stages map from PROBA-V, Sentinel-1, and the integration of PROBA-V and Sentinel-1 on three periods (10 – 21 September 2017, 22 September – 3 October 2017, and 4 – 15 October 2017)

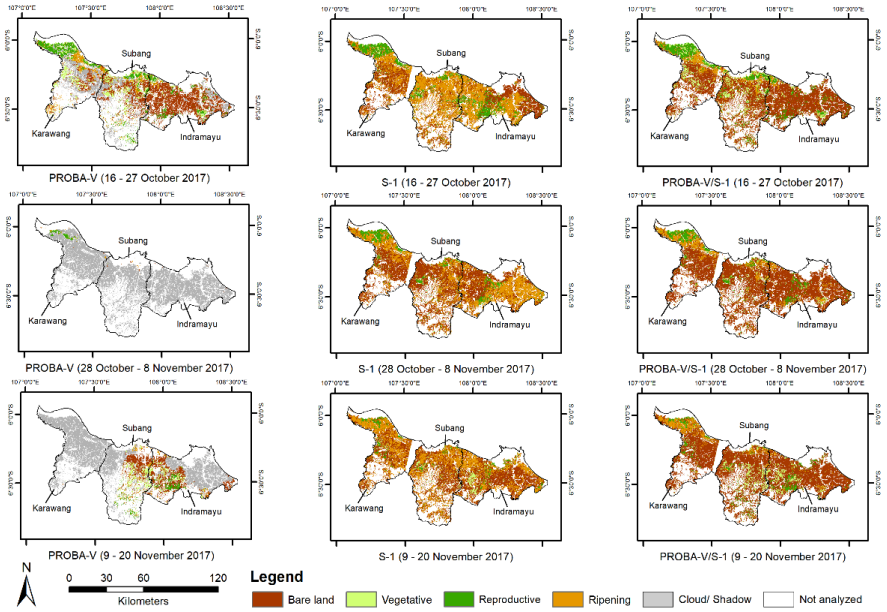

Figure 5.S9 The rice growth stages map from PROBA-V, Sentinel-1, and the integration of PROBA-V and S-1 on three periods (16 – 27 October 2017, 28 October – 8 November 2017, and 9 – 20 November 2017).

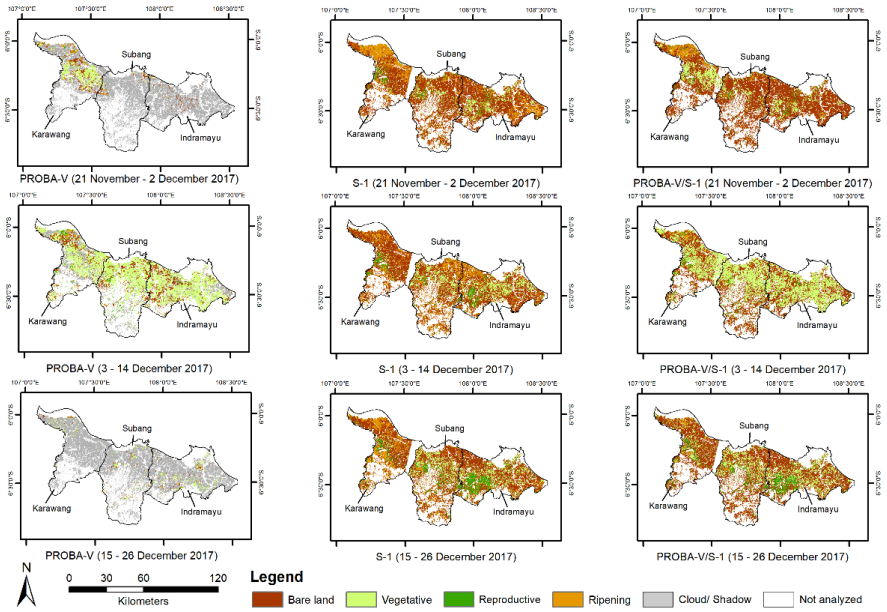

Figure 5.S10 The rice growth stages map from PROBA-V, Sentinel-1, and the integration of PROBA-V and S-1 on three periods (21 November – 2 December 2017, 3 – 14 December 2017, and 15 – 26 December 2017).

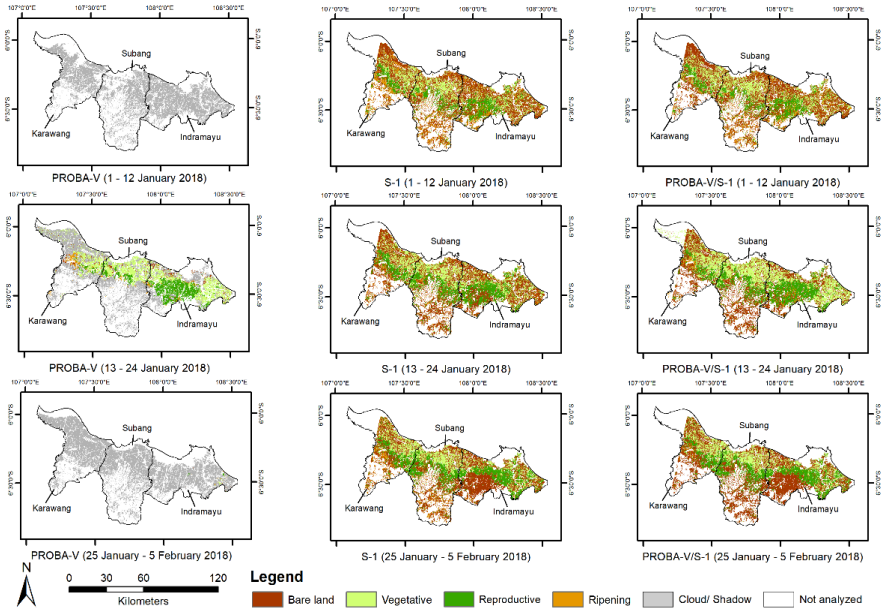

Figure 5.S11 The rice growth stages map from PROBA-V, Sentinel-1, and the integration of PROBA-V and Sentinel -1 on three periods (1 – 12 January 2018, 13 – 24 January 2018, and 25 January – 5 February 2018).

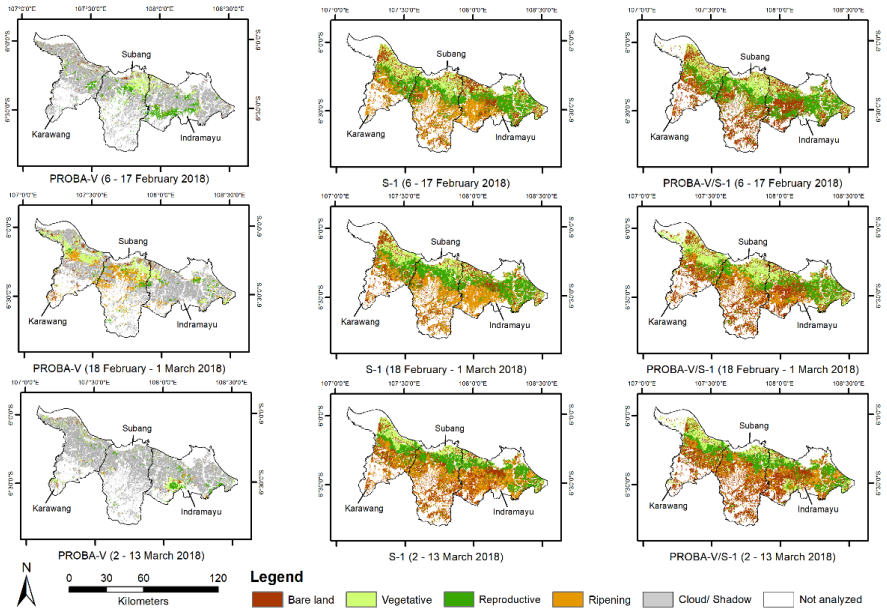

Figure 5.S12 The rice growth stages map from PROBA-V, Sentinel-1, and the integration of PROBA-V and Sentinel -1 on three periods (6 – 17 February 2018, 18 February – 1 March 2018, and 2 – 13 March 2018).

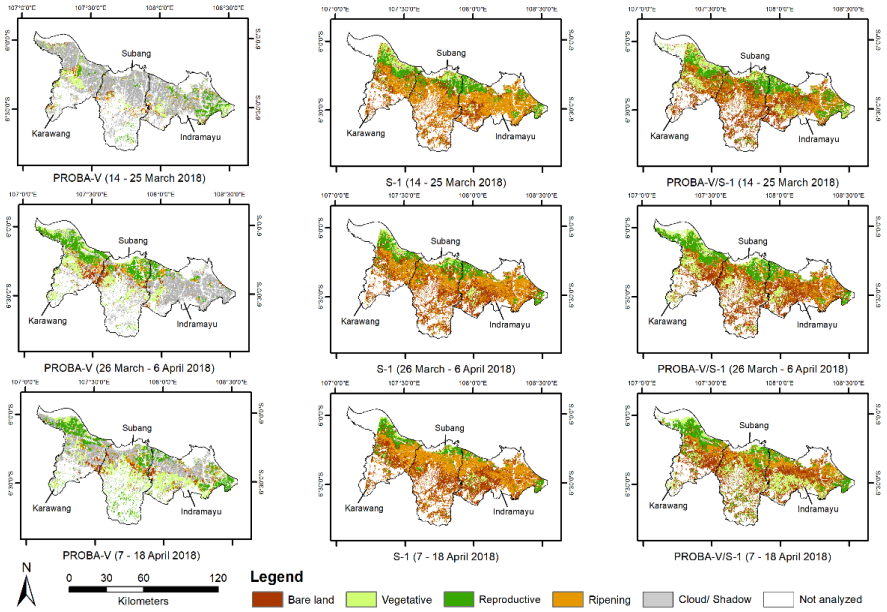

Figure 5.S13 The rice growth stages map from PROBA-V, Sentinel-1, and the integration of PROBA-V and Sentinel -1 on three periods (14 – 15 March 2018, 16 March – 6 April 2018, and 7 – 18 April 2018)

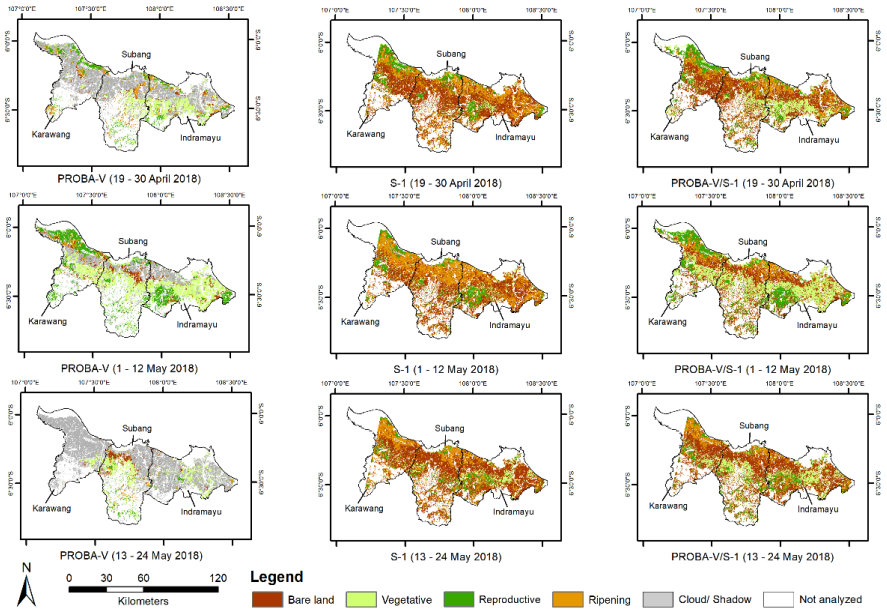

Figure 5.S14 The rice growth stages map from PROBA-V, Sentinel-1, and the integration of PROBA-V and Sentinel -1 on three periods (19 – 30 April 2018, 1 -12 May 2018, and 13 – 24 May 2018).

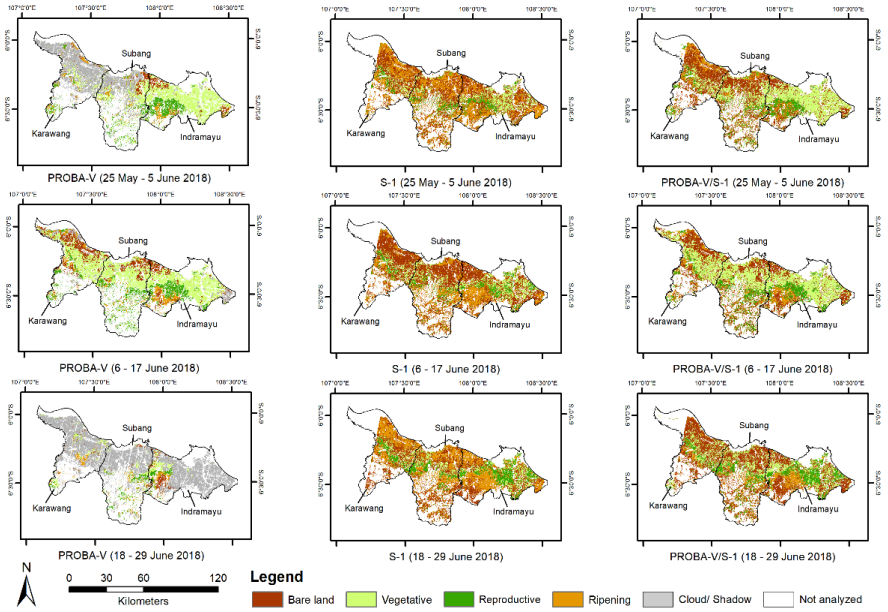

Figure 5.15 The rice growth stages map from PROBA-V, Sentinel-1, and the integration of PROBA-V and Sentinel -1 on three periods (25 May – 5 June 2018, 6 – 17 June 2018, and 18 – 29 June 2018).

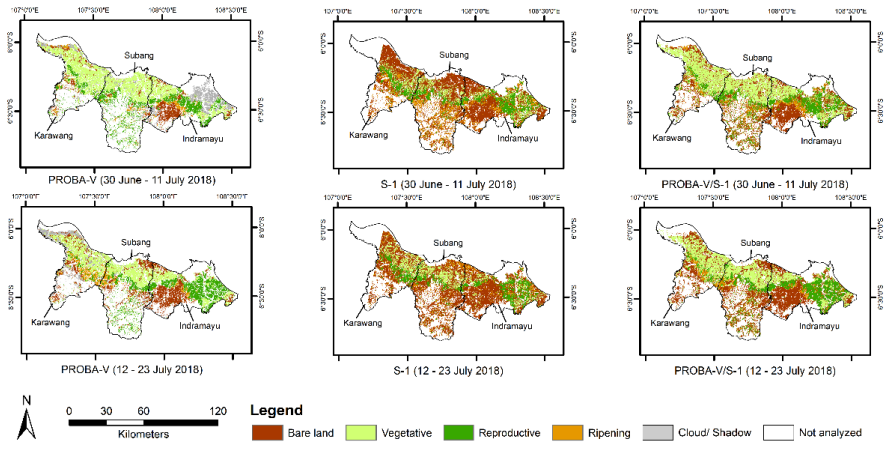

Figure 5.16 The rice growth stages map from PROBA-V, Sentinel-1, and the integration of PROBA-V and Sentinel -1 on two periods (30 June – 11 July 2018, and 12 – 23 July 2018).

Chapter 6 Monitoring rice area and its growth stages on the lowland area in Indonesia using multisource remote sensing data

The objective of chapter 6 is to investigate the use of GEE to determine rice area using multitemporal Sentinel-1 and rice growth stages using Sentinel-2, Landsat-8, MOD13Q1. This chapter is based on a manuscript which will be submitted to a respected publication. Supplementary material and source code can be downloaded on https://github.com/FadhlullahRamadhani/Rice-Growth-Stages-with-Google-Earth-Engine.

Participating authors:

- Fadhlullah Ramadhani: Conceptualization, investigation, data curation, formal analysis, methodology, software, visualization, and writing—original draft preparation
- Reddy Pullanagari: Conceptualization, methodology, supervision, and writing—review and editing,
- Gabor Kereszturi: Conceptualization, methodology, supervision, visualization, and writing—review and editing,
- Jonathan Procter: Supervision, and writing – review & editing

Abstract

Regular monitoring of rice crop using remote sensing technology is important to ensure food security in a sustainable manner under continuous pressure from climate and land cover changes. However, the traditional deployment of rice monitoring systems involves high computation costs to process a large volume of remote sensing data. Google Earth Engine (GEE) is an alternative powerful cloud-based platform made available to researchers to analyse and render remote sensing data. The objective of this study is to explore the capability of GEE to produce rice area and rice growth stage (RGS) maps on Java Island – especially within a lowland area (~2.1 million ha) using three classification algorithms (Random Forest, Classification & Regression Trees, and Support Vector Machine) in 16 days period using Sentinel-1, Sentinel-2, Landsat-8, and MOD13Q1 images. The accuracy was tested at 12 sites from 01 November 2019 to 30 October 2020. Rice area was classified based on multitemporal Sentinel-1 imagery with an accuracy of 82.8% using the random forest method relative to the Indonesian official rice area map. The classification maps for RGS were generated using Random Forest and achieved an accuracy of 76.4% relative to the Indonesian Sentinel-2 RGS monitoring project (S-2 RGS). Combining multiple remote sensing data improved the availability of RGS maps significantly in the wet season (13.6 – 56.9%). This study proved that GEE could be a great tool for developing rice monitoring systems globally. Other countries can utilise it to evaluate rice production and help to predict and minimise hunger from failed production due to climate change-related disasters.

Table of contents for Chapter 6

6.1 Introduction

Rice is an important staple crop in Asian countries as almost three billion consume it daily (FAO, 2020). Since 1970, rice production has dramatically increased due to high-yielding varieties and extensive use of chemical fertilisers (Yanai et al., 2020). Rice production is, however, put under pressure by the growing global population, which is estimated to reach 11.1 billion people in 2050 (FAOSTAT, 2020b), land-use changes (Duro et al., 2020; Schmitz et al., 2014), and climate-related disasters (Schneider & Asch, 2020). The latter is becoming more common and acute at an alarming rate, especially in lowland areas due to increased sea level, coastal flooding, and drought (Redfern et al., 2012; Surmaini et al., 2015). Thus, rice production is an important task that should be monitored closely to avoid food security issues and economic turmoil, especially in developing countries. Some rice monitoring projects have been established in recent years, such as Asia-Rice Crop Estimation & Monitoring (Asia-RiCE) with RADARSAT-2, ALOS, and ALOS-2 SAR data (Oyoshi et al., 2016), Remote Sensing-based Information and Insurance for Crops in Emerging Economies (RIICE) project with COSMO Skymed and TerraSAR-X (Nelson et al., 2014). Both projects relied on synthetic aperture radar (SAR) remote sensing data to overcome the problem of cloud cover and predicted with high accuracies. Nonetheless, the coverage of the project is limited due to the high cost of imagery and limited information of existing RGS in the rice field.

Mapping rice area using satellite images has been developed in recent decades using three types of imagery inputs: a) optical data using MODIS (Li Liu et al., 2020), Landsat (Jin et al., 2016), and Sentinel-2 (Son et al., 2020); b) SAR data COSMO Skymed (Mascolo et al., 2019), TerraSAR-X (Koppe et al., 2013), RADARSAT (Chakraborty & Panigrahy, 2000), ALOS/PALSAR (Wang et al., 2009), and Sentinel-1 (Bazzi et al., 2019); c) the combination of optical and SAR data; Sentinel-1/Landsat-8 (Tian et al., 2018), Sentinel-

1/Sentinel-2 (Fiorillo et al., 2020; Inoue et al., 2020b), and ALOS AVNIR-2/MODIS (Panuju et al., 2021). These studies claimed that accuracy varies depending on the availability of time-series data (70-95%) on a single input source in the country area depending on spatial resolution. The multisource inputs give more results at a regional level with more accuracy (~93%) (Han et al., 2021). However, the rice map area that has been reproduced is not published in the public repository, which causes difficulties investigating more in the rice area, such as rice growth stages, cropping dynamics, carbon accounting, and water management (Peng et al., 2011; Wassmann et al., 2019; G. Zhang et al., 2020).

Mapping rice growth stages (RGS) using vegetation indices from multispectral sensors such as MODIS and Landsat-8 OLI are widely used because of their availability and high sensitivity in discrimination ((LAPAN, 2019; Ramadhani et al., 2020b). Previous studies indicated that high accuracy could be achieved with Sentinel-2 (OA >90%) (Ramadhani et al., 2020a) which was higher than Landsat-8 OLI (OA >73%) (Ramadhani et al., 2020b)). A regular and operational mapping of RGS is required for making timely decisions. However, downloading and analysing the regional/national scale data required intensive resources (e.g. four workstations and two webservers) and relying on a single remote sensing data source compounded by severe cloud coverage in the wet season.

To overcome the problem of cloud cover, SAR data have been used and proved to be accurate with an accuracy of >90% to detect rice area in many countries (Clauss et al., 2018), (Bazzi et al., 2019), (J. Liu et al., 2019), (Mandal et al., 2018), (Nguyen et al., 2016), where it uses the temporal backscatter profiles to assess rice area as it has a different profile than other land uses such as urban (a flat line >-16 dB) or water body (a flat line < -22 dB) (Bazzi et al., 2019; Clauss et al., 2018; Lasko et al., 2018). The rice profiles usually have one or two decreased values in a short period on multitemporal backscattering values, indicating that it was inundated at the start of rice farming. For example, Rudiyanto et al.

(2019) has mapped rice area using Sentinel-1 combined with a semi-supervised K-Means clustering algorithm and achieved high accuracy in Malaysia (98.2%, n=500) (Rudiyanto et al., 2019) and Indonesia (94.8%). Hoang-Phi Phung [29] investigated the potential of time-series Sentinel-1 images to determine rice age where the VH polarization has a high sensitivity to changes in growth stages. However, some challenges remain using the SAR data. For example, difficulties in deploying over large areas due to variable radar incidence angle and more diversity in rice cropping. Moreover, SAR data has less potential to collect detailed information than optical sensors, which leads to misclassification errors.

The combined use of optical and SAR remote sensing data could potentially improve accuracy and minimize the cloud cover problems. Another attempt of mapping RGS without cloud intervention using Sentinel-1 and PROBA-V with 100 m resolution, and the accuracy of these two sources images is 71 and 83%, respectively (Ramadhani et al., 2021).

This study investigates the potential of integrating optical and RADAR data to map rice area and RGS at a regional scale to fill in data gaps and improve monitoring accuracy using the GEE platform. The study aims are 1) to provide accurate RGS maps using multiple sensors in GEE environment, 2) to measure the accuracy of classification on 12 sites and 12 months (23 of 16-days periods), and 3) to build an interactive application that the user can be utilized for evaluating the rice area and RGS map in a temporal perspective.

6.2 Background, study area, data, and classifier

6.2.1 Rice growth stages (RGS)

The rice cultivation period on short varieties is ~120 days which is common in Indonesia. RGS can be divided into three main stages: The vegetative stage (germination to tillering; 45-60 days), the reproductive stage (panicle initiation to flowering; 35 days), and the ripening stage (grain milking to harvest 25-30 days) (Bouman, 2019; Ramadhani et al.,

2020a, 2020b). The rice cultivation in Indonesia mainly uses the transplanting method to ensure the seeds are safe from rodents and easy to maintain in the nursery bed until 25 days after sowing- then transferred to the main field. The examples of RGS can be seen in Figure 6.1.

Figure 6.1 The example of the rice growth stages.

6.2.2 Study area

The study area is located in the lowland area of Java Island, where irrigated rice is the main crop (Figure 6.2). The area has an average elevation of 100 meters above sea level with a slope of less than 10° (Rabus et al., 2003). The main soil type is alluvial and receives an average rainfall of <2,000 mm per year. The rainy season is from October to March and the dry season is between April and September. The lowland area is also classified as a tropical rainforest climate (*Af.*) in Köppen climate classification (Kottek et al., 2006). Due to the monsoonal rainfall type, rice cultivation typically occurs two times, the first crop starts from December, and the second crop starts from February. Some areas close to irrigation lines or big rivers are cultivated three times a year. The complete rice cropping pattern in the sub-district level can be accessed on http://katam.litbang.pertanian.go.id (last accessed 11 October 2020). The main area of rice cultivation is the north of West Java province which has been repeatedly investigated as the study area in remote sensing research due to data availability in the dry season (Gandharum et al., 2021; Ramadhani et al., 2020a, 2020b; Sianturi et al., 2018). The main rice varieties are IR64 related varieties,

such as Ciherang, Inpari, glutinous rice, which have a short growing duration and are easy to maintain due to resistance to brown planthopper and rodent attacks (Triwidodo, 2020).

6.2.3 Satellite imagery

a) Sentinel-1 for rice area detection

The Sentinel-1 mission is a constellation of Sentinel-1 A and B with a C-band synthetic aperture radar with dual-polarization at a 10 m spatial resolution and a revisit time of 6-12 days. The Sentinel-1 GRD has been pre-processed into level 1-A in decibels (dB) using the Sentinel-1 toolbox (Veci et al., 2014). The Sentinel-1 instrument can transmit in vertically transmitted-horizontally received (VH), and vertically transmitted-vertically received (VV) from the ascending and descending orbits on Interferometric Wide Swath mode to classify the rice area as mentioned in many previous studies (Clauss et al., 2018; Inoue et al., 2020a; Lasko et al., 2018; Son et al., 2017). As suggested by Orengo and Petrie (2017), we aggregate the multitemporal backscatter values with the median function. Moreover, the median values were filtered using a morphological median using a 30 m circle kernel to remove the speckle noise. Complete multi-looking images from Sentinel-1 with VH/VV mode in ascending orbit for training area comprised of 109 images and in the descending orbit of 159 images from January 2014 to September 2020. Furthermore, the total images for the whole Java island area were 1,334 for ascending images and 1,410 images for descending orbit between January 2014 and September 2020 (Table 6.1). Furthermore, we used SRTM Digital Elevation from NASA (GEE id: USGS/SRTMGL1_003) with 30 m x 30 m resolution to delineate the area based on its elevation and slope.

Table 6.1 The number of images of Sentinel-1 acquired for detecting rice area on the training area and applied area.

No	Year	Training area		Applied area	
		Ascending	Descending	Ascending	Descending
1	2014	-	3	-	10
2	2015	-	19	-	66
3	2016	-	26	-	96
4	2017	26	30	310	333
5	2018	29	30	380	358
6	2019	31	28	381	333
7	2020	23	23	273	214
#	Total	109	159	1,344	1,410

b) Sentinel-2, Landsat-8 OLI, and MOD13Q1 for RGS extraction

The Sentinel-2 Multispectral Instrument (MSI) with surface reflectance (GEE id: COPERNICUS_S2_SR) is available from 2018, providing 12 bands, covering 443.9 – 2,185.7 nm wavelength spectrum from Sentinel-2A and Sentinel-2B satellites. The bands have four bands with 10 m resolution, six bands with 20 m resolution and two bands with 60 m resolution (Drusch et al., 2012). This dataset has been pre-processed, such as radiometric, geometric, and atmospheric corrections to change Top of Atmosphere reflectance into Bottom of Atmosphere reflectance (Level 2A product) using sen2cor software (Louis et al., 2016). The Level 2A product is the highest ready-to-analysis product in the GEE dataset for the Sentinel-2 processing scheme (ESA, 2015).

The composition of multispectral bands are used to build the RGS predictors are ten bands, as follows: B2, B3, B4, B5, B6, B7, B8, B8A, B11, and B12 as representative of surface reflection of rice conditions which provides better accuracy rather than depend on vegetation indices (Ramadhani et al., 2020a). All spectral bands were resampled to 10 m

spatial resolution. We also used Sentinel-2 cloud probability data (GEE id: COPERNICUS_S2_CLOUD_PROBABILITY) to mask the cloud area using 40% cloud probability images to balance the number of images with accuracy and data availability. The cloud probability was calculated using a cloud detector library with supervised classification. We used 27 images of Sentinel-2 for the training area to build the RGS model on 16 – 29 May 2020, and the Java Island area with a total of 3,963 images from 1 November 2019 to 30 October 2020 (Table 6.2).

Moreover, we also used Landsat-8 OLI surface reflectance (GEE id: LANDSAT_LC08_C01_T1_SR) with 30 m spatial resolution, which has been pre-processed using LaSRC (USGS, 2020) to cover the missing data for Sentinel-2 data. Landsat-8 has been the frontier of high-resolution providers on a global scale since 2013. The legacy of the Landsat mission continues in the Landsat-9 mission, which was launched in September 2021. Total images for training were four images from 17 – 24 May 2020. Moreover, the total images for Landsat-8 to cover Java Island was 4,102 images, with an average for 16 days was 178 images (Table 6.2).

Table 6.2 The number of images of Landsat-8 and Sentinel-2 acquired for analyzing rice growth stages for training and predicting each period.

No	Period	Landsat-8	Sentinel-2
	Training		
#	16 – 29 May 2020	4	27
	Predicted		
1	01 – 16 November 2019	191	168
2	17 November – 02 December 2019	207	165
3	03 – 18 December 2019	178	169
4	19 – 31 December 2019	129	141

5	01 – 16 January 2020	136	175
6	17 January – 01 February 2020	181	168
7	02 – 17 February 2020	175	169
8	18 February – 04 March 2020	191	176
9	05 – 20 March 2020	181	184
10	21 March – 05 April 2020	187	171
11	06 – 21 April 2020	200	176
12	22 April – 07 May 2020	196	166
13	08 – 23 May 2020	192	175
14	24 May – 08 June 2020	190	172
15	09 – 24 June 2020	176	168
16	25 June – 10 July 2020	177	183
17	11 – 26 July 2020	181	177
18	27 July – 11 August 2020	157	171
19	12 – 27 August 2020	189	178
20	28 August – 12 September 2020	181	177
21	13 – 28 September 2020	164	188
22	29 September – 14 October 2020	174	161
23	15 – 30 October 2020	169	161
#	Total	4,106	3,966

Finally, MODIS Terra was used to fill the missing data if the Sentinel-2 and Landsat-8 OLI images were covered with cloud data in a single period. MOD13Q1 is a product from compositing a daily image of MODIS Terra into 16 days period with 250 m spatial resolution (GEE id: MODIS_006_MOD13Q1). The daily acquisition would help increase data availability on RGS. The compositing scheme was the highest value of NDVI/EVI in

each day images of MODIS Terra and most little cloud and low angle (https://lpdaac.usgs.gov/products/mod13q1v006/, accessed on 16 October 2021). The complete specification of all products can be seen in Table 6.3. In this study, two vegetation indices of MODIS Terra bands are also used as predictors besides red, near-infrared (NIR), and blue bands. The two vegetative indices were a product of the reflectance, which is usually used to discriminate the rice cultivation (Pandey et al., 2015), namely NDVI and EVI, which calculated as follows:

$$\mathrm{NDVI}=\frac{\rho_{\mathrm{NIR}} - \rho_{\mathrm{Red}}}{\rho_{\mathrm{NIR}} + \rho_{\mathrm{Red}}}, \quad (1)$$

$$\mathrm{EVI}=2.5 \times \frac{\rho_{\mathrm{NIR}} - \rho_{\mathrm{Red}}}{\rho_{\mathrm{NIR}} + 6 \times \rho_{\mathrm{Red}} - 7.5 \times \rho_{\mathrm{Blue}} + 1} \quad (2)$$

where NIR = near-infrared.

Table 6.3 The specifications of remote sensing data for detecting rice area and rice growth stages (adapted from https://developers.google.com/earth-engine/datasets/catalog/, accessed 16 October 2021).

	The dataset in the Google Earth Engine data catalogue for this study				
Specification	Sentinel-1	MOD13Q1	Landsat-8	Sentinel-2	
Revisited time (days)	6-12	16	15		5-10
Source	ESA	USGS	USGS	ESA	
Constellations	2	1	1		2
Spatial resolution (m)	10	250	30		10-60
Number of bands	2	6	7		10
Details	• Radar: Type C band • Polarization: VH/VV • Orbit type: Ascending and Descending • Instrument mode: Interferometric Wide Swath	Bands: • NDVI • EVI • B1/ Red (645 nm) • B2/ NIR (858 nm) • B3/ Blue (469 nm) • B7/ MIR (2130 nm)	Bands: • B1/ Ultra blue (435-451 nm) • B2/ Blue (452-512 nm) • B3/ Green (533-590 nm) • B4/ Red (636-673 nm) • B5/ NIR (851-879 nm) • B6/ SWIR1 (1,566-1,651 nm) • B7/ SWIR2 (2,107-2,294 nm)	Bands on Sentinel-2A: Spatial resolution 10 m: • B2/ Blue (496.6 nm) • B3/ Green (560 nm) • B4/ Red (664.5 nm) • B8/ NIR (835.1 nm) Spatial resolution 20 m: • B5/ Red Edge 1 (703.9 nm) • B6/ Red Edge 2 (740.2 nm) • B7/ Red Edge 3 (782.5 nm) • B8A/ Red Edge 4 (864.8 nm) • B11/ SWIR 1 (1,613.7 nm) • B12/ SWIR 2 (2,202.4 nm) Spatial resolution 60 m: • B1/ Ultra blue (443.9nm) • B9/ Water vapour (945 nm)	Bands on Sentinel-2B: Spatial resolution 10 m: • B2/ Blue (492.1 nm) • B3/ Green (559 nm) • B4/ Red (665 nm) • B8/ NIR (833 nm) Spatial resolution 20 m: • B5/ Red Edge 1 (703.8 nm) • B6/ Red Edge 2 (729.1 nm) • B7/ Red Edge 3 (779.7 nm) • B8A/ Red Edge 4 (864 nm) • B11/ SWIR 1 (1,610.4 nm) • B12/ SWIR 2 (2,185.7 nm) Spatial resolution 60 m: • B1/ Ultra blue (442.3 nm) • B9/ Water vapour (943.5 nm)

Note: ESA: European Space Agency, USGS: United States Geological Survey, NIR: Near-infrared, MIR: Mid-infrared, and SWIR: Shortwave-infrared

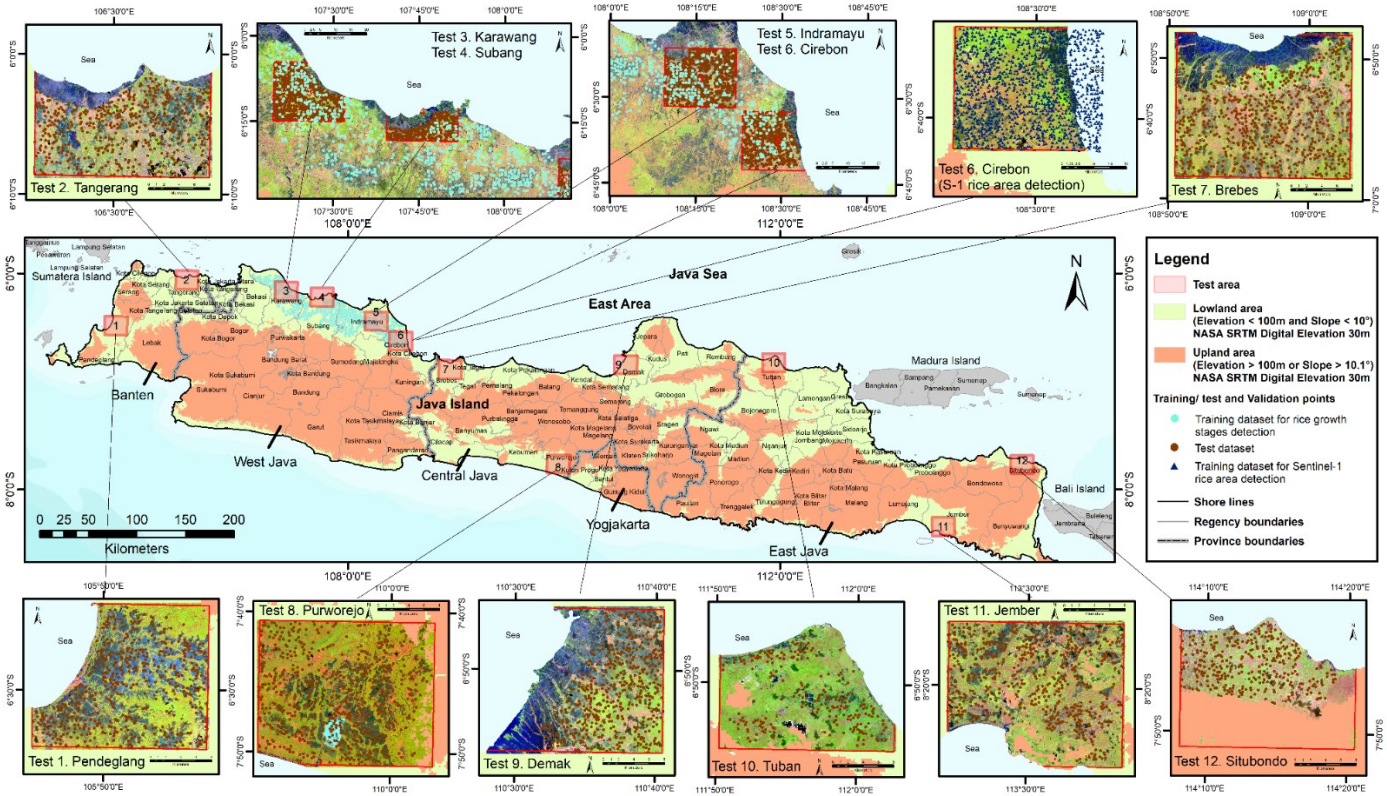

Figure 6.2 Map of the study areas on Java Island, Indonesia. The inset shows the detailed locations of the test areas. The background image of test areas is Sentinel-2 surface reflectance with false colour (SWIR 1, NIR, Green)

6.2.4 Training dataset preparation

The training dataset consists of (1) the rice area training dataset and (2) the RGS training dataset. The rice area training dataset came from Copernicus Global Landcover layers, which provide the global land cover map in 13 classes with 100 m spatial resolution (GEE id: COPERNICUS/Landcover/100m/Proba-V-C3/Global). CGLCL was downloaded from GEE with 100 m resolution (GEE id: COPERNICUS/Landcover/100m/Proba-V-C3/Global) derived from multitemporal PROBA-V from 2015-2019 (version 3.0.1). CGLCL only has one crop layer to describe the map's agricultural activity, which does not distinguish rice or other crops area. Thus, the rice training area was confirmed with the official rice area map from the Indonesian Ministry of Agriculture. Here, we reclassify into three classes which are urban/ built-up (272 points), water (343 points) and cropland on a specific area, the test area number 6 in Cirebon Regency (Figure 6.3) with a total of 1,273 points. The cropland area intersected with the official rice area to increase the accuracy; hence the total training points for the rice area was 658 points.

The training dataset for RGS model was obtained from Sentinel-2 which can be downloaded from http://katam.litbang.pertanian.go.id/SC/ (S-2 RGS) with an accuracy of 70-87% in the Indonesia rice area. We have generated random 640 points to capture the map on the north of West Java Province on 24 May 2020 due to the availability of four classes (bare land, vegetative, reproductive, and ripening) in a single 16-days period (Figure 6.3) with composition bare land (139 points), vegetative (212 points), reproductive (133 points), and ripening (156 points). All training datasets were converted into GEE assets for generating different RGS maps for training points. The spatial resolution input and output image were resampled into 30 m through the whole processing. It is worth noting that the number of training datasets can be increased, but it can lead to memory limitation or time-out issues in the GEE platform.

6.2.5 Classifiers

We have used three classifiers to train the training dataset to become a rice area and RGS classification model. They are Random Forest (RF), Classification And Regression Tree (CART), and Support Vector Machine (SVM). These are commonly used in remote sensing for solving classification problems because they have a high potential to solve complex and nonlinear problems (Bazzi et al., 2019; Son et al., 2017)

RF classifier is an ensemble classification consisting of decision tree classifiers trained individuals from the original training dataset. The output of RF is the majority voting from the output of the trees (Breiman, 2001) and has been appraised in many articles (Belgiu & Drăguţ, 2016; Cutler et al., 2007; Sarica et al., 2017). Previous studies demonstrate that RF is accurate and high performing in a high-dimensional data classifier but sensitive to sampling size (Belgiu & Drăguţ, 2016). The recommended number of trees to be calculated is between five to 128 trees to avoid memory limitation and time-consuming data analysis (Probst & Boulesteix, 2017). Moreover, RF can show the importance of predictor measurement using out-of-bag cross-validation.

CART is a simple classifier that discriminates classes by splitting two child nodes (branch) for each dataset repeatedly until it finds the maximum sensitivity and specificity (recursive partition). CART also has been used to solve classification problems in previous studies (W. Chen et al., 2017; Heung et al., 2016). However, the accuracy is less than RF and SVM, but it uses less memory due to its simplicity (Shao & Lunetta, 2012).

The SVM is one of the kernel-based machine learning approaches to classify different classes by dividing with a hyperplane and assisting with support vectors to maximize the margin between the closest data hyperplane (Cortes & Vapnik, 1995). SVM is also one of the most applied classifiers in previous studies due to its high accuracy in limited training data (Hu et al., 2019; Shelestov et al., 2017; W. Zhang et al., 2020). Our previous study shows that SVM with radial function has the best accuracy to classify the RGS than the neural network (Ramadhani et al., 2020b), thus using the same kernel function in a classification task.

6.3 Methods

Figure 6.3 shows the proposed flowchart for combining four satellite resources into a single model for mapping the rice area and the RGS within a GEE environment. In the workflow, there are four main steps as follows: 1) Rice area detection for all Java Island, 2) RGS monitoring on the detected rice area in 16 days period, and 3) Testing model performance on independent sites. 4) building an interactive application based on the GEE environment which can be quickly published using the internet.

6.3.1 Rice area mapping using multitemporal Sentinel-1 data

In this study, we used a multi-look approach to simplify the classification process in GEE and has been used by (Chini et al., 2018) to classify land use with 92% accuracy. The multi-look method uses the increase of the cross-polarization effect on the rice area where multiple-backscatter bounces in different rice growth stages. The machine learning model of rice area from multitemporal Sentinel-1 backscatter values from 2014 to 2020 with 1,887 images for ascending orbit and 1,431 images for descending one. The machine learning model for the rice area classification can be formulated as follows:

$$Rice\ area\ (Sentinel1) \sim median(VV\ Desc) + median(VV\ Asc) + median(VH\ Desc) + median(VH\ Asc) \quad (3)$$

The final classification of rice area on Java island was masked with SRTM information to delineate the rice area with elevation < 100 m and slope < 10° to mask the lowland rice area only.

6.3.2 Multi-temporal RGS maps using Sentinel-2, Landsat-8 OLI, and MOD13Q1.

The RGS maps from Sentinel-2 analysis were used as the primary source of data. If there were any gaps, they would be filled up with Landsat-8 OLI based prediction maps, and if any other gaps exist, then the MOD13Q1 based prediction maps were used. The RGS maps were highlighted by masking irrelevant information. The model for rice growth stages can be formulated based on three input datasets as follows on specific periods:

- $Rice\ growth\ stages\ (Sentinel2) \sim (B2, B3, B4, B5, B6, B7, B8, B11, B12, B$ (4)
- $Rice\ growth\ stages\ (Landsat8\ OLI) \sim (B1, B2, B3, B4, B5, B6, B7)$ (5)
- $Rice\ growth\ stages\ (MOD13Q1) \sim (NDVI, EVI, B1, B2, B3)$ (6)

The RGS maps were generated from 1 November 2019 to 30 October 2020 every 16 days, with a total of 23 temporal maps were produced.

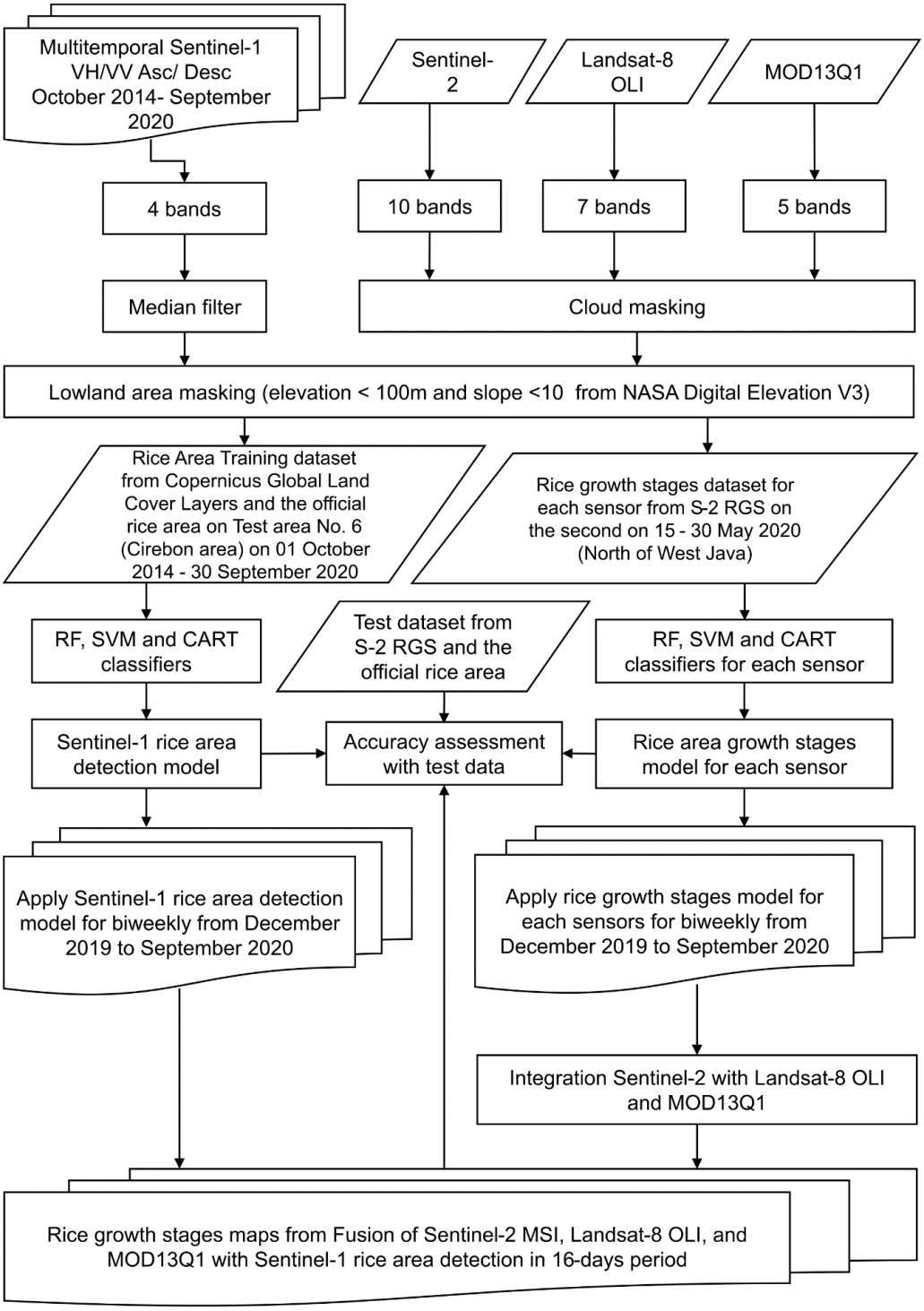

Figure 6.3 The workflow of classifying the rice area and RGS in the GEE environment.

6.3.3 Accuracy assessment

a) Confusion matrix

As shown in Figure 6.3, the performance of prediction maps was assessed on independent test areas, representing the lowland rice area in Java Island. The total rice area for 12 sites is 224,758 ha or 10.4% from a total area of lowland rice area of Java Island (2,156,805 ha) based on the official rice area map from the Indonesia Ministry of Agriculture (MoA, 2019). The rice map was released in December 2019, derived from local maps, high-resolution remote sensing data (SPOT images). Moreover, it has been validated with the Indonesia Ministry of Agrarian Affairs and Spatial Planning (Indonesia Ministry of Agrarian Affairs and Spatial Planning, 2020).

The accuracy of RGS maps was evaluated using a confusion matrix. The confusion matrix was calculated by comparing generated RGS maps with reference maps. These comparisons were conducted every 16 days during a period from November 2019 to October 2020. The original classes in S-2 RGS are five classes: bare land, flooding, vegetative, reproductive, and ripening. The original classes were reclassified as flooding, vegetative, reproductive, and ripening.

From the confusion matrix, the Producer's accuracy (PA), user's accuracy (UA), and overall accuracy (OA) are calculated as follows:

$$PA\ (class\ X) = \frac{\sum\ points\ correctly\ classified\ in\ testing\ data}{\sum points\ on\ \boldsymbol{reference}\ for\ class\ X} x100\% \quad (7)$$

$$UA\ (class\ A) = \frac{\sum\ points\ correctly\ classified\ in\ testing\ data}{\sum points\ on\ \boldsymbol{classified}\ for\ class\ X} x100\% \quad (8)$$

$$OA = \frac{\sum\ points\ correctly\ classified\ for\ all\ class}{\sum points\ for\ all\ class} x100\% \quad (9)$$

Note: PA shows the accuracy of a classifier to classify the class based on the testing dataset, UA shows the accuracy of the classified pixel belonging to a specific class on the testing data, and the OA shows the accuracy of all classes with total testing points. Class *X* is one of rice growth stages such as vegetative, reproductive, ripening, and bare land.

c) Rice area comparison

The rice area was calculated and compared with a reference map at the regency level. Based on official data, the overall lowland rice area is 2,156,805 ha or 62.1% over 3,472,864 ha

of the rice area in Java Island (BPS, 2020). The accuracy of rice area evaluated with correlation coefficient (R^2), root means square root (RMSE) and mean absolute error (MAE) as follows:

$$R^2 = 1 - \frac{\sum (actual\ value - classified\ value)^2}{\sum (actual\ value - mean\ of\ actual\ values)^2} \quad (10)$$

$$RMSE = \sqrt{\sum_{i=1}^{n} (Classified_i - Actual_i)^2} \quad (11)$$

$$MAE = \frac{1}{n} \sum |actual\ value - classified\ value| \quad (12)$$

where n = total number of regencies

Note: Higher R^2 is a better result since the classifier has a similar trend, and lower RMSE and MAE is preferable due to less error in classification.

6.3.4 Building interactive application

We built the rice monitoring application using a straightforward JavaScript programming language to support user-friendly interaction, especially for non-expert users. The flowchart of the application was started from building a machine learning model in a specific period and training dataset. The next step is applying the model to a specific area and time based on user requests. The model creates spatial prediction maps in 16-days periods for four months from the selected current date. There are four map outputs for rendering that display four 16-days period maps, allowing the user to examine rice farming's dynamic growth in certain areas based on user request. The user can change the search period, classifier, and the area.

6.4 Results

6.4.1 Backscattering profiles for extracting rice area

The backscatter values of multitemporal images of Sentinel-1 were used to detect rice areas from other land uses. The distribution backscatter values in different modes corresponding to different RGS are shown in Figure 6.4. The values are clearly separated between three land uses. The backscatter coefficients of urban/ built-up are higher than the rice area, while

the water bodies value is less than the rice area. This pattern comes from multitemporal backscatter values where even all values have fluctuated over the months, backscatter values of rice area are between urban/ built-up and water bodies (Figure 6.S1, *see Supplementary material section*)

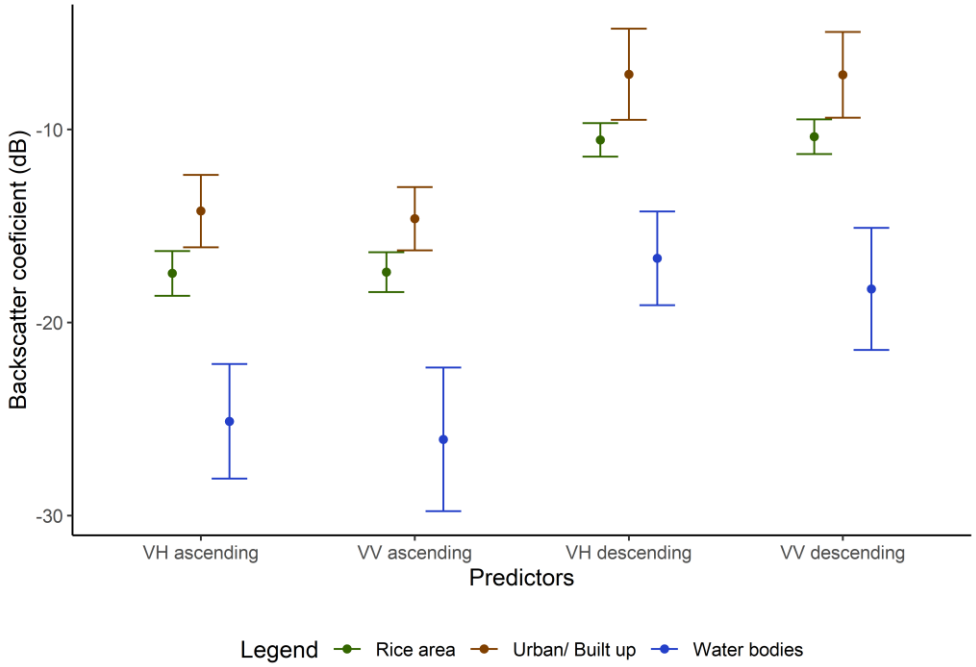

Figure 6.4 The median values of backscatter coefficients from the rice area training dataset between 2014 to 2020. Error bar indicates the standard deviation. The position of points is dodged to avoid overlap points Spectral profiles for extracting RGS.

6.4.2 Spectral profiles for extracting RGS

The mean spectral values of Sentinel-2 images of different RGS are shown in Figure 6(5a). The spectral profile of bare soil is different from the remaining RGS. The vegetative stage has less reflected values than reproductive and ripening stages but is slightly similar to the bare land profile. The apparent differences between vegetative and bare land appeared in the Red Edge 4 band, where bare land reflectance is higher than the vegetative stage. Although the spectral patterns from Landsat-8 OLI's are similar to Sentinel-2 but the RGS are clearly not distinguishable as Sentinel-2 (Figure 6(5b)).

The average spectral profiles of different RGS for MOD13Q1 are illustrated in Figure 5(c and d), where the reproductive stage had the highest values, followed by ripening, bare land, and vegetative stages. However, the bare land and vegetative stage shows have similarities on NDVI and EVI with different deviations.

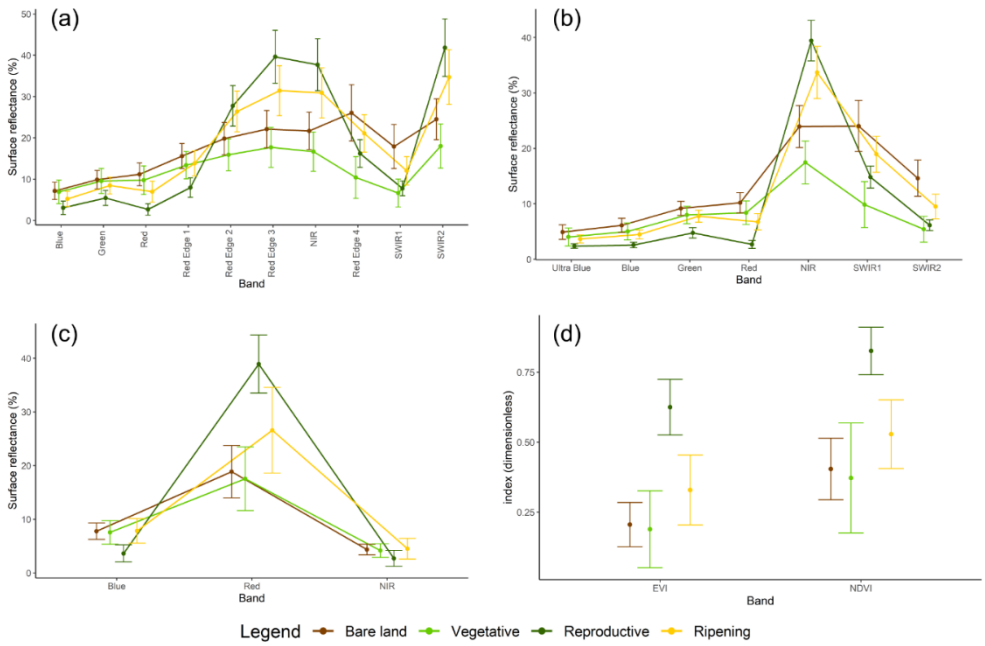

Figure 6.5 The mean values of (a) Sentinel-2, (b) Landsat-8 OLI, and (c and d) MOD13Q1 predictors from the RGS training dataset at 15 – 30 May 2020. NIR= Near-infrared and SWIR= Shortwave-infrared. Error bar indicates the standard deviation. The position of points is dodged to avoid overlap points.

6.4.3 Rice area accuracy

Table 6.4 shows that the highest OA of rice area classification is 84.5%, with SVM as a classifier with the second-best is RF (82.8%) and CART is the least accurate (77.6%). Moreover, PA and UA for all classifiers have high accuracy (>75%) except for urban/ built-up classifications. There is some confusion between rice and urban areas, which may come from the seasonal non-rice cultivation area, especially in the East Java province.

Table 6.4 The accuracy assessment based on the test dataset for the rice area.

Classifier	Rice area		Urban/ built-up		Water		OA (%)
	PA (%)	UA (%)	PA (%)	UA (%)	PA (%)	UA (%)	
Test dataset (*n*= 13,300 points)							
RF	81.3	82.1	74.9	74.3	92.6	92.1	82.8
CART	70.5	80.8	74.2	67.8	91.9	82.8	77.6
SVM	89.6	79.3	73.0	83.3	87.7	95.9	84.5

Note: *n* = number of data, PA = Producer's accuracy, UA = User's accuracy, and OA= Overall accuracy

The test areas chosen for evaluating the model performance are shown in Figure 6.6. Overall, the RF and SVM showed good matching with the official reference map, and CART based model showed the lowest accuracy. With all test sites, the RF and SVM models showed similar performance (Figure 6.S2 and 6.S3). However, test area-12 on Situbondo Regency shows that the rice area from RF and CART is different from the official rice map, except for SVM (Figure 6.S3), because of the presence of secondary crops (Ramadhani et al., 2020a).

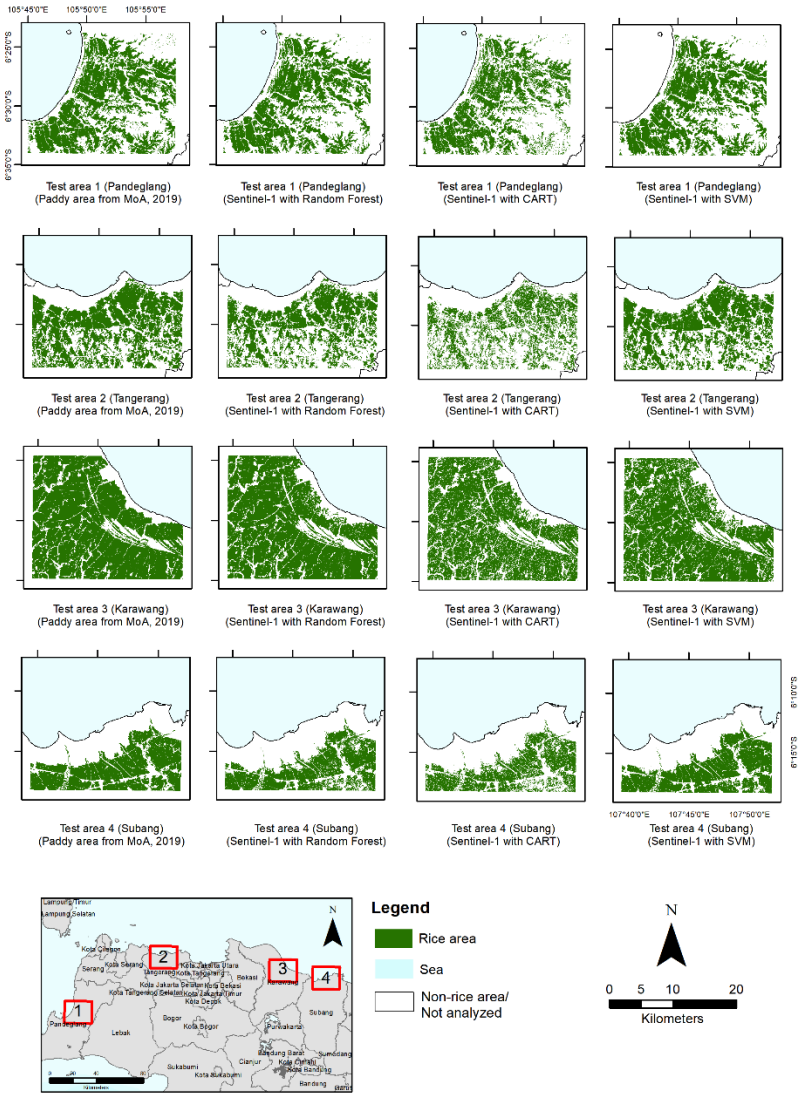

Figure 6.6 The rice area map of the four test sites (1-4) is based on the official rice area map, RF, CART, and SVM. The other test area is available on the supplementary material in Figure 6.S2 and Figure 6.S3.

Figure 6.7 illustrates the correlation between official data and predicted rice area at the regional level for 100 regencies in Java Island. It shows that RF and SVM models followed almost the same trend with a high correlation coefficient (>0.94) with RMSE=6,218 ha. The actual rice area in Java Island was 2,156,805 ha. However, the SVM slightly overestimated 2,276,026 ha using SVM, while the RF and CART model was underestimated the area, 1,887,672 and 995,739 ha, respectively.

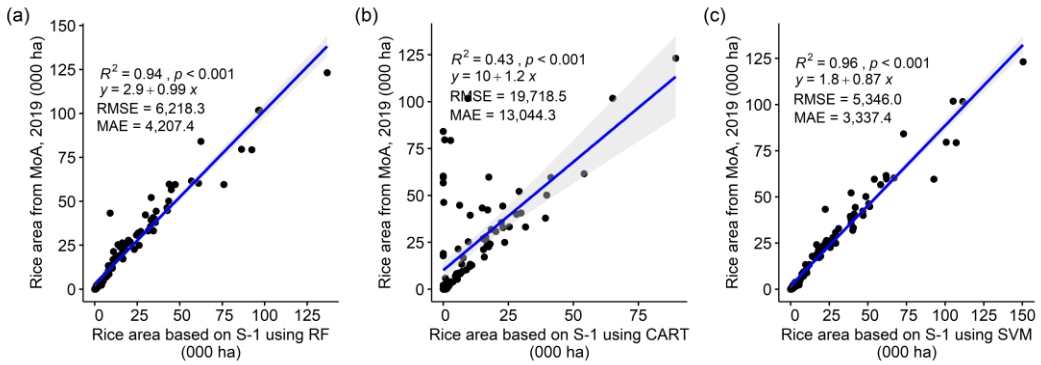

Figure 6.7 The correlation between actual and predicted rice area using (a) RF, (b) SVM, (c) CART methods over 100 regencies.

6.4.4 The prediction accuracy for different RGS

The classification accuracy for different growth stages and sensors is shown in Table 6.5. The RGS was accurately predicted with Sentinel-2 images on test sites compared to other remote sensing data, while the data from MOD13Q1 was predicted with the lowest accuracy (OA = 44.3-50.1%). Overall, most high PA and UA come from the vegetative stage and bare land due to distinctive spectral profiles. With Sentinel-2 image, the bands B4 (Red), B8A (Red Edge 4), B12 (short wave infrared [SWIR] 2) were found to be essential for discriminating the RGS. In the case of Landsat, the bands such as B5 (NIR), B7 (SWIR 2), and B6 (SWIR 1) were found to be important.

The OA of integrating three types of remote sensing data shows higher accuracy with the average of OA from 23 periods is 76.4% with RF, which is comparable with Sentinel-2's accuracy (78.8%) with the same classifier. Additionally, the PA and UA for four classes are higher than 74%, except for UA for the ripening class with the RF classifier (Table 6.5(d)). SVM and CART models show lower accuracy, with the average OA is 67.9% and 68 %, respectively.

Table 6.5 The accuracy comparison for RGS from three individual sensors and integration based on three classifiers on the 23 periods.

Classifiers	*n*	Bare land		Vegetative		Reproductive		Ripening		OA (%)
		PA (%)	UA (%)	PA (%)	UA (%)	PA (%)	UA (%)	PA (%)	UA (%)	
(a) Sentinel-2										
RF	57,968	80.8	88.7	81.1	85	74.3	78.1	75.6	58	78.8
CART	49,292	72.8	85	75.8	75.5	51.5	77.9	74.1	45.1	70.2
SVM	65,389	85.4	65.9	72.0	75.2	56.7	76.3	52.4	63.4	69.9
(b) Landsat-8 OLI										
RF	34,845	73	84.0	80	73.1	48.1	67.2	60.0	43.6	68.5
CART	29,452	64.4	76.9	77.9	67.8	48.9	68.6	54.3	40.4	64.5
SVM	39,451	76.1	77.7	77.4	71.2	42.2	70.3	58.0	44.8	67.1
(c) MOD13Q1										
RF	61,136	33.4	61.6	56.3	56.3	54.1	58.3	50.0	25.8	47.6
CART	52,024	26.4	50.5	49.7	55.5	55.9	51.1	39.5	19.3	41.9
SVM	68,897	33.4	46.7	37.9	64.0	63.0	54.6	47.9	22.5	42.7

(d) Integration (Sentinel-2/ Landsat-8 OLI/ MOD13Q1)										
RF	61,181	76.9	87.3	78.4	83.2	73.3	76.4	74.4	53.9	76.4
CART	52,053	69.0	83.9	73.4	74.1	51.1	75.2	72.6	42.3	68.0
SVM	68,997	81.7	65.7	69.1	74.6	56.3	74.1	52.3	55.5	67.9

Note: *n*= number of points, PA = Producer's accuracy, UA = User's accuracy, and OA= Overall accuracy

The classification accuracy of RGS over the periods is illustrated in Figure 6.8. Three classification methods achieved the highest OA in January 2020, while the lowest OA was recorded in December 2019. After February 2020, the OA was high (75-80%) and maintained the same level until the end of the sample period. The other classifier follows almost the same trend, but RF is higher on all periods, especially on the 02 – 17 February 2020 and 24 May – 08 June 2020 period.

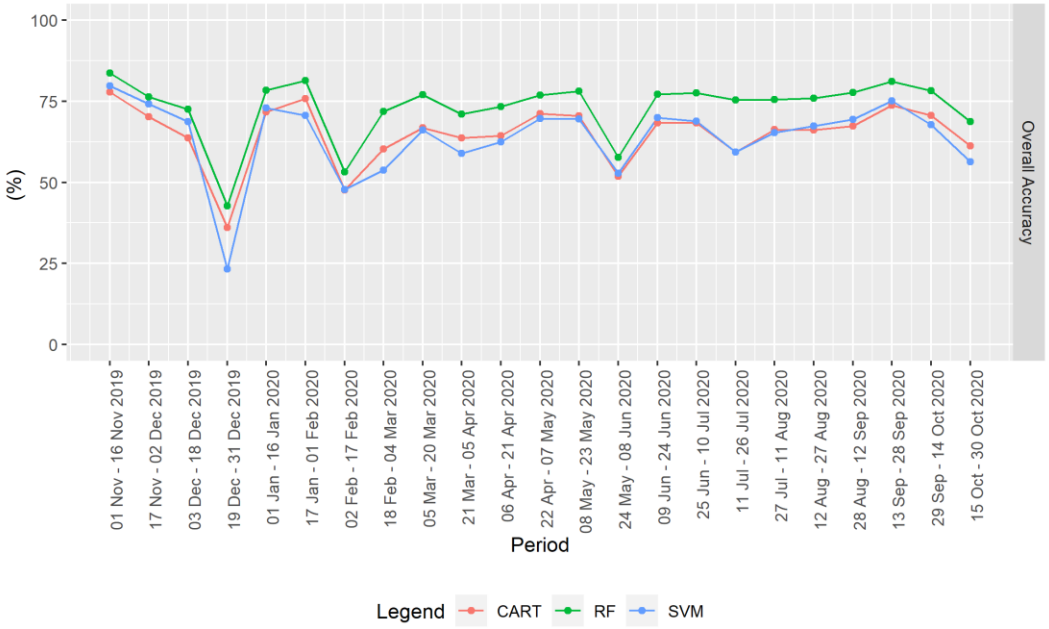

Figure 6.8 The overall accuracy (OA) of RGS maps is based on three classifiers for 23 periods.

The spatiotemporal distribution of prediction maps generated from three different methods (RF, CART and SVM) were displayed in Figure 6.9. It shows that the integration of three sources of remote sensing data can provide continuous temporal maps. The generated maps also show high consistency with the rice cultivation period, where the 16 – 21 April 2020 period was the vegetative stage for most area vegetative stages. The rice has grown to the reproductive stage from the 22 April – 07 May 2020 period until 08 – 23 May 2020 period. Moreover, the last stage is the ripening was started in the 24 May – 08 June 2020 period. Figure 6.9 also shows that RF is more consistent than the SVM classifier and the CART shows less accurate over the periods.

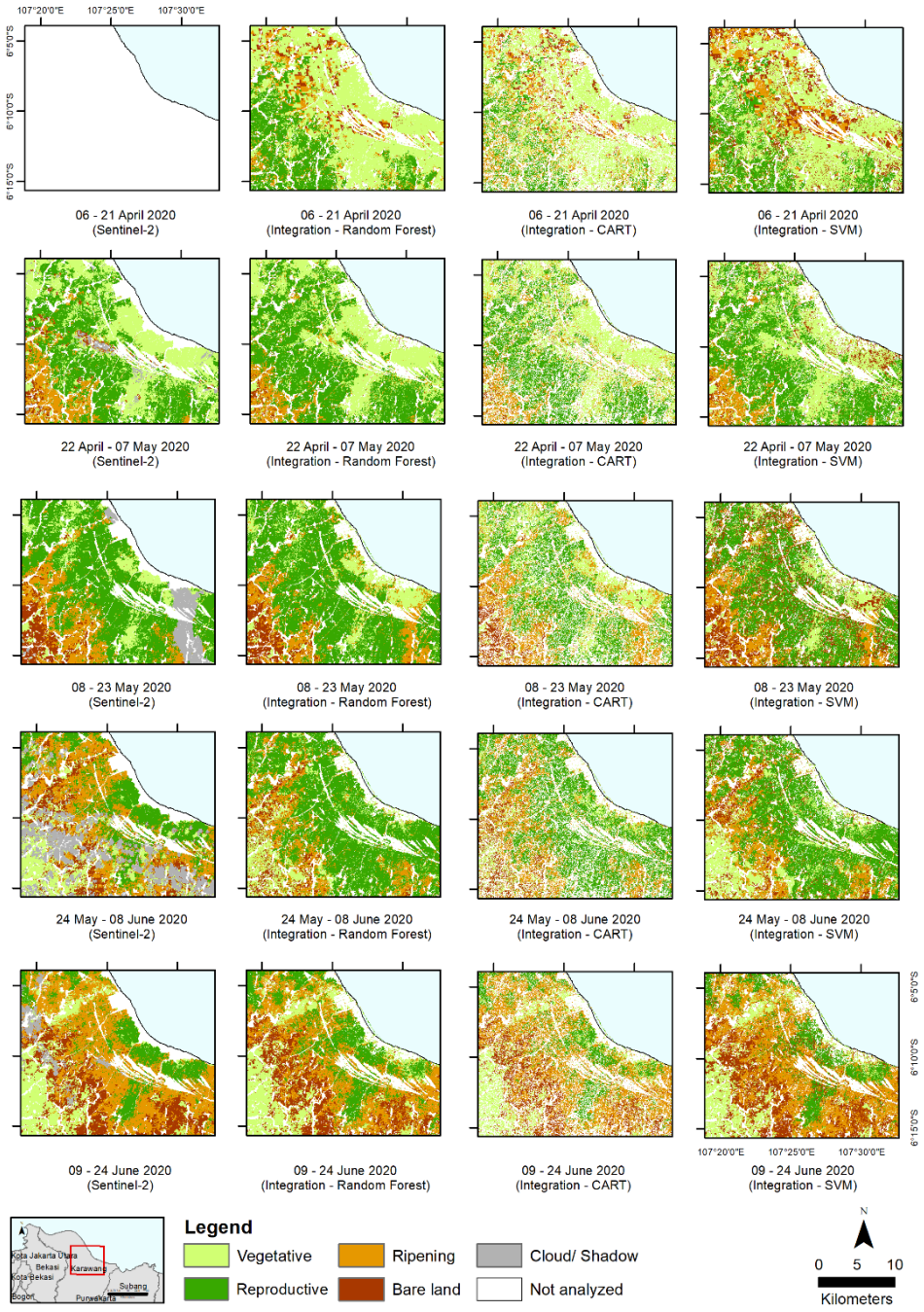

Figure 6.9 The RGS map of Test area number 3 (Karawang) from 06 April to 24 June 2020 based on Sentinel-2 rice monitoring (S-2 RGS), RF, CART, and SVM. Other periods of test area number 3 are available in Figure 6.S4 – 6.S7 (Supplementary material).

6.4.5 The data proportion of multisource

The contribution of each source of remote sensing data for 16 day periods (November 2019 to October 2020) with the RF classifier can be seen in Figure 6.10. The Sentinel-2 can provide 43.1 – 97% (average=80.4%) data and Landsat-8 has least contribution (5.8%). As expected, the data proportion of Sentinel-2 fluctuates over the periods. It has the lowest period in the wet season (January 2020) and the highest proportion was in June – August 2020 (dry season). Moreover, the Landsat-8 can significantly contribute (>10%) only on three periods where MOD13Q1 can provide it for 12 periods, which mainly during the wet season. The highest proportion of Sentinel-2 was 09 – 24 June 2020. Meanwhile, Landsat-8 and MOD13Q1 were the 22 April – 07 May 2020 and 19 – 31 December 2019.

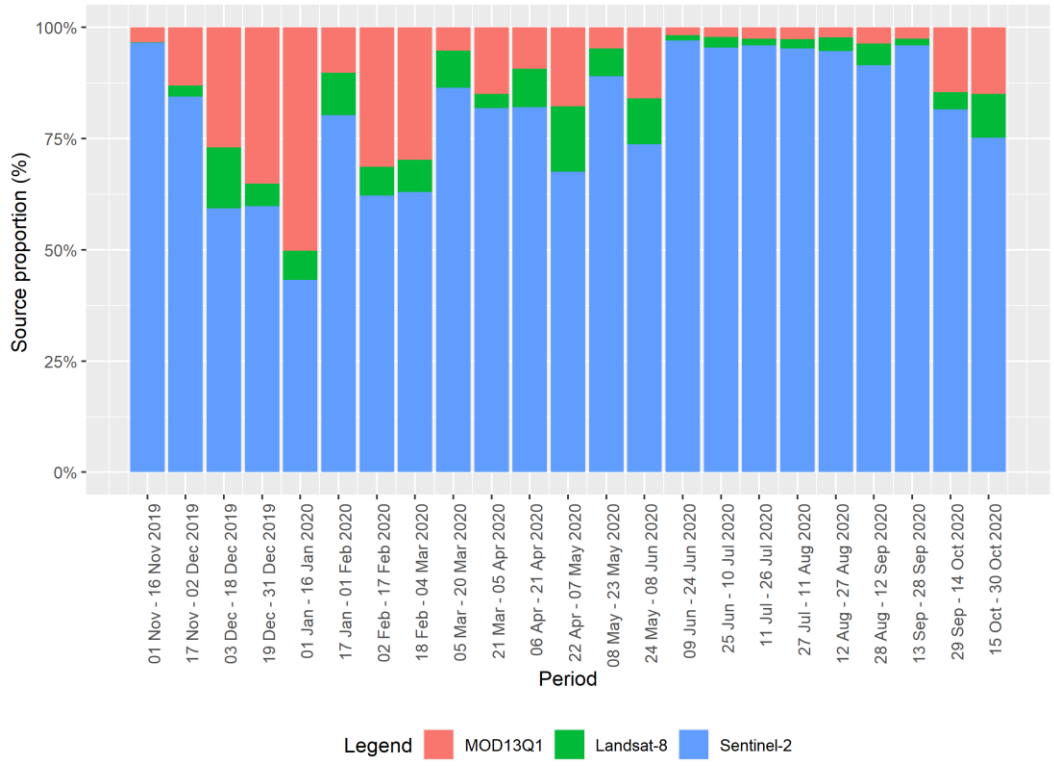

Figure 6.10 The source proportion over 23 periods between Sentinel-2, Landsat-8, and Sentinel-2 on Random Forest classifier.

6.4.6 The development of the RGS area over the periods

Figure 6.11 illustrates the area under different RGS from November 2019 to October 2020. It can be seen that the total area of bare land reduced in January 2020 as rice season began, then it became stable until March 2020. After that, the bare land area gradually increased

with the harvesting. The vegetative growth in two seasons is also captured as there are two peaks from January – to June 2020. Consequently, the reproductive growth was also detected once in February – May 2020 for the first season. The second season was a small peak in June 2020. However, the ripening phase yields entirely unexpected findings as there is no sign of peaks or big spikes and stabilization over 500,000 – 625,000 ha. Overall, RF shows a better capability to capture rice-growing areas in an extended period.

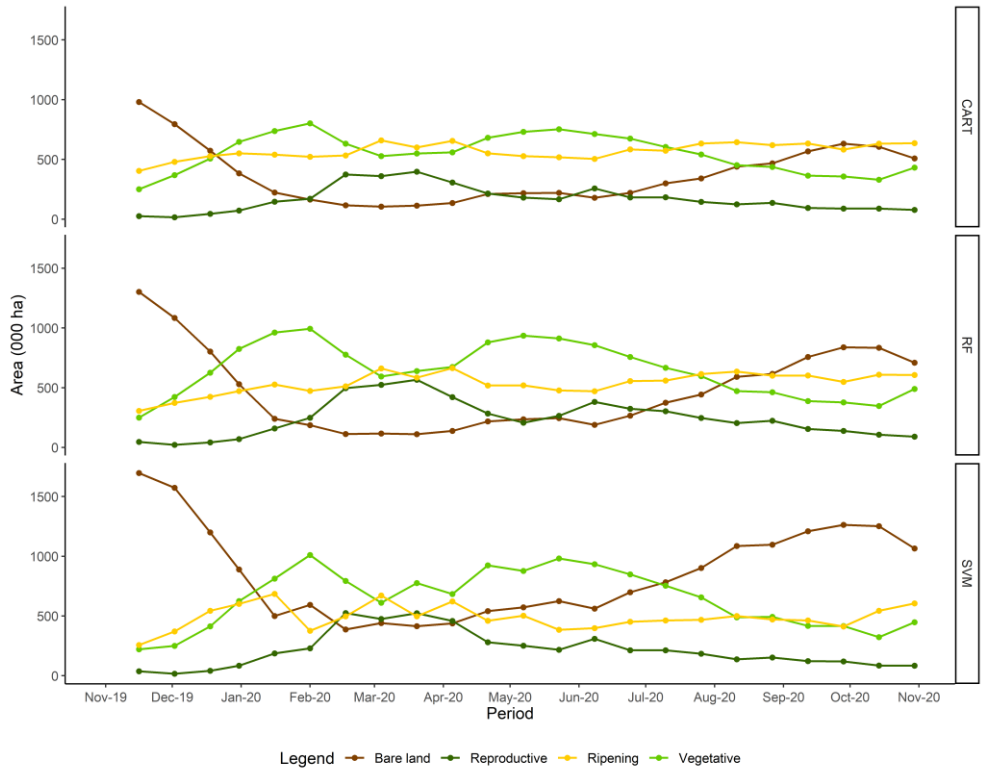

Figure 6.11 The RGS area development from 01 – 16 November 2019 to 15 – 31 October 2020.

6.4.7 Rice maps from GEE

An interactive rice monitoring system using GEE was developed (https://danicool98.users.earthengine.app/view/rice-growth-stages-monitoring-using-multisource-remote-sensing). Figure 6.12 shows that the generated RGS maps can confirm the consistency of changing RGS over four 16-days periods as the ripening stage captured on 28 August – 12 September 2020 and become harvested or bare land on the next period. Some area shows the changes from the reproductive stage on the 13 – 28 September period to the ripening stages in the next period. The speed of rendering the maps varies depending on the network and the region. The rendering maps on a specific region in Figure 6.12

required 77 seconds, and for all Java Island is 53 seconds with lower resolution. However, it took 10-20 seconds to render for zooming in or panning to another area. Furthermore, a separate script was needed to download the RGS area in raster format for further analysis which needs ~60 minutes to acquire one map for the Java Island region.

Figure 6.12 The screenshot of rice monitoring application on GEE platform from 28 August – 12 September to 15 – 30 October 2020.

6.5 Discussion

The GEE is a sophisticated geospatial computation platform for simultaneously determining rice area and RGS from multi-source remote sensing data. Despite variable cloud conditions in tropical countries, accurate rice maps were generated using multitemporal S1. The rice area accuracy was comparable with other studies OA (94-98%) (Rudiyanto et al., 2019) (Bazzi et al., 2019) (Tian et al., 2018) (Mascolo et al., 2019). This study found that dual-polarization (VV and VH) provided better accuracy than single polarization. However, it was found that VH polarization has a high potential to detect rice area as it is sensitive to structural changes of vegetation [26 and 28]. Generally, S1 data is associated with noise. Although this study has used a median filter to minimize noise, other de-noising approaches such as Lee (Lee, 1981), refined Lee, or geometric filter (Lee et al., 1994) could improve the accuracy by 4% (Bioresita et al., 2018). Since the S-1 data is a freely available and cost-effective solution to analyse large areas using GEE, continuous rice maps can be generated for effective management decisions.

The overall accuracy of detecting RGS using the integration of three optical sensors was acceptable (76.4%), which is comparable with other studies regarding rice phenology using other sensors such as PROBA-V (83.8%) (Ramadhani et al., 2021), TerraX SAR (79.3 –

84%) (Ç et al., 2016) and ALOS PALSAR (76.4%) (Miyaoka et al., 2013). Moreover, this study shows that the MOD13Q1 has the lowest accuracy and Sentinel-2 has the highest accuracy (Table 6.5). The integration accuracy is below 2.4% on Sentinel-2's accuracy, with more information revealed. Thus, multi-sensor techniques and multitemporal images with optical sensors can retain accuracy compared with single sensors by capturing rice's critical growth stages, as shown in a previous study (Sun et al., 2020).

Regarding classifiers' performance, the RF shows a better OA than CART in classifying rice area and RGS because RF can combine the output of multiple trees with cross-validation where CART depends on one tree where the model can easily have overfitting problems (W. Chen et al., 2017; W. Zhang et al., 2020). Other studies also have similar accuracy results, such as Youssef et al. (2016) on mapping landslide susceptibility and Zhang, Liu, Wu, Zhan, and Wei [46] on mapping the rice area in China. However, SVM accuracy is underperformed compared to other similar studies (Rudiyanto et al., 2019; W. Zhang et al., 2020) due to poor generalization. For discriminating against RGS, Sentinel-2 was found as a better source of information compared to other sensors data. In Sentinel-2, the bands were 670 – 864 nm and 1613 – 2202 nm.

The integration of multiple source information (Sentinel-2, Landsat-8, and MODIS) significantly improved the data availability across different times, thus increasing the information's consistency, as X. Zhang et al. (2018) reported. For instance, the data availability from Landsat-8 and MOD13Q1 was improved positively from 3 to 56.7% (average: 19.6%) compared to Sentinel-2 data alone over 23 periods (Figure 6.10). The result of the study demonstrates the novelty method for providing a cloud-free RGS map using GEE, which is easier to develop than the previous method involving unsupervised time-series analysis (Sun et al., 2020). High temporal frequency maps could enable the government and stakeholders to provide timely resources to improve productivity (Cai & Sharma, 2010). The GEE environment can be deployed on a global scale to be evaluated by other investigators without concerning the IT infrastructure, which may have a high cost for several developing countries. For example, the S-2 RGS system requires one day to download the data, classify it with a pre-trained model, and render it into an interactive web. Simultaneously, the proposed work uses the GEE environment to deliver it in less than two minutes to render the map.

The other limitation is that the model of RGS is still assuming that all vegetation on the rice area is rice during the whole year. Some areas in East Java and Banten farmers usually grow secondary crops such as maize, soybean, or watermelon to increase the land productivity when water is limited, which have similar reflectance of rice crop, especially within ripening stages during the August-September period (Figure 6.S8 and 6.S9). In the future, automated cropping pattern detection needs to be included in the classification process by detecting a sudden drop of VH value of Sentinel-1, as the previous study has been done by Ramadhani et al. (2020a).

The last limitation to be considered is from the GEE environment, where the grid search feature is not available. This feature allows the classifier to be tuned up with some hyperparameters, especially for the SVM classifier, to find the best model through cross-validation (Kuhn, 2008). However, it can be solved with Keras (Ketkar, 2017) and TensorFlow (Abadi et al., 2016) approach with a higher cost for the users. Moreover, an automated machine learning toolkit such as Google AutoML (Bisong, 2019) or AWS AutoGluon (Erickson et al., 2020) can be used to increase the accuracy and elevate this approach to an operational level with other classifiers where GEE lack, such as XGBoost, and gradient boosting.

Future study is needed to increase data availability by adding more sensors such as PROBA-V and Sentinel-3 to automatically detect RGS or using Sentinel-1 with a more extensive field campaign dataset to detect rice area. Moreover, pixel-level also need to be developed in the GEE environment because it can increase accuracy using STARFM and descendent, which combine coarse resolution such as MODIS with the Sentinel-2 Landsat image family as suggested by (Cai et al., 2019; Gevaert & García-Haro, 2015). The latest algorithm called Flexible Spatiotemporal DAta Fusion (FSDAF) version 2.0 can lower RMSE down to 7% compared with the original STARFM method with MODIS products (MOD09GA) and Landsat 7 ETM+ using spatial prediction and edge detection (Guo et al., 2020). The ideal spatial resolution for rice area is 10 m because our results show that OA Sentinel-2 is 25% higher than MOD13Q1. Research shows that using Farmosat-2 with 8 m spatial resolution and GIS-based objects can detect rice area in fragmented areas for the urban region (Shiu et al., 2012).

6.6 Conclusion

This study has developed an automated near-real-time workflow to monitor rice area and RGS using a GEE environment and multi-source remote sensing data. This study demonstrated that the big data and cloud computing approach is a cost-effective solution for regular monitoring of large areas from national to local (village) scale. This approach is more favourable for the stakeholders to predict and mitigate environmental factors (climate change) or economic factors (export-import) to secure food production by examining rice field dynamics spatially because the information of vegetative area can be used to indicate the rice cropping production in two-three months ahead. Integrating multisource remote sensing data can overcome cloud and shadow problems in tropical countries. Therefore, this workflow can be one of the alternatives of crop monitoring techniques which can be transferred easily into other significant cereal products such as maize, soybean, cassava, sugarcane cultivation on a global scale with faster and more accurate results to combat hunger and poverty, especially in developing countries with limited internet access and information technology infrastructure.

6.7 Acknowledgement

Indonesia Ministry of Agriculture through the Indonesian Centre for Agricultural Land Resources Research and Development (ICALRRD) to provide high resolution of the official rice area, researchers from Indonesia Agency for Agroclimate and Hydrology Research Institute (IAHRI) and Sentinel-2 rice monitoring team. We are grateful to the European Space Agency (ESA) and The United States Geological Survey (USGS) to provide Sentinel and MODIS data. We are also acknowledged to Google Earth Engine developers for the free platform. The source codes and scripts used in this study are freely available from https://github.com/FadhlullahRamadhani/Rice-Growth-Stages-with-Google-Earth-Engine.

Supplementary material

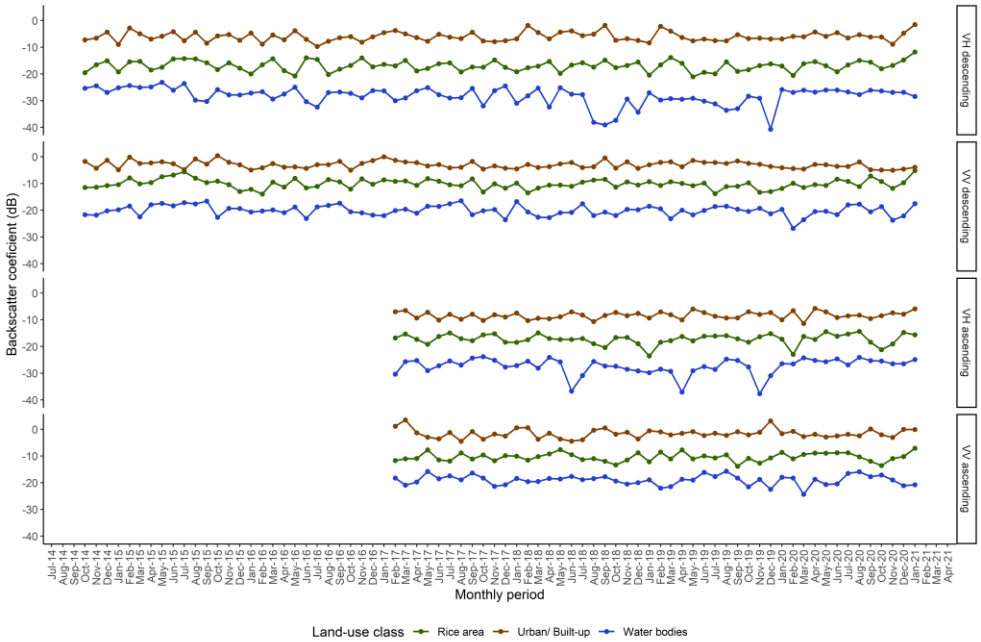

Figure 6.S1 The example of multitemporal backscatter mean value from Sentinel-1 for three land-use classes in monthly period for rice area (Long.: 108.424, Lat.: -6.709), urban/ built-up (Long.: 108.561, Lat.: -6.711), and water bodies (Long.: 108.589, Lat.: -6.711).

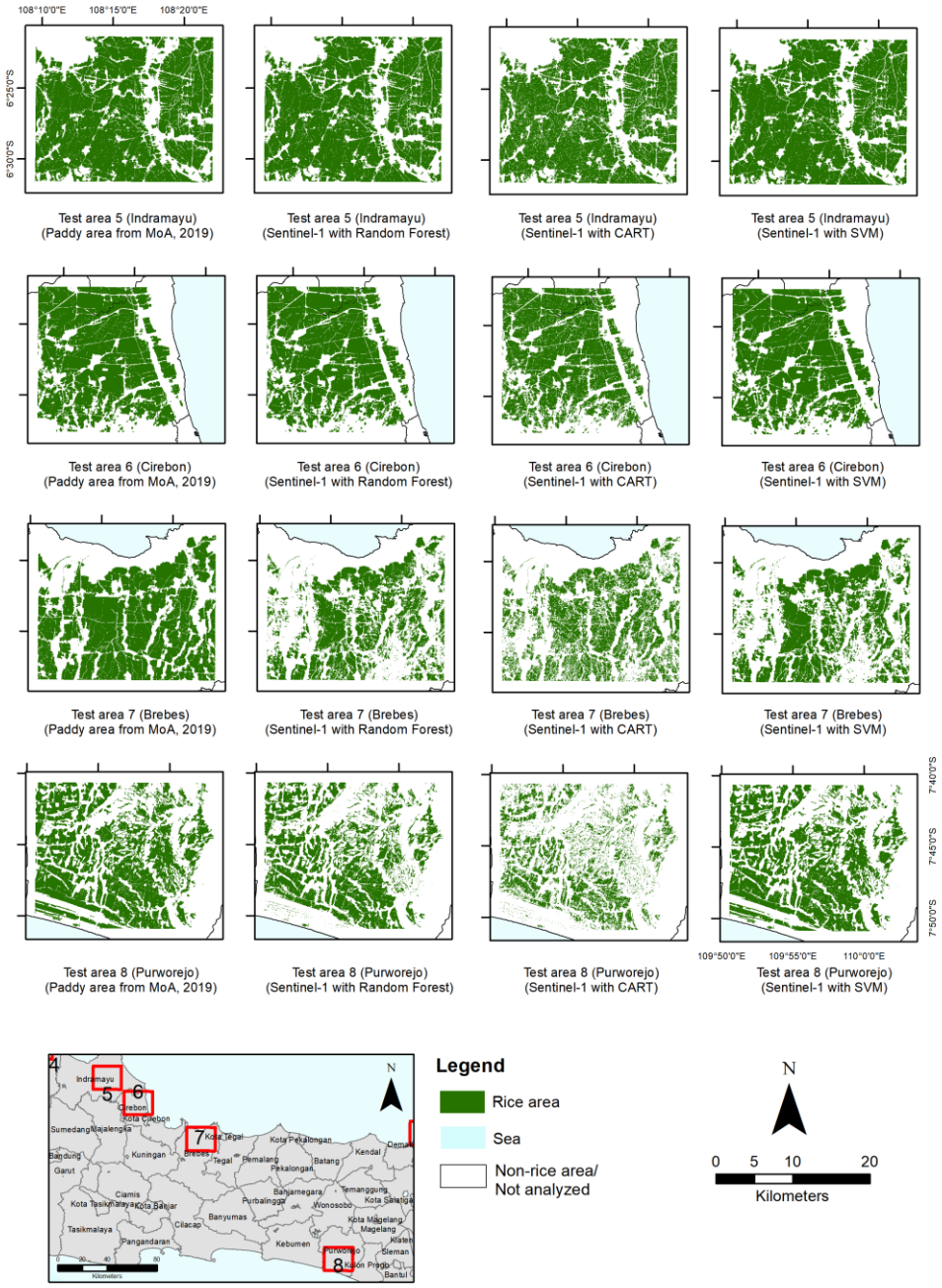

Figure 6.S2 The rice area map of the four test sites (5-8) based on the official rice area map, RF, CART, and SVM

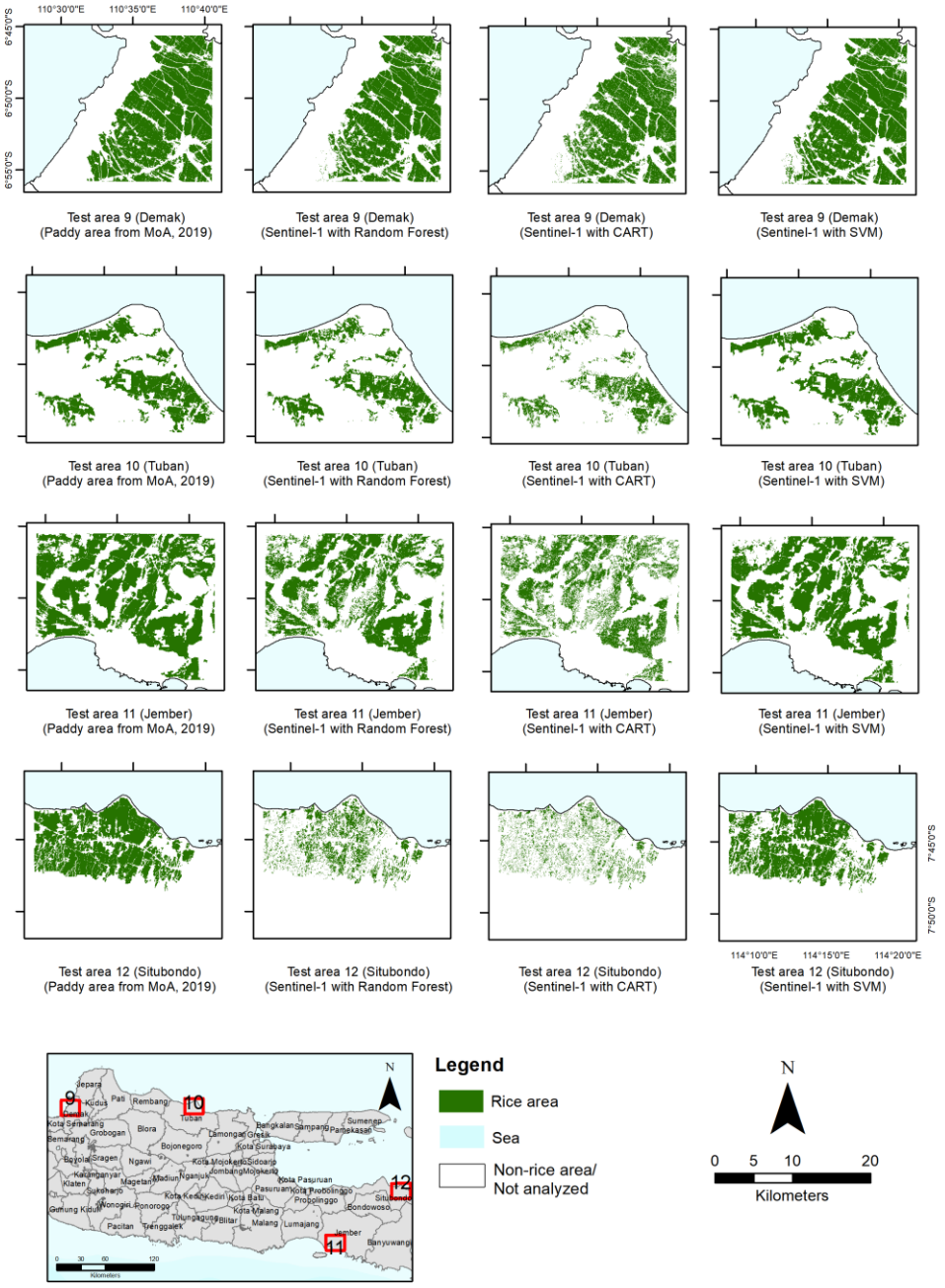

Figure 6.S3 The rice area map of the four test sites (9-12) is based on the official rice area map, RF, CART, and SVM.

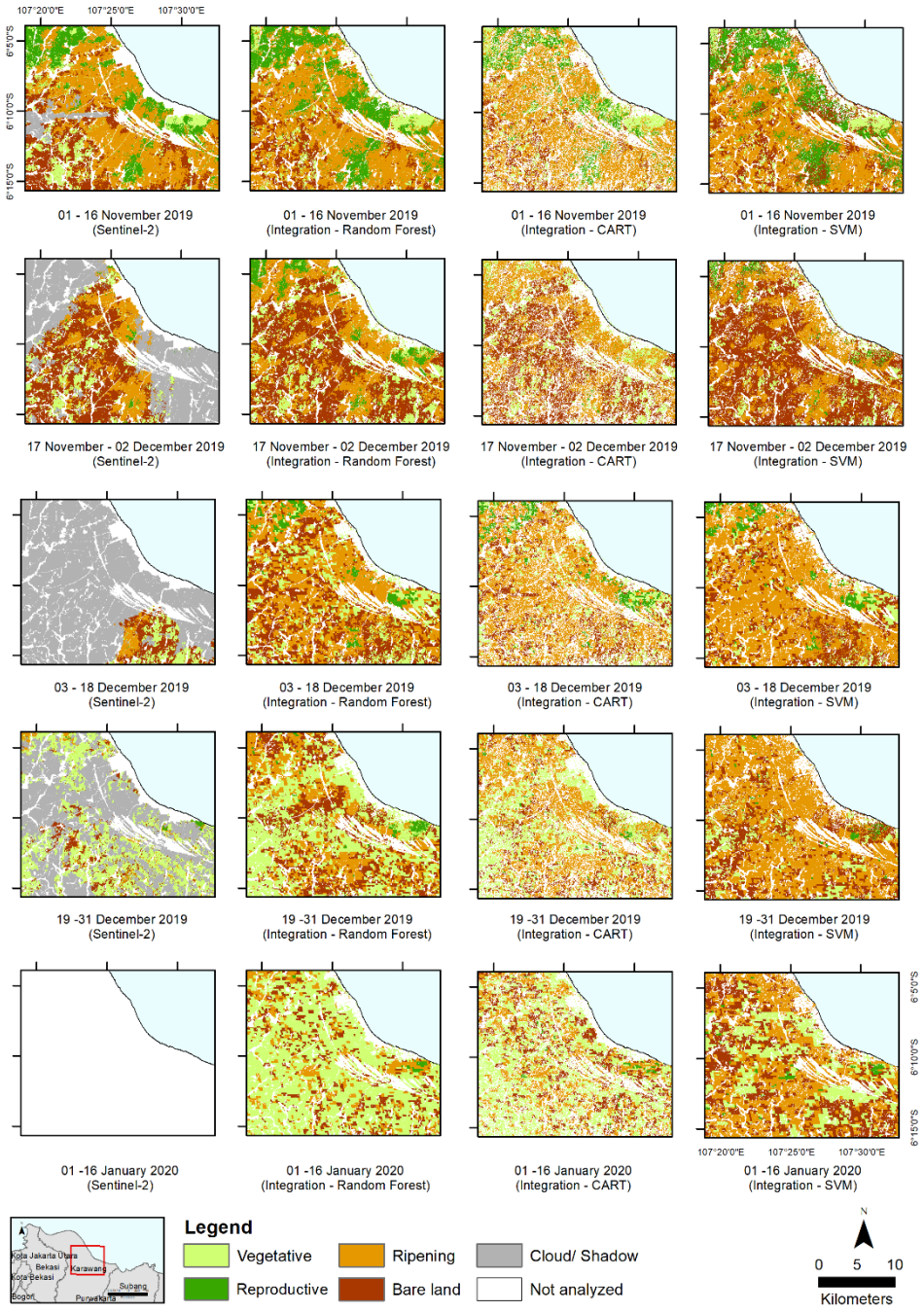

Figure 6.S4 The rice growth stages map of test area number 3 (Karawang) from 01 – 16 November 2019 to 01 – 16 January 2020 based on Sentinel-2 rice monitoring, and RF, CART, and SVM.

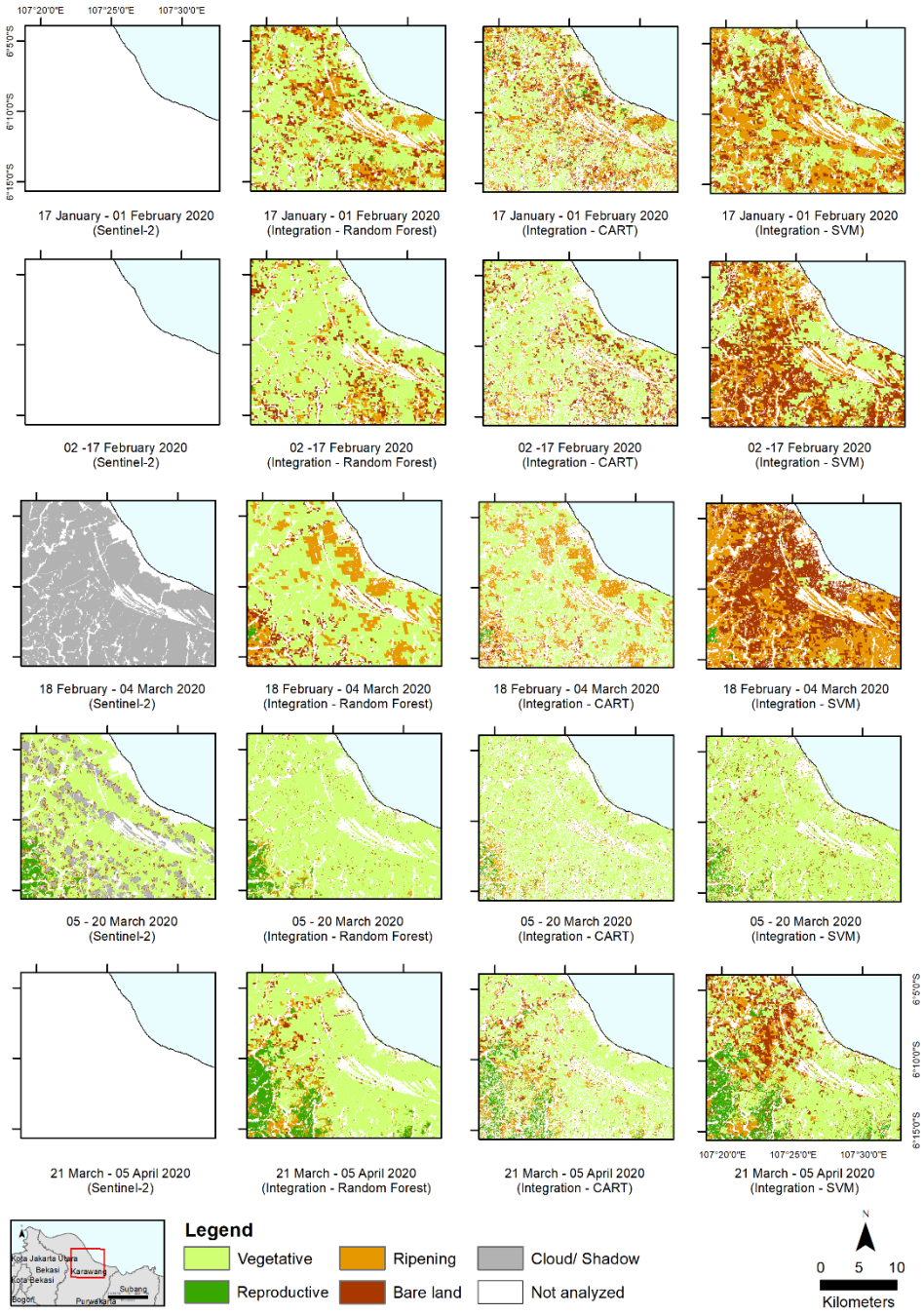

Figure 6.S5 The rice growth stages map of test area number 3 (Karawang) from 17 January – 01 February to 21 March – 05 April 2020 based on Sentinel-2 rice monitoring, RF, CART, and SVM.

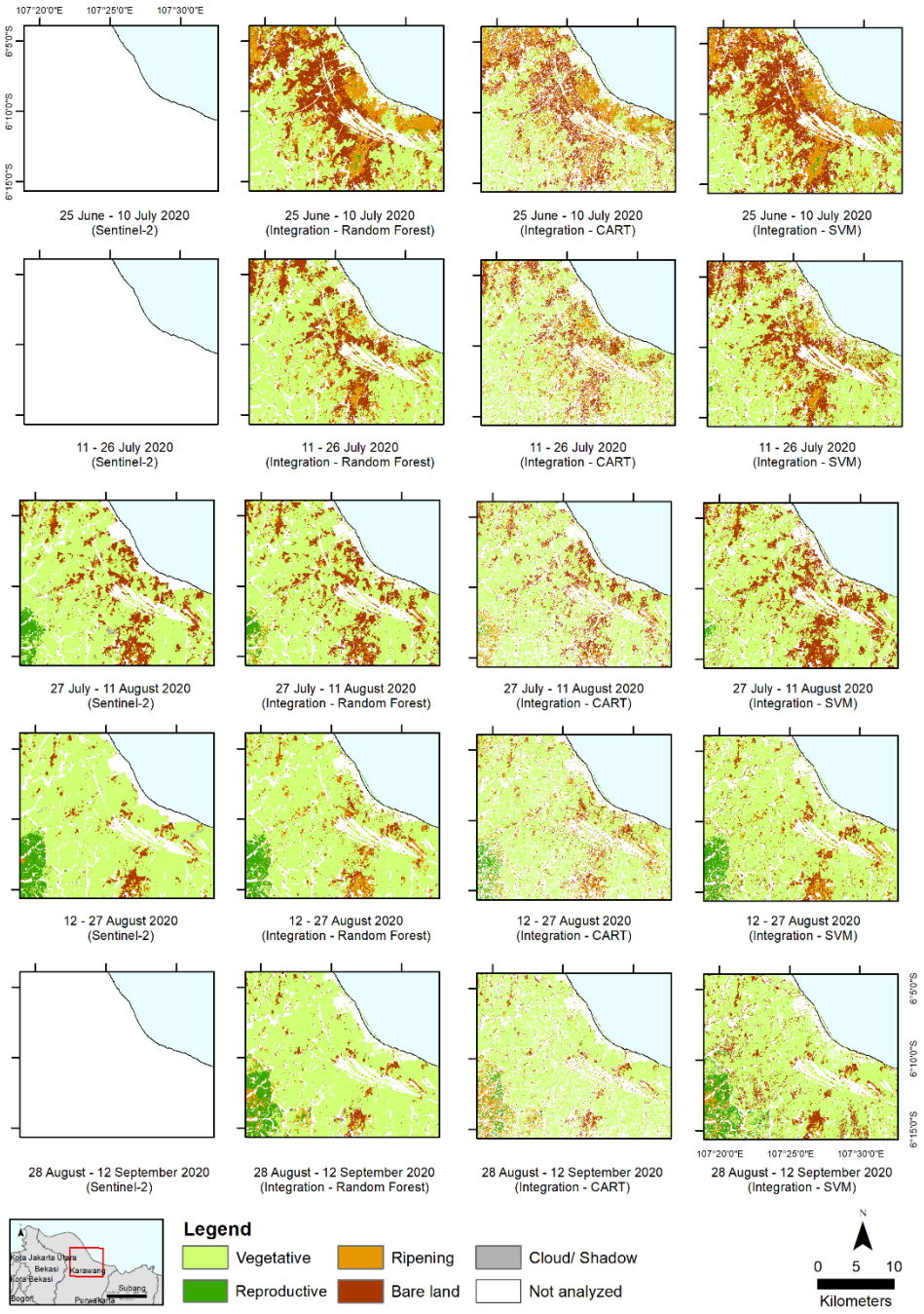

Figure 6.S6 The rice growth stages map of test area number 3 (Karawang) from 25 June – 10 July to 28 August – 12 September 2020 based on Sentinel-2 rice monitoring, RF, CART, and SVM.

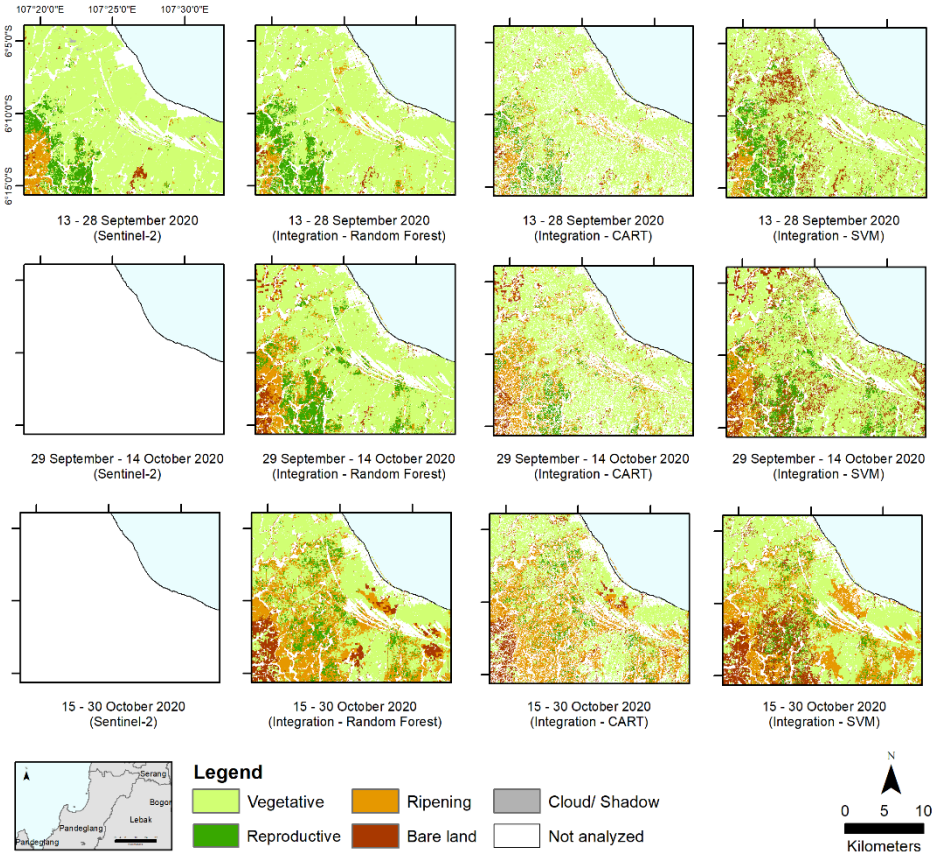

Figure 6.S7 The rice growth stages map of test area number 3 (Karawang) from 13 – 28 September to 15 – 30 October 2020 based on Sentinel-2 rice monitoring, RF, CART, and SVM.

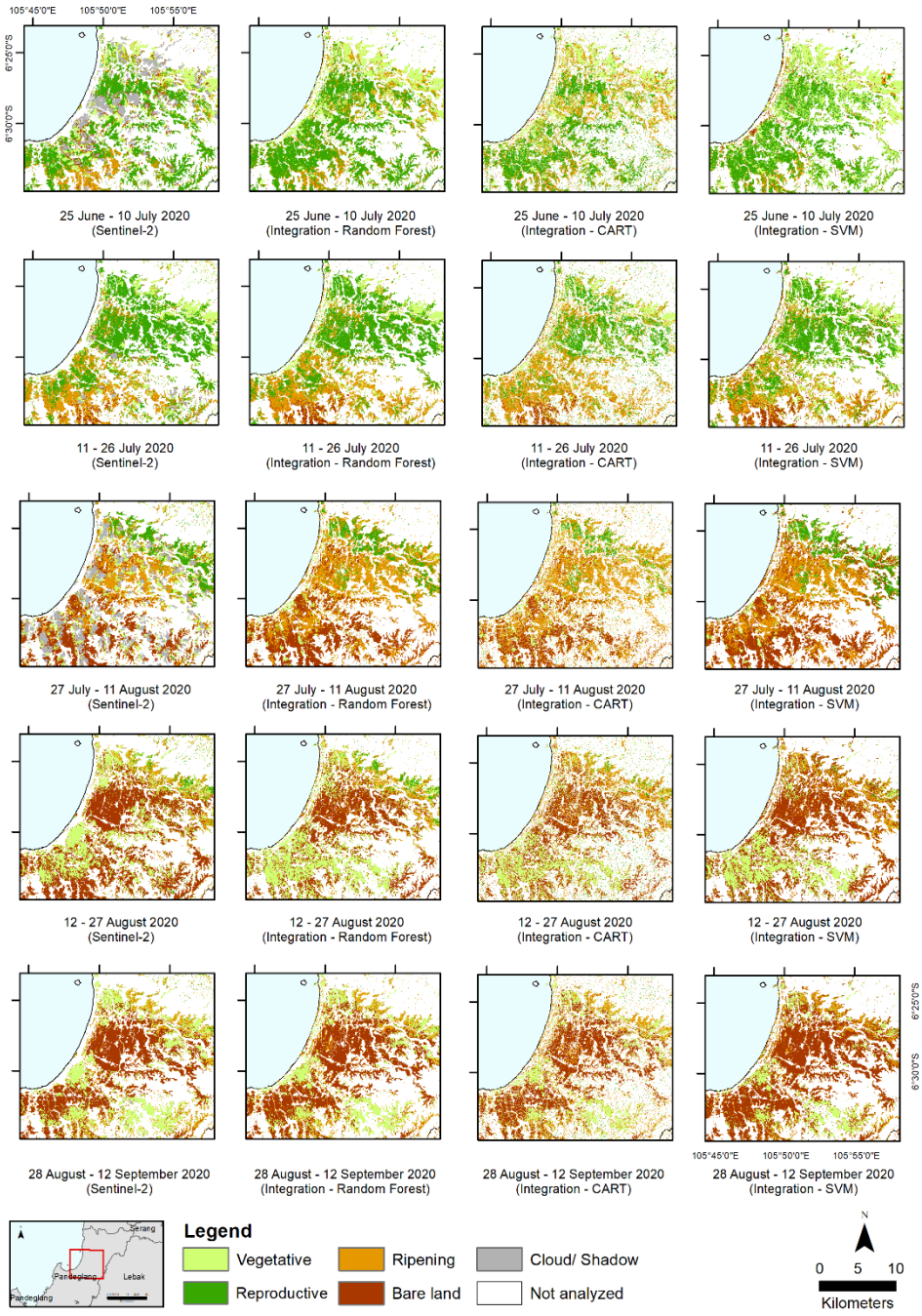

Figure 6.S8 The rice growth stages map of test area number 1 (Pandeglang) from 25 June – 10 July to 28 August – 12 September 2020 based on Sentinel-2 rice monitoring, RF, CART, and SVM.

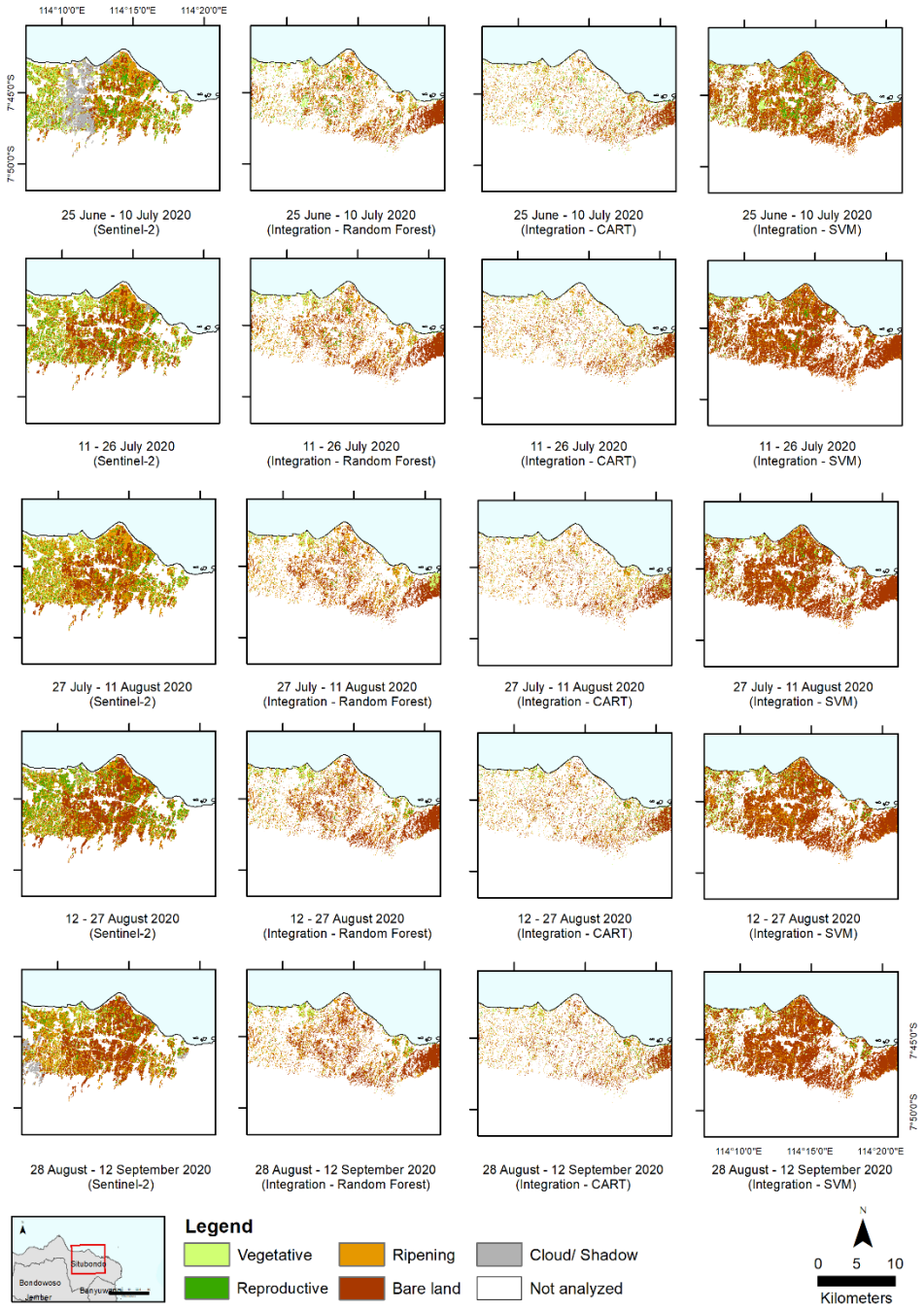

Figure 6.S9 The rice growth stages map of test area number 12 (Situbondo) from 25 June – 10 July to 28 August – 12 September 2020 based on Sentinel-2 rice monitoring, RF, CART, and SVM. Other test areas and biweekly periods are available and https://github.com/FadhlullahRamadhani/Rice-Growth-Stages-with-Google-Earth-Engine/tree/master/Temporal BoxMap.

[intentionally blank]

Chapter 7 General Discussion

Accurate and timely mapping of the rice growth stages (RGS) is important for precision input management, yield improvement, and food security. In-situ methods, such as field surveys, are widely used to assess the RGS, but those methods are associated with high costs, labour and time. Remote sensing data can provide timely information on rice crops covering large spatial extents (e.g., regional to continent scales). Many studies have been conducted using different satellites with various spectral and spatial configurations. This research aimed to investigate and develop a methodology for the accurate mapping of RGS using multiple remote sensing data with various machine learning algorithms, which would add some knowledge to the remote sensing community. Moreover, accurate RGS mapping is valuable information for government policy and decision-makers to regulate and sustainably manage the available resources, thus minimising the impact of agriculture production on the environment. In our context, the map of RGS supports the improvement of four key areas: water management, fertiliser supply, nutrient management and harvesting facilities in Indonesia. The proposed methods can also be applied elsewhere globally.

7.1 A summary of remote sensing data for detecting RGS

In this thesis, Chapter 1 explained the importance of rice crop production in Indonesia and its role in food security, while an extensive literature review has been conducted into remote sensing for mapping rice areas and growth stages in Chapter 2. The review also pointed out the research gaps, which are set as objectives in this research. Initially, we have studied the potential Landsat-8 OLI imagery combined with ground webcam stations data for mapping RGS in Chapter 3. The results showed that using all (six) bands of information as an input in the model significantly improved the accuracy by 10.3%, compared to vegetation indices, indicating the importance of multiple bands for mapping (Table 3.3). However, the prediction performance was inconsistent in the mixed and fragmented crop areas' results, leading to increased misclassification due to the mixed pixels. Consequently, the high spatial resolution imagery of Sentinel-2 was used in Chapter 4 to improve the accuracy. Since Sentinel-2 has a high spectral and spatial resolution, its classification performance proved to be 20% better than Landsat-8. Sentinel-2 images were integrated with MOD13Q1 and Sentinel-1 (S-1) to fill gaps and negate cloud interference. S-1 offers

the clear advantage of collecting information from the Earth's surface irrespective of the weather conditions. The polarised SAR backscattering profile is highly sensitive to crop phenology and canopy volume, thereby allowing continuous monitoring from space.

Alternative to MODIS, Chapter 5 explored the potential of PROBA-V combined with Sentinel-1 to produce a cloud-free map for RGS. The results show that the prediction map has a high correlation with local statistics with a moderate 100-meter resolution. The lag time between the stages is similar to the existing rice cropping pattern with an average $r > 0.52$, $p < 0.01$.

In Chapter 6, multisource remote sensing based on Sentinel-2, Landsat-8 OLI, MOD13Q1 with rice area detection from the multi look of Sentinel-1 was integrated to improve the temporal and spatial resolutions. Processing multisource remote sensing data at a national scale is challenging due to the large volume of data and high computational power required. Recently, Google Earth Engine (GEE), a sophisticated geospatial platform, was introduced for processing planetary-scale data with unprecedented speed by parallelising the analysis on many CPUs in Google data centres (Gorelick et al., 2017). Chapter 6 investigated the potential of using GEE for mapping RGS using multisource remote sensing data. Since Indonesia's spatial data infrastructure is less developed due to economic constraints, GEE provides realistic solutions for processing big data to provide timely decisions for the precision management of rice. The flowchart of the thesis's summary is illustrated in Figure 7.1.

The automation system that has been investigated in Chapters 4, 5, and 6 shows that the machine learning model can be transferred in the area as a pre-trained model to get a quick analysis of rice growth stages in a particular area. A similar method was also used in detecting damaged buildings for timely assessment for helping the disaster victims by Valentijn et al. (2020), where the collection of ground truth datasets was difficult and expensive. They also found that the machine learning model has retained its accuracy in different 19 disasters in several scenarios with very high spatial resolutions (<0.7 m) using Convolutional Neural Networks. However, they recommended that a larger dataset and collaboration with other information is needed to make better information for end-user, which this study drew the same conclusion.

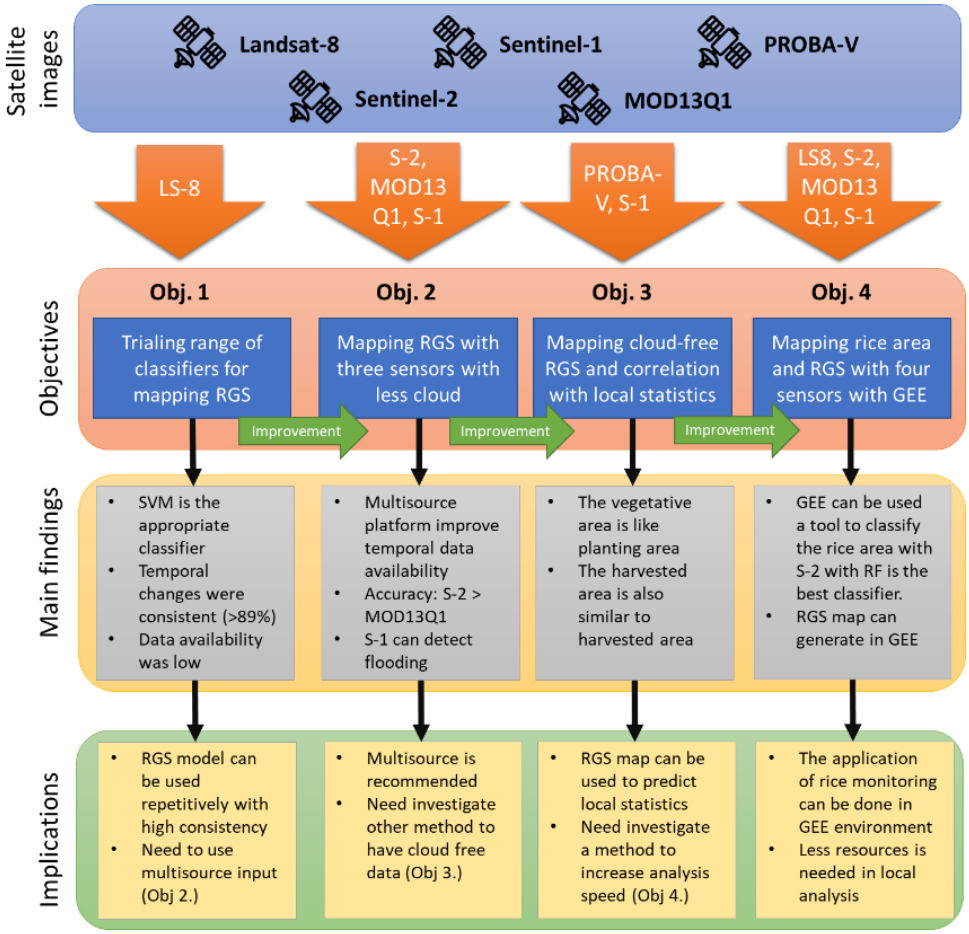

Figure 7.1 The flowchart of the research summary and its main finding for each objective.

The main reason for the integration of multisource remote sensing data is to increase its potential applications by combining each sensor's strengths. The optical sensors show greater accuracy than the radar-based sensors, but clean data's availability is minimal due to the almost permanent cloud cover and shadows, especially in tropical areas. Moreover, the strengths and weaknesses of different remote sensors are detailed in Table 7.1.

Table 7.1 The list of strengths and weaknesses of sensors and sensor combinations used for mapping RGS

Sensors/ Fusion sensors	Strengths	Weaknesses
MOD13Q1	Better accuracy than Sentinel-1 in the training model, easy to implement	Clouds, 16 days periodically, 250-meter resolution, fewer bands, mixed pixels, less accurate in ripening stages
PROBA-V	Better accuracy than MOD13Q1 in the training model, two-three days revisit time, easy to implement	Clouds, 100-meter resolution, fewer bands, mixed pixels
Sentinel-2	Highest accuracy from all sensors in the training model, better resolution: 10-60-meter resolution, five days revisit time, easy to implement	Clouds, less accurate in the ripening stage
Sentinel-1	Can penetrate through clouds, more moderate accuracy than MOD13Q1, better resolution: 10 m	12 days revisit time, difficult to implement, speckles noise, less accurate in reproductive stages
MOD13Q1/ Sentinel-1	Higher accuracy than Sentinel-1	Prone to clouds, difficult to transfer to other areas
Sentinel-2/ MOD13Q1/ Sentinel-1	No cloud, higher accuracy than Sentinel-1, 10-meter resolution	Difficult to be transferred to other areas, and in the rainy season
PROBA-V/ Sentinel-1	No cloud, lower accuracy than Sentinel-2/ MOD13Q1/Sentinel-1 but easy to implement all year round	Difficult to be transferred to other areas, 100-meter resolution
Sentinel-2/ Landsat-8 OLI/ MOD13Q1	Less cloud, higher accuracy than Sentinel-2/ MOD13Q1/Sentinel-1 but easy to deploy to other lowland areas.	No cropping pattern detection, 30-meter resolution, challenging to download in the broader area due to GEE memory limitation

7.2 The limitation of mapping rice growth stages using RS and machine learning

Vegetation indices (VI) are commonly used as an input for mapping RGS due to their inherent simplicity. Different VI have been proposed to maximise the sensitivity of the variable of interest while minimising the role of confounding factors such as soil background and the atmosphere. For modelling VI information, parametric and non-parametric methods have shown excellent results in various environments. Non-parametric approaches, such as SVM, outperform simple linear regressions and provide accurate results due to their ability to explain the complex nonlinear relationships that classify RGS. The vegetation undergoes a series of changes in volume, structure, and chemical attributes during crop growth. As most publicly available satellite sensors suffer from coarse resolution and have limited and discrete spectral bands, machine learning approaches can still extract useful information from the mixed pixel (i.e. a mix of different RGS in one course pixel).

Zhu et al. (2018) suggested that mixed pixels occurrence in course pixels cannot be avoided; thus, the higher resolution or more bands in a sensor will decrease the probability of mixed pixels (study case on classification land-use types). However, ML classification, such as the SVM, can increase the accuracy by considering more bands in a high dimensional plane with mixed training pixels and still have high accuracy (Foody & Mathur, 2006). In our case, the confusion matrix on Landsat-8 and Sentinel-2 shows that the classification accuracy for the ripening stages is lower than the vegetative stage but still can be classified over > 55%, which was acceptable (Ramadhani et al., 2020a, 2020b).

Although the study was conducted in different rice ecosystems (flood-prone, rainfed lowland and irrigated areas), the proposed methodology in this thesis provided a robust methodology for mapping RGS for near-real monitoring. However, the proposed approach still has a few limitations:

a) In the study areas, some of the farmers in particular parts of Java, such as in Brebes and Nganjuk Regency (Figure 7.2), have cultivated rice and shallots (*Allium ascalonicum* L.) interchangeably, depending on the shallots' price in the market. If their price is predicted to be high, then the farmers would prefer to grow shallots. Despite the high accuracy achieved in most of the areas in the RGS model, it failed to distinguish the shallots in the vegetative stage when mixed side-by-side with rice, using

a 10 m spatial resolution (Figure 7.2). This misclassification happened because shallots and rice have similar optical features and the same wet soil conditions. In their vegetative stage, shallots also need to have ditches/water irrigation surrounding the fields. With a lower-middle infrared band than dry soil, wet soil makes it challenging to analyse for a limited number of the bands. Moreover, the growing period of shallots and rice is nearly the same, between 115 and 130 days (Putra et al., 2020). Field level studies are required to understand the optimal bands required for discriminating shallots and rice.

Moreover, rice varieties cause different spectral profiles. However, the existing studies only used proximal/UAV sensors to capture the image. Darvishsefat et al. (2011) reported that a field spectrometer could differentiate the rice canopy of seven Iranian local rice varieties. The study shows that rice varieties significantly differ on visible and near middle infrared (1425 - 1800 nm) wavelength. Another study also concluded that rice varieties have different spectral profiles in different RGS using a UAV with RGB bands (Afdhalia et al., 2019) in Indonesia. Ciherang varieties have a higher spectral value than the other two varieties, such as IR42 and IR64. More research is needed to discriminate the rice varieties using 10-100 spatial resolution data to increase the information at the field level.

Multispectral satellites contain few spectral bands with a broad spectral resolution which has limited capacity to discriminate vegetation types. As indicated in Chapter 2, hyperspectral sensors that collect continuous high spectral resolution data such as EnMAP and PRISMA can give detailed information about different vegetation types, such as forest type classification (Jędrych et al., 2017; Vangi et al., 2021). Moreover, the data from hyperspectral satellites can improve vegetation monitoring, such as canopy nitrogen content (Verrelst et al., 2021), soil organic carbon (Ward et al., 2020), soil macronutrients (Misbah et al., 2021), and leaf chlorophyll content (Cui et al., 2019).

(a)  (b) 

Figure 7.2 The comparison between (a) shallots and (b) rice cultivation in the vegetative stage.

b) The Sentinel-1 has proven an excellent sensor to detect the total rice area and flooding and vegetative phases due to a specific profile of low backscattering values (L. R. Mansaray et al., 2017). However, the reproductive and ripening classes were poorly determined. The main reason for this poor performance is that the rice plant, in both stages, is nearly the same, where the water background is covered with a dense canopy. Due to coarse resolution, the backscattering signal is weak and confounded with other environmental factors. Moreover, the Sentinel-1 has limited polarisation modes (VH and VV) to extract structural information of different RGS. Another method to improve the accuracy is to use multi look data from ascending and descending data sets in a short period (Umutoniwase & Lee, 2021). Moreover, the temporal dataset of S-1 also increases the probability of RGS classification in better resolution because it can detect the RGS change more precise than the longer temporal resolution area (Dirgahayu & Made Parsa, 2019). In some cases, the correction of the incident angle also raises the precision by normalizing the variance of temporal incident angle, which sometimes difference over the regional area (Kaplan et al., 2021).
c) GEE has limited memory to protect against the overuse of parallel processing by free users. This limitation leads to difficulties in making a regional scale in a single request within the custom application (e.g. Arjasakusuma et al. (2020)). Moreover, with many bands used as predictors, the classification process also needs a massive memory to process a wide area. Thus, the proposed method requests a smaller area or tiles by a time-based period and then combines the tiles into a wide area. Another solution is to make the classification process into a Google machine learning product (AutoML) with a subscription fee applied.
d) The model uncertainty in this study is inevitable and one of the challenges in the machine learning approach for solving classification problems; even the ML is

considered the best and easy to apply rather than linear programming or expert rules (Maxwell et al., 2018). Model uncertainty comes from three sources such as model fit, dataset quality, and space compliance (Kläs & Vollmer, 2018). The form of uncertainty can be produced from the overfitting or underfitting in the model fit case. The training dataset which is not verified can decrease the quality of classification accuracy. For example, the training dataset, which has a longer gap than the field survey data, will cause the wrong label dataset. Moreover, the uncleared scope of the classification can increase the uncertainties in space compliance, such as applying the RGS model in the sugarcane area will cause incorrect interpretation. The advances in quality and number of data sampling using drone and machine learning techniques such as deep learning can improve the accuracy and information used for decision-making in agriculture policy (Wang et al., 2022; Wei et al., 2022).

In tropical areas, there are three main barriers to implementing monitoring RGS using remote sensing. The first is extensive cloud cover, especially in the wet season (e.g. December – February for Indonesia). The second is the availability of (free) satellites data to make monitoring operational in a timely fashion. Some projects have been operational but short due to depending on grants or external funding, such as the International Asian Harvest mOnitoring system for Rice (INAHORT) based on images from the ALOS-2 satellite (Oyoshi et al., 2016). The third is the high uncertainty of implementing SAR-based RS datasets such as Sentinel-1 alone on discriminating RGS using the supervised method. This is challenging since the farmer's planting time can be shifting in Indonesia due to water distribution problems (G. Zhang et al., 2017). Thus, multitemporal and multi-dataset should be used to discriminate the RGS in the near real-time. The supervised classification using machine learning has been investigated in previous studies in different objects, such as detecting damaged buildings and wildfires with acceptable accuracy (Sulova & Jokar Arsanjani, 2020; Valentijn et al., 2020; Wen et al., 2019).

7.3 Future opportunities

Despite a growing number of studies into rice mapping using remote sensing, producing accurate high-frequency maps remains challenging. Although our research provided promising results, we believe further research is required to advance our understanding and mapping of RGS accurately. The following areas needed more attention, as follows:

7.3.1 Increasing ground sampling for validation

In Indonesia, rice areas are categorised into different ecosystems: rain-fed lowland-, upland-, and flood-prone rice ecosystems. The spectral signatures of these ecosystems are significantly different due to their variable management practices. Thus, sampling is needed as a valuable database to represent the variability in the training database. The web camera network can be expanded across the country for timely information and to validate the satellites' images. Furthermore, the automatic system for calibrating the satellites' images using webcam data is essential to simplify the process.

7.3.2 Improving the temporal frequency of satellite information

The increased frequency of information from multiple satellites (Sentinel-2, Sentinel-1, Landsat, MODIS and PROBA) would complement filling in the temporal gaps. In Figure 7.3, we have designed a system for mapping RGS on a regular time scale. The integration of optical and radar-based data can give a 'temporary' map of RGS in near-real time (5 to 16 days). Initial mapping started with Sentinel-2 with a 5-day temporal frequency, and missing/cloudy images were filled in by PROBA-V. The same step was applied to fill the missing value using Sentinel-1, Landsat-8, and MOD13Q1 for mapping RGS every 16 days. New generation hyperspectral missions, such as PRISMA and EnMAP, can further provide complementary information to understand the role of different spectral bands for mapping RGS.

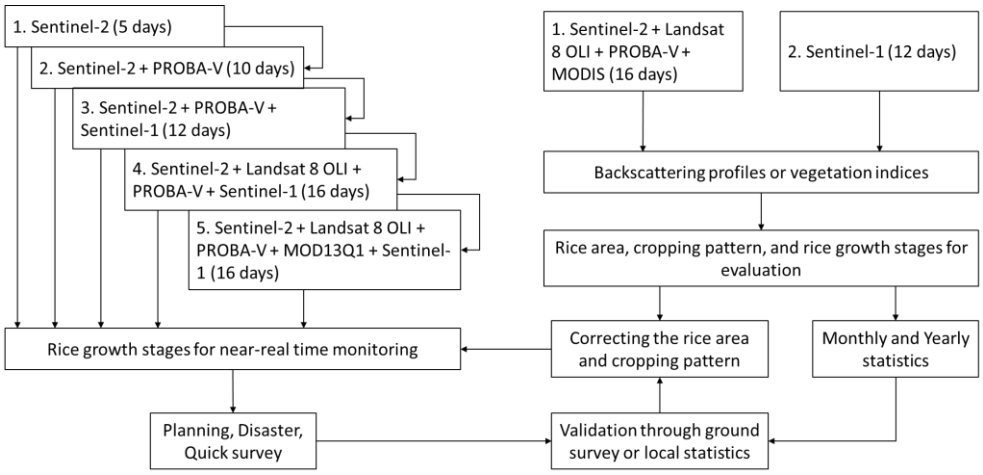

Figure 7.3 The future planning of rice monitoring with the fusion method

7.3.3 Data fusion approaches to improve the accuracy

Data fusion is another advanced approach, which takes the information from multiple sensors to improve the accuracy and temporal frequency. The accuracy of ripening stage classification can be increased with time-series data using a vegetation index, such as NDVI or EVI. The rice-growing phase can be drawn with EVI profile wherein the vegetative stage, the value of EVI is started lower than the reproductive stages. Over time, the value of EVI will reach the peak in the reproductive stages and decrease down through the ripening stages until its harvest. However, this technique needs clean data in two consecutive periods. Chen et al. (2015) and Gevaert and García-Haro (2015) reported that the models for data fusion could be implemented in different ways:

a) The spatial and temporal adaptive reflectance fusion model (STARFM)
   The STARFM implemented the prediction of a high-resolution image based on a lower resolution one with the same date and one pair of high and low-resolution sensors before or after the predicted date (Feng et al., 2006). The STARFM algorithm uses local weights to replace poor quality pixels with better quality ones based on spectral, temporal, and distance differences.
b) The enhanced spatial and temporal adaptive reflectance fusion model (ESTARFM)
   The enhanced STARFM uses two pairs before and after the predicted date of the lower resolution images (Zhu et al., 2010). It uses a weight function and a conversion coefficient. It claims to have better accuracy, even in complex landscapes, due to its consistent weighting function through the timeline.
c) The flexible spatiotemporal data fusion (FSDAF) 2.0
   This pixel-based fusion is from the ESTARFM model. The FSDAF model is effectively used for land cover detection with an enhanced pixel quality (Guo et al., 2020).

Zhang and Lin (2019) have applied the STARFM model and object-based analysis for mapping the rice area in China. They used MODIS-NDVI and Landsat-NDVI to make phenological profiles of rice and non-rice areas with a 16-day period. The result shows that the overall accuracy was increased by ~11%. Similar works were also shown with different models (Kim et al., 2020; Li et al., 2017; Zhuang et al., 2016). Moreover, another study used the ESTRAFM model for mapping sugarcane areas in China with MODIS-NDVI and HJ-1 CCD with an accuracy of >90% (Chen et al., 2020). We believe the above data fusion approaches should be considered and implemented in the GEE environment to improve the

classification accuracy and temporal frequency of RGS. Moreover, deep learning methods can be applied for RGS classification. Future research should focus on different sensor combinations, including Sentinel-2/MODIS-NDVI, Sentinel-2/PROBA-V, Sentinel-2/Sentinel-3, or Landsat/Sentinel-2/MODIS-NDVI. For example, the higher accuracy was achieved by simulated NDVI value of spectral values of lower resolution but a higher temporal resolution to predict the value of the missing data from the sensor with higher resolution but a less revisited date. Xiao et al. (2022) demonstrated that the fusion of MODIS and Sentinel-2 can achieve an overall accuracy of 87% in classifying water periods in China because the fusion method enables a shorter interval in the training datasets to detect the changes over the period.

7.3.4 Feature extraction and deep learning to improve the accuracy

Extracting textural features from optical images and combining them with existing spectral metrics improve prediction accuracy (Sun et al., 2019; Tian et al., 2019). One of the textural analyses that can be used for mapping the rice growth stages' statistical texture provides the spatial distribution of grey levels in an image using a statistical approach, such as the Grey level co-occurrence matrix (GLCM) method. GLCM can give information about features, such as homogeneity, contrast, entropy, angular second moment, variance, correlation and inverse difference moment. Okubo et al. (2010) found that homogeneity and contrast are important to increase land use separability. Moreover, Tassi and Vizzari (2020) have successfully integrated GLCM with spectral data in the GEE environment, with 82% accuracy, for mapping land cover in China from three different sources (e.g. Landsat-8, Sentinel-2, and PlanetScope).

Furthermore, deep learning methods have matured to a sufficient level to allow for quantitative analysis due to their more affordable memory and processing unit and free deep learning libraries, such as *keras* and TensorFlow. For example, a deep convolutional neural network is proved to be a robust classifier that combines spectral and spatial features to map rice areas with an accuracy of 97.06% (Zhang et al., 2018) with 31 variables from Landsat-8 and MODIS-NDVI data sources. By combining textual analysis and deep learning approaches, the accuracy of the rice growth map could be increased by >10% since the textual analysis can reveal useful hidden information and deep learning to solve high dimensional classification problems (X. M. Zhang et al., 2017). Moreover, textual analysis can also reduce the salt-and-pepper effect in the resultant prediction maps.

7.4 Future development in information dissemination

The present thesis focused on mapping RGS in near-real-time, over time with high accuracy. This can be used by agriculture stakeholders, such as public policymakers or fertiliser-, seed- and other trading companies. Moreover, online and mobile users have increased to 4.66 billion globally (Joseph, 2021). Disseminating information from remote sensing analysis to the users is quite difficult since most end-users are still on the learning curve of geospatial technology, such as Google Maps and Google Earth. Some improvements can be made in a few years to speed up the uptake of geospatial information at the decision-making level by developing a new rice monitoring system, as shown in Figure 7.4. The new rice monitoring system consists of five main subsystems: satellite data acquisition, data pre-processing, data analysis, information dissemination using an interactive website, and an android application. One of the future developments is combining RGS information with crop modelling and soil and weather data to improve the accuracy of rice yield predictions.

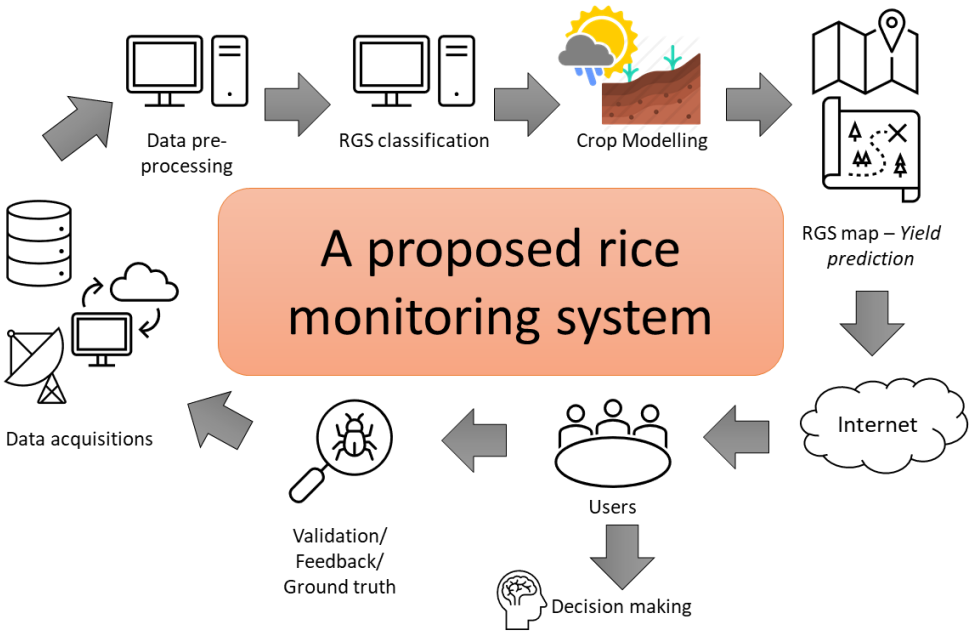

Figure 7.4 The suggested framework of a rice monitoring system

One example developed based on the thesis is the rice crop monitoring application using Sentinel-2. Chapter 4 workflow with Sentinel-2 reached overall accuracy as high as 90.6% have been used to model the RGS for rice monitoring system. This system has four

workstations and two web servers to provide a rice-growing map for Indonesia, which comprises 7.4 million ha and is available at the sub-district level. The users can use the application by browsing a website for exploring the RGS maps interactively (http://katam.litbang.pertanian.go.id/sc/). Moreover, the maps can also be viewed easily using an Android application that has been published on Google PlayStore under the name 'Monitoring of Sentinel-2 Rice Growth Stages'. Figure 7.5 shows screenshots of two interactive applications in the "Bahasa Indonesia" language.

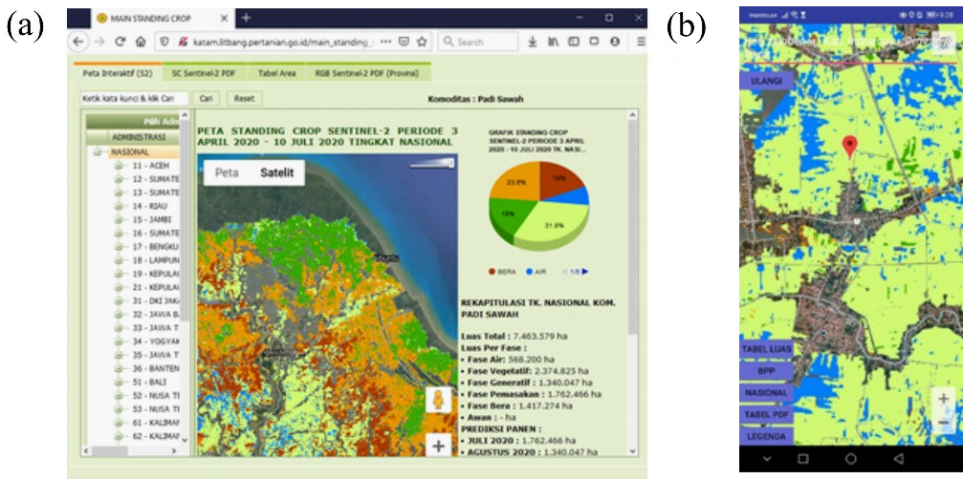

Figure 7.5 The example of remote sensing analysis for the user interface in (a) an interactive website and (b) an interactive Android application that was developed to disseminate the rice growth stage (RGS) information directly to the stakeholders.

The information of RGS in real-time will benefit the stakeholder on their related business such as farming management from the input and subsidise management until the off-farm activities such as combine harvester allocation (e.g. Table 7.2). Moreover, the RGS can be one of the alternatives for tracking rice productivity every year by combining it with a crop model, as suggested by previous studies (Ji et al., 2021; Rudiyanto et al., 2019; Setiyono et al., 2019).

Moreover, the machine learning model can be treated as a pre-trained model to predict the rice growth stages. In Indonesia, there are 73,713 extension workers distributed in 34 provinces (Apriyana et al., 2021; PUSDATIN, 2020). The extension workers or the farmers can check the RGS information using a mobile application to inform that the predicted analysis is right or wrong with any auxiliary information such as place, time, cropping calendar, or water distribution schedule. Thus, the data analysis can create a new model for

specific spatial and time to increase the temporal accuracy. Moreover, if the data collection reaches over 10,000 data points, the deep learning classifier can increase the computation time (Jo et al., 2020; Ndikumana, Minh, et al., 2018).

Table 7.2 The relationship between RGS information and farming management actions

Rice growth stage	Timespan (days after planting)	Actions	Stakeholders
Vegetative	0 – 60	• Input management (fertiliser, seeds, pesticide) • Water management and distribution	• Private Companies • Ministry of Agriculture • Ministry of Public Works • Farmers
Reproductive	61 - 90	• Pesticide allocation	• Private Companies • Ministry of Agriculture • Farmers
Ripening	91 - 120	• Combine harvester management • Estimation production of every administration level • Storage management	• Private Companies • Ministry of Agriculture • Ministry of Commerce
Bare land	-	• Secondary management for adding more crops depends on water availability	• Ministry of Agriculture • Farmers

7.5 Conclusion

The present thesis has proved new machine learning-based techniques for mapping RGS in a timely fashion with multiple sensors. Sentinel-2 returned the best accuracy among the different satellites due to its higher spatial and spectral resolution with a high level of sensitivity to rice crop changes. To fill the gaps in the optical imagery (Sentinel-2), the prediction maps from MOD13Q1 and Sentinel-1 were integrated, which improved the availability of time series maps (from one month to a 16-day period) under variable environmental conditions. The estimated vegetative and harvested areas correlated well with the local statistics monthly. The findings are encouraging for forecasting harvested areas since they indicate a moderate correlation between vegetative and harvested areas with a sufficient lag time. The proposed method and results can be a part of global rice monitoring, which consumes less time and labour than traditional practices. Additionally, our web application using multitemporal data could be one of the solutions for deploying rice monitoring to other parts of Indonesia and globally, especially for those developing countries with limited infrastructure.

Although the result of this study is promising to some extent, future research must produce better information in near-real-time combined with deep learning approaches to provide more robust solutions. Robust training data need to be developed to represent different rice ecosystems, such as rice cultivation in swampland, upland, or peatland areas. The proposed methodology can be easily embedded into other cloud computing systems such as Google Cloud, Amazon Web Service or Microsoft Azure, providing a flexible computational environment to extract additional features and implement deep learning approaches. The final maps could be combined with the existing rice monitoring projects globally, ensuring food security in regional areas. The method can also be made easily transferable to monitor other crop growth stages if the land use and cropping pattern are consistent over time.

Accurate RGS information can help farmers and stakeholders minimise risks and predict their fertiliser usage, pesticide usage, harvesting time and pricing mechanism to ensure both producer and consumer have a fair price. Moreover, the information can help the government adopt economic policies, such as to balance exports and imports, to protect smallholder farmers and food distribution in developing countries, especially in Indonesia with its 267 million people, and maintain food security on a regional scale. The technical information supports insurance companies for making transparent and reliable decisions,

enabling crop insurance schemes for smallholders viable. Overall, the mapping of RGS can be a tool to monitor the United Nations Sustainable Development Goals: Goal 2 Zero Hunger (Target 2.4) and decreased food prices anomalies by timely supply and demand information (Target 2.C) (Whitcraft et al., 2019).

[intentionally blank]

Reference List

Abadi, M., Barham, P., Chen, J., Chen, Z., Davis, A., Dean, J., Devin, M., Ghemawat, S., Irving, G., & Isard, M. (2016). Tensorflow: A system for large-scale machine learning. 12th symposium on operating systems design and implementation,

Abdi, S., & Ardiansyah. (2017). Identification of rice field using Multi-Temporal NDVI and PCA method on Landsat 8 (Case Study: Demak, Central Java). *IOP Conference Series: Earth and Environmental Science, 54*(1), 012001. http://stacks.iop.org/1755-1315/54/i=1/a=012001

Afdhalia, F., Supriatna, S., Shidiq, I. P. A., Manessa, M. D. M., & Ristya, Y. (2019). *Detection of rice varieties based on spectral value data using UAV-based images* (Vol. 11372). SPIE. https://doi.org/10.1117/12.2541473

Alajlan, N., Pasolli, E., Melgani, F., & Franzoso, A. (2014). Large-Scale Image Classification Using Active Learning. *IEEE Geoscience and Remote Sensing Letters, 11*(1), 259-263. https://doi.org/10.1109/LGRS.2013.2255258

Alam, M. S., Kalpoma, K., Karim, M. S., Al Sefat, A., & Kudoh, J. I. (2019). Boro Rice Yield Estimation Model Using Modis Ndvi Data for Bangladesh. *International Geoscience and Remote Sensing Symposium (IGARSS)*, 7330-7333. https://doi.org/10.1109/IGARSS.2019.8899084

Amani, M., Brisco, B., Afshar, M., Mirmazloumi, S. M., Mahdavi, S., Mirzadeh, S. M. J., Huang, W., & Granger, J. (2019). A generalized supervised classification scheme to produce provincial wetland inventory maps: an application of Google Earth Engine for big geo data processing. *Big Earth Data, 3*(4), 378-394. https://doi.org/10.1080/20964471.2019.1690404

Amani, M., Mahdavi, S., Afshar, M., Brisco, B., Huang, W., Mohammad Javad Mirzadeh, S., White, L., Banks, S., Montgomery, J., & Hopkinson, C. (2019). Canadian Wetland Inventory using Google Earth Engine: The First Map and Preliminary Results. *Remote Sensing, 11*(7). https://doi.org/10.3390/rs11070842

Aneece, I., & Thenkabail, P. (2018). Accuracies Achieved in Classifying Five Leading World Crop Types and their Growth Stages Using Optimal Earth Observing-1 Hyperion Hyperspectral Narrowbands on Google Earth Engine. *Remote Sensing, 10*(12). https://doi.org/10.3390/rs10122027

Apriyana, Y., Surmaini, E., Estiningtyas, W., Pramudia, A., Ramadhani, F., Suciantini, S., Susanti, E., Purnamayani, R., & Syahbuddin, H. (2021). The Integrated Cropping Calendar Information System: A Coping Mechanism to Climate Variability for Sustainable Agriculture in Indonesia. *Sustainability, 13*(11), 6495. https://www.mdpi.com/2071-1050/13/11/6495

Arévalo, P., Olofsson, P., & Woodcock, C. E. (2019, 2019/01/29/). Continuous monitoring of land change activities and post-disturbance dynamics from Landsat time series:

A test methodology for REDD+ reporting. *Remote Sensing of Environment*, 111051. https://doi.org/10.1016/j.rse.2019.01.013

Arjasakusuma, S., Swahyu Kusuma, S., Rafif, R., Saringatin, S., & Wicaksono, P. (2020). Combination of Landsat 8 OLI and Sentinel-1 SAR Time-Series Data for Mapping Paddy Fields in Parts of West and Central Java Provinces, Indonesia. *ISPRS International Journal of Geo-Information, 9*(11), 663. https://www.mdpi.com/2220-9964/9/11/663

Arumugam, P., Chemura, A., Schauberger, B., & Gornott, C. (2020). Near Real-Time Biophysical Rice (Oryza sativa L.) Yield Estimation to Support Crop Insurance Implementation in India. *Agronomy, 10*(11), 1674. https://www.mdpi.com/2073-4395/10/11/1674

Aulia, M. R., Liyantono, Setiawan, Y., & Fatikhunnada, A. (2016, //). Drought Detection of West Java's Paddy Field Using MODIS EVI Satellite Images (Case Study: Rancaekek and Rancaekek Wetan). *Procedia Environmental Sciences, 33*, 646-653. https://doi.org/10.1016/j.proenv.2016.03.119

Baghdadi, N., Cresson, R., Todoroff, P., & Moinet, S. (2010). Multitemporal Observations of Sugarcane by TerraSAR-X Images. *Sensors, 10*(10), 8899-8919. https://www.mdpi.com/1424-8220/10/10/8899

Baumann, M., Ozdogan, M., Richardson, A. D., & Radeloff, V. C. (2017, 2//). Phenology from Landsat when data is scarce: Using MODIS and Dynamic Time-Warping to combine multi-year Landsat imagery to derive annual phenology curves. *International Journal of Applied Earth Observation and Geoinformation, 54*, 72-83. https://doi.org/10.1016/j.jag.2016.09.005

Bazzi, H., Baghdadi, N., El Hajj, M., Zribi, M., Minh, D. H. T., Ndikumana, E., Courault, D., & Belhouchette, H. (2019). Mapping paddy rice using Sentinel-1 SAR time series in Camargue, France. *Remote Sensing, 11*, 1-16. https://doi.org/10.3390/RS11070887

Bégué, A., Arvor, D., Bellon, B., Betbeder, J., De Abelleyra, D., P. D. Ferraz, R., Lebourgeois, V., Lelong, C., Simões, M., & R. Verón, S. (2018). Remote Sensing and Cropping Practices: A Review. *Remote Sensing, 10*(1), 99. https://www.mdpi.com/2072-4292/10/1/99

Bégué, A., Leroux, L., Soumaré, M., Faure, J.-F., Diouf, A. A., Augusseau, X., Touré, L., & Tonneau, J.-P. (2020, 2020-May-14). Remote Sensing Products and Services in Support of Agricultural Public Policies in Africa: Overview and Challenges [Review]. *Frontiers in Sustainable Food Systems, 4*(58). https://doi.org/10.3389/fsufs.2020.00058

Belgiu, M., & Drăguţ, L. (2016, 4//). Random forest in remote sensing: A review of applications and future directions. *ISPRS Journal of Photogrammetry and Remote Sensing, 114*, 24-31. https://doi.org/10.1016/j.isprsjprs.2016.01.011

Belgiu, M., & Stein, A. (2019). Spatiotemporal image fusion in remote sensing. *Remote Sensing, 11*. https://doi.org/10.3390/rs11070818

Bharathkumar, L., & Mohammed-Aslam, M. A. (2015, //). Crop Pattern Mapping of Tumkur Taluk Using NDVI Technique: A Remote Sensing and GIS Approach. *Aquatic Procedia, 4*, 1397-1404. https://doi.org/10.1016/j.aqpro.2015.02.181

Bioresita, F., Puissant, A., Stumpf, A., & Malet, J.-P. (2018). A Method for Automatic and Rapid Mapping of Water Surfaces from Sentinel-1 Imagery. *Remote Sensing, 10*(2), 217. https://www.mdpi.com/2072-4292/10/2/217

Bisong, E. (2019). Google AutoML: Cloud Vision. In *Building Machine Learning and Deep Learning Models on Google Cloud Platform: A Comprehensive Guide for Beginners* (pp. 581-598). Apress. https://doi.org/10.1007/978-1-4842-4470-8_42

Boer, R., Dasanto, B. D., Perdinan, & Marthinus, D. (2012). Hydrologic Balance of Citarum Watershed under Current and Future Climate. In W. Leal Filho (Ed.), *Climate Change and the Sustainable Use of Water Resources* (pp. 43-59). Springer Berlin Heidelberg. https://doi.org/10.1007/978-3-642-22266-5_3

Bontkes, T. S., & Wopereis, M. (2003). *Decision Support Tools for Smallholder Agriculture in Sub-Saharan Africa: a Practical Guide*. International Center for Soil Fertility and Agriculture,.

Bórnez, K., Descals, A., Verger, A., & Peñuelas, J. (2020). Land surface phenology from VEGETATION and PROBA-V data. Assessment over deciduous forests. *International Journal of Applied Earth Observation and Geoinformation, 84*, 101974. https://doi.org/10.1016/j.jag.2019.101974

Boschetti, M., Busetto, L., Manfron, G., Laborte, A., Asilo, S., Pazhanivelan, S., & Nelson, A. (2017, 2017/06/01/). PhenoRice: A method for automatic extraction of spatio-temporal information on rice crops using satellite data time series. *Remote Sensing of Environment, 194*, 347-365. https://doi.org/10.1016/j.rse.2017.03.029

Boschetti, M., Stroppiana, D., Brivio, P. A., & Bocchi, S. (2009, 2009/08/20). Multi-year monitoring of rice crop phenology through time series analysis of MODIS images. *International Journal of Remote Sensing, 30*(18), 4643-4662. https://doi.org/10.1080/01431160802632249

Bouman, B. (2019). *Rice Knowledge Bank*. Retrieved 20 July 2019 from www.knowledgebank.irri.org

BPS-East-Java. (2018). *East Java Province in figures 2018*. Statistics of East Java Agency. https://indramayukab.bps.go.id/new/website/pdf_publikasi/Kabupaten-Indramayu-Dalam-Angka-2017.pdf

BPS-Indramayu. (2017). *Indramayu in figures 2017*. Statistics of Indramayu Regency. https://indramayukab.bps.go.id/new/website/pdf_publikasi/Kabupaten-Indramayu-Dalam-Angka-2017.pdf

BPS-West-Java. (2018). *West Java Province in figures 2018*. Statistics of West Java Agency. https://indramayukab.bps.go.id/new/website/pdf_publikasi/Kabupaten-Indramayu-Dalam-Angka-2017.pdf

BPS. (2018). *The methodology of food crop statistics*. Retrieved 20 March 2018 from https://www.bps.go.id/subject/53/tanaman-pangan.html#subjekViewTab2

BPS. (2020). *Statistical Yearbook of Indonesia 2019*

Breiman, L. (2001, October 01). Random Forests [journal article]. *Machine Learning, 45*(1), 5-32. https://doi.org/10.1023/a:1010933404324

Breiman, L., Friedman, J., Stone, C. J., & Olshen, R. A. (1984). *Classification and regression trees*. CRC press.

Brown, T. B., Hultine, K. R., Steltzer, H., Denny, E. G., Denslow, M. W., Granados, J., Henderson, S., Moore, D., Nagai, S., SanClements, M., Sánchez-Azofeifa, A., Sonnentag, O., Tazik, D., & Richardson, A. D. (2016). Using phenocams to monitor our changing Earth: toward a global phenocam network. *Frontiers in Ecology and the Environment, 14*(2), 84-93. https://doi.org/10.1002/fee.1222

Bruzzone, L. (2014). Land Use and Land Cover Mapping in Europe. *18*, 127-143. https://doi.org/10.1007/978-94-007-7969-3

Ç, K., Taşkın, G., & Erten, E. (2016). Paddy-Rice Phenology Classification Based on Machine-Learning Methods Using Multitemporal Co-Polar X-Band SAR Images. *IEEE Journal of Selected Topics in Applied Earth Observations and Remote Sensing, 9*(6), 2509-2519. https://doi.org/10.1109/JSTARS.2016.2547843

Cai, X. L., & Sharma, B. R. (2010, 2//). Integrating remote sensing, census and weather data for an assessment of rice yield, water consumption and water productivity in the Indo-Gangetic river basin. *Agricultural Water Management, 97*(2), 309-316. https://doi.org/10.1016/j.agwat.2009.09.021

Cai, Y., Lin, H., & Zhang, M. (2019, 2019/12/01/). Mapping paddy rice by the object-based random forest method using time series Sentinel-1/Sentinel-2 data. *Advances in Space Research, 64*(11), 2233-2244. https://doi.org/10.1016/j.asr.2019.08.042

Campos-Taberner, M., García-Haro, F., Camps-Valls, G., Grau-Muedra, G., Nutini, F., Busetto, L., Katsantonis, D., Stavrakoudis, D., Minakou, C., Gatti, L., Barbieri, M., Holecz, F., Stroppiana, D., & Boschetti, M. (2017). Exploitation of SAR and Optical Sentinel Data to Detect Rice Crop and Estimate Seasonal Dynamics of Leaf Area Index. *Remote Sensing, 9*(3), 248. http://www.mdpi.com/2072-4292/9/3/248

Campos-Taberner, M., García-Haro, F. J., Camps-Valls, G., Grau-Muedra, G., Nutini, F., Crema, A., & Boschetti, M. (2016, 2016/12/15/). Multitemporal and multiresolution leaf area index retrieval for operational local rice crop monitoring. *Remote Sensing of Environment, 187*, 102-118. https://doi.org/10.1016/j.rse.2016.10.009

Canisius, F., Shang, J., Liu, J., Huang, X., Ma, B., Jiao, X., Geng, X., Kovacs, J. M., & Walters, D. (2018, 2018/06/01/). Tracking crop phenological development using multi-temporal polarimetric Radarsat-2 data. *Remote Sensing of Environment, 210*, 508-518. https://doi.org/https://doi.org/10.1016/j.rse.2017.07.031

Cao, R., Tu, W., Yang, C., Li, Q., Liu, J., Zhu, J., Zhang, Q., Li, Q., & Qiu, G. (2020). Deep learning-based remote and social sensing data fusion for urban region function recognition. *ISPRS Journal of Photogrammetry and Remote Sensing, 163*, 82-97. https://doi.org/10.1016/j.isprsjprs.2020.02.014

Castillo, E. G., Tuong, T. P., Singh, U., Inubushi, K., & Padilla, J. (2006, 2006/08/01). Drought response of dry-seeded rice to water stress timing and N-fertilizer rates and sources. *Soil Science and Plant Nutrition, 52*(4), 496-508. https://doi.org/10.1111/j.1747-0765.2006.00064.x

Chakraborty, M., & Panigrahy, S. (2000, 6//). A processing and software system for rice crop inventory using multi-date RADARSAT ScanSAR data. *ISPRS Journal of Photogrammetry and Remote Sensing, 55*(2), 119-128. https://doi.org/10.1016/S0924-2716(00)00012-5

Chandna, P. K., & Mondal, S. (2020). Analyzing multi-year rice-fallow dynamics in Odisha using multi-temporal Landsat-8 OLI and Sentinel-1 Data. *GIScience and Remote Sensing, 57*, 431-449. https://doi.org/10.1080/15481603.2020.1731074

Chang, K.-W., Shen, Y., & Lo, J.-C. (2005). Predicting Rice Yield Using Canopy Reflectance Measured at Booting Stage. *Agronomy Journal, 97*(3), 872-878. https://doi.org/10.2134/agronj2004.0162

Chang, K. W., Shen, Y., & Lo, J. C. (2005). Predicting rice yield using canopy reflectance measured at booting stage. *Agronomy Journal, 97*(3), 872-878. https://doi.org/10.2134/agronj2004.0162

Chen, B., Huang, B., & Xu, B. (2015). Comparison of Spatiotemporal Fusion Models: A Review. *Remote Sensing, 7*(2), 1798-1835. https://www.mdpi.com/2072-4292/7/2/1798

Chen, C.-F., Chen, C.-R., & Son, N.-T. (2012, 2012/01/01). Investigating Rice Cropping Practices and Growing Areas from MODIS Data Using Empirical Mode Decomposition and Support Vector Machines. *GIScience & Remote Sensing, 49*(1), 117-138. https://doi.org/10.2747/1548-1603.49.1.117

Chen, C., Quilang, E. J. P., Alosnos, E. D., & Finnigan, J. (2011, 2011/10/14). Rice area mapping, yield, and production forecast for the province of Nueva Ecija using RADARSAT imagery. *Canadian Journal of Remote Sensing, 37*(1), 1-16. https://doi.org/10.5589/m11-024

Chen, C. F., Son, N. T., & Chang, L. Y. (2012, 1/15/). Monitoring of rice cropping intensity in the upper Mekong Delta, Vietnam using time-series MODIS data. *Advances in Space Research, 49*(2), 292-301. https://doi.org/10.1016/j.asr.2011.09.011

Chen, W., Xie, X., Wang, J., Pradhan, B., Hong, H., Bui, D. T., Duan, Z., & Ma, J. (2017, 2017/04/01/). A comparative study of logistic model tree, random forest, and classification and regression tree models for spatial prediction of landslide susceptibility. *CATENA, 151*, 147-160. https://doi.org/10.1016/j.catena.2016.11.032

Chen, Y., Feng, L., Mo, J., Mo, W., Ding, M., & Liu, Z. (2020, 2020/02/01). Identification of Sugarcane with NDVI Time Series Based on HJ-1 CCD and MODIS Fusion. *Journal of the Indian Society of Remote Sensing, 48*(2), 249-262. https://doi.org/10.1007/s12524-019-01042-1

Chen, Y., Li, C., Ghamisi, P., Jia, X., & Gu, Y. (2017). Deep fusion of remote sensing data for accurate classification. *IEEE Geoscience and Remote Sensing Letters, 14*, 1253-1257. https://doi.org/10.1109/LGRS.2017.2704625

Cheng, Y., Yu, L., Xu, Y., Lu, H., Cracknell, A. P., Kanniah, K., & Gong, P. (2018, 2018/01/17). Mapping oil palm extent in Malaysia using ALOS-2 PALSAR-2 data. *International Journal of Remote Sensing, 39*(2), 432-452. https://doi.org/10.1080/01431161.2017.1387309

Chini, M., Pelich, R., Hostache, R., Matgen, P., & Lopez-Martinez, C. (2018). Towards a 20 m Global Building Map from Sentinel-1 SAR Data. *Remote Sensing, 10*(11), 1833. https://www.mdpi.com/2072-4292/10/11/1833

Chung, S., Breshears, L. E., & Yoon, J.-Y. (2018, 2018/11/01/). Smartphone near infrared monitoring of plant stress. *Computers and Electronics in Agriculture, 154*, 93-98. https://doi.org/10.1016/j.compag.2018.08.046

Clauss, K., Ottinger, M., & Kuenzer, C. (2018, 2018/03/04). Mapping rice areas with Sentinel-1 time series and superpixel segmentation. *International Journal of Remote Sensing, 39*(5), 1399-1420. https://doi.org/10.1080/01431161.2017.1404162

Clauss, K., Yan, H., & Kuenzer, C. (2016). Mapping Paddy Rice in China in 2002, 2005, 2010 and 2014 with MODIS Time Series. *Remote Sensing, 8*(5), 434. http://www.mdpi.com/2072-4292/8/5/434

Cogliati, S., Sarti, F., Chiarantini, L., Cosi, M., Lorusso, R., Lopinto, E., Miglietta, F., Genesio, L., Guanter, L., Damm, A., Pérez-López, S., Scheffler, D., Tagliabue, G., Panigada, C., Rascher, U., Dowling, T. P. F., Giardino, C., & Colombo, R. (2021, 2021/09/01/). The PRISMA imaging spectroscopy mission: overview and first performance analysis. *Remote Sensing of Environment, 262*, 112499. https://doi.org/https://doi.org/10.1016/j.rse.2021.112499

Congalton, R. G., & Green, K. (2008). *Assessing the accuracy of remotely sensed data: Principles and practices*. CRC Press.

Conrad, C., Colditz, R. R., Dech, S., Klein, D., & Vlek, P. L. G. (2011, 2011/12/10). Temporal segmentation of MODIS time series for improving crop classification in

Central Asian irrigation systems. *International Journal of Remote Sensing, 32*(23), 8763-8778. https://doi.org/10.1080/01431161.2010.550647

Corcione, V., Nunziata, F., Mascolo, L., & Migliaccio, M. (2016, 2016/02/01). A study of the use of COSMO-SkyMed SAR PingPong polarimetric mode for rice growth monitoring. *International Journal of Remote Sensing, 37*(3), 633-647. https://doi.org/10.1080/01431161.2015.1131902

Cortes, C., & Vapnik, V. (1995). Support-Vector Networks. *Machine Learning, 20*(3), 273-297. https://doi.org/10.1023/A:1022627411411

Courault, D., Hossard, L., Flamain, F., Baghdadi, N., & Irfan, K. (2020). Assessment of Agricultural Practices From Sentinel 1 and 2 Images Applied on Rice Fields to Develop a Farm Typology in the Camargue Region. *IEEE Journal of Selected Topics in Applied Earth Observations and Remote Sensing, 13*, 5027-5035. https://doi.org/10.1109/JSTARS.2020.3018881

Cui, B., Zhao, Q.-j., Huang, W.-j., Song, X.-y., Ye, H.-c., & Zhou, X.-f. (2019, 2019/06/01/). Leaf chlorophyll content retrieval of wheat by simulated RapidEye, Sentinel-2 and EnMAP data. *Journal of Integrative Agriculture, 18*(6), 1230-1245. https://doi.org/https://doi.org/10.1016/S2095-3119(18)62093-3

Cutler, D. R., Edwards, T. C., Beard, K. H., Cutler, A., Hess, K. T., Gibson, J., & Lawler, J. J. (2007). Random Forests for Classification in Ecology. *Ecology, 88*(11), 2783-2792. https://doi.org/10.1890/07-0539.1

D'Arrigo, R., & Wilson, R. (2008). El Niño and Indian Ocean influences on Indonesian drought: implications for forecasting rainfall and crop productivity. *International Journal of Climatology, 28*(5), 611-616. https://doi.org/https://doi.org/10.1002/joc.1654

Darvishsefat, A. A., Abbasi, M., & Schaepman, M. E. (2011). Evaluation of spectral reflectance of seven Iranian rice varieties canopies. *Journal of Agricultural Science and Technology (JAST), 13*, 1091-1104. https://www.zora.uzh.ch/id/eprint/76772/

Daulay, A. R., Eka Intan, K. P., Barus, B., & Pramudya, N. B. (2016, 2016/07/14/). Rice Land Conversion into Plantation Crop and Challenges on Sustainable Land Use System in the East Tanjung Jabung Regency. *Procedia - Social and Behavioral Sciences, 227*, 174-180. https://doi.org/https://doi.org/10.1016/j.sbspro.2016.06.059

De Boissezon, H. (1995). Rapid estimates of acreage and potential yield in the European Union. *Proc Workshop for the Central and Eastern Europe on: Agrometereological Models: Theory and Applications in the MARS Project, Ispra. 21–25 Nov 1994*.

Dinas Pertanian, K. I. (2018). *Rice statistics in Indramayu Regency (in Bahasa Indonesia)*. Dinas Pertanian Kab. Indramayu.

Dinas Pertanian, K. K. (2018). *Rice statistics in Karawang Regency (in Bahasa Indonesia)*. Dinas Pertanian Kab. Karawang.

Dinas Pertanian, K. S. (2018). *Rice statistics in Subang Regency (in Bahasa Indonesia)*. Dinas Pertanian Kab. Subang.

Ding, M., Guan, Q., Li, L., Zhang, H., Liu, C., & Zhang, L. (2020). Phenology-based rice paddy mapping using multi-source satellite imagery and a fusion algorithm applied to the Poyang Lake plain, Southern China. *Remote Sensing, 12*. https://doi.org/10.3390/rs12061022

Dirgahayu, D., & Made Parsa, I. (2019). Detection Phase Growth of Paddy Crop Using SAR Sentinel-1 Data. *IOP Conference Series: Earth and Environmental Science, 280*. https://doi.org/10.1088/1755-1315/280/1/012020

Djurfeldt, G., & Jirström, M. (2005). The puzzle of the policy shift—The early Green Revolution in India, Indonesia and the Philippines. *The African food crisis: Lessons from the Asian Green Revolution. Wallingford (UK): CABI Publishing*, 43-63.

Domiri, D. D. (2017). The method for detecting biological parameter of rice growth and early planting of paddy crop by using multi temporal remote sensing data. *IOP Conference Series: Earth and Environmental Science, 54*(1), 012002. http://stacks.iop.org/1755-1315/54/i=1/a=012002

Dong, J., & Xiao, X. (2016, 9//). Evolution of regional to global paddy rice mapping methods: A review. *ISPRS Journal of Photogrammetry and Remote Sensing, 119*, 214-227. https://doi.org/10.1016/j.isprsjprs.2016.05.010

Dong, J., Xiao, X., Kou, W., Qin, Y., Zhang, G., Li, L., Jin, C., Zhou, Y., Wang, J., Biradar, C., Liu, J., & Moore Iii, B. (2015, 4//). Tracking the dynamics of paddy rice planting area in 1986–2010 through time series Landsat images and phenology-based algorithms. *Remote Sensing of Environment, 160*, 99-113. https://doi.org/10.1016/j.rse.2015.01.004

Dong, J., Xiao, X., Menarguez, M. A., Zhang, G., Qin, Y., Thau, D., Biradar, C., & Moore Iii, B. (2016, 11//). Mapping paddy rice planting area in northeastern Asia with Landsat 8 images, phenology-based algorithm and Google Earth Engine. *Remote Sensing of Environment, 185*, 142-154. https://doi.org/10.1016/j.rse.2016.02.016

Drusch, M., Del Bello, U., Carlier, S., Colin, O., Fernandez, V., Gascon, F., Hoersch, B., Isola, C., Laberinti, P., Martimort, P., Meygret, A., Spoto, F., Sy, O., Marchese, F., & Bargellini, P. (2012, 2012/05/15/). Sentinel-2: ESA's Optical High-Resolution Mission for GMES Operational Services. *Remote Sensing of Environment, 120*, 25-36. https://doi.org/10.1016/j.rse.2011.11.026

Duro, J. A., Lauk, C., Kastner, T., Erb, K.-H., & Haberl, H. (2020, 2020/09/01/). Global inequalities in food consumption, cropland demand and land-use efficiency: A decomposition analysis. *Global Environmental Change, 64*, 102124. https://doi.org/10.1016/j.gloenvcha.2020.102124

Ehlersa, M., Klonusa, S., Åstrandb, P. J., & Rossoa, P. (2010). Multi-sensor image fusion for pansharpening in remote sensing. *International Journal of Image and Data Fusion, 1*, 25-45. https://doi.org/10.1080/19479830903561985

Elagouz, M. H., Abou-Shleel, S. M., Belal, A. A., & El-Mohandes, M. A. O. (2019, 2019/01/06/). Detection of land use/cover change in Egyptian Nile Delta using remote sensing. *The Egyptian Journal of Remote Sensing and Space Science*. https://doi.org/10.1016/j.ejrs.2018.10.004

Erickson, N., Mueller, J., Shirkov, A., Zhang, H., Larroy, P., Li, M., & Smola, A. (2020). AutoGluon-Tabular: Robust and Accurate AutoML for Structured Data. *arXiv preprint arXiv:2003.06505*.

ESA. (2015). *Sentinel-2 User Handbook* [Handbook]. European Space Agency.

Fageria, N. K. (2007, 2007/05/09). Yield Physiology of Rice. *Journal of Plant Nutrition, 30*(6), 843-879. https://doi.org/10.1080/15226510701374831

Faisal, B. M. R., Rahman, H., Sharifee, N. H., Sultana, N., Islam, M. I., Habib, S. M. A., & Ahammad, a. T. (2020). Integrated Application of Remote Sensing and GIS in Crop Information System—A Case Study on Aman Rice Production Forecasting Using MODIS-NDVI in Bangladesh. *AgriEngineering, 2*, 264-279. https://doi.org/10.3390/agriengineering2020017

FAO. (2020). *Food Agriculture Organization. FAOSTAT citation database results. FAO*. Retrieved 1 July 2020 from

FAOSTAT. (2014). *Comparison paddy rice production between Indonesia and Asia in 2014*. the Food and Agriculture Organization Corporate Statistical Database. Retrieved October 2017 from http://www.fao.org/faostat/en/#data/QC

FAOSTAT. (2016). *Agriculture Organization of the United Nations Statistics Division (2014)*. http://faostat3.fao.org/browse/Q/QC/S

FAOSTAT. (2017). *Indonesia at a glance*. the Food and Agriculture Organization Corporate Statistical Database. Retrieved October 2017 from http://www.fao.org/indonesia/fao-in-indonesia/indonesia-at-a-glance/en/

FAOSTAT. (2019). *Agriculture database*. the Food and Agriculture Organization Corporate Statistical Database. Retrieved 15 April 2020 from http://www.fao.org/indonesia/fao-in-indonesia/indonesia-at-a-glance/en/

FAOSTAT. (2020a). *Agriculture and Population database*. the Food and Agriculture Organization Corporate Statistical Database. Retrieved 27 November 2020 from http://www.fao.org/faostat/en/#data

FAOSTAT. (2020b). *Population database*. the Food and Agriculture Organization Corporate Statistical Database. Retrieved 17 November 2020 from http://www.fao.org/faostat/en/#data/OA

FAOSTAT. (2021). *Agriculture Organization of the United Nations Statistics Division (2019)*. https://www.fao.org/faostat/en/#data/QCL

Fatikhunnada, A., Liyantono, Solahudin, M., Buono, A., Kato, T., & Seminar, K. B. (2020, 2020/01/01/). Assessment of pre-treatment and classification methods for Java paddy field cropping pattern detection on MODIS images. *Remote Sensing Applications: Society and Environment, 17*, 100281. https://doi.org/10.1016/j.rsase.2019.100281

Feng, G., Masek, J., Schwaller, M., & Hall, F. (2006). On the blending of the Landsat and MODIS surface reflectance: predicting daily Landsat surface reflectance. *IEEE Transactions on Geoscience and Remote Sensing, 44*(8), 2207-2218. https://doi.org/10.1109/TGRS.2006.872081

Fiorillo, E., Di Giuseppe, E., Fontanelli, G., & Maselli, F. (2020). Lowland Rice Mapping in Sédhiou Region (Senegal) Using Sentinel 1 and Sentinel 2 Data and Random Forest. *Remote Sensing, 12*(20), 3403. https://www.mdpi.com/2072-4292/12/20/3403

Flores-Anderson, A. I., Herndon, K. E., Thapa, R. B., & Cherrington, E. (2019). The SAR Handbook: Comprehensive Methodologies for Forest Monitoring and Biomass Estimation.

Foga, S., Scaramuzza, P. L., Guo, S., Zhu, Z., Dilley, R. D., Beckmann, T., Schmidt, G. L., Dwyer, J. L., Joseph Hughes, M., & Laue, B. (2017, 2017/06/01/). Cloud detection algorithm comparison and validation for operational Landsat data products. *Remote Sensing of Environment, 194*, 379-390. https://doi.org/10.1016/j.rse.2017.03.026

Foody, G. M. (2002, 2002/04/01/). Status of land cover classification accuracy assessment. *Remote Sensing of Environment, 80*(1), 185-201. https://doi.org/10.1016/S0034-4257(01)00295-4

Foody, G. M., & Mathur, A. (2006). The use of small training sets containing mixed pixels for accurate hard image classification: Training on mixed spectral responses for classification by a SVM. *Remote Sensing of Environment, 103*(2), 179-189. https://doi.org/10.1016/j.rse.2006.04.001

Frampton, W. J., Dash, J., Watmough, G., & Milton, E. J. (2013). Evaluating the capabilities of Sentinel-2 for quantitative estimation of biophysical variables in vegetation. *ISPRS Journal of Photogrammetry and Remote Sensing, 82*, 83-92. https://doi.org/10.1016/j.isprsjprs.2013.04.007

Franjaya, E. E., Syartinilia, & Setiawan, Y. (2017, 2017/01). Monitoring of landscape change in paddy fields: Case study of Karawang District - West Java Province. *IOP Conference Series: Earth and Environmental Science, 54*, 012016. https://doi.org/10.1088/1755-1315/54/1/012016

Gandharum, L., Mulyani, M. E., Hartono, D. M., Karsidi, A., & Ahmad, M. (2021, 2021/03/04). Remote sensing versus the area sampling frame method in paddy rice acreage estimation in Indramayu regency, West Java province, Indonesia. *International Journal of Remote Sensing, 42*(5), 1738-1767. https://doi.org/10.1080/01431161.2020.1842541

Gao, F., Anderson, M. C., Zhang, X., Yang, Z., Alfieri, J. G., Kustas, W. P., Mueller, R., Johnson, D. M., & Prueger, J. H. (2017, 1//). Toward mapping crop progress at field scales through fusion of Landsat and MODIS imagery. *Remote Sensing of Environment, 188*, 9-25. https://doi.org/10.1016/j.rse.2016.11.004

Gardner, M. W., & Dorling, S. R. (1998, 1998/08/01/). Artificial neural networks (the multilayer perceptron)—a review of applications in the atmospheric sciences. *Atmospheric Environment, 32*(14), 2627-2636. https://doi.org/10.1016/S1352-2310(97)00447-0

Gascon, F., Bouzinac, C., Thépaut, O., Jung, M., Francesconi, B., Louis, J., Lonjou, V., Lafrance, B., Massera, S., Gaudel-Vacaresse, A., Languille, F., Alhammoud, B., Viallefont, F., Pflug, B., Bieniarz, J., Clerc, S., Pessiot, L., Trémas, T., Cadau, E., De Bonis, R., Isola, C., Martimort, P., & Fernandez, V. (2017). Copernicus Sentinel-2A Calibration and Products Validation Status. *Remote Sensing, 9*(6), 584. https://www.mdpi.com/2072-4292/9/6/584

Gevaert, C. M., & García-Haro, F. J. (2015, 2015/01/01/). A comparison of STARFM and an unmixing-based algorithm for Landsat and MODIS data fusion. *Remote Sensing of Environment, 156*, 34-44. https://doi.org/10.1016/j.rse.2014.09.012

Ghassemian, H. (2016, 11//). A review of remote sensing image fusion methods. *Information Fusion, 32, Part A*, 75-89. https://doi.org/10.1016/j.inffus.2016.03.003

Gilbertson, J. K., Kemp, J., & van Niekerk, A. (2017, 2017/03/01/). Effect of pan-sharpening multi-temporal Landsat 8 imagery for crop type differentiation using different classification techniques. *Computers and Electronics in Agriculture, 134*, 151-159. https://doi.org/10.1016/j.compag.2016.12.006

Gomes, V. C. F., Queiroz, G. R., & Ferreira, K. R. (2020). An Overview of Platforms for Big Earth Observation Data Management and Analysis. *12*(8), 1253. https://www.mdpi.com/2072-4292/12/8/1253

Gorelick, N., Hancher, M., Dixon, M., Ilyushchenko, S., Thau, D., & Moore, R. (2017, 2017/07/06/). Google Earth Engine: Planetary-scale geospatial analysis for everyone. *Remote Sensing of Environment*. https://doi.org/10.1016/j.rse.2017.06.031

Griffiths, P., Hostert, P., Gruebner, O., & der Linden, S. v. (2010). Mapping megacity growth with multi-sensor data. *Remote Sensing of Environment, 114*(2), 426-439. https://doi.org/10.1016/j.rse.2009.09.012

Griffiths, P., Nendel, C., & Hostert, P. (2019). Intra-annual reflectance composites from Sentinel-2 and Landsat for national-scale crop and land cover mapping. *Remote Sensing of Environment, 220*, 135-151. https://doi.org/10.1016/j.rse.2018.10.031

Guan, K., Li, Z., Rao, L. N., Gao, F., Xie, D., Hien, N. T., & Zeng, Z. (2018). Mapping Paddy Rice Area and Yields Over Thai Binh Province in Viet Nam From MODIS, Landsat, and ALOS-2/PALSAR-2. *IEEE Journal of Selected Topics in Applied Earth Observations and Remote Sensing, 11*(7), 2238-2252. https://doi.org/10.1109/JSTARS.2018.2834383

Guan, X., Huang, C., Liu, G., Meng, X., & Liu, Q. (2016). Mapping Rice Cropping Systems in Vietnam Using an NDVI-Based Time-Series Similarity Measurement Based on DTW Distance. *Remote Sensing, 8*(1), 19. https://www.mdpi.com/2072-4292/8/1/19

Guanter, L., Kaufmann, H., Segl, K., Foerster, S., Rogass, C., Chabrillat, S., Kuester, T., Hollstein, A., Rossner, G., Chlebek, C., Straif, C., Fischer, S., Schrader, S., Storch, T., Heiden, U., Mueller, A., Bachmann, M., Mühle, H., Müller, R., Habermeyer, M., Ohndorf, A., Hill, J., Buddenbaum, H., Hostert, P., Van der Linden, S., Leitão, P. J., Rabe, A., Doerffer, R., Krasemann, H., Xi, H., Mauser, W., Hank, T., Locherer, M., Rast, M., Staenz, K., & Sang, B. (2015). The EnMAP Spaceborne Imaging Spectroscopy Mission for Earth Observation. *Remote Sensing, 7*(7), 8830-8857. https://www.mdpi.com/2072-4292/7/7/8830

Gumma, M. K., Nelson, A., Thenkabail, P. S., & Singh, A. N. (2011). Mapping rice areas of South Asia using MODIS multitemporal data. *Journal of Applied Remote Sensing, 5*(1), Article 053547. https://doi.org/10.1117/1.3619838

Gumma, M. K., Nelson, A., & Yamano, T. (2019, 2019/11/02). Mapping drought-induced changes in rice area in India. *International Journal of Remote Sensing, 40*(21), 8146-8173. https://doi.org/10.1080/01431161.2018.1547456

Guo, B., Yang, G., Zhang, F., Han, F., & Liu, C. (2018). Dynamic monitoring of soil erosion in the upper Minjiang catchment using an improved soil loss equation based on remote sensing and geographic information system. *Land Degradation & Development, 29*(3), 521-533. https://doi.org/10.1002/ldr.2882

Guo, D., Shi, W., Hao, M., & Zhu, X. (2020, 2020/10/01/). FSDAF 2.0: Improving the performance of retrieving land cover changes and preserving spatial details. *Remote Sensing of Environment, 248*, 111973. https://doi.org/10.1016/j.rse.2020.111973

Gururaj, P., Umesh, P., & Shetty, A. (2021, 2021/04/01). Assessment of surface soil moisture from ALOS PALSAR-2 in small-scale maize fields using polarimetric decomposition technique. *Acta Geophysica, 69*(2), 579-588. https://doi.org/10.1007/s11600-021-00557-x

Guyon, I., Vapnik, V., Boser, B., Bottou, L., & Solla, S. A. (1992). Capacity control in linear classifiers for pattern recognition. *Proc. 11th Int. Conf. on Pattern Recognition, 2*, 385-388.

Han, D., Yang, H., Yang, G., & Qiu, C. (2018, //). Monitoring model of maize lodging based on Sentinel-1 radar image. *Transactions of the Chinese Society of Agricultural Engineering, 34*(3), 166-172. https://www.ingentaconnect.com/content/tcsae/tcsae/2018/00000034/00000003/art00022

Han, J., Zhang, Z., Luo, Y., Cao, J., Zhang, L., Cheng, F., Zhuang, H., Zhang, J., & Tao, F. (2021). NESEA-Rice10: high-resolution annual paddy rice maps for Northeast and Southeast Asia from 2017 to 2019. *Earth Syst. Sci. Data, 13*(12), 5969-5986. https://doi.org/10.5194/essd-13-5969-2021

Hao, B., Ma, M., Li, S., Li, Q., Hao, D., Huang, J., Ge, Z., Yang, H., & Han, X. (2019, May 7). Land Use Change and Climate Variation in the Three Gorges Reservoir Catchment from 2000 to 2015 Based on the Google Earth Engine. *Sensors (Basel), 19*(9). https://doi.org/10.3390/s19092118

Hardke, J. T. (2013). Arkansas rice production handbook. *Misc. Publ, 192*.

Hazaymeh, K., & Hassan, Q. K. (2017, 2017/06/01). A remote sensing-based agricultural drought indicator and its implementation over a semi-arid region, Jordan. *Journal of Arid Land, 9*(3), 319-330. https://doi.org/10.1007/s40333-017-0014-6

He, Z., Li, S., Wang, Y., Dai, L., & Lin, S. (2018). Monitoring Rice Phenology Based on Backscattering Characteristics of Multi-Temporal RADARSAT-2 Datasets. *Remote Sensing, 10*(2), 340. https://www.mdpi.com/2072-4292/10/2/340

Heung, B., Ho, H. C., Zhang, J., Knudby, A., Bulmer, C. E., & Schmidt, M. G. (2016, 3/1/). An overview and comparison of machine-learning techniques for classification purposes in digital soil mapping. *Geoderma, 265*, 62-77. https://doi.org/10.1016/j.geoderma.2015.11.014

Hijmans, R. J. (2016). *raster: Geographic Data Analysis and Modeling.* In https://CRAN.R-project.org/package=raster

Hoang, H. K., Bernier, M., Duchesne, S., & Tran, Y. M. (2016). Rice Mapping Using RADARSAT-2 Dual- and Quad-Pol Data in a Complex Land-Use Watershed: Cau River Basin (Vietnam). *IEEE Journal of Selected Topics in Applied Earth Observations and Remote Sensing, 9*(7), 3082-3096. https://doi.org/10.1109/JSTARS.2016.2586102

Holecz, F., Barbieri, M., Collivignarelli, F., Gatti, L., Nelson, A., Setiyono, T. D., Boschetti, M., Manfron, G., Brivio, P. A., Quilang, E. J., Obico, M. R., Minh, V. Q., Kieu, D. P., Huu, Q. N., Veasna, T., Intrman, A., Wahyunto, P., & Pazhanivelan, S. (2013). an Operational Remote Sensing Based Service for Rice Production Estimation At National Scale. *ESA Living Planet Symposium*. https://doi.org/10.13140/2.1.1492.8643

Holloway, J., & Mengersen, K. (2018). Statistical Machine Learning Methods and Remote Sensing for Sustainable Development Goals: A Review. *Remote Sensing, 10*(9), 1365. https://www.mdpi.com/2072-4292/10/9/1365

Holmes, E., & Ward, E. (2019). Applied Time Series Analysis for Fisheries and Environmental Sciences. *University of Washington, lecture material*.

Hu, Q., Sulla-Menashe, D., Xu, B., Yin, H., Tang, H., Yang, P., & Wu, W. (2019, 2019/08/01/). A phenology-based spectral and temporal feature selection method for crop mapping from satellite time series. *International Journal of Applied Earth Observation and Geoinformation, 80*, 218-229. https://doi.org/10.1016/j.jag.2019.04.014

Huang, H., Gong, P., Clinton, N., & Hui, F. (2008). Reduction of atmospheric and topographic effect on Landsat TM data for forest classification. *International Journal of Remote Sensing, 29*(19), 5623-5642. https://doi.org/10.1080/01431160802082148

Huang, J., Liao, H., Zhu, Y., Sun, J., Sun, Q., & Liu, X. (2012, 2012/03/01/). Hyperspectral detection of rice damaged by rice leaf folder (Cnaphalocrocis medinalis). *Computers and Electronics in Agriculture, 82*, 100-107. https://doi.org/https://doi.org/10.1016/j.compag.2012.01.002

IAARD. (2011). *Pedoman umum adaptasi perubahan iklim sektor pertanian (The general guideline adaptation to climate change in the agricultural sector)*. IAARD Press.

Indonesia Ministry of Agrarian Affairs and Spatial Planning. (2020). *The Official of National Rice Field Area in 2019*. Retrieved 19 September 2020 from https://databoks.katadata.co.id/datapublish/2020/02/05/indonesia-miliki-luas-baku-sawah-746-juta-hektare

Inoue, S., Ito, A., & Yonezawa, C. (2020a). Mapping Paddy Fields in Japan by Using a Sentinel-1 SAR Time Series Supplemented by Sentinel-2 Images on Google Earth Engine. *Remote Sensing*. https://doi.org/10.3390/rs12101622

Inoue, S., Ito, A., & Yonezawa, C. (2020b). Mapping Paddy Fields in Japan by Using a Sentinel-1 SAR Time Series Supplemented by Sentinel-2 Images on Google Earth Engine. *Remote Sensing, 12*(10), 1622.

Inoue, Y., Kurosu, T., Maeno, H., Uratsuka, S., Kozu, T., Dabrowska-Zielinska, K., & Qi, J. (2002). Season-long daily measurements of multifrequency (Ka, Ku, X, C, and L) and full-polarization backscatter signatures over paddy rice field and their relationship with biological variables. *Remote Sensing of Environment, 81*(2-3), 194-204. https://doi.org/10.1016/S0034-4257(01)00343-1

Jana, A., Maiti, S., & Biswas, A. (2016). Seasonal change monitoring and mapping of coastal vegetation types along Midnapur-Balasore Coast, Bay of Bengal using multi-temporal landsat data. *Modeling Earth Systems and Environment, 2*, 1-12. https://doi.org/10.1007/s40808-015-0062-x

Jędrych, M., Zagajewski, B., & Marcinkowska-Ochtyra, A. (2017). Application of Sentinel-2 and EnMAP new satellite data to the mapping of alpine vegetation of the Karkonosze Mountains. *Polish Cartographical Review, 49*(3), 107-119.

Jensen, J. R. (2015). *Introductory digital image processing: A remote sensing perspective (4th ed.)*. Prentice Hall Press.

Ji, Z., Pan, Y., Zhu, X., Wang, J., & Li, Q. (2021). Prediction of Crop Yield Using Phenological Information Extracted from Remote Sensing Vegetation Index. *Sensors, 21*(4), 1406. https://www.mdpi.com/1424-8220/21/4/1406

Jiao, X., McNairn, H., Shang, J., Pattey, E., Liu, J., & Champagne, C. (2011, 2011/02/01). The sensitivity of RADARSAT-2 polarimetric SAR data to corn and soybean leaf area index. *Canadian Journal of Remote Sensing, 37*(1), 69-81. https://doi.org/10.5589/m11-023

Jin, C., Xiao, X., Dong, J., Qin, Y., & Wang, Z. (2016, 2016/03/01). Mapping paddy rice distribution using multi-temporal Landsat imagery in the Sanjiang Plain, northeast China. *Frontiers of Earth Science, 10*(1), 49-62. https://doi.org/10.1007/s11707-015-0518-3

Jo, H.-W., Lee, S., Park, E., Lim, C.-H., Song, C., Lee, H., Ko, Y., Cha, S., Yoon, H., & Lee, W.-K. (2020). Deep Learning Applications on Multitemporal SAR (Sentinel-1) Image Classification Using Confined Labeled Data: The Case of Detecting Rice Paddy in South Korea. *IEEE Transactions on Geoscience and Remote Sensing, PP*, 1-13. https://doi.org/10.1109/tgrs.2020.2981671

Joseph, J. (2021). *Global digital population as of January 2021*. Statista. Retrieved 22 August 2021 from https://www.statista.com/statistics/617136/digital-population-worldwide/

Joshi, N., Baumann, M., Ehammer, A., Fensholt, R., Grogan, K., Hostert, P., Jepsen, M. R., Kuemmerle, T., Meyfroidt, P., Mitchard, E. T. A., Reiche, J., Ryan, C. M., & Waske, B. (2016). A review of the application of optical and radar remote sensing data fusion to land use mapping and monitoring. *Remote Sensing*. https://doi.org/10.3390/rs8010070

Kalpoma, K. A., Chowdhury, A., Arony, N. N., Nowshin, M., & Kudoh, J. I. (2019). New Modis Vegetation Index for Boro Rice Model Using 3d Plot and K-NN: Bangladesh Haor Region Perspective. *International Geoscience and Remote Sensing Symposium (IGARSS)*, 7322-7325. https://doi.org/10.1109/IGARSS.2019.8898950

Kang, J., Hong, D., Liu, J., Baier, G., Yokoya, N., & Demir, B. (2020). Learning Convolutional Sparse Coding on Complex Domain for Interferometric Phase Restoration. *IEEE Transactions on Neural Networks and Learning Systems*, 1-15. https://doi.org/10.1109/TNNLS.2020.2979546

Kaplan, G., Fine, L., Lukyanov, V., Manivasagam, V. S., Tanny, J., & Rozenstein, O. (2021). Normalizing the Local Incidence Angle in Sentinel-1 Imagery to Improve

Leaf Area Index, Vegetation Height, and Crop Coefficient Estimations. *Land, 10*(7), 680. https://www.mdpi.com/2073-445X/10/7/680

Kavzoglu, T., & Colkesen, I. (2009, 2009/10/01/). A kernel functions analysis for support vector machines for land cover classification. *International Journal of Applied Earth Observation and Geoinformation, 11*(5), 352-359. https://doi.org/10.1016/j.jag.2009.06.002

Kawamura, K., Ikeura, H., Phongchanmaixay, S., & Khanthavong, P. (2018). Canopy Hyperspectral Sensing of Paddy Fields at the Booting Stage and PLS Regression can Assess Grain Yield. *Remote Sensing, 10*(8), 1249. https://www.mdpi.com/2072-4292/10/8/1249

Ketkar, N. (2017). Introduction to keras. In *Deep learning with Python* (pp. 97-111). Springer.

Khabbazan, S., Vermunt, P., Steele-Dunne, S., Ratering Arntz, L., Marinetti, C., van der Valk, D., Iannini, L., Molijn, R., Westerdijk, K., & van der Sande, C. (2019). Crop Monitoring Using Sentinel-1 Data: A Case Study from The Netherlands. *Remote Sensing, 11*(16), 1887. https://www.mdpi.com/2072-4292/11/16/1887

Kim, Y., Hong, S., Lee, K., Jang, S., Lee, H., & Oh, Y. (2013). Monitoring wheat growth by COSMO-SkyMed SAR Images. *Korean Journal of Remote Sensing, 29*(1), 35-43.

Kim, Y., Kyriakidis, P. C., & Park, N.-W. (2020). A Cross-Resolution, Spatiotemporal Geostatistical Fusion Model for Combining Satellite Image Time-Series of Different Spatial and Temporal Resolutions. *Remote Sensing, 12*(10), 1553. https://www.mdpi.com/2072-4292/12/10/1553

King, R. L., & Jianwen, W. (2001, 9-13 July 2001). A wavelet based algorithm for pan sharpening Landsat 7 imagery. IGARSS 2001. Scanning the Present and Resolving the Future. Proceedings. IEEE 2001 International Geoscience and Remote Sensing Symposium (Cat. No.01CH37217),

Kläs, M., & Vollmer, A. M. (2018, 2018//). Uncertainty in Machine Learning Applications: A Practice-Driven Classification of Uncertainty. Computer Safety, Reliability, and Security, Cham.

Knox, S. H., Dronova, I., Sturtevant, C., Oikawa, P. Y., Matthes, J. H., Verfaillie, J., & Baldocchi, D. (2017, 2017/05/01/). Using digital camera and Landsat imagery with eddy covariance data to model gross primary production in restored wetlands. *Agricultural and Forest Meteorology, 237*, 233-245. https://doi.org/10.1016/j.agrformet.2017.02.020

Kogan, F., Guo, W., & Yang, W. (2019, 2019/01/01). Drought and food security prediction from NOAA new generation of operational satellites. *Geomatics, Natural Hazards and Risk, 10*(1), 651-666. https://doi.org/10.1080/19475705.2018.1541257

Konishi, T., Omatu, S., & Suga, Y. (2007, July 01). Extraction rice-planted areas by RADARSAT data using neural networks [journal article]. *Artificial Life and Robotics, 11*(2), 211-214. https://doi.org/10.1007/s10015-007-0430-3

Kontgis, C., Schneider, A., & Ozdogan, M. (2015, 11//). Mapping rice paddy extent and intensification in the Vietnamese Mekong River Delta with dense time stacks of Landsat data. *Remote Sensing of Environment, 169*, 255-269. https://doi.org/10.1016/j.rse.2015.08.004

Kontgis, C., Warren, M. S., Skillman, S. W., Chartrand, R., & Moody, D. I. (2017). Leveraging Sentinel-1 time-series data for mapping agricultural land cover and land use in the tropics. *2017 9th International Workshop on the Analysis of Multitemporal Remote Sensing Images, MultiTemp 2017*, 1-4. https://doi.org/10.1109/Multi-Temp.2017.8035199

Koppe, W., Gnyp, M. L., Hütt, C., Yao, Y., Miao, Y., Chen, X., & Bareth, G. (2012). Rice monitoring with multi-temporal and dual-polarimetric terrasar-X data. *International Journal of Applied Earth Observation and Geoinformation, 21*, 568-576. https://doi.org/10.1016/j.jag.2012.07.016

Koppe, W., Gnyp, M. L., Hütt, C., Yao, Y., Miao, Y., Chen, X., & Bareth, G. (2013, 4//). Rice monitoring with multi-temporal and dual-polarimetric TerraSAR-X data. *International Journal of Applied Earth Observation and Geoinformation, 21*, 568-576. https://doi.org/10.1016/j.jag.2012.07.016

Kottek, M., Grieser, J., Beck, C., Rudolf, B., & Rubel, F. (2006). World map of the Köppen-Geiger climate classification updated. *Meteorologische Zeitschrift, 15*(3), 259-263. https://doi.org/10.1127/0941-2948/2006/0130

Kuenzer, C., & Knauer, K. (2013). Remote sensing of rice crop areas. *International Journal of Remote Sensing, 34*(6), 2101-2139. https://doi.org/10.1080/01431161.2012.738946

Kuhn, M. (2008, 2008-11-10). Building Predictive Models in R Using the caret Package. *Journal of Statistical Software; Vol 1, Issue 5 (2008), 28*(5), 26. https://doi.org/10.18637/jss.v028.i05

Kuhn, M., & Johnson, K. (2013). *Applied predictive modeling* (Vol. 810). Springer.

Kwak, Y., Arifuzzanman, B., & Iwami, Y. (2015). Prompt proxy mapping of flood damaged rice fields using MODIS-derived indices. *Remote Sensing, 7*, 15969-15988. https://doi.org/10.3390/rs71215805

Landis, J. R., & Koch, G. G. (1977). The Measurement of Observer Agreement for Categorical Data. *Biometrics, 33*(1), 159-174. https://doi.org/10.2307/2529310

LAPAN. (2019). *Rice growth stages with Terra MODIS (in Indonesian)*. Retrieved 25 February 2019 from http://sipandora.lapan.go.id/site/fasepertumbuhanpadi

Lasko, K., Vadrevu, K. P., Tran, V. T., & Justice, C. (2018). Mapping Double and Single Crop Paddy Rice with Sentinel-1A at Varying Spatial Scales and Polarizations in Hanoi, Vietnam. *IEEE Journal of Selected Topics in Applied Earth Observations and Remote Sensing, 11*, 498-512. https://doi.org/10.1109/JSTARS.2017.2784784

Lavreniuk, M., Kussul, N., Meretsky, M., Lukin, V., Abramov, S., & Rubel, O. (2017, 29 May-2 June 2017). Impact of SAR data filtering on crop classification accuracy. 2017 IEEE First Ukraine Conference on Electrical and Computer Engineering (UKRCON),

Lebourgeois, V., Bégué, A., Labbé, S., Mallavan, B., Prévot, L., & Roux, B. (2008). Can Commercial Digital Cameras Be Used as Multispectral Sensors? A Crop Monitoring Test. *Sensors, 8*(11), 7300-7322. https://www.mdpi.com/1424-8220/8/11/7300

Lebrini, Y., Boudhar, A., Hadria, R., Lionboui, H., Elmansouri, L., Arrach, R., Ceccato, P., & Benabdelouahab, T. (2019, August 01). Identifying Agricultural Systems Using SVM Classification Approach Based on Phenological Metrics in a Semi-arid Region of Morocco [journal article]. *Earth Systems and Environment, 3*(2), 277-288. https://doi.org/10.1007/s41748-019-00106-z

Lee, J.-S. (1981, 1981/04/01/). Refined filtering of image noise using local statistics. *Computer Graphics and Image Processing, 15*(4), 380-389. https://doi.org/10.1016/S0146-664X(81)80018-4

Lee, J. S., Jurkevich, L., Dewaele, P., Wambacq, P., & Oosterlinck, A. (1994, 1994/02/01). Speckle filtering of synthetic aperture radar images: A review. *Remote Sensing Reviews, 8*(4), 313-340. https://doi.org/10.1080/02757259409532206

Lewis, D. J., Barham, B. L., & Zimmerer, K. S. (2008, 2008/10/01/). Spatial Externalities in Agriculture: Empirical Analysis, Statistical Identification, and Policy Implications. *World Development, 36*(10), 1813-1829. https://doi.org/10.1016/j.worlddev.2007.10.017

Li, F., Chen, W., Zeng, Y., Zhao, Q., & Wu, B. (2014). Improving Estimates of Grassland Fractional Vegetation Cover Based on a Pixel Dichotomy Model: A Case Study in Inner Mongolia, China. *Remote Sensing, 6*(6), 4705. http://www.mdpi.com/2072-4292/6/6/4705

Li, H., Wan, W., Fang, Y., Zhu, S., Chen, X., Liu, B., & Hong, Y. (2019). A Google Earth Engine-enabled software for efficiently generating high-quality user-ready Landsat mosaic images. *Environmental Modelling & Software, 112*, 16-22. https://doi.org/10.1016/j.envsoft.2018.11.004

Li, K., Brisco, B., Yun, S., & Touzi, R. (2012, 2012/01/01). Polarimetric decomposition with RADARSAT-2 for rice mapping and monitoring. *Canadian Journal of Remote Sensing, 38*(2), 169-179. https://doi.org/10.5589/m12-024

Li, L., Zhao, Y., Fu, Y., Pan, Y., Yu, L., & Xin, Q. (2017). High Resolution Mapping of Cropping Cycles by Fusion of Landsat and MODIS Data. *Remote Sensing, 9*(12), 1232. https://www.mdpi.com/2072-4292/9/12/1232

Li, R., Xu, M., Chen, Z., Gao, B., Cai, J., Shen, F., He, X., Zhuang, Y., & Chen, D. (2021, 2021/02/01/). Phenology-based classification of crop species and rotation types using fused MODIS and Landsat data: The comparison of a random-forest-based model and a decision-rule-based model. *Soil and Tillage Research, 206*, 104838. https://doi.org/https://doi.org/10.1016/j.still.2020.104838

Li, Y., Liao, Q., Li, X., Liao, S., Chi, G., & Peng, S. (2003). Towards an operational system for regional-scale rice yield estimation using a time-series of Radarsat ScanSAR images. *International Journal of Remote Sensing, 24*, 4207-4220. https://doi.org/10.1080/0143116031000095970

Liakos, K. G., Busato, P., Moshou, D., Pearson, S., & Bochtis, D. (2018). Machine Learning in Agriculture: A Review. *Sensors, 18*(8), 2674. https://www.mdpi.com/1424-8220/18/8/2674

Liao, C., Wang, J., Shang, J., Huang, X., Liu, J., & Huffman, T. (2018, 2018/03/04). Sensitivity study of Radarsat-2 polarimetric SAR to crop height and fractional vegetation cover of corn and wheat. *International Journal of Remote Sensing, 39*(5), 1475-1490. https://doi.org/10.1080/01431161.2017.1407046

Liaw, A., & Wiener, M. (2002). Classification and Regression by randomForest. *R News, 2*(3), 18-22. http://CRAN.R-project.org/doc/Rnews/

Lillesand, T., Kiefer, R. W., & Chipman, J. (2015). *Remote sensing and image interpretation*. John Wiley & Sons.

Liu, J., Li, L., Huang, X., Liu, Y., & Li, T. (2019, 2019/03/01). Mapping paddy rice in Jiangsu Province, China, based on phenological parameters and a decision tree model. *Frontiers of Earth Science, 13*(1), 111-123. https://doi.org/10.1007/s11707-018-0723-y

Liu, J., Zhang, Z., Xu, X., Kuang, W., Zhou, W., Zhang, S., Li, R., Yan, C., Yu, D., Wu, S., & Jiang, N. (2010). Spatial patterns and driving forces of land use change in China during the early 21st century. *Journal of Geographical Sciences, 20*(4), 483-494. https://doi.org/10.1007/s11442-010-0483-4

Liu, L., Huang, J., Xiong, Q., Zhang, H., Song, P., Huang, Y., Dou, Y., & Wang, X. (2020). Optimal MODIS data processing for accurate multi-year paddy rice area mapping in China Optimal MODIS data processing for accurate multi-year paddy rice area mapping. *GIScience & Remote Sensing, 00*, 1-17. https://doi.org/10.1080/15481603.2020.1773012

Liu, L., Xiao, X., Qin, Y., Wang, J., Xu, X., Hu, Y., & Qiao, Z. (2020). Mapping cropping intensity in China using time series Landsat and Sentinel-2 images and Google Earth Engine. *Remote Sensing of Environment, 239*, 111624. https://doi.org/10.1016/j.rse.2019.111624

Liu, Y., Chen, K., Xu, P., & Li, Z. (2016). Modeling and Characteristics of Microwave Backscattering From Rice Canopy Over Growth Stages. *IEEE Transactions on Geoscience and Remote Sensing, 54*(11), 6757-6770. https://doi.org/10.1109/TGRS.2016.2590439

Liu, Y., Hill, M. J., Zhang, X., Wang, Z., Richardson, A. D., Hufkens, K., Filippa, G., Baldocchi, D. D., Ma, S., Verfaillie, J., & Schaaf, C. B. (2017, 2017/05/01/). Using data from Landsat, MODIS, VIIRS and PhenoCams to monitor the phenology of California oak/grass savanna and open grassland across spatial scales. *Agricultural and Forest Meteorology, 237*, 311-325. https://doi.org/10.1016/j.agrformet.2017.02.026

Liu, Z., Hu, Q., Tan, J., & Zou, J. (2019, 2019/04/03). Regional scale mapping of fractional rice cropping change using a phenology-based temporal mixture analysis. *International Journal of Remote Sensing, 40*(7), 2703-2716. https://doi.org/10.1080/01431161.2018.1530812

Lopes, M., Frison, P.-L., Crowson, M., Warren-Thomas, E., Hariyadi, B., Kartika, W. D., Agus, F., Hamer, K. C., Stringer, L., Hill, J. K., & Pettorelli, N. (2020). Improving the accuracy of land cover classification in cloud persistent areas using optical and radar satellite image time series. *Methods in Ecology and Evolution, 11*(4), 532-541. https://doi.org/10.1111/2041-210x.13359

Louis, J., Debaecker, V., Pflug, B., Main-Knorn, M., Bieniarz, J., Mueller-Wilm, U., Cadau, E., & Gascon, F. (2016). *SENTINEL-2 SEN2COR: L2A Processor for Users* ESA Living Planet Symposium 2016, Prague, Czech Republic. https://elib.dlr.de/107381/

Lowder, S. K., Skoet, J., & Raney, T. (2016, 2016/11/01/). The Number, Size, and Distribution of Farms, Smallholder Farms, and Family Farms Worldwide. *World Development, 87*, 16-29. https://doi.org/10.1016/j.worlddev.2015.10.041

Lu, Y., Coops, N. C., & Hermosilla, T. (2017, 2017/04/01/). Estimating urban vegetation fraction across 25 cities in pan-Pacific using Landsat time series data. *ISPRS Journal of Photogrammetry and Remote Sensing, 126*(Supplement C), 11-23. https://doi.org/10.1016/j.isprsjprs.2016.12.014

Lunetta, R. S., Shao, Y., Ediriwickrema, J., & Lyon, J. G. (2010). Monitoring agricultural cropping patterns across the Laurentian Great Lakes Basin using MODIS-NDVI data. *International Journal of Applied Earth Observation and Geoinformation, 12*(2), 81-88. https://doi.org/10.1016/j.jag.2009.11.005

Lyu, S., Noguchi, N., Ospina, R., & Kishima, Y. (2021). Development of phenotyping system using low altitude UAV imagery and deep learning. *International Journal of Agricultural and Biological Engineering, 14*(1), 207-215.

Mahdianpari, M., Salehi, B., Mohammadimanesh, F., Brisco, B., Homayouni, S., Gill, E., DeLancey, E. R., & Bourgeau-Chavez, L. (2020). Big Data for a Big Country: The First Generation of Canadian Wetland Inventory Map at a Spatial Resolution of

10-m Using Sentinel-1 and Sentinel-2 Data on the Google Earth Engine Cloud Computing Platform. *Canadian Journal of Remote Sensing, 46*(1), 15-33. https://doi.org/10.1080/07038992.2019.1711366

Mahdianpari, M., Salehi, B., Mohammadimanesh, F., Homayouni, S., & Gill, E. (2018). The First Wetland Inventory Map of Newfoundland at a Spatial Resolution of 10 m Using Sentinel-1 and Sentinel-2 Data on the Google Earth Engine Cloud Computing Platform. *Remote Sensing, 11*(1). https://doi.org/10.3390/rs11010043

Malenovský, Z., Rott, H., Cihlar, J., Schaepman, M. E., García-Santos, G., Fernandes, R., & Berger, M. (2012, 2012/05/15/). Sentinels for science: Potential of Sentinel-1, -2, and -3 missions for scientific observations of ocean, cryosphere, and land. *Remote Sensing of Environment, 120*, 91-101. https://doi.org/10.1016/j.rse.2011.09.026

Mandal, D., Kumar, V., Bhattacharya, A., Rao, Y. S., Siqueira, P., & Bera, S. (2018). Sen4Rice: A Processing Chain for Differentiating Early and Late Transplanted Rice Using Time-Series Sentinel-1 SAR Data With Google Earth Engine. *IEEE Geoscience and Remote Sensing Letters, 15*(12), 1947-1951. https://doi.org/10.1109/LGRS.2018.2865816

Mandal, D., Kumar, V., Ratha, D., Dey, S., Bhattacharya, A., Lopez-Sanchez, J. M., McNairn, H., & Rao, Y. S. (2020, 2020/09/15/). Dual polarimetric radar vegetation index for crop growth monitoring using sentinel-1 SAR data. *Remote Sensing of Environment, 247*, 111954. https://doi.org/https://doi.org/10.1016/j.rse.2020.111954

Mano, Y., Takahashi, K., & Otsuka, K. (2020). Mechanization in land preparation and agricultural intensification: The case of rice farming in the Cote d'Ivoire. *Agricultural Economics, 51*(6), 899-908. https://doi.org/10.1111/agec.12599

Mansaray, L., Huang, W., Zhang, D., Huang, J., & Li, J. (2017). Mapping Rice Fields in Urban Shanghai, Southeast China, Using Sentinel-1A and Landsat 8 Datasets. *Remote Sensing, 9*(3), 257. http://www.mdpi.com/2072-4292/9/3/257

Mansaray, L. R., Wang, F., Kanu, A. S., Yang, L., Mansaray, L. R., Wang, F., Kanu, A. S., & Yang, L. (2020). Evaluating Sentinel-1A datasets for rice leaf area index estimation based on machine learning regression models. *Geocarto International, 0*, 1-12. https://doi.org/10.1080/10106049.2020.1773545

Mansaray, L. R., Zhang, D., Zhou, Z., & Huang, J. (2017). Evaluating the potential of temporal Sentinel-1A data for paddy rice discrimination at local scales. *Remote Sensing Letters, 8*, 967-976. https://doi.org/10.1080/2150704X.2017.1331472

Mantero, P., Moser, G., & Serpico, S. B. (2005). Partially supervised classification of remote sensing images through SVM-based probability density estimation. *IEEE Transactions on Geoscience and Remote Sensing, 43*(3), 559-570. https://doi.org/10.1109/TGRS.2004.842022

Mascolo, L., Forino, G., Nunziata, F., Pugliano, G., & Migliaccio, M. (2019). A New Methodology for Rice Area Monitoring with COSMO-SkyMed HH-VV PingPong Mode SAR Data. *IEEE Journal of Selected Topics in Applied Earth Observations and Remote Sensing, 12*, 1076-1084. https://doi.org/10.1109/JSTARS.2019.2898727

Maxwell, A. E., Warner, T. A., & Fang, F. (2018, 2018/05/03). Implementation of machine-learning classification in remote sensing: an applied review. *International Journal of Remote Sensing, 39*(9), 2784-2817. https://doi.org/10.1080/01431161.2018.1433343

McCloy, K. R., Smith, F. R., & Robinson, M. R. (1987). Monitoring rice areas using LANDSAT MSS data. *International Journal of Remote Sensing, 8*(5), 741-749. https://doi.org/10.1080/01431168708948685

McNairn, H., Kross, A., Lapen, D., Caves, R., & Shang, J. (2014, 5//). Early season monitoring of corn and soybeans with TerraSAR-X and RADARSAT-2. *International Journal of Applied Earth Observation and Geoinformation, 28*, 252-259. https://doi.org/10.1016/j.jag.2013.12.015

Meroni, M., Fasbender, D., Balaghi, R., Dali, M., Haffani, M., Haythem, I., Hooker, J., Lahlou, M., Lopez-Lozano, R., Mahyou, H., Ben Moussa, M., Sghaier, N., Wafa, T., & Leo, O. (2016). Evaluating NDVI Data Continuity Between SPOT-VEGETATION and PROBA-V Missions for Operational Yield Forecasting in North African Countries. *IEEE Transactions on Geoscience and Remote Sensing, 54*, 795-804. https://doi.org/10.1109/TGRS.2015.2466438

Minh, H. V. T., Avtar, R., Mohan, G., Misra, P., & Kurasaki, M. (2019). Monitoring and mapping of rice cropping pattern in flooding area in the Vietnamese Mekong delta using Sentinel-1A data: A case of an Giang province. *ISPRS International Journal of Geo-Information, 8*. https://doi.org/10.3390/ijgi8050211

Misbah, K., Laamrani, A., Chehbouni, A., Dhiba, D., & Ezzahar, J. (2021, 11-16 July 2021). Use of Hyperspectral Prisma Level-1 Data and ISDA Soil Fertility Map for Soil Macronutrient Availability Quantification in a Moroccan Agricultural Land. 2021 IEEE International Geoscience and Remote Sensing Symposium IGARSS,

Miyaoka, K., Maki, M., Susaki, J., Homma, K., Noda, K., & Oki, K. (2013). Rice-Planted Area Mapping Using Small Sets of Multi-Temporal SAR Data. *IEEE Geoscience and Remote Sensing Letters, 10*(6), 1507-1511. https://doi.org/10.1109/LGRS.2013.2261049

Modanesi, S., Lannoy, G. J. M. D., Gruber, A., Massari, C., Lievens, H., & Morbidelli, R. (2020). Irrigation detection with Sentinel-1 radar backscatter observations over an agricultural area in the Po River Valley (Italy). 5194.

Moldenhauer, K., Wilson, C. E. J., Counce, P., & Hardke, J. T. (2013). Rice Growth and Development. In J. T. Hardke (Ed.), *Arkansas rice production handbook (MP 192)* (pp. 212). University of Arkansas Division of Agriculture. https://www.uaex.edu/publications/MP-192.aspx

Mondal, S., Jeganathan, C., Amarnath, G., & Pani, P. (2017, 2017/03/04). Time-series cloud noise mapping and reduction algorithm for improved vegetation and drought monitoring. *GIScience & Remote Sensing, 54*(2), 202-229. https://doi.org/10.1080/15481603.2017.1286726

Mosleh, M. K., Hassan, Q. K., & Chowdhury, E. H. (2015). Application of remote sensors in mapping rice area and forecasting its production: a review. *Sensors (Basel, Switzerland), 15*(1), 769-791. https://doi.org/10.3390/s150100769

Mountrakis, G., Im, J., & Ogole, C. (2011, 5//). Support vector machines in remote sensing: A review. *ISPRS Journal of Photogrammetry and Remote Sensing, 66*(3), 247-259. https://doi.org/10.1016/j.isprsjprs.2010.11.001

Murmu, S., & Biswas, S. (2015, //). Application of Fuzzy Logic and Neural Network in Crop Classification: A Review. *Aquatic Procedia, 4*, 1203-1210. https://doi.org/10.1016/j.aqpro.2015.02.153

Nasirzadehdizaji, R., Cakir, Z., Balik Sanli, F., Abdikan, S., Pepe, A., & Calò, F. (2021, 2021/06/01/). Sentinel-1 interferometric coherence and backscattering analysis for crop monitoring. *Computers and Electronics in Agriculture, 185*, 106118. https://doi.org/https://doi.org/10.1016/j.compag.2021.106118

Nasrallah, A., Baghdadi, N., El Hajj, M., Darwish, T., Belhouchette, H., Faour, G., Darwich, S., & Mhawej, M. (2019). Sentinel-1 Data for Winter Wheat Phenology Monitoring and Mapping. *Remote Sensing, 11*(19), 2228. https://www.mdpi.com/2072-4292/11/19/2228

Naylor, R. L., Falcon, W. P., Rochberg, D., & Wada, N. (2001, Aug). Using El Nino/Southern oscillation climate data to predict rice production in Indonesia. *Climatic Change, 50*(3), 255-265. https://doi.org/10.1023/a:1010662115348

Ndikumana, E., Ho Tong Minh, D., Baghdadi, N., Courault, D., & Hossard, L. (2018). Deep Recurrent Neural Network for Agricultural Classification using multitemporal SAR Sentinel-1 for Camargue, France. *Remote Sensing, 10*(8), 1217. https://www.mdpi.com/2072-4292/10/8/1217

Ndikumana, E., Ho Tong Minh, D., Dang Nguyen, H. T., Baghdadi, N., Courault, D., Hossard, L., & El Moussawi, I. (2018). Estimation of Rice Height and Biomass Using Multitemporal SAR Sentinel-1 for Camargue, Southern France. *Remote Sensing, 10*(9), 1394. https://www.mdpi.com/2072-4292/10/9/1394

Ndikumana, E., Minh, D. H. T., Baghdadi, N., Courault, D., & Hossard, L. (2018). Deep recurrent neural network for agricultural classification using multitemporal SAR Sentinel-1 for Camargue, France. *Remote Sensing, 10*, 1-16. https://doi.org/10.3390/rs10081217

Nelson, A., Setiyono, T., Rala, A., Quicho, E., Raviz, J., Abonete, P., Maunahan, A., Garcia, C., Bhatti, H., Villano, L., Thongbai, P., Holecz, F., Barbieri, M., Collivignarelli, F., Gatti, L., Quilang, E., Mabalay, M., Mabalot, P., Barroga, M.,

Bacong, A., Detoito, N., Berja, G., Varquez, F., Wahyunto, Kuntjoro, D., Murdiyati, S., Pazhanivelan, S., Kannan, P., Mary, P., Subramanian, E., Rakwatin, P., Intrman, A., Setapayak, T., Lertna, S., Minh, V., Tuan, V., Duong, T., Quyen, N., Van Kham, D., Hin, S., Veasna, T., Yadav, M., Chin, C., & Ninh, N. (2014). Towards an Operational SAR-Based Rice Monitoring System in Asia: Examples from 13 Demonstration Sites across Asia in the RIICE Project. *Remote Sensing, 6*(11), 10773. http://www.mdpi.com/2072-4292/6/11/10773

Nguyen, D. B., Gruber, A., & Wagner, W. (2016, 2016/12/01). Mapping rice extent and cropping scheme in the Mekong Delta using Sentinel-1A data. *Remote Sensing Letters, 7*(12), 1209-1218. https://doi.org/10.1080/2150704X.2016.1225172

Nguyen, T. T. H., de Bie, C. A. J. M., Ali, A., Smaling, E. M. A., & Chu, T. H. (2012). Mapping the irrigated rice cropping patterns of the Mekong delta, Vietnam, through hyper-temporal spot NDVI image analysis. *International Journal of Remote Sensing, 33*(2), 415-434. https://doi.org/10.1080/01431161.2010.532826

Niel, T. G. V., & McVicar, T. R. (2004). Current and potential uses of optical remote sensing in rice-based irrigation systems: a review. *Australian Journal of Agricultural Research, 55*(2), 155-185. https://doi.org/10.1071/AR03149

Normile, D. (2008). Reinventing Rice to Feed the World. *Science, 321*(5887), 330. https://doi.org/10.1126/science.321.5887.330

OECD. (2015). *Rice projections: Consumption, per capita*. OECD Publishing. /content/table/agr_outlook-2015-table125-en
http://dx.doi.org/10.1787/agr_outlook-2015-table125-en

Oguro, Y., Suga, Y., Takeuchi, S., Ogawa, H., & Tsuchiya, K. (2003, 2003/12/01/). Monitoring of a rice field using landsat-5 TM and landsat-7 ETM+ data. *Advances in Space Research, 32*(11), 2223-2228. https://doi.org/https://doi.org/10.1016/S0273-1177(03)90546-1

Okamoto, K., & Fukuhara, M. (1996, 1996/06/01). Estimation of paddy field area using the area ratio of categories in each mixel of Landsat TM. *International Journal of Remote Sensing, 17*(9), 1735-1749. https://doi.org/10.1080/01431169608948736

Okubo, S., Parikesit, Muhamad, D., Harashina, K., Takeuchi, K., & Umezaki, M. (2010, 2010/12/01). Land use/cover classification of a complex agricultural landscape using single-dated very high spatial resolution satellite-sensed imagery. *Canadian Journal of Remote Sensing, 36*(6), 722-736. https://doi.org/10.5589/m11-010

Olofsson, P., Foody, G. M., Herold, M., Stehman, S. V., Woodcock, C. E., & Wulder, M. A. (2014, 2014/05/25/). Good practices for estimating area and assessing accuracy of land change. *Remote Sensing of Environment, 148*, 42-57. https://doi.org/10.1016/j.rse.2014.02.015

Onojeghuo, A. O., Blackburn, G. A., Wang, Q., Atkinson, P. M., Kindred, D., & Miao, Y. (2018, 2018/02/16). Mapping paddy rice fields by applying machine learning algorithms to multi-temporal Sentinel-1A and Landsat data. *International Journal*

of Remote Sensing, 39(4), 1042-1067. https://doi.org/10.1080/01431161.2017.1395969

Orynbaikyzy, A., Gessner, U., & Conrad, C. (2019, 2019/09/02). Crop type classification using a combination of optical and radar remote sensing data: a review. *International Journal of Remote Sensing, 40*(17), 6553-6595. https://doi.org/10.1080/01431161.2019.1569791

Oyoshi, K., Tomiyama, N., Okumura, T., Sobue, S., & Sato, J. (2016, October 01). Mapping rice-planted areas using time-series synthetic aperture radar data for the Asia-RiCE activity [journal article]. *Paddy and Water Environment, 14*(4), 463-472. https://doi.org/10.1007/s10333-015-0515-x

Pagani, V., Guarneri, T., Busetto, L., Ranghetti, L., Boschetti, M., Movedi, E., Campos-Taberner, M., Garcia-Haro, F. J., Katsantonis, D., Stavrakoudis, D., Ricciardelli, E., Romano, F., Holecz, F., Collivignarelli, F., Granell, C., Casteleyn, S., & Confalonieri, R. (2019). A high-resolution, integrated system for rice yield forecasting at district level. *Agricultural Systems, 168*, 181-190. https://doi.org/10.1016/j.agsy.2018.05.007

Pan, Z., Huang, J., Zhou, Q., Wang, L., Cheng, Y., Zhang, H., Blackburn, G. A., Yan, J., & Liu, J. (2015, 2015/02/01/). Mapping crop phenology using NDVI time-series derived from HJ-1 A/B data. *International Journal of Applied Earth Observation and Geoinformation, 34*, 188-197. https://doi.org/10.1016/j.jag.2014.08.011

Panday, U. S., Pratihast, A. K., Aryal, J., & Kayastha, R. B. (2020). A Review on Drone-Based Data Solutions for Cereal Crops. *Drones, 4*(3), 41. https://www.mdpi.com/2504-446X/4/3/41

Pandey, P. C., Mandal, V. P., Katiyar, S., Kumar, P., Tomar, V., Patairiya, S., Ravisankar, N., & Gangwar, B. (2015). Geospatial approach to assess the impact of nutrients on rice equivalent yield using MODIS sensors'-based MOD13Q1-NDVI data. *IEEE Sensors Journal, 15*, 6108-6115. https://doi.org/10.1109/JSEN.2015.2451113

Panuju, D. R., Mizuno, K., & Trisasongko, B. H. (2013, 2013/01/01/). The dynamics of rice production in Indonesia 1961–2009. *Journal of the Saudi Society of Agricultural Sciences, 12*(1), 27-37. https://doi.org/10.1016/j.jssas.2012.05.002

Panuju, D. R., Paull, D. J., Griffin, A. L., & Trisasongko, B. H. (2021). Mapping Rice Growth Stages Employing MODIS NDVI and ALOS AVNIR-2. In P. Kumar, H. Sajjad, B. S. Chaudhary, J. S. Rawat, & M. Rani (Eds.), *Remote Sensing and GIScience : Challenges and Future Directions* (pp. 185-203). Springer International Publishing. https://doi.org/10.1007/978-3-030-55092-9_11

Parida, B. R., Collado, W. B., Borah, R., Hazarika, M. K., & Samarakoon, L. (2008, 2008/01/01). Detecting Drought-Prone Areas of Rice Agriculture Using a MODIS-Derived Soil Moisture Index. *GIScience & Remote Sensing, 45*(1), 109-129. https://doi.org/10.2747/1548-1603.45.1.109

Park, S., Im, J., Park, S., Yoo, C., Han, H., & Rhee, J. (2018). Classification and mapping of paddy rice by combining Landsat and SAR time series data. *Remote Sensing, 10*, 1-22. https://doi.org/10.3390/rs10030447

Parry, M., Rosenzweig, C., & Livermore, M. (2005). Climate change, global food supply and risk of hunger. *Philosophical Transactions of the Royal Society B: Biological Sciences, 360*(1463), 2125-2138. https://doi.org/doi:10.1098/rstb.2005.1751

Parsa, I. M., & Dirgahayu, D. (2013). Multitemporal Landsat Data to Quick Mapping of Paddy Field Based On Statistical Parameters of Vegetation Index (Case Study: Tanggamus, Lampung). *International Journal of Remote Sensing and Earth Sciences (IJReSES), 10*(1).

Pedregosa, F., Varoquaux, G., Gramfort, A., Michel, V., Thirion, B., Grisel, O., Blondel, M., Prettenhofer, P., Weiss, R., & Dubourg, V. (2011). Scikit-learn: Machine learning in Python. *the Journal of machine Learning research, 12*, 2825-2830.

Peng, D. (2009). The Study on the Method of Rice Yield Estimation Using Statistical and MODIS Data. *Doctoral Thesis*.

Peng, D., Huang, J., Li, C., Liu, L., Huang, W., Wang, F., & Yang, X. (2014, 1/15/). Modelling paddy rice yield using MODIS data. *Agricultural and Forest Meteorology, 184*, 107-116. https://doi.org/10.1016/j.agrformet.2013.09.006

Peng, D., Huete, A. R., Huang, J., Wang, F., & Sun, H. (2011, 2//). Detection and estimation of mixed paddy rice cropping patterns with MODIS data. *International Journal of Applied Earth Observation and Geoinformation, 13*(1), 13-23. https://doi.org/10.1016/j.jag.2010.06.001

Perbet, P., Fortin, M., Ville, A., & Béland, M. (2019, 2019/10/02). Near real-time deforestation detection in Malaysia and Indonesia using change vector analysis with three sensors. *International Journal of Remote Sensing, 40*(19), 7439-7458. https://doi.org/10.1080/01431161.2019.1579390

Pham-Duc, B., Prigent, C., & Aires, F. (2017). Surface Water Monitoring within Cambodia and the Vietnamese Mekong Delta over a Year, with Sentinel-1 SAR Observations. *Water, 9*(6), 366. https://www.mdpi.com/2073-4441/9/6/366

Phung, H.-P., Nguyen, L.-D., Nguyen-Huy, T., Le-Toan, T., & Apan, A. (2020). Monitoring rice growth status in the Mekong Delta, Vietnam using multitemporal Sentinel-1 data. *Journal of Applied Remote Sensing, 14*(1), 014518. https://doi.org/10.1117/1.JRS.14.014518

Pi-Fuei, H., Lee, L. C., & Nai-Yu, C. (2001). Effect of spatial resolution on classification errors of pure and mixed pixels in remote sensing. *IEEE Transactions on Geoscience and Remote Sensing, 39*(12), 2657-2663. https://doi.org/10.1109/36.975000

Pignatti, S., Palombo, A., Pascucci, S., Romano, F., Santini, F., Simoniello, T., Umberto, A., Vincenzo, C., Acito, N., Diani, M., Matteoli, S., Corsini, G., Casa, R., Bonis,

R. D., Laneve, G., & Ananasso, C. (2013, 21-26 July 2013). The PRISMA hyperspectral mission: Science activities and opportunities for agriculture and land monitoring. 2013 IEEE International Geoscience and Remote Sensing Symposium - IGARSS,

Plank, S., Jüssi, M., Martinis, S., & Twele, A. (2017, 2017/07/03). Mapping of flooded vegetation by means of polarimetric Sentinel-1 and ALOS-2/PALSAR-2 imagery. *International Journal of Remote Sensing, 38*(13), 3831-3850. https://doi.org/10.1080/01431161.2017.1306143

Prasannakumar, N. R., Chander, S., & Sahoo, R. N. (2014, 2014/07/01). Characterization of brown planthopper damage on rice crops through hyperspectral remote sensing under field conditions. *Phytoparasitica, 42*(3), 387-395. https://doi.org/10.1007/s12600-013-0375-0

Probst, P., & Boulesteix, A.-L. (2017). To tune or not to tune the number of trees in random forest. *J. Mach. Learn. Res., 18*(1), 6673–6690.

Proy, C., Tanré, D., & Deschamps, P. Y. (1989, 1989/10/01/). Evaluation of topographic effects in remotely sensed data. *Remote Sensing of Environment, 30*(1), 21-32. https://doi.org/10.1016/0034-4257(89)90044-8

Pulighe, G., & Lupia, F. (2016). Mapping spatial patterns of urban agriculture in Rome (Italy) using Google Earth and web-mapping services. *Land Use Policy, 59*, 49-58. https://doi.org/10.1016/j.landusepol.2016.08.001

Pullanagari, R. R., Kereszturi, G., & Yule, I. J. (2016, 2016/07/01/). Mapping of macro and micro nutrients of mixed pastures using airborne AisaFENIX hyperspectral imagery. *ISPRS Journal of Photogrammetry and Remote Sensing, 117*, 1-10. https://doi.org/https://doi.org/10.1016/j.isprsjprs.2016.03.010

PUSDATIN. (2019). *Manual of SIMOTANDI application (in Indonesian)*. Retrieved 28 March 2019 from http://sig.pertanian.go.id/pdf/Pedoman_Pemanfaatan_Aplikasi%20_Simotandi.pdf

PUSDATIN. (2020). *Statistics of Agricultural Human Resources and Farmer Institution*. Indonesian Center for Agricultural Data and Information System for Ministry of Agriculture. Retrieved 28 December 2021 from http://epublikasi.setjen.pertanian.go.id/download/file/556-buku-statistik-sdm-pertanian-dan-kelembagaan-petani-tahun-2020

Putra, E. I., Hayasaka, H., Takahashi, H., & Usup, A. (2008). Recent peat fire activity in the mega rice project area, Central Kalimantan, Indonesia. *Journal of disaster research, 3*(5), 334-341.

Putra, R. E., Ramadan, D. B., Adin, A., Kinasih, I., Rosmiati, M., Oktaviani, I., & Leksikowati, S. S. (2020). Vernalization And Benzyl Amino Purin Application Unable To Enhance True Shallot Seed (TSS) Production during Off-Season. *BIOTROPIA-The Southeast Asian Journal of Tropical Biology*.

Qin, Z., & Zhang, M. (2005, 2005/08/01/). Detection of rice sheath blight for in-season disease management using multispectral remote sensing. *International Journal of Applied Earth Observation and Geoinformation, 7*(2), 115-128. https://doi.org/https://doi.org/10.1016/j.jag.2005.03.004

Qiu, B., Li, W., Tang, Z., Chen, C., & Qi, W. (2015, 9//). Mapping paddy rice areas based on vegetation phenology and surface moisture conditions. *Ecological Indicators, 56*, 79-86. https://doi.org/10.1016/j.ecolind.2015.03.039

Qiu, B., Zhong, M., Tang, Z., & Wang, C. (2014, 2//). A new methodology to map double-cropping croplands based on continuous wavelet transform. *International Journal of Applied Earth Observation and Geoinformation, 26*, 97-104. https://doi.org/10.1016/j.jag.2013.05.016

Rabus, B., Eineder, M., Roth, A., & Bamler, R. (2003, 2003/02/01/). The shuttle radar topography mission—a new class of digital elevation models acquired by spaceborne radar. *ISPRS Journal of Photogrammetry and Remote Sensing, 57*(4), 241-262. https://doi.org/10.1016/S0924-2716(02)00124-7

Raedeke, A. H., & Rikoon, J. S. (1997, 1997/06/01). Temporal and spatial dimensions of knowledge: Implications for sustainable agriculture. *Agriculture and Human Values, 14*(2), 145-158. https://doi.org/10.1023/A:1007346929150

Raghavendra, S., & Deka, P. C. (2014, 6//). Support vector machine applications in the field of hydrology: A review. *Applied Soft Computing, 19*, 372-386. https://doi.org/10.1016/j.asoc.2014.02.002

Rahaman, K. R., Hassan, Q. K., & Ahmed, M. R. (2017). Pan-Sharpening of Landsat-8 Images and Its Application in Calculating Vegetation Greenness and Canopy Water Contents. *ISPRS International Journal of Geo-Information, 6*(6), 168. https://www.mdpi.com/2220-9964/6/6/168

Ramadhani, F., Pullanagari, R., Kereszturi, G., & Procter, J. (2020a). Automatic Mapping of Rice Growth Stages Using the Integration of SENTINEL-2, MOD13Q1, and SENTINEL-1. *Remote Sensing, 12*(21), 3613. https://www.mdpi.com/2072-4292/12/21/3613

Ramadhani, F., Pullanagari, R., Kereszturi, G., & Procter, J. (2020b, 2020/11/01). Mapping of rice growth phases and bare land using Landsat-8 OLI with machine learning. *International Journal of Remote Sensing, 41*(21), 8428-8452. https://doi.org/10.1080/01431161.2020.1779378

Ramadhani, F., Pullanagari, R., Kereszturi, G., & Procter, J. (2021). Mapping a Cloud-Free Rice Growth Stages Using the Integration of PROBA-V and Sentinel-1 and Its Temporal Correlation with Sub-District Statistics. *Remote Sensing, 13*(8), 1498. https://www.mdpi.com/2072-4292/13/8/1498

Rebala, G., Ravi, A., & Churiwala, S. (2019). *An introduction to machine learning*. Springer.

Redfern, S. K., Azzu, N., & Binamira, J. S. (2012). Rice in Southeast Asia: facing risks and vulnerabilities to respond to climate change. *Build Resilience Adapt Climate Change Agri Sector, 23*, 295.

Rocchini, D., Petras, V., Petrasova, A., Horning, N., Furtkevicova, L., Neteler, M., Leutner, B., & Wegmann, M. (2017, 2017/07/01/). Open data and open source for remote sensing training in ecology. *Ecological Informatics, 40*, 57-61. https://doi.org/10.1016/j.ecoinf.2017.05.004

Rousselet, J., Imbert, C.-E., Dekri, A., Garcia, J., Goussard, F., Vincent, B., Denux, O., Robinet, C., Dorkeld, F., Roques, A., & Rossi, J.-P. (2013). Assessing Species Distribution Using Google Street View: A Pilot Study with the Pine Processionary Moth. *PLoS ONE, 8*(10), e74918. https://doi.org/10.1371/journal.pone.0074918

Roy, D. P., Huang, H., Boschetti, L., Giglio, L., Yan, L., Zhang, H. H., & Li, Z. (2019). Landsat-8 and Sentinel-2 burned area mapping - A combined sensor multi-temporal change detection approach. *Remote Sensing of Environment, 231*, 111254. https://doi.org/10.1016/j.rse.2019.111254

Rudiyanto, Minasny, B., Shah, R. M., Che Soh, N., Arif, C., & Indra Setiawan, B. (2019). Automated Near-Real-Time Mapping and Monitoring of Rice Extent, Cropping Patterns, and Growth Stages in Southeast Asia Using Sentinel-1 Time Series on a Google Earth Engine Platform. *Remote Sensing, 11*(14), 1666. https://www.mdpi.com/2072-4292/11/14/1666

Sakamoto, T., Van Nguyen, N., Ohno, H., Ishitsuka, N., & Yokozawa, M. (2006, 1/15/). Spatio–temporal distribution of rice phenology and cropping systems in the Mekong Delta with special reference to the seasonal water flow of the Mekong and Bassac rivers. *Remote Sensing of Environment, 100*(1), 1-16. https://doi.org/10.1016/j.rse.2005.09.007

Sakamoto, T., Yokozawa, M., Toritani, H., Shibayama, M., Ishitsuka, N., & Ohno, H. (2005, 6/30/). A crop phenology detection method using time-series MODIS data. *Remote Sensing of Environment, 96*(3–4), 366-374. https://doi.org/10.1016/j.rse.2005.03.008

Salmon, J. M., Friedl, M. A., Frolking, S., Wisser, D., & Douglas, E. M. (2015, 6//). Global rain-fed, irrigated, and paddy croplands: A new high resolution map derived from remote sensing, crop inventories and climate data. *International Journal of Applied Earth Observation and Geoinformation, 38*, 321-334. https://doi.org/10.1016/j.jag.2015.01.014

Sari, D. K., Ismullah, I. H., Sulasdi, W. N., & Harto, A. B. (2013). Detecting Rice Phenology in Paddy Fields with Complex Cropping Pattern Using Time Series MODIS Data. *Journal of Mathematical and Fundamental Sciences 42*(2), 91-106. http://journals.itb.ac.id/index.php/jmfs/article/view/63/59

Sarica, A., Cerasa, A., & Quattrone, A. (2017, 2017-October-06). Random Forest Algorithm for the Classification of Neuroimaging Data in Alzheimer's Disease: A

Systematic Review [Review]. *Frontiers in Aging Neuroscience, 9*(329). https://doi.org/10.3389/fnagi.2017.00329

Satalino, G., Balenzano, A., & Mattia, F. (2012). Sentinel-1 SAR Data for Mapping Agricultural Crops Not Dominated by Volume Scattering. 6801-6804.

Schmitt, M., & Zhu, X. X. (2016). Data Fusion and Remote Sensing: An ever-growing relationship. *IEEE Geoscience and Remote Sensing Magazine, 4*, 6-23. https://doi.org/10.1109/MGRS.2016.2561021

Schmitz, C., van Meijl, H., Kyle, P., Nelson, G. C., Fujimori, S., Gurgel, A., Havlik, P., Heyhoe, E., d'Croz, D. M., Popp, A., Sands, R., Tabeau, A., van der Mensbrugghe, D., von Lampe, M., Wise, M., Blanc, E., Hasegawa, T., Kavallari, A., & Valin, H. (2014). Land-use change trajectories up to 2050: insights from a global agro-economic model comparison. *Agricultural Economics, 45*(1), 69-84. https://doi.org/10.1111/agec.12090

Schneider, P., & Asch, F. (2020). Rice production and food security in Asian Mega deltas—A review on characteristics, vulnerabilities and agricultural adaptation options to cope with climate change. *Journal of Agronomy and Crop Science, 206*(4), 491-503. https://doi.org/10.1111/jac.12415

Schramm, M., Pebesma, E., Milenković, M., Foresta, L., Dries, J., Jacob, A., Wagner, W., Mohr, M., Neteler, M., Kadunc, M., Miksa, T., Kempeneers, P., Verbesselt, J., Gößwein, B., Navacchi, C., Lippens, S., & Reiche, J. (2021). The openEO API–Harmonising the Use of Earth Observation Cloud Services Using Virtual Data Cube Functionalities. *13*(6), 1125. https://www.mdpi.com/2072-4292/13/6/1125

Selvaraj, S., Srivastava, H. S., Haldar, D., & Chauhan, P. (2021). Eigen vector-based classification of pearl millet crop in presence of other similar structured (sorghum and maize) crops using fully polarimetric Radarsat-2 SAR data. *Geocarto International*, 1-13. https://doi.org/10.1080/10106049.2021.1903581

Setiawan, Y., Rustiadi, E., Yoshino, K., Liyantono, & Effendi, H. (2014). Assessing the Seasonal Dynamics of the Java's Paddy Field Using MODIS Satellite Images. *ISPRS International Journal of Geo-Information, 3*(1), 110-129. https://www.mdpi.com/2220-9964/3/1/110

Setiawan, Y., & Yoshino, K. (2014, 2014/07/03). Detecting land-use change from seasonal vegetation dynamics on regional scale with MODIS EVI 250-m time-series imagery. *Journal of Land Use Science, 9*(3), 304-330. https://doi.org/10.1080/1747423X.2013.786151

Setiyono, T. D., Quicho, E. D., Holecz, F. H., Khan, N. I., Romuga, G., Maunahan, A., Garcia, C., Rala, A., Raviz, J., Collivignarelli, F., Gatti, L., Barbieri, M., Phuong, D. M., Minh, V. Q., Vo, Q. T., Intrman, A., Rakwatin, P., Sothy, M., Veasna, T., Pazhanivelan, S., & Mabalay, M. R. O. (2019, 2019/11/02). Rice yield estimation using synthetic aperture radar (SAR) and the ORYZA crop growth model: development and application of the system in South and South-east Asian

countries. *International Journal of Remote Sensing, 40*(21), 8093-8124. https://doi.org/10.1080/01431161.2018.1547457

Shao, Y., Fan, X., Liu, H., Xiao, J., Ross, S., Brisco, B., Brown, R., & Staples, G. (2001). Rice monitoring and production estimation using multitemporal RADARSAT. *Remote Sensing of Environment, 76*(3), 310-325. https://doi.org/10.1016/S0034-4257(00)00212-1

Shao, Y., & Lunetta, R. S. (2012, 2012/06/01/). Comparison of support vector machine, neural network, and CART algorithms for the land-cover classification using limited training data points. *ISPRS Journal of Photogrammetry and Remote Sensing, 70*, 78-87. https://doi.org/10.1016/j.isprsjprs.2012.04.001

Shelestov, A., Lavreniuk, M., Kussul, N., Novikov, A., & Skakun, S. (2017, 2017-February-24). Exploring Google Earth Engine Platform for Big Data Processing: Classification of Multi-Temporal Satellite Imagery for Crop Mapping [Original Research]. *Frontiers in Earth Science, 5*(17). https://doi.org/10.3389/feart.2017.00017

Shimabukuro, Y. E., Ieee, S., Arai, E., Duarte, V., & Dutra, A. C. (2020). Discriminating Land Use and Land Cover Classes in Brazil Based on the Annual PROBA-V 100 m Time Series. https://doi.org/10.1109/JSTARS.2020.2994893

Shiu, Y. S., Lin, M. L., Huang, C. H., & Chu, T. H. (2012). Mapping paddy rice agriculture in a highly fragmented area using a geographic information system object-based post classification process. *J. Appl. Remote Sens., 6*, 063526.

Shu, M., Zhou, L., Gu, X., Ma, Y., Sun, Q., Yang, G., & Zhou, C. (2020, 2020/01/01/). Monitoring of maize lodging using multi-temporal Sentinel-1 SAR data. *Advances in Space Research, 65*(1), 470-480. https://doi.org/https://doi.org/10.1016/j.asr.2019.09.034

Shuai, G., Zhang, J., Basso, B., Pan, Y., Zhu, X., Zhu, S., & Liu, H. (2019, 2019/02/01/). Multi-temporal RADARSAT-2 polarimetric SAR for maize mapping supported by segmentations from high-resolution optical image. *International Journal of Applied Earth Observation and Geoinformation, 74*, 1-15. https://doi.org/https://doi.org/10.1016/j.jag.2018.08.021

Sianturi, R., Jetten, V. G., & Sartohadi, J. (2018, 2018/04/01/). Mapping cropping patterns in irrigated rice fields in West Java: Towards mapping vulnerability to flooding using time-series MODIS imageries. *International Journal of Applied Earth Observation and Geoinformation, 66*, 1-13. https://doi.org/10.1016/j.jag.2017.10.013

Sica, F., Gobbi, G., Rizzoli, P., & Bruzzone, L. (2020). ϕ-Net: Deep Residual Learning for InSAR Parameters Estimation. *IEEE Transactions on Geoscience and Remote Sensing*, 1-25. https://doi.org/10.1109/TGRS.2020.3020427

Sidhu, N., Pebesma, E., & Câmara, G. (2018). Using Google Earth Engine to detect land cover change: Singapore as a use case. *European Journal of Remote Sensing, 51*(1), 486-500. https://doi.org/10.1080/22797254.2018.1451782

Simatupang, P., & Peter Timmer, C. (2008, 2008/04/01). Indonesian Rice Production: Policies and Realities. *Bulletin of Indonesian Economic Studies, 44*(1), 65-80. https://doi.org/10.1080/00074910802001587

Singha, M., Dong, J., Zhang, G., & Xiao, X. (2019). High resolution paddy rice maps in cloud-prone Bangladesh and Northeast India using Sentinel-1 data. *Scientific Data, 6*, 1-10. https://doi.org/10.1038/s41597-019-0036-3

Singha, M., Wu, B., & Zhang, M. (2016). An Object-Based Paddy Rice Classification Using Multi-Spectral Data and Crop Phenology in Assam, Northeast India. *Remote Sensing, 8*(6), 479. https://www.mdpi.com/2072-4292/8/6/479

Siregar, P. R., & Crane, T. A. (2011). Climate Information and Agricultural Practice in Adaptation to Climate Variability: The Case of Climate Field Schools in Indramayu, Indonesia. *Culture, Agriculture, Food and Environment, 33*(2), 55-69. https://doi.org/10.1111/j.2153-9561.2011.01050.x

Skakun, S., Roger, J.-C., Vermote, E. F., Masek, J. G., & Justice, C. O. (2017). Automatic sub-pixel co-registration of Landsat-8 Operational Land Imager and Sentinel-2A Multi-Spectral Instrument images using phase correlation and machine learning based mapping. *International Journal of Digital Earth*, 1-17. https://doi.org/10.1080/17538947.2017.1304586

Son, N.-T., Chen, C.-F., Chang, L.-Y., Chen, C.-R., Sobue, S.-I., Minh, V.-Q., Chiang, S.-H., Nguyen, L.-D., & Lin, Y.-W. (2016, 2016/01/01). A logistic-based method for rice monitoring from multitemporal MODIS-Landsat fusion data. *European Journal of Remote Sensing, 49*(1), 39-56. https://doi.org/10.5721/EuJRS20164903

Son, N.-T., Chen, C.-F., Chen, C.-R., & Minh, V.-Q. (2017). Assessment of Sentinel-1A data for rice crop classification using random forests and support vector machines. *Geocarto International*, 1-15. https://doi.org/10.1080/10106049.2017.1289555

Son, N. T., Chen, C. F., Chen, C. R., & Guo, H. Y. (2020). Classification of multitemporal Sentinel-2 data for field-level monitoring of rice cropping practices in Taiwan. *Advances in Space Research, 65*, 1910-1921. https://doi.org/10.1016/j.asr.2020.01.028

Son, N. T., Chen, C. F., Chen, C. R., Minh, V. Q., & Trung, N. H. (2014, 10/15/). A comparative analysis of multitemporal MODIS EVI and NDVI data for large-scale rice yield estimation. *Agricultural and Forest Meteorology, 197*, 52-64. https://doi.org/10.1016/j.agrformet.2014.06.007

Son, N. T., & Thanh, B. X. (2020). Remotely sensed drought evaluation over rice cultivated areas in Cambodia during 2000 to 2019. *Geocarto International*, 1-19. https://doi.org/10.1080/10106049.2020.1773546

Song, Y., & Wang, J. (2019). Mapping Winter Wheat Planting Area and Monitoring Its Phenology Using Sentinel-1 Backscatter Time Series. *Remote Sensing, 11*(4), 449. https://www.mdpi.com/2072-4292/11/4/449

Sonobe, R., Tani, H., Wang, X., Kobayashi, N., & Shimamura, H. (2015, 2015/01/01/). Discrimination of crop types with TerraSAR-X-derived information. *Physics and Chemistry of the Earth, Parts A/B/C, 83-84*, 2-13. https://doi.org/https://doi.org/10.1016/j.pce.2014.11.001

Sonobe, R., Yamaya, Y., Tani, H., Wang, X., Kobayashi, N., & Mochizuki, K.-i. (2017, 2017/08/03). Mapping crop cover using multi-temporal Landsat 8 OLI imagery. *International Journal of Remote Sensing, 38*(15), 4348-4361. https://doi.org/10.1080/01431161.2017.1323286

Soo Chin, L., Suan-Pheng, K., To-Phuc, T., Ping, C., Vo Quang, M., & Hock, L. (1998). Application of multitemporal ERS-2 synthetic aperture radar in delineating rice cropping systems in the Mekong River Delta, Vietnam. *IEEE Transactions on Geoscience and Remote Sensing, 36*(5), 1412-1420. https://doi.org/10.1109/36.718845

Steinhausen, M. J., Wagner, P. D., Narasimhan, B., & Waske, B. (2018, 2018/12/01/). Combining Sentinel-1 and Sentinel-2 data for improved land use and land cover mapping of monsoon regions. *International Journal of Applied Earth Observation and Geoinformation, 73*, 595-604. https://doi.org/10.1016/j.jag.2018.08.011

Sterckx, S., Benhadj, I., Duhoux, G., Livens, S., Dierckx, W., Goor, E., Adriaensen, S., Heyns, W., Van Hoof, K., Strackx, G., Nackaerts, K., Reusen, I., Van Achteren, T., Dries, J., Van Roey, T., Mellab, K., Duca, R., & Zender, J. (2014). The PROBA-V mission: image processing and calibration. *International Journal of Remote Sensing, 35*, 2565-2588. https://doi.org/10.1080/01431161.2014.883094

Strobl, C., Boulesteix, A.-L., Kneib, T., Augustin, T., & Zeileis, A. (2008, July 11). Conditional variable importance for random forests [journal article]. *BMC Bioinformatics, 9*(1), 307. https://doi.org/10.1186/1471-2105-9-307

Su, T. (2017, 2017/05/04). Efficient paddy field mapping using Landsat-8 imagery and object-based image analysis based on advanced fractel net evolution approach. *GIScience & Remote Sensing, 54*(3), 354-380. https://doi.org/10.1080/15481603.2016.1273438

Sulova, A., & Jokar Arsanjani, J. (2020). Exploratory Analysis of Driving Force of Wildfires in Australia: An Application of Machine Learning within Google Earth Engine. *Remote Sensing, 13*(1). https://doi.org/10.3390/rs13010010

Sun, C., Bian, Y., Zhou, T., & Pan, J. (2019). Using of Multi-Source and Multi-Temporal Remote Sensing Data Improves Crop-Type Mapping in the Subtropical Agriculture Region. *Sensors, 19*(10), 2401. https://www.mdpi.com/1424-8220/19/10/2401

Sun, J., Shi, S., Gong, W., Yang, J., Du, L., Song, S., Chen, B., & Zhang, Z. (2017, 2017/01/16). Evaluation of hyperspectral LiDAR for monitoring rice leaf nitrogen by comparison with multispectral LiDAR and passive spectrometer. *Scientific Reports, 7*(1), 40362. https://doi.org/10.1038/srep40362

Sun, L., Chen, J., Guo, S., Deng, X., & Han, Y. (2020). Integration of time series sentinel-1 and sentinel-2 imagery for crop type mapping over oasis agricultural areas. *Remote Sensing, 12*. https://doi.org/10.3390/RS12010158

Sun, P., Zhang, J., Zhu, X., Pan, Y., & Liu, H. (2017, 2017/01/01). A highly efficient temporal-spatial probability synthesized model from multi-temporal remote sensing for paddy rice identification. *European Journal of Remote Sensing, 50*(1), 98-110. https://doi.org/10.1080/22797254.2017.1279819

Sun, T., Fang, H., Liu, W., & Ye, Y. (2017, 2017/02/15/). Impact of water background on canopy reflectance anisotropy of a paddy rice field from multi-angle measurements. *Agricultural and Forest Meteorology, 233*, 143-152. https://doi.org/10.1016/j.agrformet.2016.11.010

Surmaini, E., Hadi, T. W., Subagyono, K., & Puspito, N. T. (2015). Early detection of drought impact on rice paddies in Indonesia by means of Niño 3.4 index. *Theoretical and Applied Climatology, 121*(3), 669-684. https://doi.org/10.1007/s00704-014-1258-0

Tassi, A., & Vizzari, M. (2020). Object-Oriented LULC Classification in Google Earth Engine Combining SNIC, GLCM, and Machine Learning Algorithms. *Remote Sensing, 12*(22). https://doi.org/10.3390/rs12223776

Tatsumi, K., Yamashiki, Y., Canales Torres, M. A., & Taipe, C. L. R. (2015, 2015/07/01/). Crop classification of upland fields using Random forest of time-series Landsat 7 ETM+ data. *Computers and Electronics in Agriculture, 115*, 171-179. https://doi.org/10.1016/j.compag.2015.05.001

Team, R. C. (2017). *R: A Language and Environment for Statistical Computing*. In https://www.R-project.org/

Teluguntla, P., Thenkabail, P. S., Oliphant, A., Xiong, J., Gumma, M. K., Congalton, R. G., Yadav, K., & Huete, A. (2018). A 30-m landsat-derived cropland extent product of Australia and China using random forest machine learning algorithm on Google Earth Engine cloud computing platform. *ISPRS Journal of Photogrammetry and Remote Sensing, 144*, 325-340. https://doi.org/10.1016/j.isprsjprs.2018.07.017

Tennakoon, S. B., Murty, V. V., & Eiumnoh, A. (1992). Estimation of cropped area and grain yield of rice using remote sensing data. *International Journal of Remote Sensing, 13*(3), 427-439. https://doi.org/10.1080/01431169208904047

Tian, H., Huang, N., Niu, Z., Qin, Y., Pei, J., & Wang, J. (2019). Mapping Winter Crops in China with Multi-Source Satellite Imagery and Phenology-Based Algorithm. *Remote Sensing, 11*(7), 820. https://www.mdpi.com/2072-4292/11/7/820

Tian, H., Wu, M., Wang, L., & Niu, Z. (2018). Mapping early, middle and late rice extent using Sentinel-1A and Landsat-8 data in the poyang lake plain, China. *Sensors (Switzerland)*. https://doi.org/10.3390/s18010185

Tingting, L., & Chuang, L. (2010, 3/15/). Study on extraction of crop information using time-series MODIS data in the Chao Phraya Basin of Thailand. *Advances in Space Research, 45*(6), 775-784. https://doi.org/10.1016/j.asr.2009.11.013

Torbick, N., Chowdhury, D., Salas, W., & Qi, J. (2017). Monitoring Rice Agriculture across Myanmar Using Time Series Sentinel-1 Assisted by Landsat-8 and PALSAR-2. *Remote Sensing, 9*(2), 119. http://www.mdpi.com/2072-4292/9/2/119

Torbick, N., Salas, W., Chowdhury, D., Ingraham, P., & Trinh, M. (2017, 2017/01/02). Mapping rice greenhouse gas emissions in the Red River Delta, Vietnam. *Carbon Management, 8*(1), 99-108. https://doi.org/10.1080/17583004.2016.1275816

Torbick, N., Salas, W., Xiao, X., Ingraham, P., Fearon, M., Biradar, C., Zhao, D., Liu, Y., Li, P., & Zhao, Y. (2011, 2011/02/01). Integrating SAR and optical imagery for regional mapping of paddy rice attributes in the Poyang Lake Watershed, China. *Canadian Journal of Remote Sensing, 37*(1), 17-26. https://doi.org/10.5589/m11-020

Torres, R., Snoeij, P., Geudtner, D., Bibby, D., Davidson, M., Attema, E., Potin, P., Rommen, B., Floury, N., Brown, M., Traver, I. N., Deghaye, P., Duesmann, B., Rosich, B., Miranda, N., Bruno, C., L'Abbate, M., Croci, R., Pietropaolo, A., Huchler, M., & Rostan, F. (2012, 2012/05/15/). GMES Sentinel-1 mission. *Remote Sensing of Environment, 120*, 9-24. https://doi.org/10.1016/j.rse.2011.05.028

Tran, H. T., Campbell, J. B., Tran, T. D., & Tran, H. T. (2017, 2017/03/04). Monitoring drought vulnerability using multispectral indices observed from sequential remote sensing (Case Study: Tuy Phong, Binh Thuan, Vietnam). *GIScience & Remote Sensing, 54*(2), 167-184. https://doi.org/10.1080/15481603.2017.1287838

Triwidodo, H. (2020, 2020-06-02). Brown Planthoppers Infestations and Insecticides Use Pattern in Java, Indonesia [Integrated pest management; Nilaparvata lugens; Pesticides misuse]. *2020, 42*(2), 11. https://doi.org/10.17503/agrivita.v0i0.2501

Tsujimoto, K., Ohta, T., Hirooka, Y., & Homma, K. (2019). Estimation of planting date in paddy fields by time-series MODIS data for basin-scale rice production modeling. *Paddy and Water Environment, 17*, 83-90. https://doi.org/10.1007/s10333-019-00700-x

Ulaby, F., Cihlar, J., & Moore, R. (1974). Active microwave measurement of soil water content. *Remote Sensing of Environment, 3*(3), 185-203.

Umutoniwase, N., & Lee, S.-K. (2021). The Potential of Sentinel-1 SAR Parameters in Monitoring Rice Paddy Phenological Stages in Gimhae, South Korea. *Korean Journal of Remote Sensing, 37*(4), 789-802.

USGS. (2017). *Product Guide of Landsat Surface Reflectance Code (LaSRC)* United States Geological Survey

USGS. (2020). Landsat 8 surface reflectance code (LaSRC) product version 3.0. *Department of the Interior US Geological Survey: Reston, VG, USA*.

Valentijn, T., Margutti, J., van den Homberg, M., & Laaksonen, J. (2020). Multi-Hazard and Spatial Transferability of a CNN for Automated Building Damage Assessment. *Remote Sensing, 12*(17), 2839. https://www.mdpi.com/2072-4292/12/17/2839

Van der Velde, M., & Bareuth, B. (2015). A quality assessment of the MARS crop yield forecasting system for the European Union. *European Geosciences Union General Assembly 2015, Vienna, Austria, Geophysical Research, EGU2015-3042*.

Van Ittersum, M. K., Cassman, K. G., Grassini, P., Wolf, J., Tittonell, P., & Hochman, Z. (2013). Yield gap analysis with local to global relevance-A review. *Field Crops Research, 143*, 4-17. https://doi.org/10.1016/j.fcr.2012.09.009

Vangi, E., D'Amico, G., Francini, S., Giannetti, F., Lasserre, B., Marchetti, M., & Chirici, G. (2021). The New Hyperspectral Satellite PRISMA: Imagery for Forest Types Discrimination. *Sensors, 21*(4), 1182. https://www.mdpi.com/1424-8220/21/4/1182

Veci, L., Prats-Iraola, P., Scheiber, R., Collard, F., Fomferra, N., & Engdahl, M. (2014). The sentinel-1 toolbox. Proceedings of the IEEE International Geoscience and Remote Sensing Symposium (IGARSS),

Veloso, A., Mermoz, S., Bouvet, A., Le Toan, T., Planells, M., Dejoux, J.-F., & Ceschia, E. (2017, 2017/09/15/). Understanding the temporal behavior of crops using Sentinel-1 and Sentinel-2-like data for agricultural applications. *Remote Sensing of Environment, 199*, 415-426. https://doi.org/10.1016/j.rse.2017.07.015

Venables, W. N., & Ripley, B. D. (2013). *Modern applied statistics with S-PLUS*. Springer Science & Business Media.

Venkatappa, Sasaki, Shrestha, Tripathi, & Ma. (2019). Determination of Vegetation Thresholds for Assessing Land Use and Land Use Changes in Cambodia using the Google Earth Engine Cloud-Computing Platform. *Remote Sensing, 11*(13). https://doi.org/10.3390/rs11131514

Vergara, B. S. (1991). Rice Plant Growth and Development. In B. S. Luh (Ed.), *Rice: Volume I. Production/Volume II. Utilization* (pp. 13-22). Springer US. https://doi.org/10.1007/978-1-4899-3754-4_2

Vermeulen, S. J., Aggarwal, P. K., Ainslie, A., Angelone, C., Campbell, B. M., Challinor, A. J., Hansen, J. W., Ingram, J. S. I., Jarvis, A., Kristjanson, P., Lau, C., Nelson, G. C., Thornton, P. K., & Wollenberg, E. (2012, 2012/01/01/). Options for support to agriculture and food security under climate change. *Environmental Science & Policy, 15*(1), 136-144. https://doi.org/10.1016/j.envsci.2011.09.003

Verrelst, J., Camps-Valls, G., Muñoz-Marí, J., Rivera, J. P., Veroustraete, F., Clevers, J. G. P. W., & Moreno, J. Optical remote sensing and the retrieval of terrestrial vegetation bio-geophysical properties – A review. *ISPRS Journal of Photogrammetry and Remote Sensing*(0). https://doi.org/http://dx.doi.org/10.1016/j.isprsjprs.2015.05.005

Verrelst, J., Camps-Valls, G., Muñoz-Marí, J., Rivera, J. P., Veroustraete, F., Clevers, J. G. P. W., & Moreno, J. (2015, 10//). Optical remote sensing and the retrieval of terrestrial vegetation bio-geophysical properties – A review. *ISPRS Journal of Photogrammetry and Remote Sensing, 108*, 273-290. https://doi.org/10.1016/j.isprsjprs.2015.05.005

Verrelst, J., Rivera-Caicedo, J. P., Reyes-Muñoz, P., Morata, M., Amin, E., Tagliabue, G., Panigada, C., Hank, T., & Berger, K. (2021, 2021/08/01/). Mapping landscape canopy nitrogen content from space using PRISMA data. *ISPRS Journal of Photogrammetry and Remote Sensing, 178*, 382-395. https://doi.org/https://doi.org/10.1016/j.isprsjprs.2021.06.017

Vuolo, F., Neuwirth, M., Immitzer, M., Atzberger, C., & Ng, W.-T. (2018, 2018/10/01/). How much does multi-temporal Sentinel-2 data improve crop type classification? *International Journal of Applied Earth Observation and Geoinformation, 72*, 122-130. https://doi.org/https://doi.org/10.1016/j.jag.2018.06.007

Wakabayashi, H., Motohashi, K., Kitagami, T., Tjahjono, B., Dewayani, S., Hidayat, D., & Hongo, C. (2019). Flooded area extraction of rice paddy field in Indonesia using Sentinel-1 SAR data. *Int. Arch. Photogramm. Remote Sens. Spatial Inf. Sci., XLII-3/W7*, 73-76. https://doi.org/10.5194/isprs-archives-XLII-3-W7-73-2019

Wang, C., Wu, J., Zhang, Y., Pan, G., Qi, J., & Salas, W. A. (2009). Characterizing L-band scattering of paddy rice in southeast china with radiative transfer model and multitemporal ALOS/PALSAR imagery. *IEEE Transactions on Geoscience and Remote Sensing, 47*(4), 988-998, Article 4801683. https://doi.org/10.1109/TGRS.2008.2008309

Wang, D., Cao, W., Zhang, F., Li, Z., Xu, S., & Wu, X. (2022). A Review of Deep Learning in Multiscale Agricultural Sensing. *Remote Sensing, 14*(3), 559. https://www.mdpi.com/2072-4292/14/3/559

Wang, J., Huang, J.-f., Wang, X.-z., Jin, M.-t., Zhou, Z., Guo, Q.-y., Zhao, Z.-w., Huang, W.-j., Zhang, Y., & Song, X.-d. (2015, October 01). Estimation of rice phenology date using integrated HJ-1 CCD and Landsat-8 OLI vegetation indices time-series images [journal article]. *Journal of Zhejiang University-SCIENCE B, 16*(10), 832-844. https://doi.org/10.1631/jzus.B1500087

Wang, J., Wu, B., Kohnen, M. V., Lin, D., Yang, C., Wang, X., Qiang, A., Liu, W., Kang, J., Li, H., Shen, J., Yao, T., Su, J., Li, B., & Gu, L. (2021, 2021/03/30). Classification of Rice Yield Using UAV-Based Hyperspectral Imagery and Lodging Feature. *Plant Phenomics, 2021*, 9765952. https://doi.org/10.34133/2021/9765952

Wang, L., Zhang, F.-c., Jing, Y.-s., Jiang, X.-d., Yang, S.-b., & Han, X.-m. (2014, 3//). Multi-Temporal Detection of Rice Phenological Stages Using Canopy Spectrum. *Rice Science, 21*(2), 108-115. https://doi.org/10.1016/S1672-6308(13)60170-5

Ward, K. J., Chabrillat, S., Brell, M., Castaldi, F., Spengler, D., & Foerster, S. (2020). Mapping Soil Organic Carbon for Airborne and Simulated EnMAP Imagery Using the LUCAS Soil Database and a Local PLSR. *Remote Sensing, 12*(20), 3451. https://www.mdpi.com/2072-4292/12/20/3451

Waske, B., & Benediktsson, J. A. (2007). Fusion of support vector machines for classification of multisensor data. *IEEE Transactions on Geoscience and Remote Sensing, 45*(12), 3858-3866. https://doi.org/10.1109/TGRS.2007.898446

Wassmann, R., Jagadish, S. V. K., Sumfleth, K., Pathak, H., Howell, G., Ismail, A., Serraj, R., Redona, E., Singh, R. K., & Heuer, S. (2009). Regional Vulnerability of Climate Change Impacts on Asian Rice Production and Scope for Adaptation. In *Advances in Agronomy* (Vol. 102, pp. 91-133). Academic Press. https://doi.org/10.1016/S0065-2113(09)01003-7

Wassmann, R., Phong, N. D., Tho, T. Q., Hoanh, C. T., Khoi, N. H., Hien, N. X., Vo, T. B. T., & Tuong, T. P. (2019, 2019/04/15/). High-resolution mapping of flood and salinity risks for rice production in the Vietnamese Mekong Delta. *Field Crops Research, 236*, 111-120. https://doi.org/https://doi.org/10.1016/j.fcr.2019.03.007

Wei, L., Luo, Y., Xu, L., Zhang, Q., Cai, Q., & Shen, M. (2022). Deep Convolutional Neural Network for Rice Density Prescription Map at Ripening Stage Using Unmanned Aerial Vehicle-Based Remotely Sensed Images. *Remote Sensing, 14*(1), 46. https://www.mdpi.com/2072-4292/14/1/46

Wen, Q., Jiang, K., Wang, W., Liu, Q., Guo, Q., Li, L., & Wang, P. (2019, Jan 15). Automatic Building Extraction from Google Earth Images under Complex Backgrounds Based on Deep Instance Segmentation Network. *Sensors (Basel), 19*(2). https://doi.org/10.3390/s19020333

Whelen, T., & Siqueira, P. (2018). Time-series classification of Sentinel-1 agricultural data over North Dakota. *Remote Sensing Letters, 9*, 411-420. https://doi.org/10.1080/2150704X.2018.1430393

Whitcraft, A., Becker-Reshef, I., & Justice, C. (2015). A Framework for Defining Spatially Explicit Earth Observation Requirements for a Global Agricultural Monitoring Initiative (GEOGLAM). *Remote Sensing, 7*(2), 1461. http://www.mdpi.com/2072-4292/7/2/1461

Whitcraft, A. K., Becker-Reshef, I., Justice, C. O., Gifford, L., Kavvada, A., & Jarvis, I. (2019, 2019/12/15/). No pixel left behind: Toward integrating Earth Observations for agriculture into the United Nations Sustainable Development Goals framework. *Remote Sensing of Environment, 235*, 111470. https://doi.org/https://doi.org/10.1016/j.rse.2019.111470

Wood, S., Sebastian, K., Nachtergaele, F., Nielsen, D., & Dai, A. (1999). *Spatial Aspects of the Design and Targeting of Agricultural Development Strategies* (EPTD Discussion paper, Issue.

Wu, B., Meng, J., Li, Q., Yan, N., Du, X., & Zhang, M. (2014, 2014/02/07). Remote sensing-based global crop monitoring: experiences with China's CropWatch system. *International Journal of Digital Earth, 7*(2), 113-137. https://doi.org/10.1080/17538947.2013.821185

Wu, F., Wang, C., Zhang, H., Zhang, B., & Tang, Y. (2011). Rice Crop Monitoring in South China With RADARSAT-2 Quad-Polarization SAR Data. *IEEE Geoscience and Remote Sensing Letters, 8*(2), 196-200. https://doi.org/10.1109/LGRS.2010.2055830

Xiao, D., Niu, H., Guo, F., Zhao, S., & Fan, L. (2022, 2022/04/01/). Monitoring irrigation dynamics in paddy fields using spatiotemporal fusion of Sentinel-2 and MODIS. *Agricultural Water Management, 263*, 107409. https://doi.org/https://doi.org/10.1016/j.agwat.2021.107409

Xiao, X., Boles, S., Frolking, S., Li, C., Babu, J. Y., Salas, W., & Moore Iii, B. (2006, 1/15/). Mapping paddy rice agriculture in South and Southeast Asia using multi-temporal MODIS images. *Remote Sensing of Environment, 100*(1), 95-113. https://doi.org/10.1016/j.rse.2005.10.004

Xiao, X., Boles, S., Liu, J., Zhuang, D., Frolking, S., Li, C., Salas, W., & Moore Iii, B. (2005, 4/30/). Mapping paddy rice agriculture in southern China using multi-temporal MODIS images. *Remote Sensing of Environment, 95*(4), 480-492. https://doi.org/10.1016/j.rse.2004.12.009

Xiao, X., Braswell, B., Zhang, Q., Boles, S., Frolking, S., & Moore Iii, B. (2003). Sensitivity of vegetation indices to atmospheric aerosols: Continental-scale observations in Northern Asia. *Remote Sensing of Environment, 84*(3), 385-392. https://doi.org/10.1016/S0034-4257(02)00129-3

Xie, Q., Lai, K., Wang, J., Lopez-Sanchez, J. M., Shang, J., Liao, C., Zhu, J., Fu, H., & Peng, X. (2021). Crop Monitoring and Classification Using Polarimetric RADARSAT-2 Time-Series Data Across Growing Season: A Case Study in Southwestern Ontario, Canada. *Remote Sensing, 13*(7), 1394. https://www.mdpi.com/2072-4292/13/7/1394

Xie, Q., Wang, J., Lopez-Sanchez, J. M., Peng, X., Liao, C., Shang, J., Zhu, J., Fu, H., & Ballester-Berman, J. D. (2021). Crop Height Estimation of Corn from Multi-Year RADARSAT-2 Polarimetric Observables Using Machine Learning. *Remote Sensing, 13*(3), 392. https://www.mdpi.com/2072-4292/13/3/392

Xu, J., Li, Z., Tian, B., Huang, L., Chen, Q., & Fu, S. (2014, 2014/05/19). Polarimetric analysis of multi-temporal RADARSAT-2 SAR images for wheat monitoring and mapping. *International Journal of Remote Sensing, 35*(10), 3840-3858. https://doi.org/10.1080/01431161.2014.919679

Yanai, J., Hirose, M., Tanaka, S., Sakamoto, K., Nakao, A., Dejbhimon, K., Sriprachote, A., Kanyawongha, P., Lattirasuvan, T., & Abe, S. (2020). Changes in paddy soil fertility in Thailand due to the Green Revolution during the last 50 years. *Soil Science and Plant Nutrition*, 1-11. https://doi.org/10.1080/00380768.2020.1814115

Yang, C.-C., Prasher, S. O., Enright, P., Madramootoo, C., Burgess, M., Goel, P. K., & Callum, I. (2003, 2003/06/01/). Application of decision tree technology for image classification using remote sensing data. *Agricultural Systems, 76*(3), 1101-1117. https://doi.org/10.1016/S0308-521X(02)00051-3

Yang, H., Chen, E., Li, Z., Zhao, C., Yang, G., Pignatti, S., Casa, R., & Zhao, L. (2015, 2015/02/01/). Wheat lodging monitoring using polarimetric index from RADARSAT-2 data. *International Journal of Applied Earth Observation and Geoinformation, 34*, 157-166. https://doi.org/https://doi.org/10.1016/j.jag.2014.08.010

Yang, Q., Shi, L., Han, J., Yu, J., & Huang, K. (2020, 2020/06/15/). A near real-time deep learning approach for detecting rice phenology based on UAV images. *Agricultural and Forest Meteorology, 287*, 107938. https://doi.org/https://doi.org/10.1016/j.agrformet.2020.107938

Yang, S., Zhao, X., Li, B., & Hua, G. (2012). Interpreting RADARSAT-2 Quad-Polarization SAR Signatures From Rice Paddy Based on Experiments. *IEEE Geoscience and Remote Sensing Letters, 9*(1), 65-69. https://doi.org/10.1109/LGRS.2011.2160613

Yang, X., Chen, Y., & Wang, J. (2020). Combined use of Sentinel-2 and Landsat 8 to monitor water surface area dynamics using Google Earth Engine. *Remote Sensing Letters, 11*, 687-696. https://doi.org/10.1080/2150704X.2020.1757780

Ye, S., Rogan, J., & Sangermano, F. (2018, 2018/02/01/). Monitoring rubber plantation expansion using Landsat data time series and a Shapelet-based approach. *ISPRS Journal of Photogrammetry and Remote Sensing, 136*, 134-143. https://doi.org/10.1016/j.isprsjprs.2018.01.002

Yin, Q., Liu, M., Cheng, J., Ke, Y., & Chen, X. (2019). Mapping paddy rice planting area in northeastern China using spatiotemporal data fusion and phenology-based method. *Remote Sensing, 11*. https://doi.org/10.3390/rs11141699

Yonezawa, C., Negishi, M., Azuma, K., Watanabe, M., Ishitsuka, N., Ogawa, S., & Saito, G. (2012, 2012/09/20). Growth monitoring and classification of rice fields using multitemporal RADARSAT-2 full-polarimetric data. *International Journal of Remote Sensing, 33*(18), 5696-5711. https://doi.org/10.1080/01431161.2012.665194

Youssef, A. M., Pourghasemi, H. R., Pourtaghi, Z. S., & Al-Katheeri, M. M. (2016, 2016/10/01). Landslide susceptibility mapping using random forest, boosted regression tree, classification and regression tree, and general linear models and

comparison of their performance at Wadi Tayyah Basin, Asir Region, Saudi Arabia. *Landslides, 13*(5), 839-856. https://doi.org/10.1007/s10346-015-0614-1

Yu, S., Ali, J., Zhang, C., Li, Z., & Zhang, Q. (2020, 2020/05/01). Genomic Breeding of Green Super Rice Varieties and Their Deployment in Asia and Africa. *Theoretical and Applied Genetics, 133*(5), 1427-1442. https://doi.org/10.1007/s00122-019-03516-9

Yuzugullu, O., Erten, E., & Hajnsek, I. (2015). Rice Growth Monitoring by Means of X-Band Co-polar SAR: Feature Clustering and BBCH Scale. *IEEE Geoscience and Remote Sensing Letters, 12*, 1218-1222. https://doi.org/10.1109/LGRS.2015.2388953

Zhang, G., Xiao, X., Biradar, C. M., Dong, J., Qin, Y., Menarguez, M. A., Zhou, Y., Zhang, Y., Jin, C., Wang, J., Doughty, R. B., Ding, M., & Moore Iii, B. (2017, 2/1/). Spatiotemporal patterns of paddy rice croplands in China and India from 2000 to 2015. *Science of The Total Environment, 579*, 82-92. https://doi.org/10.1016/j.scitotenv.2016.10.223

Zhang, G., Xiao, X., Dong, J., Kou, W., Jin, C., Qin, Y., Zhou, Y., Wang, J., Menarguez, M. A., & Biradar, C. (2015, 8//). Mapping paddy rice planting areas through time series analysis of MODIS land surface temperature and vegetation index data. *ISPRS Journal of Photogrammetry and Remote Sensing, 106*, 157-171. https://doi.org/10.1016/j.isprsjprs.2015.05.011

Zhang, G., Xiao, X., Dong, J., Xin, F., Zhang, Y., Qin, Y., Doughty, R. B., & Moore, B. (2020). Fingerprint of rice paddies in spatial–temporal dynamics of atmospheric methane concentration in monsoon Asia. *Nature Communications, 11*. https://doi.org/10.1038/s41467-019-14155-5

Zhang, H., Li, Q., Liu, J., Shang, J., Du, X., Zhao, L., Wang, N., & Dong, T. (2017, 2017/05/04). Crop classification and acreage estimation in North Korea using phenology features. *GIScience & Remote Sensing, 54*(3), 381-406. https://doi.org/10.1080/15481603.2016.1276255

Zhang, M., & Lin, H. (2019, 2019/01/01/). Object-based rice mapping using time-series and phenological data. *Advances in Space Research, 63*(1), 190-202. https://doi.org/10.1016/j.asr.2018.09.018

Zhang, M., Lin, H., Wang, G., Sun, H., & Fu, J. (2018). Mapping Paddy Rice Using a Convolutional Neural Network (CNN) with Landsat 8 Datasets in the Dongting Lake Area, China. *Remote Sensing, 10*(11), 1840. https://www.mdpi.com/2072-4292/10/11/1840

Zhang, W., Liu, H., Wu, W., Zhan, L., & Wei, J. (2020). Mapping rice paddy based on machine learning with sentinel-2 multi-temporal data: Model comparison and transferability. *Remote Sensing, 12*. https://doi.org/10.3390/rs12101620

Zhang, X., Zhang, M., Zheng, Y., & Wu, B. (2016). Crop mapping using PROBA-V time series data at the Yucheng and hongxing farm in China. *Remote Sensing, 8*, 1-18. https://doi.org/10.3390/rs8110915

Zhang, X. M., He, G. J., Zhang, Z. M., Peng, Y., & Long, T. F. (2017, 2017/09/01). Spectral-spatial multi-feature classification of remote sensing big data based on a random forest classifier for land cover mapping. *Cluster Computing, 20*(3), 2311-2321. https://doi.org/10.1007/s10586-017-0950-0

Zhang, Y., Liu, X., Su, S., & Wang, C. (2014, 5//). Retrieving canopy height and density of paddy rice from Radarsat-2 images with a canopy scattering model. *International Journal of Applied Earth Observation and Geoinformation, 28*, 170-180. https://doi.org/10.1016/j.jag.2013.12.005

Zhang, Y., Wang, C., Wu, J., Qi, J., & Salas, W. A. (2009). Mapping paddy rice with multitemporal ALOS/PALSAR imagery in Southeast China. *International Journal of Remote Sensing, 30*(23), 6301-6315. https://doi.org/10.1080/01431160902842391

Zhang, Y., Wang, Y. Y., Su, S. L., & Li, C. S. (2011). Quantifying methane emissions from rice paddies in Northeast China by integrating remote sensing mapping with a biogeochemical model. *Biogeosciences, 8*(5), 1225-1235. https://doi.org/10.5194/bg-8-1225-2011

Zhang, Y., Yang, B., Liu, X., & Wang, C. (2017, 2017/05/01/). Estimation of rice grain yield from dual-polarization Radarsat-2 SAR data by integrating a rice canopy scattering model and a genetic algorithm. *International Journal of Applied Earth Observation and Geoinformation, 57*, 75-85. https://doi.org/10.1016/j.jag.2016.12.014

Zhao, L., Yang, J., Li, P., Shi, L., & Zhang, L. (2017, 2017/07/03). Characterizing Lodging Damage in Wheat and Canola Using Radarsat-2 Polarimetric SAR Data. *Remote Sensing Letters, 8*(7), 667-675. https://doi.org/10.1080/2150704X.2017.1312028

Zheng, H., Cheng, T., Yao, X., Deng, X., Tian, Y., Cao, W., & Zhu, Y. (2016, 11//). Detection of rice phenology through time series analysis of ground-based spectral index data. *Field Crops Research, 198*, 131-139. https://doi.org/10.1016/j.fcr.2016.08.027

Zhihao, Q., Minghua, Z., Christensen, T., Wenjuan, L., & Huajun, T. (2003, 21-25 July 2003). Remote sensing analysis of rice disease stresses for farm pest management using wide-band airborne data. IGARSS 2003. 2003 IEEE International Geoscience and Remote Sensing Symposium. Proceedings (IEEE Cat. No.03CH37477),

Zhou, X., Zheng, H. B., Xu, X. Q., He, J. Y., Ge, X. K., Yao, X., Cheng, T., Zhu, Y., Cao, W. X., & Tian, Y. C. (2017, 2017/08/01/). Predicting grain yield in rice using multi-temporal vegetation indices from UAV-based multispectral and digital imagery. *ISPRS Journal of Photogrammetry and Remote Sensing, 130*, 246-255. https://doi.org/10.1016/j.isprsjprs.2017.05.003

Zhou, Y., Xiao, X., Qin, Y., Dong, J., Zhang, G., Kou, W., Jin, C., Wang, J., & Li, X. (2016, 4//). Mapping paddy rice planting area in rice-wetland coexistent areas through analysis of Landsat 8 OLI and MODIS images. *International Journal of Applied Earth Observation and Geoinformation, 46*, 1-12. https://doi.org/10.1016/j.jag.2015.11.001

Zhu, H., Ma, W., Li, L., Jiao, L., Yang, S., & Hou, B. (2020). A Dual–Branch Attention fusion deep network for multiresolution remote–Sensing image classification. *Information Fusion, 58*, 116-131. https://doi.org/10.1016/j.inffus.2019.12.013

Zhu, W., Li, H., Chen, J., Zhou, T., & Han, Y. (2019). Dynamic monitoring of multiple cropping index of paddy field based on MODIS-EVI data in Guangdong province. *2019 8th International Conference on Agro-Geoinformatics, Agro-Geoinformatics 2019*. https://doi.org/10.1109/Agro-Geoinformatics.2019.8820547

Zhu, X., Cai, F., Tian, J., & Williams, T. K.-A. (2018). Spatiotemporal Fusion of Multisource Remote Sensing Data: Literature Survey, Taxonomy, Principles, Applications, and Future Directions. *Remote Sensing, 10*(4), 527. https://www.mdpi.com/2072-4292/10/4/527

Zhu, X., Chen, J., Gao, F., Chen, X., & Masek, J. G. (2010, 2010/11/15/). An enhanced spatial and temporal adaptive reflectance fusion model for complex heterogeneous regions. *Remote Sensing of Environment, 114*(11), 2610-2623. https://doi.org/10.1016/j.rse.2010.05.032

Zhuang, X., Zhao, S., Li, X., & Cong, D. (2016, 10-15 July 2016). Landsat and MODIS Data Fusion products based phenology analysis of dryland in Shan Dong province. 2016 IEEE International Geoscience and Remote Sensing Symposium (IGARSS),

Zurqani, H. A., Post, C. J., Mikhailova, E. A., Schlautman, M. A., & Sharp, J. L. (2018). Geospatial analysis of land use change in the Savannah River Basin using Google Earth Engine. *International Journal of Applied Earth Observation and Geoinformation, 69*, 175-185. https://doi.org/10.1016/j.jag.2017.12.006

[intentionally blank]

Appendices

Appendix 1 Github address for source codes, data, and maps

1. Chapter 3
   https://github.com/FadhlullahRamadhani/LS8-OLI-MAPPING
2. Chapter 4:
   https://github.com/FadhlullahRamadhani/S2-PADDY-MAPPING
3. Chapter 5:
   https://github.com/FadhlullahRamadhani/Remote-sensed-correlation-statistics
4. Chapter 6:
   https://github.com/FadhlullahRamadhani/Rice-Growth-Stages-with-Google-Earth-Engine
5. Some field survey photos and documents:
   https://github.com/FadhlullahRamadhani/Mapping-Rice-Growth-Stages---A-Thesis

Appendix 2 - Statements of contribution doctorate with publications/manuscripts (DRC 16).

1. Chapter 3.

DRC 16

MASSEY UNIVERSITY
TE KUNENGA KI PŪREHUROA
UNIVERSITY OF NEW ZEALAND

GRADUATE RESEARCH SCHOOL

STATEMENT OF CONTRIBUTION
DOCTORATE WITH PUBLICATIONS/MANUSCRIPTS

We, the candidate and the candidate's Primary Supervisor, certify that all co-authors have consented to their work being included in the thesis and they have accepted the candidate's contribution as indicated below in the *Statement of Originality*.

Name of candidate:	Fadhlullah Ramadhani
Name/title of Primary Supervisor:	Reddy Pullanagari
In which chapter is the manuscript /published work:	Chapter 3

Please select one of the following three options:

(●) The manuscript/published work is published or in press

- Please provide the full reference of the Research Output:

Ramadhani, F., Pullanagari, R., Kereszturi, G., & Procter, J. (2020). Mapping of rice growth phases and bare land using Landsat-8 OLI with machine learning. International Journal of Remote Sensing, 41(21), 8428-8452. https://doi.org/10.1080/01431161.2020.1779378

( ) The manuscript is currently under review for publication – please indicate:

- The name of the journal:
- The percentage of the manuscript/published work that was contributed by the candidate:
- Describe the contribution that the candidate has made to the manuscript/published work:

( ) It is intended that the manuscript will be published, but it has not yet been submitted to a journal

Candidate's Signature:	Fadhlullah Ramadhani — Digitally signed by Fadhlullah Ramadhani Date: 2021.02.03 13:57:26 +13'00'
Date:	03-Feb-2021
Primary Supervisor's Signature:	Pullanagari Rajasheker Reddy — Digitally signed by Pullanagari Rajasheker Reddy Date: 2021.02.03 21:02:46 +13'00'
Date:	3-Feb-2021

This form should appear at the end of each thesis chapter/section/appendix submitted as a manuscript/ publication or collected as an appendix at the end of the thesis.

GRS Version 5 – 13 December 2019
DRC 19/09/10

2. Chapter 4.

DRC 16

MASSEY UNIVERSITY
TE KUNENGA KI PŪREHUROA
UNIVERSITY OF NEW ZEALAND

GRADUATE RESEARCH SCHOOL

STATEMENT OF CONTRIBUTION
DOCTORATE WITH PUBLICATIONS/MANUSCRIPTS

We, the candidate and the candidate's Primary Supervisor, certify that all co-authors have consented to their work being included in the thesis and they have accepted the candidate's contribution as indicated below in the *Statement of Originality*.

Name of candidate:	Fadhlullah Ramadhani
Name/title of Primary Supervisor:	Reddy Pullanagari
In which chapter is the manuscript /published work:	Chapter 4

Please select one of the following three options:

(●) The manuscript/published work is published or in press

- Please provide the full reference of the Research Output:

Ramadhani, F., Pullanagari, R., Kereszturi, G., & Procter, J. (2020). Automatic Mapping of Rice Growth Stages Using the Integration of SENTINEL-2, MOD13Q1, and SENTINEL-1. Remote Sensing, 12(21), 3613. https://www.mdpi.com/2072-4292/12/21/3613

( ) The manuscript is currently under review for publication – please indicate:

- The name of the journal:
- The percentage of the manuscript/published work that was contributed by the candidate:
- Describe the contribution that the candidate has made to the manuscript/published work:

( ) It is intended that the manuscript will be published, but it has not yet been submitted to a journal

Candidate's Signature:	Fadhlullah Ramadhani — Digitally signed by Fadhlullah Ramadhani Date: 2021.02.03 13:57:44 +13'00'
Date:	03-Feb-2021
Primary Supervisor's Signature:	Pullanagari Rajasheker Reddy — Digitally signed by Pullanagari Rajasheker Reddy Date: 2021.02.04 10:07:12 +13'00'
Date:	4-Feb-2021

This form should appear at the end of each thesis chapter/section/appendix submitted as a manuscript/ publication or collected as an appendix at the end of the thesis.

GRS Version 5 – 13 December 2019
DRC 19/09/10

3. Chapter 5.

DRC 16

MASSEY UNIVERSITY
TE KUNENGA KI PŪREHUROA
UNIVERSITY OF NEW ZEALAND

GRADUATE RESEARCH SCHOOL

STATEMENT OF CONTRIBUTION
DOCTORATE WITH PUBLICATIONS/MANUSCRIPTS

We, the candidate and the candidate's Primary Supervisor, certify that all co-authors have consented to their work being included in the thesis and they have accepted the candidate's contribution as indicated below in the *Statement of Originality*.

Name of candidate:	Fadhlullah Ramadhani
Name/title of Primary Supervisor:	Reddy Pullanagari
In which chapter is the manuscript /published work:	Chapter 5

Please select one of the following three options:

(●) The manuscript/published work is published or in press

- Please provide the full reference of the Research Output:

Ramadhani, F., Pullanagari, R., Kereszturi, G., & Procter, J. (2021). Mapping a Cloud-Free Rice Growth Stages Using the Integration of PROBA-V and Sentinel-1 and Its Temporal Correlation with Sub-District Statistics. Remote Sensing, 13(8), 1498. https://www.mdpi.com/2072-4292/13/8/1498

( ) The manuscript is currently under review for publication – please indicate:

- The name of the journal:

Remote sensing

- The percentage of the manuscript/published work that was contributed by the candidate: 85.00

- Describe the contribution that the candidate has made to the manuscript/published work:

The candidate designed the experiment. Ground truth measurements conducted by the candidate. He analysed the data and drafted the manuscript.

( ) It is intended that the manuscript will be published, but it has not yet been submitted to a journal

Candidate's Signature:	Fadhlullah Ramadhani — Digitally signed by Fadhlullah Ramadhani Date: 2021.04.15 08:45:06 +07'00'
Date:	15-Apr-2021
Primary Supervisor's Signature:	Pullanagari Rajasheker Reddy — Digitally signed by Pullanagari Rajasheker Reddy Date: 2021.04.18 12:12:29 +12'00'
Date:	18-Apr-2021

This form should appear at the end of each thesis chapter/section/appendix submitted as a manuscript/ publication or collected as an appendix at the end of the thesis.

GRS Version 5 – 13 December 2019
DRC 19/09/10

4. Chapter 6.

DRC 16

MASSEY UNIVERSITY
TE KUNENGA KI PŪREHUROA
UNIVERSITY OF NEW ZEALAND

GRADUATE RESEARCH SCHOOL

STATEMENT OF CONTRIBUTION
DOCTORATE WITH PUBLICATIONS/MANUSCRIPTS

We, the candidate and the candidate's Primary Supervisor, certify that all co-authors have consented to their work being included in the thesis and they have accepted the candidate's contribution as indicated below in the *Statement of Originality*.

Name of candidate:	Fadhlullah Ramadhani
Name/title of Primary Supervisor:	Reddy Pullanagari
In which chapter is the manuscript /published work:	Chapter 6

Please select one of the following three options:

○ The manuscript/published work is published or in press

- Please provide the full reference of the Research Output:

○ The manuscript is currently under review for publication – please indicate:

- The name of the journal:
- The percentage of the manuscript/published work that was contributed by the candidate:
- Describe the contribution that the candidate has made to the manuscript/published work:

◉ It is intended that the manuscript will be published, but it has not yet been submitted to a journal

Candidate's Signature:	Fadhlullah Ramadhani Digitally signed by Fadhlullah Ramadhani Date: 2021.08.27 16:09:09 +07'00'
Date:	27-Aug-2021
Primary Supervisor's Signature:	Pullanagari Rajasheker Reddy Digitally signed by Pullanagari Rajasheker Reddy Date: 2021.08.27 22:52:04 +12'00'
Date:	27-Aug-2021

This form should appear at the end of each thesis chapter/section/appendix submitted as a manuscript/ publication or collected as an appendix at the end of the thesis.

GRS Version 5 – 13 December 2019
DRC 19/09/10

Appendix 3 Specifications of satellite-based sensors/satellites

1. PROBA-V and MODIS Terra

a) Platform, orbit, and geometric specifications

	PROBA-V	MODIS Terra
Altitude	820 km	705 km
Inclination	Sun-synchronous orbit + 0.13°	sun-synchronous, near-polar, circular
Coverage	daily above 35° latitude; full coverage every 2 days	2,330 km and views the entire surface of the Earth every one to two days.
Payload Mass	33.3 kg	228.7 kg
Payload dimensions	0.2 m × 0.8 m × 0.35 m	1.0 x 1.6 x 1.0 m
Power	43.2 W payload	162.5 W
Life	2.5–5 years	6 years
Downlink	11.1 Mb s–1 (after compression)	10.6 Mbps (peak daytime); 6.1 Mbps (orbital average)
Field-of-view and swath	102.4° and 2295 km	2330 km (cross track) by 10 km (along track at nadir)
Launched year	7 May 2013	18 December 1999

b) Radiometric specifications for PROBA-V

Band Name/ Description	Band centre (nm)	Bandwidth (nm)	Wavelength range (nm)	Pixel size (m)
Blue	463	56	435-491	100
RED	655	79	615-694	100
NIR	845	144	773-917	100
SWIR	1600	73	1563-1636	100

a) Radiometric specifications for MODIS Terra

Band Name/ Description	Band center (nm)	Bandwidth (nm)	Wavelength range (nm)	Pixel size (m)
Band 1/ Red	645	50	620 - 670	250
Band 2/ NIR1	858	35	841 - 876	250
Band 3/ Blue	469	20	459 - 479	500
Band 4/ Green	555	20	545 - 565	500
Band 5/ NIR2	1240	20	1230 - 1250	500
Band 6/ SWIR1	1640	24	1628 - 1652	500
Band 7/ SWIR2	2130	50	2105 - 2155	500
Band 8-36	-	-	405 - 14385	1000

2. Sentinel-2 and Landsat-8 OLI

a) Platform, orbit, and geometric specifications

	Sentinel-2A/B	Landsat-8
Altitude	786 km	705 km
Inclination	Sun-synchronous	Sun-synchronous, near-polar orbit
Coverage	All land areas/islands covered (except Antarctica) /Five days from two-satellite constellation (at equator)	16-day repeat cycle with an equatorial crossing
Payload Mass	275	1,512
Payload dimensions	3.4 × 1.8 × 2.35 m	3 m x 2.4 m
Power	1,700 W	3.750 watt
Life	Seven years	Five-year life span

Downlink	1.3 Gbit/s to 0.45 Gbit/s	384 Mbps on X-band frequency; 260.92 Mbps on S-band
Field-of-view and swath	290 km	185 km x 180 km
Launched year	6 January 2015 & 7 March 2017	February 11, 2013

b) Radiometric specifications for Sentinel-2A

Band Name/ Description	Band center (nm)	Bandwidth (nm)	Wavelength range (nm)	Pixel size (m)
Band 1/ Aerosols	443	27	430–457	60
Band 2/ Blue	497	98	448–546	10
Band 3/ Green	560	45	538–583	10
Band 4/ Red	665	38	646–684	10
Band 5/ Red Edge 1	703	19	694–713	20
Band 6/ Red Edge 2	740	18	731–749	20
Band 7/ Red Edge 3	783	28	769–797	20
Band 8/ NIR	835	145	763–908	10
Band 8A/ Red Edge 4	864	33	848–881	20
Band 9/ Water vapor	945	26	932–958	60
Band 10/ Cirrus	1373	75	1336–1411	60
Band 11/ SWIR 1	1613	143	1542–1685	20
Band 12/ SWIR 2	2202	242	2081–2323	20

c) Radiometric specifications for Sentinel-2B

Band Name/ Description	Band center (nm)	Bandwidth (nm)	Wavelength range (nm)	Pixel size (m)
Band 1/ Aerosols	442.3	45	419-464	60
Band 2/ Blue	492.1	98	443-541	10
Band 3/ Green	559	46	536-582	10
Band 4/ Red	665	39	645-684	10
Band 5/ Red Edge 1	703.8	20	693-713	20
Band 6/ Red Edge 2	739.1	18	730-748	20
Band 7/ Red Edge 3	779.7	28	765-793	20
Band 8/ NIR	833	133	766-899	10
Band 8A/ Red Edge 4	864	32	848-880	20
Band 9/ Water vapor	943.2	27	929-956	60
Band 10/ Cirrus	1376.9	76	1338-1414	60
Band 11/ SWIR 1	1640.4	141	1569-1710	20
Band 12/ SWIR 2	2185.7	238	2066-2304	20

d) Radiometric specifications for Landsat-8 OLI

Band Name/ Description	Band center (nm)	Bandwidth (nm)	Wavelength range (nm)	Pixel size (m)
Band 1/ Coastal aerosol	443	20	433–453	30
Band 2/ Blue	482	65	450–515	30
Band 3/ Green	562	75	525–600	30
Band 4/ Red	655	50	630–680	30
Band 5/ NIR	865	40	845–885	30
Band 9/ Cirrus	1375	30	1360–1390	30

Band 6/ SWIR1	1610	100	1560–1660	30
Band 7/ SWIR2	2200	200	2100–2300	30
Band 8/ Panchromatic	590	180	500–680	15
Band B10/ Brightness temperature	1089	59	1060-1119	100 to 30
Band B11/ Brightness temperature	1200	101	1150-1251	100 to 30

3. Sentinel-1

a) Platform, orbit, and geometric specifications

	Sentinel-1A
Altitude	693 km
Inclination	Sun-synchronous orbit
Coverage	12-day repeat cycle
Payload Mass	2,170 kg
Payload dimensions	3.9 m × 2.6 m × 2.5 m
Power	5,900 W
Life	7-year lifetime (12 years for consumables)
Downlink	520 Mbit/s; S-band 64 kbps uplink and 128 kbps / 2 Mbps downlink for TM/TC.
Field-of-view and swath	Interferometric Wide Swath 250 km
Launched year	3 April 2014

b) Backscattering specifications

- VV: single band co-polarization, transmit in vertical / receive in vertical

- HH: single band co-polarization, transmit in horizontal / receive in horizontal
- VV + VH: dual-band cross-polarization, transmit in vertical / receive in horizontal
- HH + HV: dual-band cross-polarization, transmit in horizontal / receive in vertical

4. Source of the specifications:
   a) Sterckx, S., Benhadj, I., Duhoux, G., Livens, S., Dierckx, W., Goor, E., Adriaensen, S., Heyns, W., Van Hoof, K., Strackx, G., Nackaerts, K., Reusen, I., Van Achteren, T., Dries, J., Van Roey, T., Mellab, K., Duca, R., & Zender, J. (2014). The PROBA-V mission: image processing and calibration. *International Journal of Remote Sensing*, *35*(7), 2565-2588. https://doi.org/10.1080/01431161.2014.883094
   b) https://modis.gsfc.nasa.gov/about/specifications.php
   c) https://sentinel.esa.int/documents/247904/685211/Sentinel-2-Products-Specification-Document
   d) https://www.usgs.gov/media/files/landsat-8-data-users-handbook
   e) https://sentinel.esa.int/documents/247904/1877131/Sentinel-1-Product-Specification

Appendix 4 The webcam station list and its attributes

ID	Code	Name	Province	Regency	Sub District	Village	Latitude	Longitude	Altitude	Direction	Irrigation type
0	balitklimat1	Sukamandi	West Java	Subang	Sukamandi	Sukamandi	-6.3579943	107.646811	100	150	TI
2	CCTV02	Kedunggalar	East Java	Ngawi	Kedunggalar	Njenggrik	-7.4070458	111.3274918	86	164	TI
3	CCTV03	Banggal Sari	East Java	jember	Banggal Sari	Sukorejo	-8.2378611	113.5255556	34	180	Semi-TI
4	CCTV04	Tenggarang	East Java	Bondowoso	Tenggarang	Tamsil Kulon	-7.90583333	113.8607222	242	280	Semi-TI
5	CCTV05	Sumberrejo	East Java	Bojonegoro	Sumberrejo	Pekuwon	-7.1828132	111.9931946	24	207	TI
6	CCTV06	Pontang	Banten	Serang	Pontang	Sukanegara	-6.0608292	106.2623749	12	2	TI
7	CCTV07	Songgom	Central Java	Brebes	Songgom	Jati Roket	-6.99894	109.01736	24	315	TI
8	CCTV08	Dukuhwaru	Central Java	Tegal	Dukuh Waru	Dukuh Waru	-6.96976	109.09492	28	180	Semi-TI
9	CCTV09	Kebonpedes	West Java	Sukabumi	Kebonpedes	Sasagaran	-6.9489465	106.9631577	568	176	Village irrigation
10	CCTV10	Kepanjen	East Java	Malang	Kepanjen	Tegal Sari	-8.1656944	112.5739722	337	0	Semi-TI
13	CCTV13	Bangsal	East Java	Mojokerto	Bangsal	Ngrowo	-7.500699	112.5141296	33	28	Semi-TI
14	CCTV14	Rogo Jampi	East Java	Banyuwangi	Rogo Jampi	Watugebo	-8.3236111	114.3343611	54	0	TI
15	CCTV15	Kota Anyar	East Java	Probolinggo	Kota Anyar	Sukorejo	-7.7570278	112.5423056	68	330	Semi-TI
16	CCTV16	Cibadak	Banten	Lebak	Cibadak	Tambakbaya	-6.3701558	106.1986313	28	32	Semi-TI
17	CCTV17	Sidoharjo	Central Java	Sragen	Sidoharjo	Jetak	-7.435961	110.977272	124.8	313	TI
18	CCTV18	Godong	Central Java	Purwodadi	Godong	Ketitang	-7.024819	110.757754	39.8	200	TI
19	CCTV19	Wonosari	Central Java	Klaten	Wonosari	Sukorejo	-7.603896	110.719147	164.5	37	TI

20	CCTV20	Petarukan	Central Java	Pemalang	Petarukan	Petarukan	-6.89645	109.4596	10	225	TI
22	CCTV22	Binangun	Central Java	Cilacap	Binangun	Binangun	-7.66415	109.26797	11	20	TI
23	CCTV23	Tambakromo	Central Java	Pati	Tambakromo	Tambakromo	-6.873058	111.044163	41.5	338	TI
24	CCTV24	Tanjunganom	East Java	Nganjuk	Tanjunganom	Kedungrejo	-7.6034384	112.0178757	60	33	TI
25	CCTV25	Papar	East Java	Kediri	Papar	Ngampel	-7.70433333	112.1084167	105	10	TI
26	CCTV26	Grogol	Central Java	Sukoharjo	Grogol	Parangjoro	-7.637659	110.808781	133.9	189	TI
27	CCTV27	Cepu	Central Java	Blora	Cepu	Kentong	-7.167052	111.562841	70.3	132	TI
28	CCTV28	Bandongan	Central Java	Magelang	Bandongan	Bandongan	-7.46424	110.19247	418	135	Semi-TI
30	CCTV30	Nanggulan	Jogjakarta	Progo Kulon	Nanggulan	Kembang	-7.742206	110.204971	138	180	TI
31	CCTV31	Wates	Jogjakarta	Progo Kulon	Wates	Kulwaru	-7.891701	110.120255	25.5	180	Semi-TI
32	CCTV32	Sukaratu	West Java	Tasikmalaya	Sukaratu	Sukaratu	-7.2765684	108.1466827	517	60	Semi-TI
35	CCTV35	Kertajati	West Java	Majalengka	Kertajati	Babakan	-6.693284	108.1843262	75	30	TI
36	CCTV36	Rancaekek	West Java	Bandung	Ranca Ekek	Haurpugur	-6.99	107.7882	685	8	Simple irrigation
37	CCTV37	Ponjong	Jogjakarta	Gunung Kidul	Ponjong	Genjahan	-7.973322	110.708369	235	360	TI
38	CCTV38	Tikung	East Java	Lamongan	Tikung	Bakalan Pule	-7.1751986	112.3983688	25	156	
39	CCTV39	Lelea	West Java	Indramayu	Lelea	Telaga Sari	-6.4722905	108.2275696	26	343	TI
40	CCTV40	Kasemen	Banten	Kota Serang	Kasemen	Sawah Luhur	-6.0437851	106.2035065	20	160	TI
42	CCTV42	Pandak	Jogjakarta	Bantul	Pandak	Gilang Harjo	-7.897091	110.307341	63.1	180	Semi-TI

45	CCTV45	Kadungora	West Java	Garut	Kadungora	Gandamekar	-7.1816773	107.8966263	706	356	TI
46	CCTV46	Haurwangi	West Java	Cianjur	Ciranjang	Karangwangi	-6.8083773	107.2738495	280	181	TI
47	CCTV47	Kronjo	Banten	Tangerang	Kronjo	Kronjo	-6.060047	106.4210892	20	188	TI
49	CCTV49	Talagasari	West Java	Karawang	Telagasari	Pasirkamuning	-6.254	107.395	27	21	TI
50	CCTV50	Gegesik	West Java	Cirebon	Gegesik	Gegesik Kidul	-6.6019359	108.4152985	21	358	TI
51	CCTV51	Cimanuk	Banten	Pandeglang	Cimanuk	Sekong	-6.3826122	106.0387421	154	200	TI
53	CCTV53	Cariu	West Java	Bogor	Cariu	Cariu	-6.5017605	107.1215363	84	332	TI
54	CCTV54	Compreng	West Java	Subang	Compreng	Mekarjaya	-6.3747673	107.8795776	32	155	TI
55	CCTV55	Prambanan	Jogjakarta	Sleman	Prambanan	Madurejo	-7.7898488	110.491188	144	180	Semi-TI
56	CCTV56	Imogiri	Jogjakarta	Bantul	Imogiri	Kebon Agung	-7.927869	110.381589	68.2	360	TI

Note: TI = Technical irrigation

Appendix 5 The raw data of field campaign in 2018

No	Date	By	Regency	code	UTM	X	Y	GPS	DEM	Phase	Cropping Pattern
1	20-Jul-18	Ronal	Bojonegoro	E2361	49S	612012	9201338	G76	28	Soybean	PPO
2	20-Jul-18	Ronal	Bojonegoro	E2368	49S	611385	9201588	G76	24	Soybean	PPO
3	20-Jul-18	Ronal	Bojonegoro	E2393	49S	613234	9202110	G76	32	Soybean	PPO
4	20-Jul-18	Ronal	Bojonegoro	E2433	49S	612934	9206897	G76	18	Ratoon	PPO
5	20-Jul-18	Ronal	Bojonegoro	E2436	49S	614874	9202853	G76	26	Maize	PPO
6	20-Jul-18	Ronal	Bojonegoro	E2478	49S	602153	9204057	G76	24	Ratoon	PPO
7	20-Jul-18	Ronal	Bojonegoro	E2479	49S	600603	9203921	G76	24	Ratoon	PPO
8	20-Jul-18	Ronal	Bojonegoro	E2483	49S	611379	9203672	G76	22	Soybean	PPO
9	20-Jul-18	Ronal	Bojonegoro	E2507	49S	606264	9204574	G76	21	Soybean	PPO
10	20-Jul-18	Ronal	Bojonegoro	E2509	49S	614178	9204712	G76	23	Soybean	PPO
11	20-Jul-18	Ronal	Bojonegoro	E2511	49S	615571	9204657	G76	23	Soybean	PPO
12	20-Jul-18	Ronal	Bojonegoro	E2548	49S	599112	9205249	G76	19	Soybean	PPO
13	20-Jul-18	Ronal	Bojonegoro	E2564	49S	609301	9205173	G76	23	Soybean	PPO
14	20-Jul-18	Ronal	Bojonegoro	E2583	49S	615717	9206056	G76	18	Soybean	PPO
15	20-Jul-18	Ronal	Bojonegoro	E2661	49S	597387	9206663	G76	17	Soybean	PPO
16	20-Jul-18	Ronal	Bojonegoro	E2669	49S	596283	9207510	G76	19	Soybean	PPO
17	20-Jul-18	Ronal	Bojonegoro	E2683	49S	615404	9207581	G76	18	Ratoon	PPO
18	20-Jul-18	Dani	Bojonegoro	E2463	49S	612931	9206897	TJ	18	Ratoon	PPO
19	20-Jul-18	Dani	Bojonegoro	E2566	49S	604616	9205622	TJ	21	Soybean	NA
20	20-Jul-18	Dani	Bojonegoro	E2619	49S	601344	9206581	TJ	18	Late ripening	NA
21	20-Jul-18	Dani	Bojonegoro	E2632	49S	609947	9206765	TJ	18	Ratoon	NA
22	20-Jul-18	Dani	Bojonegoro	E2636	49S	606028	9206028	TJ	20	Ratoon	PPO

23	20-Jul-18	Dani	Bojonegoro	E2710D	49S	604744	9207773	TJ	16	Late ripening	NA
24	20-Jul-18	Dani	Bojonegoro	E2714	49S	600678	9208170	TJ	16	Late ripening	NA
25	20-Jul-18	Dani	Bojonegoro	E2760	49S	613328	9209230	TJ	15	Ratoon	PPO
26	20-Jul-18	Dani	Bojonegoro	E2771	49S	615782	9208779	TJ	14	Ratoon	NA
27	21-Jul-18	Ronal	Bojonegoro	E0000	49S	606001	9209708	G76	15	Late vegetative	PPP
28	21-Jul-18	Ronal	Bojonegoro	E0001	49S	599564	9210029	G76	18	Late vegetative	PPP
29	21-Jul-18	Ronal	Bojonegoro	E0002	49S	617976	9216827	G76	10	Late vegetative	PPP
30	21-Jul-18	Ronal	Bojonegoro	E2710R	49S	604702	9207756	G76	17	Late ripening	PPO
31	21-Jul-18	Ronal	Bojonegoro	E2749	49S	624949	9208311	G76	14	Drought	PPT
32	21-Jul-18	Ronal	Bojonegoro	E2793	49S	626863	9209245	G76	14	Drought	PPO
33	21-Jul-18	Ronal	Bojonegoro	E2863	49S	601973	9211400	G76	18	Early ripening	PPP
34	21-Jul-18	Ronal	Bojonegoro	E2903	49S	610117	9212227	G76	15	Early-Middle Vegetative	PPP
35	21-Jul-18	Ronal	Bojonegoro	E2985	49S	618574	9214231	G76	10	Middle vegetative	PPP
36	21-Jul-18	Ronal	Bojonegoro	E2989	49S	623013	9215090	G76	13	Middle vegetative	PPO
37	21-Jul-18	Ronal	Bojonegoro	E3003	49S	613534	9216590	G76	10	Land preparation	PPP
38	21-Jul-18	Ronal	Bojonegoro	E3013	49S	612905	9218015	G76	14	Land preparation	PPP
39	21-Jul-18	Dani	Bojonegoro	E2520	49S	562742	9204966	TJ	30	Early-Middle Vegetative	PPP
40	21-Jul-18	Dani	Bojonegoro	E2524	49S	563292	9205225	TJ	31	Early-Middle Vegetative	NA
41	21-Jul-18	Dani	Bojonegoro	E2573	49S	565232	9206127	TJ	31	Early-Middle Vegetative	NA
42	21-Jul-18	Dani	Bojonegoro	E2593	49S	565858	9205758	TJ	38	Groundnut	NA
43	21-Jul-18	Dani	Bojonegoro	E2690	49S	570444	9207259	TJ	33	Early-Middle Vegetative	NA
44	21-Jul-18	Dani	Bojonegoro	E2743	49S	574157	9208941	TJ	27	Early-Middle Vegetative	NA
45	21-Jul-18	Dani	Bojonegoro	E2780	49S	577166	9209684	TJ	24	Ratoon	NA
46	21-Jul-18	Dani	Bojonegoro	E2789	49S	594066	9209044	TJ	17	Ratoon	NA
47	21-Jul-18	Dani	Bojonegoro	E2846	49S	590753	9210956	TJ	21	Early-Middle Vegetative	PPB

48	21-Jul-18	Dani	Bojonegoro	E2872	49S	590169	9211418	TJ	20	Early reproductive	PPO
49	21-Jul-18	Dani	Bojonegoro	E2914	49S	588248	9212441	TJ	22	Ratoon	NA
50	21-Jul-18	Dani	Bojonegoro	E2925	49S	581459	9212695	TJ	24	Early-Middle Vegetative	NA
51	21-Jul-18	Dani	Bojonegoro	E2943	49S	587350	9212621	TJ	21	Ratoon	PPB
52	21-Jul-18	Dani	Bojonegoro	E2955	49S	585844	9213622	TJ	22	Ratoon	NA
53	22-Jul-18	Ronal	Bojonegoro	E2070	49S	572001	9194631	G76	96	Maize	POB
54	22-Jul-18	Ronal	Bojonegoro	E2108	49S	569375	9195587	G76	68	Other crop	PTB
55	22-Jul-18	Ronal	Bojonegoro	E2110	49S	570641	9195879	G76	71	Tobacco	POB
56	22-Jul-18	Ronal	Bojonegoro	E2116	49S	570161	9196057	G76	70	Maize	POB
57	22-Jul-18	Ronal	Bojonegoro	E2121	49S	572927	9195484	G76	82	Maize	POB
58	22-Jul-18	Ronal	Bojonegoro	E2189	49S	569037	9197241	G76	68	Maize	POB
59	22-Jul-18	Ronal	Bojonegoro	E2213	49S	568570	9198203	G76	66	Maize	POB
60	22-Jul-18	Ronal	Bojonegoro	E2265	49S	571505	9199083	G76	56	Maize	POB
61	22-Jul-18	Ronal	Bojonegoro	E2289	49S	571517	9199824	G76	53	Green beans	POB
62	22-Jul-18	Ronal	Bojonegoro	E2301	49S	572565	9199897	G76	57	maize	POB
63	22-Jul-18	Ronal	Bojonegoro	E2371	49S	573233	9201782	G76	46	Maize	POB
64	22-Jul-18	Ronal	Bojonegoro	E2409	49S	568795	9202377	G76	44	Maize	POB
65	22-Jul-18	Ronal	Bojonegoro	E2442	49S	572683	9203425	G76	40	Maize	POB
66	22-Jul-18	Ronal	Bojonegoro	E2540	49S	571561	9205062	G76	51	Early-Middle Vegetative	PPB
67	22-Jul-18	Ronal	Bojonegoro	E2582	49S	572351	9206069	G76	37	Bare land	POB
68	22-Jul-18	Dani	Bojonegoro	E2020	49S	580289	9192950	TJ	70	Bare land	NA
69	22-Jul-18	Dani	Bojonegoro	E2050	49S	583921	9193977	TJ	93	Maize	NA
70	22-Jul-18	Dani	Bojonegoro	E2084	49S	579793	9194799	TJ	66	Maize	NA
71	22-Jul-18	Dani	Bojonegoro	E2131	49S	578256	9196182	TJ	61	Tobacco	PB
72	22-Jul-18	Dani	Bojonegoro	E2220	49S	584413	9198313	TJ	63	Maize	NA

73	22-Jul-18	Dani	Bojonegoro	E2338	49S	583435	9198700	TJ	70	Maize	NA
74	22-Jul-18	Dani	Bojonegoro	E2377	49S	584026	9201040	TJ	54	Bare land	PB
75	22-Jul-18	Dani	Bojonegoro	E2499	49S	583476	9203491	TJ	49	Maize	NA
76	22-Jul-18	Dani	Bojonegoro	E2587	49S	583364	9205543	TJ	44	Maize	PB
77	22-Jul-18	Dani	Bojonegoro	E2591	49S	578834	9205315	TJ	38	Maize	NA
78	22-Jul-18	Dani	Bojonegoro	E2591E	49S	579446	9209364	TJ	27	Early-Middle Vegetative	NA
79	22-Jul-18	Dani	Bojonegoro	E2627	49S	582668	9206820	TJ	39	Maize	NA
80	22-Jul-18	Dani	Bojonegoro	E2670	49S	584114	9207536	TJ	38	Green beans	NA
81	22-Jul-18	Dani	Bojonegoro	E2735	49S	583040	9208487	TJ	33	Maize	NA
82	26-Jul-18	Ronal	Lamongan	E3195	49S	651013	9195532	G76	48	Other crop	PPO
83	26-Jul-18	Ronal	Lamongan	E3203	49S	652222	9197503	G76	46	Other crop	PPO
84	26-Jul-18	Ronal	Lamongan	E3211	49S	653570	9198281	G76	39	Bare land	PPO
85	26-Jul-18	Ronal	Lamongan	E3220	49S	655461	9198842	G76	31	Other crop	PPO
86	26-Jul-18	Ronal	Lamongan	E3231	49S	649829	9199403	G76	49	Green beans	PB
87	26-Jul-18	Ronal	Lamongan	E3304	49S	656495	9207705	G76	7	Other crop	PPB
88	26-Jul-18	Ronal	Lamongan	E3374	49S	656832	9205592	G76	16	Drought	PPB
89	26-Jul-18	Ronal	Lamongan	E3414	49S	656217	9206840	G76	10	Drought	PPB
90	26-Jul-18	Ronal	Lamongan	E3431	49S	656495	9207705	G76	7	Drought	PPB
91	26-Jul-18	Ronal	Lamongan	E3442	49S	660487	9207527	G76	20	Bare land	PPB
92	26-Jul-18	Ronal	Lamongan	E3452	49S	660176	9208546	G76	24	Bare land	PPB
93	26-Jul-18	Ronal	Lamongan	E3463	49S	659071	9208059	G76	25	Bare land	PPO
94	26-Jul-18	Ronal	Lamongan	E3476	49S	617083	9216358	G76	11	Bare land	PPB
95	26-Jul-18	Ronal	Lamongan	E3520	49S	656845	9210745	G76	6	Bare land	PPO
96	27-Jul-18	Ronal	Lamongan	E3551	49S	663006	9212590	G76	5	Late ripening	Paddy-pond
97	27-Jul-18	Ronal	Lamongan	E3619	49S	661984	9214519	G76	5	Early ripening	Paddy-pond

98	27-Jul-18	Ronal	Lamongan	E3628	49S	663101	9214700	G76	4	Early ripening	Paddy-pond
99	27-Jul-18	Ronal	Lamongan	E3649	49S	665375	9215461	G76	4	Early ripening	Paddy-pond
100	27-Jul-18	Ronal	Lamongan	E3717	49S	667639	9216871	G76	6	Early ripening	Paddy-pond
101	27-Jul-18	Ronal	Lamongan	E3773	49S	668500	9218393	G76	6	Early ripening	PB
102	27-Jul-18	Ronal	Lamongan	E3793	49S	665428	9218833	G76	3	Late vegetative	Paddy-pond
103	27-Jul-18	Ronal	Lamongan	E3880	49S	664756	9223398	G76	7	late vegetative	Paddy-pond
104	27-Jul-18	Ronal	Lamongan	E3902	49S	666555	9224258	G76	3	Land Use Change	Fish pond
105	27-Jul-18	Ronal	Lamongan	E3911	49S	659744	9224761	G76	8	Early ripening	PB
106	27-Jul-18	Ronal	Lamongan	E3950	49S	652701	9226259	G76	4	Late ripening	Paddy-pond
107	27-Jul-18	Dani	Lamongan	E3580	49S	638867	9213001	TJ	11	Bare land	NA
108	27-Jul-18	Dani	Lamongan	E3584	49S	635117	9213502	TJ	14	Bare land	NA
109	27-Jul-18	Dani	Lamongan	E3615	49S	641053	9214231	TJ	7	Bare land	NA
110	27-Jul-18	Dani	Lamongan	E3623	49S	638729	9214073	TJ	9	Maize	NA
111	27-Jul-18	Dani	Lamongan	E3641	49S	634197	9215175	TJ	8	Early ripening	PPO
112	29-Jul-18	Ronal	Lamongan	E3050	49S	631502	9187161	G76	97	Tobacco	PPT
113	29-Jul-18	Ronal	Lamongan	E3065	49S	628271	9187729	G76	81	Tobacco	PPT
114	29-Jul-18	Ronal	Lamongan	E3136	49S	642880	9192618	G76	60	Ratoon	PPT
115	29-Jul-18	Ronal	Lamongan	E3159	49S	639443	9191517	G76	72	Tobacco	PPT
116	29-Jul-18	Ronal	Lamongan	E3170	49S	645022	9193400	G76	66	Bare land	NA
117	29-Jul-18	Ronal	Lamongan	E3177	49S	633654	9194001	G76	84	Maize	PPT
118	29-Jul-18	Ronal	Lamongan	E3178	49S	638620	9194353	G76	95	Maize	PPT
119	29-Jul-18	Ronal	Lamongan	E3233	49S	633088	9199928	G76	62	Tobacco	PPT
120	29-Jul-18	Ronal	Lamongan	E3273	49S	627225	9201235	G76	37	Drought	PPT
121	29-Jul-18	Ronal	Lamongan	E3322	49S	627015	9204489	G76	22	Tobacco	PPT
122	29-Jul-18	Ronal	Lamongan	E3394	49S	626954	9206616	G76	17	Tobacco	PPT

123	29-Jul-18	Dani	Lamongan	E3341	49S	638219	9205042	TJ	36	Green beans	POB
124	29-Jul-18	Dani	Lamongan	E3343	49S	631115	9205136	TJ	29	Ratoon	PPB
125	29-Jul-18	Dani	Lamongan	E3352	49S	635545	9204815	TJ	30	Ratoon	PPB
126	29-Jul-18	Dani	Lamongan	E3363	49S	642635	9205167	TJ	41	Maize	PPB
127	29-Jul-18	Dani	Lamongan	E3367	49S	632060	9206311	TJ	20	Weed	PPB
128	29-Jul-18	Dani	Lamongan	E3386	49S	647591	9206387	TJ	28	Bare land	PPB
129	29-Jul-18	Dani	Lamongan	E3411	49S	647863	9207564	TJ	14	Bare land	PPB
130	29-Jul-18	Dani	Lamongan	E3416	49S	637812	9206319	TJ	26	Soybean	PPB
131	29-Jul-18	Dani	Lamongan	E3458	49S	645041	9209036	TJ	15	Soybean	PPB
132	29-Jul-18	Dani	Lamongan	E3469	49S	649853	9209421	TJ	10	Ratoon	PB
133	29-Jul-18	Dani	Lamongan	E3515	49S	643272	9209875	TJ	19	Ratoon	PPB
134	29-Jul-18	Dani	Lamongan	E3522	49S	646538	9211004	TJ	9	Green beans	PPO
135	29-Jul-18	Dani	Lamongan	E3526	49S	649895	9210644	TJ	7	Bare land	PPB
136	29-Jul-18	Dani	Lamongan	E3605	49S	650284	9212852	TJ	5	Maize	PPO
137	31-Jul-18	Ronal	Jombang	E0527	49S	639640	9167690	G76	32	Sugarcane	PPO
138	31-Jul-18	Ronal	Jombang	E0557	49S	641154	9168528	G76	30	Maize	PPO
139	31-Jul-18	Ronal	Jombang	E0591	49S	647666	9169555	G76	27	Sugarcane	PPO
140	31-Jul-18	Ronal	Jombang	E0604	49S	645728	9169838	G76	26	Sugarcane	PPO
141	31-Jul-18	Ronal	Jombang	E0628	49S	642501	9170313	G76	26	Late ripening	PPO
142	31-Jul-18	Ronal	Jombang	E0634	49S	648845	9170628	G76	24	Early ripening	PPB
143	31-Jul-18	Ronal	Jombang	E0661	49S	638403	9171386	G76	32	Ratoon	PPO
144	31-Jul-18	Ronal	Jombang	E0694	49S	640234	9172299	G76	28	Late ripening	PPB
145	31-Jul-18	Ronal	Jombang	E0702	49S	645836	9172671	G76	25	Early ripening	PPB
146	31-Jul-18	Ronal	Jombang	E0738R	49S	636477	9173748	G76	29	Late ripening	PPO
147	31-Jul-18	Ronal	Jombang	E0744	49S	646156	9174040	G76	25	Late ripening	PPB

148	31-Jul-18	Ronal	Jombang	E0782	49S	642487	9175149	G76	29	Late ripening	PPO
149	31-Jul-18	Ronal	Jombang	E0783R	49S	640471	9174858	G76	30	Ratoon	PPO
150	01-Aug-18	Ronal	Jombang	E0825	49S	636417	9177231	G76	34	Land Use Change	NA
151	01-Aug-18	Ronal	Jombang	E0831	49S	639228	9177535	G76	30	Late ripening	PTB
152	01-Aug-18	Ronal	Jombang	E0846	49S	635720	9178043	G76	35	Tobacco	PTB
153	01-Aug-18	Ronal	Jombang	E0874	49S	633436	9179035	G76	37	Tobacco	PTB
154	01-Aug-18	Ronal	Jombang	E0876	49S	631087	9179472	G76	46	Tobacco	PTB
155	01-Aug-18	Ronal	Jombang	E0883	49S	639744	9179798	G76	32	Tobacco	PTB
156	01-Aug-18	Ronal	Jombang	E0906	49S	640951	9180235	G76	32	Tobacco	PTB
157	01-Aug-18	Ronal	Jombang	E0913	49S	640290	9180720	G76	34	Tobacco	PTB
158	01-Aug-18	Ronal	Jombang	E0916	49S	636117	9181233	G76	38	Tobacco	PTB
159	01-Aug-18	Ronal	Jombang	E0925	49S	640298	9181963	G76	47	Land Use Change	NA
160	01-Aug-18	Ronal	Jombang	E0936	49S	635006	9183348	G76	55	Tobacco	PTB
161	01-Aug-18	Ronal	Jombang	E0946	49S	634219	9184468	G76	75	Maize	POB
162	01-Aug-18	Ronal	Jombang	E0955	49S	634217	9185322	G76	73	Maize	POB
163	01-Aug-18	Dani	Jombang	E0411	49S	630935	9163445	TJ	44	Maize	PPO
164	01-Aug-18	Dani	Jombang	E0433	49S	630775	9164525	TJ	44	Harvested	PPO
165	01-Aug-18	Dani	Jombang	E0466	49S	626369	9165158	TJ	39	Ratoon	PPO
166	01-Aug-18	Dani	Jombang	E0472	49S	629807	9165700	TJ	42	Harvested	PPO
167	01-Aug-18	Dani	Jombang	E0485	49S	625843	9166111	TJ	42	Bare land	PPO
168	01-Aug-18	Dani	Jombang	E0532	49S	634117	9168076	TJ	36	Ratoon	PPO
169	01-Aug-18	Dani	Jombang	E0550	49S	634906	9168079	TJ	34	Ratoon	PPO
170	01-Aug-18	Dani	Jombang	E0565	49S	628403	9169993	TJ	35	Late reproductive	PPO
171	01-Aug-18	Dani	Jombang	E0571	49S	633192	9168355	TJ	37	Late ripening	PPO
172	01-Aug-18	Dani	Jombang	E0592	49S	637327	9169169	TJ	33	Maize	POB

173	01-Aug-18	Dani	Jombang	E0646	49S	631499	9170807	TJ	33	Early ripening	PPO
174	01-Aug-18	Dani	Jombang	E0684	49S	634864	9171757	TJ	32	late ripening	PPO
175	01-Aug-18	Dani	Jombang	E0738D	49S	636307	9173474	TJ	30	late ripening	PPO
176	01-Aug-18	Dani	Jombang	E0783D	49S	640100	9174541	TJ	29	Soybean	PPO
177	02-Aug-18	Ronal	Jombang	E0044	49S	641069	9149255	G76	96	Early ripening	PPB
178	02-Aug-18	Ronal	Jombang	E0048	49S	638162	9149805	G76	106	Bare land	NA
179	02-Aug-18	Ronal	Jombang	E0059	49S	643819	9150445	G76	88	Early ripening	PPP
180	02-Aug-18	Ronal	Jombang	E0068	49S	638536	9151081	G76	90	Sugarcane	PPO
181	02-Aug-18	Ronal	Jombang	E0077	49S	636936	9151601	G76	94	Other crop	POB
182	02-Aug-18	Ronal	Jombang	E0107	49S	640101	9153055	G76	75	Late ripening	PPB
183	02-Aug-18	Ronal	Jombang	E0118	49S	635814	9153531	G76	82	Ratoon	PPO
184	02-Aug-18	Ronal	Jombang	E0127	49S	636886	9154262	G76	81	Maize	PPO
185	02-Aug-18	Ronal	Jombang	E0145	49S	640101	9154618	G76	70	Maize	PPO
186	02-Aug-18	Ronal	Jombang	E0146	49S	634460	9155252	G76	73	Maize	PPO
187	02-Aug-18	Ronal	Jombang	E0160	49S	631332	9155789	G76	66	Land preparation	PPB
188	02-Aug-18	Ronal	Jombang	E0187	49S	638884	9157197	G76	65	Groundnut	PPO
189	02-Aug-18	Ronal	Jombang	E0199	49S	640414	9157740	G76	59	Bare land	PPB
190	02-Aug-18	Ronal	Jombang	E0230	49S	639140	9158620	G76	61	Groundnut	PPO
191	02-Aug-18	Ronal	Jombang	E0257	49S	637899	9158980	G76	59	Maize	PPO
192	02-Aug-18	Ronal	Jombang	E0275	49S	633395	9159855	G76	55	Maize	PPO
193	02-Aug-18	Dani	Jombang	E0214	49S	641108	9158263	TJ	57	land preparation	PPP
194	02-Aug-18	Dani	Jombang	E0217	49S	644063	9157638	TJ	52	Maize	PPO
195	02-Aug-18	Dani	Jombang	E0280	49S	646984	9159893	TJ	43	Maize	PPO
196	02-Aug-18	Dani	Jombang	E0319	49S	642172	9161248	TJ	45	Maize	PPO
197	02-Aug-18	Dani	Jombang	E0334	49S	645310	9161337	TJ	38	Maize	PPO

198	02-Aug-18	Dani	Jombang	E0337	49S	640279	9161625	TJ	46	Bare land	NA
199	02-Aug-18	Dani	Jombang	E0362	49S	641535	9162538	TJ	40	Maize	PPO
200	02-Aug-18	Dani	Jombang	E0379	49S	647049	9162792	TJ	36	Maize	PPO
201	02-Aug-18	Dani	Jombang	E0424	49S	638977	9164056	TJ	41	Maize	PPO
202	02-Aug-18	Dani	Jombang	E0427	49S	647718	9164303	TJ	34	Maize	PPO
203	02-Aug-18	Dani	Jombang	E0440	49S	637672	9164578	TJ	43	Bare land	PB
204	02-Aug-18	Dani	Jombang	E0460	49S	644725	9164863	TJ	32	Maize	POB
205	02-Aug-18	Dani	Jombang	E0495	49S	645856	9166536	TJ	29	Maize	PPO
206	02-Aug-18	Dani	Jombang	E0503	49S	647085	9166993	TJ	28	Maize	PPO
207	04-Aug-18	Ronal	Nganjuk	E0979	49S	611573	9143966	G76	58	Early-Middle Vegetative	PPP
208	04-Aug-18	Ronal	Nganjuk	E0987	49S	611873	9144611	G76	61	Maize	PPO
209	04-Aug-18	Ronal	Nganjuk	E1019	49S	615414	9147046	G76	54	Maize	PPO
210	04-Aug-18	Ronal	Nganjuk	E1023	49S	613845	9147582	G76	57	Maize	PPO
211	04-Aug-18	Ronal	Nganjuk	E1036	49S	616653	9147768	G76	54	Maize	PPO
212	04-Aug-18	Ronal	Nganjuk	E1064	49S	616034	9148974	G76	51	Maize	PPO
213	04-Aug-18	Ronal	Nganjuk	E1136	49S	613156	9151290	G76	51	Sugarcane	Sugarcane
214	04-Aug-18	Ronal	Nganjuk	E1195	49S	614307	9152519	G76	54	Other crop	Other crop
215	04-Aug-18	Ronal	Nganjuk	E1220	49S	618788	9153047	G76	49	Maize	PPP
216	04-Aug-18	Ronal	Nganjuk	E1272	49S	613315	9154054	G76	49	Other crop	PPO
217	04-Aug-18	Ronal	Nganjuk	E1315	49S	613092	9155469	G76	52	Early-Middle Vegetative	PPP
218	04-Aug-18	Ronal	Nganjuk	E1334	49S	614244	9155910	G76	48	Early-Middle Vegetative	PPP
219	04-Aug-18	Ronal	Nganjuk	E1345	49S	619999	9155810	G76	45	Sugarcane	PPO
220	04-Aug-18	Ronal	Nganjuk	E1402	49S	617253	9157575	G76	49	Other crop	PPO
221	04-Aug-18	Ronal	Nganjuk	E1421	49S	615165	9158052	G76	46	Maize	PPO
222	04-Aug-18	Dani	Nganjuk	E1009	49S	609625	9146251	TJ	55	Maize	PPO

223	04-Aug-18	Dani	Nganjuk	E1035	49S	611274	9148485	TJ	53	Early-Middle Vegetative	PPO
224	04-Aug-18	Dani	Nganjuk	E1082	49S	604406	9149896	TJ	55	Maize	PPO
225	04-Aug-18	Dani	Nganjuk	E1116	49S	609221	9150913	TJ	52	Maize	PPO
226	04-Aug-18	Dani	Nganjuk	E1126	49S	604968	9151162	TJ	53	Maize	PPO
227	04-Aug-18	Dani	Nganjuk	E1187	49S	605313	9152216	TJ	52	Maize	PPO
228	04-Aug-18	Dani	Nganjuk	E1203	49S	608598	9152692	TJ	50	Maize	PPO
229	04-Aug-18	Dani	Nganjuk	E1215	49S	605654	9153122	TJ	52	Maize	PPO
230	04-Aug-18	Dani	Nganjuk	E1247	49S	604537	9154263	TJ	51	Maize	PPO
231	04-Aug-18	Dani	Nganjuk	E1343	49S	605091	9155766	TJ	50	Maize	PPO
232	04-Aug-18	Dani	Nganjuk	E1394	49S	606691	9157548	TJ	48	Land preparation	PPO
233	04-Aug-18	Dani	Nganjuk	E1426	49S	604870	9157991	TJ	49	Ratoon	PPO
234	04-Aug-18	Dani	Nganjuk	E1452	49S	606945	9158678	TJ	46	Maize	PPO
235	05-Aug-18	Ronal	Nganjuk	E1527	49S	615504	9160764	G76	44	Maize	PPO
236	05-Aug-18	Ronal	Nganjuk	E1581	49S	618016	9162223	G76	41	Ratoon	PPB
237	05-Aug-18	Ronal	Nganjuk	E1603	49S	620461	9162679	G76	41	Ratoon	PPB
238	05-Aug-18	Ronal	Nganjuk	E1615	49S	619010	9163002	G76	41	Ratoon	PPB
239	05-Aug-18	Ronal	Nganjuk	E1678	49S	614533	9164780	G76	45	Early-Middle Vegetative	PPB
240	05-Aug-18	Ronal	Nganjuk	E1705	49S	623418	9165565	G76	42	Maize	PPB
241	05-Aug-18	Ronal	Nganjuk	E1761	49S	621271	9167154	G76	42	Sugarcane	Sugarcane
242	05-Aug-18	Ronal	Nganjuk	E1791	49S	623704	9167797	G76	41	Early ripening	PPP
243	05-Aug-18	Ronal	Nganjuk	E1826	49S	621381	9168719	G76	41	Ratoon	PPB
244	05-Aug-18	Ronal	Nganjuk	E1838	49S	620172	9170079	G76	48	Ratoon	PPB
245	05-Aug-18	Ronal	Nganjuk	E1847	49S	617998	9170841	G76	58	Ratoon	PPB
246	05-Aug-18	Ronal	Nganjuk	E1892	49S	626684	9169463	G76	39	Late ripening	PPB
247	05-Aug-18	Dani	Nganjuk	E1627	49S	609102	9163477	TJ	47	Shallots	PB

248	05-Aug-18	Dani	Nganjuk	E1628	49S	611200	9163840	TJ	47	Early-Middle Vegetative	PPP
249	05-Aug-18	Dani	Nganjuk	E1680	49S	597987	9164091	TJ	57	Shallots	PB
250	05-Aug-18	Dani	Nganjuk	E1684	49S	605195	9164357	TJ	52	Shallots	PB
251	05-Aug-18	Dani	Nganjuk	E1697	49S	600750	9165300	TJ	56	Soybean	PPO
252	05-Aug-18	Dani	Nganjuk	E1704	49S	598129	9165463	TJ	59	Shallots	PB
253	05-Aug-18	Dani	Nganjuk	E1744	49S	600213	9166112	TJ	62	Soybean	PPO
254	05-Aug-18	Dani	Nganjuk	E1763	49S	598072	9166815	TJ	59	Shallots	PB
255	05-Aug-18	Dani	Nganjuk	E1770	49S	601662	9166784	TJ	60	Soybean	PPO
256	05-Aug-18	Dani	Nganjuk	E1792	49S	601260	9168144	TJ	64	Maize	PPO
257	05-Aug-18	Dani	Nganjuk	E1803	49S	602639	9168895	TJ	65	Early-Middle Vegetative	PPP
258	05-Aug-18	Dani	Nganjuk	E1805	49S	597232	9168077	TJ	67	Shallots	PB
259	05-Aug-18	Dani	Nganjuk	E1833JGNG	49S	601358	9169947	TJ	70	Maize	PPO
260	05-Aug-18	Dani	Nganjuk	E1833PADI	49S	601418	9169874	TJ	69	late vegetative	PB
261	06-Aug-18	Ronal	Nganjuk	E1150	49S	602220	9151572	G76	61	Maize	PPO
262	06-Aug-18	Ronal	Nganjuk	E1170	49S	599872	9152123	G76	65	Maize	PPO
263	06-Aug-18	Ronal	Nganjuk	E1290	49S	596327	9154751	G76	76	Maize	PPO
264	06-Aug-18	Ronal	Nganjuk	E1328	49S	596199	9155985	G76	71	Maize	PPO
265	06-Aug-18	Ronal	Nganjuk	E1370	49S	593060	9156229	G76	86	Maize	PPO
266	06-Aug-18	Ronal	Nganjuk	E1398	49S	595572	9157172	G76	69	Maize	PPO
267	06-Aug-18	Ronal	Nganjuk	E1454	49S	596975	9158906	G76	61	Maize	PPO
268	06-Aug-18	Ronal	Nganjuk	E1459	49S	595243	9158720	G76	63	Vegetative	PPP
269	06-Aug-18	Ronal	Nganjuk	E1561	49S	592608	9161787	G76	77	Shallots	PPO
270	06-Aug-18	Ronal	Nganjuk	E1637	49S	590575	9163671	G76	84	Shallots	PPO
271	06-Aug-18	Ronal	Nganjuk	E1650	49S	592858	9163981	G76	71	Shallots	PPO
272	06-Aug-18	Ronal	Nganjuk	E1669	49S	591524	9164636	G76	75	Early-Middle Vegetative	PPP

273	13-Aug-18	Ronal	Indramayu	W1567	49S	209502	9288064	G76	4	Early reproductive	PPB
274	13-Aug-18	Ronal	Indramayu	W1667	49S	208011	9288779	G76	2	Reproductive	PPB
275	13-Aug-18	Ronal	Indramayu	W1727	49S	210560	9288898	G76	6	Late ripening	PPB
276	13-Aug-18	Ronal	Indramayu	W1807R	49S	208093	9289841	G76	3	Late reproductive	PPB
277	13-Aug-18	Ronal	Indramayu	W1887	49S	211199	9290402	G76	4	Early ripening	PPB
278	13-Aug-18	Ronal	Indramayu	W1997	49S	210004	9291760	G76	4	Late ripening	PPB
279	13-Aug-18	Ronal	Indramayu	W2127	49S	210382	9293106	G76	3	Late ripening	PPB
280	13-Aug-18	Ronal	Indramayu	W2187	49S	208258	9293614	G76	3	Early ripening	PPB
281	13-Aug-18	Ronal	Indramayu	W2207	49S	206423	9293859	G76	-1	Early ripening	PPB
282	13-Aug-18	Ronal	Indramayu	W2407	49S	204770	9295896	G76	1	Early-Middle Vegetative	PPB
283	13-Aug-18	Ronal	Indramayu	W2607	49S	205438	9299495	G76	1	Ratoon	PPB
284	13-Aug-18	Ronal	Indramayu	W2687	49S	205223	9301372	G76	0	Ratoon	PPB
285	13-Aug-18	Ronal	Indramayu	W2707	49S	202996	9302542	G76	0	Ratoon	PPB
286	13-Aug-18	Ronal	Indramayu	W2727	49S	203539	9303156	G76	0	Ratoon	PPB
287	14-Aug-18	Ronal	Indramayu	W0370	49S	202137	9276291	G76	12	late vegetative	PPB
288	14-Aug-18	Ronal	Indramayu	W0451	49S	200613	9277355	G76	11	Early-Middle Vegetative	PPB
289	14-Aug-18	Ronal	Indramayu	W0594	49S	202772	9279159	G76	10	Early reproductive	PPB
290	14-Aug-18	Ronal	Indramayu	W0875	49S	201657	9281529	G76	7	Late ripening	PPB
291	14-Aug-18	Ronal	Indramayu	W0956	49S	199818	9282572	G76	9	Ratoon	PPO
292	14-Aug-18	Ronal	Indramayu	W1036	49S	198966	9283367	G76	7	Ratoon	PPB
293	14-Aug-18	Ronal	Indramayu	W1177	49S	197177	9284550	G76	7	Ratoon	PPB
294	14-Aug-18	Ronal	Indramayu	W1337	49S	197867	9285236	G76	8	Ratoon	PPB
295	14-Aug-18	Ronal	Indramayu	W1597	49S	198167	9287730	G76	7	Ratoon	PPB
296	14-Aug-18	Ronal	Indramayu	W2037	49S	200712	9292050	G76	4	Land preparation	PPB
297	14-Aug-18	Ronal	Indramayu	W2057	49S	196933	9292291	G76	3	Late ripening	PPB

298	14-Aug-18	Ronal	Indramayu	W2097	49S	199138	9292942	G76	3	Late ripening	PPB
299	15-Aug-18	Ronal	Indramayu	W0513	49S	191357	9278148	G76	13	Other crop	PPO
300	15-Aug-18	Ronal	Indramayu	W0614	49S	189058	9278589	G76	16	Bare land	PPB
301	15-Aug-18	Ronal	Indramayu	W0674	49S	192672	9279968	G76	11	Late ripening	PPB
302	15-Aug-18	Ronal	Indramayu	W0855	49S	191319	9281604	G76	10	Late ripening	PPB
303	15-Aug-18	Ronal	Indramayu	W0896	49S	188806	9281742	G76	9	Ratoon	PPB
304	15-Aug-18	Ronal	Indramayu	W1076	49S	186479	9283356	G76	8	Ratoon	PPB
305	15-Aug-18	Ronal	Indramayu	W1157	49S	194138	9284356	G76	5	Ratoon	PPB
306	15-Aug-18	Ronal	Indramayu	W1357	49S	192467	9284998	G76	5	Late ripening	PPB
307	15-Aug-18	Ronal	Indramayu	W1557	49S	191804	9287333	G76	2	Early ripening	PPB
308	15-Aug-18	Ronal	Indramayu	W1577	49S	186562	9287628	G76	5	Ratoon	PPB
309	15-Aug-18	Ronal	Indramayu	W1697	49S	186594	9288405	G76	5	Ratoon	PPB
310	15-Aug-18	Ronal	Indramayu	W1837	49S	191917	9290157	G76	2	Late ripening	PPB
311	16-Aug-18	Ronal	Indramayu	W1197	49S	168713	9284008	G76	21	Bare land	PPB
312	16-Aug-18	Ronal	Indramayu	W1297	49S	171640	9285259	G76	15	Bare land	PPB
313	16-Aug-18	Ronal	Indramayu	W1377	49S	170260	9284841	G76	18	Bare land	PPB
314	16-Aug-18	Ronal	Indramayu	W1477	49S	176169	9286700	G76	14	Bare land	PPB
315	16-Aug-18	Ronal	Indramayu	W1497	49S	175361	9286937	G76	14	Ratoon	PPB
316	16-Aug-18	Ronal	Indramayu	W1777	49S	175755	9289650	G76	10	Ratoon	PPB
317	16-Aug-18	Ronal	Indramayu	W1857	49S	175102	9290267	G76	6	Harvested	PPB
318	16-Aug-18	Ronal	Indramayu	W2157	49S	177433	9293393	G76	2	Early ripening	PPB
319	16-Aug-18	Ronal	Indramayu	W2257	49S	178434	9294573	G76	2	Early ripening	PPB
320	16-Aug-18	Ronal	Indramayu	W2457	49S	184599	9296748	G76	2	Drought	PPB
321	16-Aug-18	Dani	Indramayu	W1056	49S	180141	9283509	TJ	12	Ratoon	PPB
322	16-Aug-18	Dani	Indramayu	W1277	49S	177353	9284547	TJ	15	Ratoon	PPB

323	16-Aug-18	Dani	Indramayu	W1317	49S	179250	9284963	TJ	13	Ratoon	PPB
324	16-Aug-18	Dani	Indramayu	W1417	49S	177627	9285925	TJ	11	Ratoon	PPB
325	16-Aug-18	Dani	Indramayu	W1637	49S	178467	9288093	TJ	9	Ratoon	PPB
326	16-Aug-18	Dani	Indramayu	W1677	49S	177336	9288293	TJ	11	Ratoon	PPB
327	16-Aug-18	Dani	Indramayu	W1717	49S	179220	9288914	TJ	7	Drought	PPB
328	16-Aug-18	Dani	Indramayu	W1737	49S	187938	9289006	TJ	4	Early ripening	NA
329	16-Aug-18	Dani	Indramayu	W1807D	49S	184504	9290776	TJ	3	late ripening	PPB
330	16-Aug-18	Dani	Indramayu	W1877	49S	181190	9292024	TJ	4	Drought	PPB
331	16-Aug-18	Dani	Indramayu	W1917	49S	179946	9290338	TJ	6	Drought	PPB
332	16-Aug-18	Dani	Indramayu	W1937	49S	183502	9290857	TJ	4	Ratoon	PPB
333	17-Aug-18	Ronal	Indramayu	W2117	49S	168680	9292858	G76	9	Early ripening	PPB
334	17-Aug-18	Ronal	Indramayu	W2177	49S	172381	9293108	G76	5	Early reproductive	PPB
335	17-Aug-18	Ronal	Indramayu	W2517	48S	828994	9297651	G76	11	Early-Middle Vegetative	PPB
336	17-Aug-18	Ronal	Indramayu	W2557	48S	830771	9298280	G76	8	Early-Middle Vegetative	PPB
337	17-Aug-18	Ronal	Indramayu	W2617	48S	826525	9299109	G76	9	Land preparation	PPB
338	17-Aug-18	Ronal	Indramayu	W2637	49S	175420	9299906	G76	3	Early-Middle Vegetative	PPB
339	17-Aug-18	Ronal	Indramayu	W2677	49S	168319	9301101	G76	1	Early-Middle Vegetative	PPB
340	17-Aug-18	Ronal	Indramayu	W2717	48S	829803	9302561	G76	6	Bare land	PPB
341	17-Aug-18	Ronal	Indramayu	W2757	48S	826394	9303372	G76	5	Early-Middle Vegetative	PB
342	17-Aug-18	Dani	Indramayu	W0183	49S	173813	9272938	TJ	46	Ratoon	PPB
343	17-Aug-18	Dani	Indramayu	W0245	48S	828607	9274918	TJ	45	Ratoon	PPB
344	17-Aug-18	Dani	Indramayu	W0267	48S	826836	9273391	TJ	56	Ratoon	PPB
345	17-Aug-18	Dani	Indramayu	W0289	48S	830295	9276982	TJ	39	Ratoon	PPB
346	17-Aug-18	Dani	Indramayu	W0350	49S	170908	9275429	TJ	40	Ratoon	PPB
347	17-Aug-18	Dani	Indramayu	W0390	49S	169838	9277692	TJ	34	Ratoon	PPB

348	17-Aug-18	Dani	Indramayu	W0410	49S	176461	9275363	TJ	36	Ratoon	PPB
349	17-Aug-18	Dani	Indramayu	W0431	49S	180899	9277358	TJ	24	Ratoon	PPB
350	17-Aug-18	Dani	Indramayu	W0472	49S	177926	9276939	TJ	30	Ratoon	PPB
351	17-Aug-18	Dani	Indramayu	W0694	48S	827191	9279067	TJ	32	Ratoon	PPB
352	17-Aug-18	Dani	Indramayu	W0755	49S	181399	9279497	TJ	21	Ratoon	PPB
353	17-Aug-18	Dani	Indramayu	W1116	48S	826978	9283028	TJ	23	Ratoon	PPB
354	17-Aug-18	Dani	Indramayu	W2577E	48S	829882	9300120	TJ	8	Early-Middle Vegetative	PPB
355	23-Aug-18	Ronal	Subang	W3490	48S	818655	9286954	G76	21	Late ripening	PPB
356	23-Aug-18	Ronal	Subang	W3572	48S	816659	9287948	G76	20	Early reproductive	PPB
357	23-Aug-18	Ronal	Subang	W3653	48S	814536	9288365	G76	19	Late vegetative	PPB
358	23-Aug-18	Ronal	Subang	W3773	48S	813576	9291510	G76	15	Early-Middle Vegetative	PPB
359	23-Aug-18	Ronal	Subang	W4194	48S	820895	9298129	G76	9	Early-Middle Vegetative	PPB
360	23-Aug-18	Ronal	Subang	W4375	48S	817961	9301679	G76	9	Early-Middle Vegetative	PPB
361	23-Aug-18	Ronal	Subang	W4475	48S	820952	9302873	G76	7	Early-Middle Vegetative	PPB
362	23-Aug-18	Ronal	Subang	W4575	48S	817769	9304971	G76	7	Ratoon	PPB
363	23-Aug-18	Ronal	Subang	W4696	48S	821383	9306670	G76	4	Other crop	PPO
364	24-Aug-18	Ronal	Subang	W3224	48S	804510	9280525	G76	59	Early-Middle Vegetative	PPB
365	24-Aug-18	Ronal	Subang	W3245	48S	811590	9280774	G76	41	Ratoon	PPB
366	24-Aug-18	Ronal	Subang	W3348	48S	810013	9283832	G76	34	Ratoon	PPB
367	24-Aug-18	Ronal	Subang	W3388	48S	804697	9284919	G76	41	Ratoon	PPB
368	24-Aug-18	Ronal	Subang	W3449	48S	810994	9286466	G76	29	Ratoon	PPB
369	24-Aug-18	Ronal	Subang	W3469	48S	806009	9286744	G76	30	Ratoon	PPB
370	24-Aug-18	Ronal	Subang	W3693	48S	806069	9290328	G76	22	Late ripening	PPB
371	24-Aug-18	Ronal	Subang	W3833	48S	808028	9291543	G76	23	Early ripening	PPB
372	24-Aug-18	Ronal	Subang	W3853	48S	809219	9292949	G76	17	Late vegetative	PPB

373	24-Aug-18	Ronal	Subang	W4154	48S	807279	9297861	G76	9	Late vegetative	PPB
374	24-Aug-18	Ronal	Subang	W4215	48S	805413	9297966	G76	11	Late vegetative	PPB
375	24-Aug-18	Ronal	Subang	W4275	48S	810120	9299334	G76	9	Early-Middle Vegetative	PPB
376	24-Aug-18	Dani	Subang	W4315D	48S	786382	9301451	TJ	15	Early ripening	PPB
377	24-Aug-18	Dani	Subang	W4535	48S	787520	9304603	TJ	10	Early reproductive	PPB
378	24-Aug-18	Dani	Subang	W4555	48S	785676	9303749	TJ	10	Early ripening	PPB
379	24-Aug-18	Dani	Subang	W4615	48S	803516	9304089	TJ	2	Early-Middle Vegetative	PPB
380	24-Aug-18	Dani	Subang	W4635	48S	802103	9304840	TJ	2	Early-Middle Vegetative	PPB
381	24-Aug-18	Dani	Subang	W4655	48S	795505	9305803	TJ	1	Late vegetative	PPB
382	24-Aug-18	Dani	Subang	W4716	48S	792234	9307481	TJ	0	Early reproductive	NA
383	24-Aug-18	Dani	Subang	W4736	48S	790471	9307996	TJ	0	Early reproductive	NA
384	24-Aug-18	Dani	Subang	W4756	48S	804836	9306813	TJ	0	Early-Middle Vegetative	PPB
385	24-Aug-18	Dani	Subang	W4776	48S	789213	9308703	TJ	1	Late vegetative	NA
386	25-Aug-18	Ronal	Subang	W3368	48S	793553	9284461	G76	57	Early-Middle Vegetative	PPB
387	25-Aug-18	Ronal	Subang	W3428	48S	789440	9285677	G76	42	Early-Middle Vegetative	PPB
388	25-Aug-18	Ronal	Subang	W3592	48S	783055	9288882	G76	34	Ratoon	PPB
389	25-Aug-18	Ronal	Subang	W3632	48S	791595	9288839	G76	25	Early-Middle Vegetative	PPB
390	25-Aug-18	Ronal	Subang	W3673	48S	795547	9289720	G76	23	Ratoon	PPB
391	25-Aug-18	Ronal	Subang	W3753	48S	786951	9291386	G76	25	Ratoon	PPB
392	25-Aug-18	Ronal	Subang	W3793	48S	784471	9291920	G76	30	Ratoon	PPB
393	25-Aug-18	Ronal	Subang	W3874	48S	781620	9293358	G76	32	Late ripening	PPB
394	25-Aug-18	Ronal	Subang	W3954	48S	793100	9294173	G76	19	Ratoon	PPB
395	25-Aug-18	Ronal	Subang	W4014	48S	795334	9295611	G76	12	Ratoon	PPB
396	25-Aug-18	Ronal	Subang	W4074	48S	798098	9296162	G76	9	Late ripening	PPB
397	25-Aug-18	Ronal	Subang	W4235	48S	800301	9298717	G76	9	Early-Middle Vegetative	PPB

398	25-Aug-18	Ronal	Subang	W4255	48S	796965	9299754	G76	9	Late ripening	PPB
399	25-Aug-18	Ronal	Subang	W4295	48S	800697	9299924	G76	7	Early-Middle Vegetative	PPB
400	25-Aug-18	Dani	Subang	WSBG01	48S	819606	9305068	TJ	5	Weed	NA
401	25-Aug-18	Dani	Subang	WSBG02	48S	818606	9307449	TJ	4	Weed	NA
402	25-Aug-18	Dani	Subang	WSBG03	48S	817010	9308291	TJ	3	Bare land	PPB
403	25-Aug-18	Dani	Subang	WSBG04	48S	815614	9305473	TJ	5	Early-Middle Vegetative	PPB
404	25-Aug-18	Dani	Subang	WSBG05	48S	812720	9307090	TJ	2	Bare land	NA
405	25-Aug-18	Dani	Subang	WSBG06-W4796	48S	813163	9308927	TJ	1	Bare land	NA
406	25-Aug-18	Dani	Subang	WSBG07	48S	810091	9308353	TJ	1	Early-Middle Vegetative	PPB
407	25-Aug-18	Dani	Subang	WSBG08	48S	807711	9307047	TJ	0	Early-Middle Vegetative	PPB
408	25-Aug-18	Dani	Subang	WSBG09	48S	805446	9305278	TJ	2	Early-Middle Vegetative	PPB
409	25-Aug-18	Dani	Subang	WSBG10	48S	801330	9302763	TJ	6	Early-Middle Vegetative	PPB
410	25-Aug-18	Dani	Subang	WSBG11	48S	798223	9304119	TJ	2	Late vegetative	PPB
411	25-Aug-18	Dani	Subang	WSBG12	48S	797460	9301834	TJ	6	Early reproductive	PPB
412	26-Aug-18	Ronal	Subang	W4054	48S	783572	9295742	G76	25	Ratoon	PPB
413	26-Aug-18	Ronal	Subang	W4094	48S	788250	9295858	G76	20	Late ripening	PPB
414	26-Aug-18	Ronal	Subang	W4315R	48S	786411	9300846	G76	16	Early ripening	PPB
415	26-Aug-18	Ronal	Subang	WSBGR_1	48S	807562	9301301	G76	8	Late vegetative	PPB
416	26-Aug-18	Ronal	Subang	WSBGR_10	48S	781469	9291051	G76	34	Green beans	PPO
417	26-Aug-18	Ronal	Subang	WSBGR_11	48S	787465	9298727	G76	19	Early reproductive	PPB
418	26-Aug-18	Ronal	Subang	WSBGR_2	48S	803399	9300240	G76	8	Early-Middle Vegetative	PPB
419	26-Aug-18	Ronal	Subang	WSBGR_3	48S	794908	9302448	G76	8	Late vegetative	PPB
420	26-Aug-18	Ronal	Subang	WSBGR_4	48S	800312	9295759	G76	5	Late vegetative	PPB
421	26-Aug-18	Ronal	Subang	WSBGR_5	48S	796686	9297220	G76	9	Ratoon	PPB

422	26-Aug-18	Ronal	Subang	WSBGR_6	48S	794659	9291592	G76	17	Ratoon	PPB
423	26-Aug-18	Ronal	Subang	WSBGR_8	48S	789731	9288431	G76	28	Ratoon	PPB
424	26-Aug-18	Ronal	Subang	WSBGR_9	48S	786559	9289017	G76	29	Ratoon	PPB
425	26-Aug-18	Dani	Subang	WSBG15	48S	821851	9300941	TJ	7	Late vegetative	PPB
426	26-Aug-18	Dani	Subang	WSBG16	48S	819611	9298898	TJ	11	Early-Middle Vegetative	PPB
427	26-Aug-18	Dani	Subang	WSBG17	48S	819430	9295515	TJ	13	Late vegetative	PPB
428	26-Aug-18	Dani	Subang	WSBG18	48S	817764	9290422	TJ	20	Early ripening	PPB
429	26-Aug-18	Dani	Subang	WSBG19	48S	814958	9294860	TJ	12	Early-Middle Vegetative	PPB
430	26-Aug-18	Dani	Subang	WSBG20	48S	813669	9297781	TJ	10	Early-Middle Vegetative	PPB
431	26-Aug-18	Dani	Subang	WSBG21	48S	813687	9303152	TJ	5	Early-Middle Vegetative	PPB
432	26-Aug-18	Dani	Subang	WSBG22	48S	810194	9302827	TJ	5	Early-Middle Vegetative	PPB
433	26-Aug-18	Dani	Subang	WSBG23	48S	819375	9302872	TJ	7	Early-Middle Vegetative	PPB
434	26-Aug-18	Dani	Subang	WSBG24	48S	816417	9304378	TJ	5	Early-Middle Vegetative	PPB
435	26-Aug-18	Dani	Subang	WSBG25	48S	809243	9305969	TJ	3	Early-Middle Vegetative	PPB
436	30-Aug-18	Ronal	Karawang	W5347R	48S	755467	9306017	G76	-4	Early-Middle Vegetative	PPB
437	30-Aug-18	Ronal	Karawang	W5367	48S	755547	9307619	G76	6	Early-Middle Vegetative	PPB
438	30-Aug-18	Ronal	Karawang	W5377	48S	757996	9308323	G76	7	Ratoon	PPB
439	30-Aug-18	Ronal	Karawang	W5387	48S	753219	9307867	G76	9	Early-Middle Vegetative	PPB
440	30-Aug-18	Ronal	Karawang	W5404	48S	759063	9309067	G76	7	Ratoon	PPB
441	30-Aug-18	Ronal	Karawang	W5427	48S	754587	9310218	G76	12	Ratoon	PPB
442	30-Aug-18	Ronal	Karawang	W5474	48S	759616	9311107	G76	5	Ratoon	PPB
443	30-Aug-18	Ronal	Karawang	W5514	48S	754785	9312951	G76	5	Land Use Change	NA
444	30-Aug-18	Ronal	Karawang	W5534	48S	759691	9313723	G76	7	Late ripening	PPB
445	30-Aug-18	Ronal	Karawang	W5607	48S	759485	9315277	G76	3	Late ripening	PPB
446	30-Aug-18	Ronal	Karawang	W5614	48S	758076	9316606	G76	4	Ratoon	PPB

447	30-Aug-18	Ronal	Karawang	W5624	48S	755755	9315632	G76	3	Late ripening	PPB
448	30-Aug-18	Ronal	Karawang	W5634	48S	760719	9316756	G76	3	Late vegetative	PPB
449	31-Aug-18	Ronal	Karawang	W5317	48S	769225	9305619	G76	7	Early ripening	PPB
450	31-Aug-18	Ronal	Karawang	W5357	48S	767254	9307221	G76	4	Late ripening	PPB
451	31-Aug-18	Ronal	Karawang	W5374	48S	769563	9307981	G76	1	Land preparation	PPB
452	31-Aug-18	Ronal	Karawang	W5407	48S	761703	9309398	G76	6	Ratoon	PPB
453	31-Aug-18	Ronal	Karawang	W5434	48S	762419	9309429	G76	6	Ratoon	PPB
454	31-Aug-18	Ronal	Karawang	W5444	48S	763730	9310259	G76	3	Ratoon	PPB
455	31-Aug-18	Ronal	Karawang	W5447	48S	762035	9310919	G76	5	Ratoon	PPB
456	31-Aug-18	Ronal	Karawang	W5454	48S	766309	9311167	G76	4	Early-Middle Vegetative	PPB
457	31-Aug-18	Ronal	Karawang	W5457	48S	771172	9308904	G76	0	Early-Middle Vegetative	PPB
458	31-Aug-18	Ronal	Karawang	W5484	48S	767186	9311613	G76	1	Early-Middle Vegetative	PPB
459	31-Aug-18	Ronal	Karawang	W5487	48S	760885	9311694	G76	5	Ratoon	PPB
460	31-Aug-18	Ronal	Karawang	W5494	48S	763151	9312062	G76	4	Late ripening	PPB
461	31-Aug-18	Ronal	Karawang	W5504	48S	765304	9312517	G76	5	Early ripening	PPB
462	31-Aug-18	Ronal	Karawang	W5517	48S	761519	9312494	G76	6	Late ripening	PPB
463	31-Aug-18	Ronal	Karawang	W5544	48S	767425	9313140	G76	1	Early-Middle Vegetative	PPB
464	31-Aug-18	Ronal	Karawang	W5577	48S	763257	9313509	G76	3	Early reproductive	PPB
465	31-Aug-18	Dani	Karawang	W5657	48S	755899	9319078	TJ	4	Early-Middle Vegetative	PPB
466	31-Aug-18	Dani	Karawang	W5687	48S	753991	9321449	TJ	7	Early-Middle Vegetative	PPB
467	31-Aug-18	Dani	Karawang	W5717	48S	753983	9323971	TJ	5	Early-Middle Vegetative	PPB
468	31-Aug-18	Dani	Karawang	W5744	48S	753366	9325854	TJ	2	Land preparation	PPB
469	31-Aug-18	Dani	Karawang	W5774	48S	750683	9327492	TJ	3	Early-Middle Vegetative	PPB
470	31-Aug-18	Dani	Karawang	W5787	48S	748436	9329592	TJ	2	Early-Middle Vegetative	PPB
471	31-Aug-18	Dani	Karawang	W5794	48S	745411	9329595	TJ	2	Land preparation	PPB

472	31-Aug-18	Dani	Karawang	W5827	48S	754061	9330409	TJ	1	Land preparation	PPB
473	31-Aug-18	Dani	Karawang	W5834	48S	746688	9330108	TJ	0	Early-Middle Vegetative	PPB
474	31-Aug-18	Dani	Karawang	W5874	48S	753291	9333785	TJ	1	Early-Middle Vegetative	PPB
475	01-Sep-18	Ronal	Karawang	W5234	48S	782882	9301490	G76	14	Late vegetative	PPB
476	01-Sep-18	Ronal	Karawang	W5237	48S	778134	9301851	G76	15	Late ripening	PPB
477	01-Sep-18	Ronal	Karawang	W5257	48S	768958	9303223	G76	9	Ratoon	PPB
478	01-Sep-18	Ronal	Karawang	W5264	48S	777367	9302801	G76	13	Early ripening	PPB
479	01-Sep-18	Ronal	Karawang	W5267	48S	765353	9299650	G76	14	Ratoon	PPB
480	01-Sep-18	Ronal	Karawang	W5274	48S	770409	9303286	G76	9	Ratoon	PPB
481	01-Sep-18	Ronal	Karawang	W5304	48S	772679	9304961	G76	7	Late ripening	PPB
482	01-Sep-18	Ronal	Karawang	W5307	48S	782238	9304561	G76	10	Late ripening	PPB
483	01-Sep-18	Ronal	Karawang	W5327	48S	781265	9306171	G76	6	Early reproductive	PPB
484	01-Sep-18	Ronal	Karawang	W5344	48S	778082	9306783	G76	7	Late vegetative	PPB
485	01-Sep-18	Ronal	Karawang	W5354	48S	780317	9307262	G76	6	Late vegetative	PPB
486	01-Sep-18	Dani	Karawang	W5347D	48S	781282	9312462	TJ	8	Early-Middle Vegetative	NA
487	01-Sep-18	Dani	Karawang	W5364	48S	770863	9306774	TJ	2	Early ripening	PPB
488	01-Sep-18	Dani	Karawang	W5464	48S	786359	9312386	TJ	-1	Early-Middle Vegetative	PPB
489	01-Sep-18	Dani	Karawang	W5467	48S	784295	9313414	TJ	-2	Early-Middle Vegetative	PPB
490	01-Sep-18	Dani	Karawang	W5477	48S	772832	9310841	TJ	-1	Early-Middle Vegetative	PPB
491	01-Sep-18	Dani	Karawang	W5529	48S	774829	9312925	TJ	-1	Early-Middle Vegetative	PPB
492	01-Sep-18	Dani	Karawang	W5554	48S	778092	9314594	TJ	-2	Early-Middle Vegetative	PPB
493	01-Sep-18	Dani	Karawang	W5564	48S	785375	9314012	TJ	0	Early reproductive	NA
494	01-Sep-18	Dani	Karawang	W5617	48S	775726	9316351	TJ	0	Early-Middle Vegetative	PPB
495	03-Sep-18	Dani	Karawang	W5837	48S	735696	9331026	MI A1	1	Early-Middle Vegetative	PPB

496	03-Sep-18	Dani	Karawang	W5847	48S	738077	9330595	TJ	4	Late vegetative	PPB
497	03-Sep-18	Dani	Karawang	W5864	48S	735346	9331961	TJ	0	Early-Middle Vegetative	PPB
498	03-Sep-18	Dani	Karawang	W5894	48S	736660	9334509	TJ	0	Late vegetative	PPB
499	03-Sep-18	Dani	Karawang	W5897	48S	734071	9334494	TJ	0	Late vegetative	PPB
500	03-Sep-18	Dani	Karawang	W5904	48S	732868	9336068	TJ	2	Early-Middle Vegetative	PPB
501	03-Sep-18	Dani	Karawang	W5907	48S	732200	9336923	TJ	2	Bare land	PPB
502	03-Sep-18	Dani	Karawang	WKRWG1	48S	742304	9330507	TJ	1	Early-Middle Vegetative	PPB
503	03-Sep-18	Dani	Karawang	WKRWG2	48S	741329	9331931	TJ	2	Early-Middle Vegetative	PPB
504	04-Sep-18	Ronal	Karawang	W4877	48S	745448	9278717	G76	101	Early-Middle Vegetative	PPB
505	04-Sep-18	Ronal	Karawang	W4914	48S	743423	9281191	G76	72	Ratoon	PPB
506	04-Sep-18	Ronal	Karawang	W4917	48S	747757	9281861	G76	75	Ratoon	PPB
507	04-Sep-18	Ronal	Karawang	W4924	48S	743271	9282950	G76	51	Ratoon	PPB
508	04-Sep-18	Ronal	Karawang	W4927	48S	747924	9282512	G76	69	harvested	PPB
509	04-Sep-18	Ronal	Karawang	W4944	48S	746102	9284782	G76	37	Ratoon	PPB
510	04-Sep-18	Ronal	Karawang	W4967	48S	747555	9288557	G76	36	Other crop	PPO
511	04-Sep-18	Ronal	Karawang	W4997	48S	744556	9289816	G76	27	Ratoon	PPB
512	04-Sep-18	Ronal	Karawang	W5097	48S	744913	9295640	G76	23	Ratoon	PPB
513	04-Sep-18	Ronal	Karawang	W5114	48S	746488	9297596	G76	22	Early ripening	PPB
514	04-Sep-18	Ronal	Karawang	W5177	48S	748656	9300065	G76	16	Land preparation	PPB
515	04-Sep-18	Ronal	Karawang	W5214	48S	748812	9301766	G76	14	Ratoon	PPB
516	04-Sep-18	Ronal	Karawang	W5287	48S	750036	9303949	G76	14	Early reproductive	PPB
517	04-Sep-18	Dani	Karawang	W5594	48S	764892	9315461	TJ	-1	Late vegetative	PPB
518	04-Sep-18	Dani	Karawang	W5644	48S	769227	9318295	TJ	2	Early-Middle Vegetative	PPB
519	04-Sep-18	Dani	Karawang	W5654	48S	772439	9318029	TJ	0	Early-Middle Vegetative	PPB
520	04-Sep-18	Dani	Karawang	W5674	48S	770943	9319581	TJ	1	Land preparation	PPB

521	04-Sep-18	Dani	Karawang	W5677	48S	761074	9322183	TJ	5	Early-Middle Vegetative	PPB
522	04-Sep-18	Dani	Karawang	W5684	48S	768082	9321029	TJ	1	Early-Middle Vegetative	PPB
523	04-Sep-18	Dani	Karawang	W5754	48S	765102	9326511	TJ	3	Early-Middle Vegetative	PPB
524	04-Sep-18	Dani	Karawang	W5797	48S	761782	9328696	TJ	5	Early-Middle Vegetative	PPB
525	04-Sep-18	Dani	Karawang	W5887	48S	759170	9332807	TJ	2	land preparation	PPB
526	04-Sep-18	Dani	Karawang	WKRWG3	48S	770835	9313531	TJ	1	Early-Middle Vegetative	PPB
527	04-Sep-18	Dani	Karawang	WKRWG4	48S	764274	9319077	TJ	0	Early-Middle Vegetative	PPB
528	04-Sep-18	Dani	Karawang	WKRWG5	48S	755854	9329701	TJ	-1	Ratoon	PPB
529	04-Sep-18	Dani	Karawang	WKRWG6	48S	760025	9326531	TJ	2	Early-Middle Vegetative	PPB

Note: G76 = Garmin 76CSx, TJ = Trimble Juno, PPO = Paddy-paddy-other crop, PPP = Paddy-paddy-paddy, POB = Paddy-other crop-bare land, PPB = Paddy-paddy-bare land, PPT = Paddy-paddy-tobacco, PTB = Paddy-tobacco-bare land, PB = Paddy-bare land, and NA = Not applicable

Appendix 6 The examples of webcam images

BALITBANGTAN CCTV16 2014-01-28 08:49:18

BALITBANGTAN CCTV37 2014-01-06 08:56:10

BALITBANGTAN CCTV16 2015-03-19 07:12:25

BALITBANGTAN CCTV37 2014-02-27 07:16:09

BALITBANGTAN CCTV16 2015-11-29 08:54:58

BALITBANGTAN CCTV37 2014-08-02 09:34:29

BALITBANGTAN CCTV16 2015-12-25 07:17:52

BALITBANGTAN CCTV37 2016-06-22 07:59:43

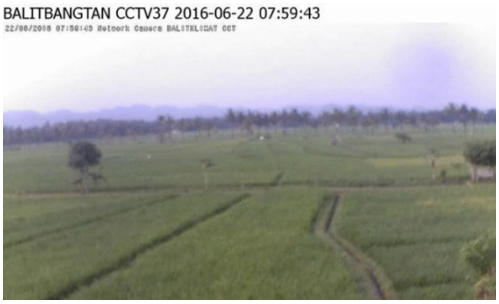

Appendix 7 The examples of field survey photos.

E2478- 20 July 2018

W0183 – 17 August 2018

E2524 – 21 July 2018

W4535 – 24 August 2018

E2872 – 21 July 2018

W4255 – 25 August 2018

E0571 – 1 August 2018

W5717 – 31 August 2018